Dissertation
submitted to the
Combined Faculties for the Natural Sciences and for Mathematics
of the Ruperto-Carola University of Heidelberg, Germany
for the degree of
Doctor of Natural Sciences

Put forward by
Dipl.-Phys. Werner Maneschg
Born in: Brunico, Italy
Oral examination: May 11, 2011

Low-energy solar neutrino spectroscopy with Borexino: Towards the detection of the solar pep and CNO neutrino flux

Referees:
Prof. Dr. Wolfgang Hampel
Prof. Dr. Wolfgang Krätschmer

Low-energy solar neutrino spectroscopy with Borexino:
Towards the detection of the solar *pep* and CNO neutrino flux

Borexino is a large-volume organic liquid scintillator detector of unprecedented high radiopurity which has been designed for low-energy neutrino spectroscopy in real time. Besides the main objective of the experiment, the measurement of the solar ^{7}Be neutrino flux, Borexino also aims at detecting solar neutrinos from the *pep* fusion process and from the CNO cycle. The detectability of these neutrinos is strictly connected to a successful rejection of all relevant background components. The identification and reduction of these background signals is the central subject of this dissertation. In the first part, contaminants induced by cosmic-ray muons and muon showers were analyzed. The dominant background is the cosmogenic radioisotope ^{11}C. Its rate is ∼10 times higher than the expected combined *pep* and CNO neutrino rate in the preferred energy window of observation at [0.8,1.3] MeV. Since ^{11}C is mostly produced under the release of a free neutron, ^{11}C can be tagged with a threefold coincidence (TFC) consisting of the muon signal, the neutron capture and the subsequent ^{11}C decay. By optimizing the TFC method and other rejection techniques, a ^{11}C rejection efficiency of 80% was achieved. This led to a neutrino-to-background ratio of 1:1.7, whereby 61% of statistics is lost. The second part of the work concerns the study of the external background. Especially long-range 2.6 MeV gamma rays from ^{208}Tl decays in the outer detector parts can reach the scintillator in the innermost region of the detector. For the determination of the resultant spectral shape, a custom-made ∼5 MBq ^{228}Th source was produced and an external calibration was carried out for the first time. The obtained calibration data and the achieved ^{11}C rejection efficiency will allow for the direct detection of solar *pep* and possibly also CNO neutrinos with Borexino.

Spektroskopie niederenergetischer Sonnenneutrinos in Borexino:
Analysen zum Nachweis des solaren *pep*- und CNO-Neutrinoflusses

Borexino ist ein großvolumiger Detektor, der mit organischem Flüssigszintillator von einer bisher noch nie erreichten geringen Eigenradioaktivität gefüllt ist und für die Echtzeitspektroskopie niederenergetischer Neutrinos konzipiert wurde. Neben dem Hauptziel des Experiments, der Messung des solaren ^{7}Be Neutrinoflusses, wird auch der Nachweis von Sonnenneutrinos aus dem *pep*-Fusionsprozess und dem CNO-Zyklus angestrebt. Die Nachweisbarkeit dieser Neutrinos hängt von der erfolgreichen Unterdrückung aller relevanten Untergrundkomponenten ab. Die Identifizierung und Reduktion verschiedener Untergrundsignale ist das Hauptthema dieser Dissertation. Im ersten Teil der Arbeit werden myon-induzierte Untergründe analysiert. Der dominierende Untergrund ist das kosmogene Radioisotop ^{11}C, dessen Rate ∼10 mal höher ist als die erwartete *pep*- und CNO-Neutrinorate im bevorzugten Beobachtungsfenster von [0.8,1.3] MeV. Da ^{11}C meistens unter Emission eines Neutrons entsteht, kann ^{11}C über eine Dreifachkoinzidenz (DFK), bestehend aus dem Myon-Signal, dem Neutroneinfang und dem ^{11}C-Zerfall identifiziert werden. Die DFK-Methode und weitere Techniken zur Unterdrückung von ^{11}C wurden optimiert, dadurch wurde eine ^{11}C-Unterdrückungseffizienz von 80% und ein Neutrino-zu-Untergrund-Verhältnis von 1:1.7 erreicht. Dabei geht 61% der Statistik verloren. Der zweite Teil der Arbeit beschäftigt sich mit der Untersuchung des externen Untergrundes. Vorwiegend langreichweitige 2.6 MeV Photonen, die durch ^{208}Tl Zerfälle in den äußeren Detektorkomponenten emittiert werden, können den Szintillator im inneren Bereich des Detektors erreichen. Um die spektrale Form des externen Untergrundes zu bestimmen, wurde eine ∼5 MBq ^{228}Th-Quelle eigens angefertigt und damit erstmals eine externe Kalibration durchgeführt. Die gewonnenen Kalibrationsdaten werden zusammen mit den optimierten ^{11}C-Unterdrückungsmethoden den direkten Nachweis solarer *pep*- und womöglich auch CNO-Neutrinos in Borexino ermöglichen.

Contents

1 Introduction

Μὰ Δί ', ὦ ἄνδρες δικασταί,
ἐπεὶ τὸν μὲν ἥλιον λίθον φησὶν εἶναι, τὴν δὲ σελήνην γῆν.

No, by Zeus, judges, since he says
that the sun is a stone and the moon is earth.

Plato, Apol. D 26

Our Sun has been often referred to as the *Rosetta Stone* of astrophysics. Due to its proximity to our home planet, astronomers have the opportunity to study in detail dynamic processes occurring in the visible outer stellar layers and to record vast spectroscopic data from the solar photosphere. Over the last decades, the detection of solar neutrinos and helioseismogical measurements has provided information about the interior of the Sun. Several theoretical models of the solar structure were developed, they make use of some of this information (as boundary conditions) and predict subsequent observables.
The so-called *Standard Solar Model* (SSM) which is based on the thermal and mechanical equilibrium, the nuclear energy production and the observed chemical abundances in the photosphere, also makes predictions about the solar neutrino fluxes. Since the early beginnings, solar neutrino experiments have faced several discrepancies between the SSM predicted and measured solar neutrino fluxes, known as the "solar neutrino problems" [1, 2, 3, 4]. The puzzle was finally solved by the non-astrophysical explanation of the existence of neutrino oscillations, which provided the first hint of physics beyond the Standard Model of elementary particle physics. This discovery has led to a rapidly evolving field of neutrino physics which includes elementary particle physics, astrophysics, cosmology and geology.

The work presented in this thesis has been carried out in the framework of the solar neutrino experiment Borexino. It is located deep underground at the *Laboratori Nazionali del Gran Sasso* in Middle Italy and has collected data since May 2007. The detector is filled with 300 tons of organic liquid scintillator of unprecedented radiopurity, which has the unique possibility to probe solar neutrinos in real time and in the sub-MeV region, but also to detect geo-, reactor- and supernova-antineutrinos.
Besides the already measured solar ^{7}Be and ^{8}B neutrino fluxes, Borexino also has the potential in principle to measure neutrinos from the *pep* fusion reactions and from the CNO cycle taking place in the solar core. Both neutrino fluxes can be observed in Borexino in the same energy window and they are of special interest. On the one hand, the *pep* neutrino rate is almost model-independently related to the rate of the *pp* neutrinos, which constitute $\sim$90% of the total solar neutrino flux. On the other hand, the CNO cycle is expected to contribute only $\sim$1.5% to the total solar energy production, but to become dominant in heavy and late-stage stars. Thus both measurements are of paramount importance for solar physics and the development of a theory of the structure and evolution of stars.

The objective of this thesis was the identification, characterisation and rejection of backgrounds in Borexino, aiming at detecting the solar *pep* and CNO neutrinos.
A primary background is induced by the residual muon flux at the experimental site. Muons and muon showers crossing the scintillator can produce radioisotopes in large quantities which mimic the neutrino signals. As shown in this work, a detailed data analysis was carried out in order to describe the muons and muon-induced signals. Based on this analysis a sophisticated strategy, including a special coincidence method, has been applied and optimized to suppress the muon-

induced backgrounds.
The external background was found to be a second relevant contaminant. It mainly consists of gamma radiation which originates from radioimpurities in the outer detector parts and which can penetrate the scintillator. The strategy adopted in this project was the execution of an external calibration of the detector with a custom-made gamma source. The obtained calibration data turned out to be important not only for the upcoming *pep* and CNO neutrino analysis, but also for a broad range of other applications. This includes, among others, reliability tests of the position and energy reconstruction algorithms and comparison studies with Monte Carlo simulations.

2 Neutrinos and solar physics

The present chapter intends to give a brief overview of fundamental concepts in neutrino and solar physics, focusing on the current status of research and problems yet unsolved.

2.1 Neutrinos: a door to physics beyond the Standard Model

2.1.1 Neutrino oscillations

The concept of neutrino oscillations was originally introduced by Bruno Pontecorvo in 1958 for the neutrino and its antiparticle [5]. In the following decade the model was extended to the oscillation of flavor eigenstates by Maki et al. and Pontecorvo [6, 7]. In contrast to the present Standard Model of elementary particle physics, the neutrinos are assumed to be massive. As a consequence, the three neutrino flavor eigenstates $|\nu_\alpha\rangle$ with $\alpha = e,\mu,\tau$ are no longer eigenstates of their propagation Hamiltonian, but the propagation is described by an orthogonal basis of mass eigenstates $|\nu_i\rangle$, $i = 1,2,3$. The flavor and mass eigenstates can be related by introducing a unitary mixing matrix $U_{\alpha i}$, such that

$$|\nu_\alpha\rangle = \sum_i \mathrm{U}_{\alpha\mathrm{i}}|\nu_i\rangle. \tag{2.1}$$

For the three-flavor oscillation a (3×3) rotation matrix known as Maki-Nakagawa-Sakata-Pontecorvo matrix (MNSP matrix) is introduced. Three mixing angles are introduced which are typically denoted by θ_{12}, θ_{23} and θ_{13}. A condition for the observation of neutrino oscillations is that at least one of the angles must be different from $\pi/2$. Moreover, if CP violation occurs one has to introduce a phase δ. In case that the neutrino is its own antiparticle, two additional Majorana phases α and β have to be added. The MNSP-matrix can be expressed as the product of four separate matrices,

$$U_{MNSP} = \begin{pmatrix} 1 & 0 & 0 \\ 0 & \mathrm{c}_{23} & \mathrm{s}_{23} \\ 0 & -\mathrm{s}_{23} & \mathrm{c}_{23} \end{pmatrix} \cdot \begin{pmatrix} \mathrm{c}_{13} & 0 & \mathrm{s}_{13}\mathrm{e}^{-\mathrm{i}\delta} \\ 0 & 1 & 0 \\ -\mathrm{s}_{13}\mathrm{e}^{\mathrm{i}\delta} & 0 & \mathrm{c}_{13} \end{pmatrix} \cdot \begin{pmatrix} \mathrm{c}_{12} & \mathrm{s}_{12} & 0 \\ \mathrm{s}_{12} & \mathrm{c}_{12} & 0 \\ 0 & 0 & 1 \end{pmatrix} \cdot \begin{pmatrix} 1 & 0 & 0 \\ 0 & e^{-i\alpha} & 0 \\ 0 & 0 & e^{-i\beta} \end{pmatrix} \tag{2.2}$$

where c_{ij}=cos(ϑ_{ij}) and s_{ij}=sin(ϑ_{ij}).
Neutrinos are emitted in weak interactions as pure flavor eigenstates. The quantum mechanical probability to observe one neutrino flavor oscillating into another depends not only on the finite values of the parameters of the MNSP matrix, but also on the distance propagated by the mass eigenstates, their energy, and the mass differences between them. Since neutrinos are weakly interacting particles, the probability is expected to depend also on the medium the neutrinos have to travel through. For this reason, flavor oscillations in vacuum and in matter will be discussed separately in the following two subsections.

Oscillations in vacuum Neutrino oscillations in vacuum are described here by the simplest model, including only two-flavor mixing. In this case, the unitary mixing matrix contains one single mixing angle ϑ and no complex phase. The neutrino flavor eigenstates $|\nu_\alpha\rangle$ and $|\nu_\beta\rangle$ are given by [8]

$$\begin{pmatrix} |\nu_\alpha\rangle \\ |\nu_\beta\rangle \end{pmatrix} = \begin{pmatrix} \cos\vartheta & \sin\vartheta \\ -\sin\vartheta & \cos\vartheta \end{pmatrix} \cdot \begin{pmatrix} |\nu_1\rangle \\ |\nu_2\rangle \end{pmatrix} \tag{2.3}$$

The propagation of a neutrino born as the eigenstate $|\nu_\alpha\rangle$ can be described by means of the quantum mechanical propagation factor $e^{-i(E_1 t - p\cdot x)}$, from the stationary eigenstate solution of the Schrödinger equation, so that

$$|\nu_\alpha(x,t)\rangle = \cos\vartheta|\nu_1\rangle e^{-i(E_1 t - p\cdot x)} + \sin\vartheta|\nu_2\rangle e^{-i(E_2 t - p\cdot x)} \tag{2.4}$$

Assuming the neutrinos to be relativistic and to have small masses, the energy expressed by $E^2 = p_i^2 c^2 + m_i^2 c^4$ can be in most cases Taylor-expanded to $E + m_i^2/2E$. Herein, i stands for i = 1,2. Moreover, the time-dependent probability amplitude for the oscillation of $|\nu_\alpha\rangle$ to $|\nu_\beta\rangle$ becomes $A(|\nu_\alpha\rangle \to |\nu_\beta\rangle) = \langle\nu_\beta|\nu_\alpha(t)\rangle$. The oscillation probability $P(|\nu_\alpha\rangle \to |\nu_\beta\rangle)$ is then defined as

$$\begin{aligned} P(|\nu_\alpha\rangle \to |\nu_\beta\rangle) \equiv |A(|\nu_\alpha\rangle \to |\nu_\beta\rangle)|^2 &= |\langle\nu_\beta|\nu_\alpha(t)\rangle|^2 \\ &= \sin^2(2\vartheta) \cdot \sin^2\frac{\Delta m^2}{4E} \end{aligned} \tag{2.5}$$

with $\Delta m^2 = (m_2^2 - m_1^2)$ the neutrino mass-squared difference. The probability to observe the $|\nu_\alpha\rangle$ eigenstate is calculated in an analogous way, and turns out to be $1 - |\langle\nu_\beta|\nu_\alpha(t)\rangle|^2$. The first term in Equation (2.5) depends only on the mixing angle ϑ, while the second term determines the frequency of the oscillation via a characteristic vacuum oscillation length λ_v, given by

$$\lambda_v = \frac{4\pi E}{\Delta m^2} \tag{2.6}$$

From Equations (2.5) and (2.6) the oscillation probability $P(|\nu_\alpha\rangle \to |\nu_\beta\rangle)$ can be written as follows:

$$P(|\nu_\alpha\rangle \to |\nu_\beta\rangle) = \sin^2(2\vartheta) \cdot \sin^2\frac{\pi L}{\lambda_v} \tag{2.7}$$

On the other hand, $P(|\nu_\alpha\rangle \to |\nu_\alpha\rangle) = 1 - P(|\nu_\alpha\rangle \to |\nu_\beta\rangle)$. The variable L is the distance between the neutrino source and the detector, commonly referred to as *baseline*.
A closer look at Equation (2.5) reveals that neutrino oscillations are observable only if at least one neutrino mass m_α is different from zero and simultaneously different from the other mass m_β. This is also true for the three-flavor mixing scenario. Equation (2.6) contains one more detail: the squared masses Δm^2 are measured by the ratio λ_v/E. Under this premise, oscillation experiments using different neutrino sources and baselines are sensitive to different ranges; this is shown in Table 1 [9].

Oscillations in matter In matter, the neutrino propagation is affected by interactions [12]. Neutral current interactions (NC) mediated by the Z^0 boson add an additional potential V_{nc} to the existing Hamiltonian H_0 deduced for vacuum oscillations. However, this potential is equal for all three neutrino flavors, and does not change the relative phase difference and the conversion

Neutrino source	Baseline [m]	Energy [MeV]	Δm^2 $[eV^2]$
Solar	10^{11}	1	10^{-11}
Atmospheric	10^4-10^7	10^2-10^5	10^{-1}-10^{-4}
Reactor	10-10^5	1	10^{-2}-10^{-5}
Accelerator	10^2-10^6	10^3-10^4	10^{-1}-10^{-3}

Table 1: Characteristic values of the *baseline* L and the kinematic energy E for neutrino detection from various sources. The corresponding ranges, for which the particular configuration has the highest sensitivity for Δm^2, are given in the last column [9].

probability of one neutrino flavor into another. Charged current interactions (CC) with electrons in the solar interior, on the other hand, are only possible for $|\nu_e\rangle$. The potential V_e for $|\nu_e\rangle$ differs from that for the other flavors $|\nu_\alpha\rangle$, $\alpha = \mu,\tau$, leading to a non-negligible term V_{cc} in the Hamiltonian in matter, $H_m = H_0 + V_{CC}$, where V_{CC} is given by

$$V_{CC} = V_e - V_\alpha = \sqrt{2} G_F n_e. \tag{2.8}$$

Here G_F is the Fermi coupling constant and n_e the local electron density. The new term in the Hamiltonian leads to effective squared mass differences and mixing angles that differ from them describing the oscillations in vacuum. It follows that the acquired effective mass can enhance neutrino oscillations also for the case of small vacuum mixing angles. This oscillation enhancement is known as the Mikheyev-Smirnov-Wolfenstein effect (MSW effect) [30, 31]. For clarity its description is given here again using the two-flavor scenario. Starting from the mass matrix used in the Hamiltonian for vacuum oscillations [13, 14],

$$\left(M_V^2\right) = \frac{1}{2}\begin{pmatrix} m_e^2 + m_\alpha^2 & 0 \\ 0 & m_e^2 + m_\alpha^2 \end{pmatrix} + \frac{1}{2}\Delta m^2 \begin{pmatrix} \cos\vartheta & \sin\vartheta \\ -\sin\vartheta & \cos\vartheta \end{pmatrix} \tag{2.9}$$

the Hamiltonian for neutrino oscillations in matter is to be expanded to

$$i\frac{d}{dt}\begin{pmatrix} |\nu_\alpha\rangle \\ |\nu_\beta\rangle \end{pmatrix} = -\frac{M_m^2}{2E}\begin{pmatrix} |\nu_1\rangle \\ |\nu_2\rangle \end{pmatrix}, \tag{2.10}$$

with a mass matrix M_m^2 defined as

$$\left(M_m^2\right) = \frac{1}{2}\begin{pmatrix} m_e^2 + m_\alpha^2 - \Delta m^2\cos(2\vartheta) + 4\sqrt{2}G_F n_e E & \Delta m^2\sin(2\vartheta) \\ \Delta m^2\sin(2\vartheta) & m_e^2 + m_\alpha^2 + \Delta m^2\cos(2\vartheta). \end{pmatrix} \tag{2.11}$$

Herein, the term $2\sqrt{2}G_F n_e E$ is an approximation which is derived from the relativistic energy-momentum relation $p_i^2c^2 + m_i^2 = (E - V_{cc})^2 + V_{cc}^2 \approx E^2 - 2EV_{cc}$, for E^2 much larger than V_{cc}^2. After diagonalisation of M_m^2 one obtains two energy eigenvalues, E_1 and E_2. The related eigenstates $|\nu_{m1}\rangle$ and $|\nu_{m2}\rangle$ are admixtures of $|\nu_e\rangle$ and $|\nu_\alpha\rangle$, which are weighted by coefficients depending on a characteristic mixing angle ϑ_m, given by

$$\sin^2(2\vartheta_m) = \frac{\Delta m^2\sin(2\vartheta)}{\sqrt{(2\sqrt{2}G_F n_e E - \Delta m^2\cos(2\vartheta))^2 + (\Delta m^2\sin(2\vartheta))^2}}. \tag{2.12}$$

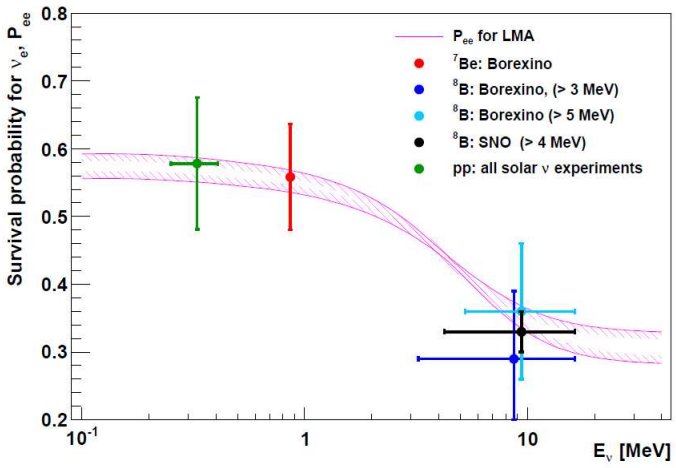

Figure 1: Predicted electron neutrino survival probability of solar neutrinos as a function of their energy under the assumption of the standard solar model BPS09(GS98) and the oscillation parameters from the MSW-LMA solution. The predicted curve contains the experimental uncertainty of the oscillations parameters. The results from different solar neutrino experiments are also included showing a good agreement with the predicted curve. However, in the transition region between matter and vacuum dominated regime a measurement was still missing in 2010 (taken from [15]).

The effective mass-squared difference Δm^2_m turns out to be

$$\Delta m^2_m = \sqrt{(\Delta m^2 \cos(2\vartheta) - 2\sqrt{2} G_F n_e E)^2 + (\Delta m^2 \sin^2(2\vartheta))^2} \tag{2.13}$$

and the characteristic oscillation length in matter becomes $\lambda_m = 4\pi E / \Delta m^2_m$. With the introduction of $\sin^2(2\vartheta_m)$, Δm^2_m and the related λ_m the probability to find an electron neutrino $|\nu_e\rangle$ in another flavor state and vice versa is formally equal to the solution in the vacuum:

$$P(|\nu_e\rangle \rightarrow |\nu_\alpha\rangle) = sin^2(2\vartheta_m) \cdot \sin^2 \frac{\pi L}{\lambda_m} \tag{2.14}$$

The probability in Equation (2.14) can vary significantly. A higher electron density n_e and a higher energy E lead to a higher probability.
The most interesting implication from Equation (2.13) is given by the condition

$$\cos(2\vartheta) = \frac{2\sqrt{2} G_F n_e E}{\Delta m^2}. \tag{2.15}$$

If this case appears, $\sin^2(2\vartheta_m)$ becomes equal to 1 and it is independent of the value of ϑ. The mixing angle ϑ_m must be equal to $\pi/4$, which leads to a maximal mixing of the eigenstates $|\nu_e\rangle$ and $|\nu_\alpha\rangle$. The phenomenon is known as the MSW resonance. This happens if the neutrino energy E is large enough and/or if the electron density in the region that the neutrino passes through is high enough (compare with Equation (2.15)). This energy limit is defined here by E_{min}. Below E_{min} the MSW effect is weak and the oscillation properties of the neutrinos can be approximated by the vacuum solution. In the vacuum dominated regime the survival probability P_{ee} is given by

Parameter	Best fit value (1σ and 3σ)
Δm^2_{21}	$7.59\pm0.20(^{+0.61}_{-0.69})\times10^{-5}$ eV^2
Δm^2_{31}	-2.36$\pm$0.11($\pm$0.37)$\times10^{-3}$ eV^2
	+2.46$\pm$0.12($\pm$0.37)$\times10^{-3}$ eV^2
ϑ_{12}	$34.4\pm1.0\ (^{+0.018}_{-0.014})^\circ$
ϑ_{23}	$42.8\pm\ ^{+4.7}_{-2.9}\ (^{+10.7}_{-7.3})^\circ$
ϑ_{13}	$5.6\ ^{+3.0}_{-2.7}\ (<12.5)^\circ$
δ	$\in[0^\circ,360^\circ]$

Table 2: Best fit values for the six free parameters of the MNSP matrix obtained from the three-flavor oscillation global analysis in [11]. The uncertainties of the values are given at the 1σ (3σ) level.

1-(1/2sin$^2(2\vartheta)$), while in the matter dominated regime it is sin$^2(\vartheta)$. A transition region around E_{min} between the vacuum and matter enhanced oscillation region is expected.
A further distinction is sometimes required: the electron density n_e might change along the path of the neutrinos, i.e. during their propagation time t. Thus, $n_e = n_e(t)$ and the Hamiltonian becomes time-dependent $H = H(t)$. As a consequence, the mixing angle changes in time and a transition from one eigenstate admixture $|\nu_{m1}\rangle$ to the other $|\nu_{m2}\rangle$ can take place.

Neutrinos from the Sun (see Section 2.2) are ideal probes for the observation of neutrino oscillations in matter (including the MSW effect) and in vacuum. Figure 1 depicts the predicted survival probability of neutrinos of different energies originating from the Sun. In the vacuum dominated regime below $\lesssim$1 MeV one expects $P_{ee} \approx 0.6$, in the matter dominated region above $\gtrsim$4 MeV $P_{ee} \approx$ 0.33. The values obtained from all solar neutrino experiments so far are also represented.

Global analysis of oscillation data Various experiments with solar, atmospheric and man-made neutrino sources have implied non-trivial lepton mixing angles, as well as non-zero and non-degenerate neutrino masses. Their values are extremely suppressed with respect to the masses of the other electrically charged fermions of the Standard Model. The first solar neutrino experiments (Homestake, SAGE, GALLEX/GNO) originally allowed four regions in the parameter space Δm^2-$sin^2(2\vartheta)$. The four possible solutions were: the "small mixing angle solution"(SMA, $\Delta m^2_{12} \approx 10^{-5}$ eV^2, sin$^2(2\vartheta) \approx 10^{-2}...10^{-3}$), the "large mixing angle solution" (LMA, $\Delta m^2_{12} \approx 10^{-4}...10^{-5}$ eV^2, sin$^2(2\vartheta) > 0.5$), the "low solution" (LOW, $\Delta m^2_{12} \approx 10^{-7}$ eV^2, sin$^2(2\vartheta) \approx 0.9$), and the "just-so solution" ($\Delta m^2_{12} < 10^{-9}$ eV^2). During the last decade global analyses of all available oscillation data found that the experimental results are in best agreement with the predictions of the LMA solution. The most updated analysis from 2010 is reported in [11]. Table 2 summarizes the results of the oscillation observables obtained in this study.

2.1.2 Open questions in the neutrino sector

Some phenomenological properties of neutrinos are currently under extensive study.
The exact value of the mixing angle ϑ_{13} is a high-priority topic, with several experiments under way searching for neutrino oscillations induced by this angle.
Concerning the neutrino masses, there are three main questions: What is the hierarchy of the three different neutrino masses?, What is the mass of the lightest neutrino mass (absolute mass scale)?, Are neutrinos Dirac or Majorana particles and why are neutrino masses so small compared to the other (electrically charged) fermions in the Standard Model?

Mixing angle ϑ_{13} The last unknown mixing angle is ϑ_{13}. It is constrained to be small compared to the other angles. The limit on the squared sinus of the appropriate angle is given in Table 2 (see Section 2.1). Note that currently ϑ_{13} cannot be distinguished from zero. The current best bounds value of ϑ_{13} stem from the CHOOZ reactor experiment combined with atmospheric, long-baseline and solar neutrino experiments [16, 17]. Moreover, from the parametrisation of the MNSP matrix in Equation (2.2) one can deduce that the CP violating Dirac phase δ has no effect if ϑ_{13} is zero. Leptonic CP violation will manifest itself in a difference of the vacuum oscillation probabilities for neutrinos and antineutrinos. A non-zero value of ϑ_{13} would also have a large impact on other fields. For instance, leptogenesis, which provides a very attractive mechanism to explain the generation of the matter-antimatter asymmetry in the early Universe, requires CP violation in the lepton sector in order to work [18].
A detailed review of the current status and future prospects in the investigation of ϑ_{13} is given in [10, 19].

Neutrino masses So far, neutrino oscillation experiments have provided information about the mass-squared differences Δm^2, but not absolute values of the single neutrino masses m_i, $i = 1,2,3$ (see Equation (2.5)). There are two possibilities: (1) a first possibility is a normal hierarchy (NH), with $m_3 > m_2 > m_1$, $m_2^2 = m_1^2 + \Delta m_{21}^2$ and $m_3^2 = m_1^2 + \Delta m_{31}^2$; or (2) an inverted hierarchy (IH), which $m_2 > m_1 > m_3$, $m_2^2 = m_3^2 + \Delta m_{21}^2$ and $m_1^2 = m_3^2 + \Delta m_{31}^2$. Finally, a quasi-degenerate scenario is given in case $m_{1,2,3}^2 \gg \Delta m_{21}^2, \Delta m_{31}^2$. The determination of the real neutrino mass ordering, i.e. the sign of Δm_{31}, and the determination of the absolute mass scale are the major goals of current research.
Another fundamental question is whether neutrinos have a Majorana or a Dirac mass. If neutrinos have a Majorana mass term, neutrinos are their own antiparticles, and a phenomenological consequence is that the neutrinoless double beta decay ($0\nu\beta\beta$) is possible. This decay of certain nuclei, $(A,Z) \rightarrow (A,Z+2) + 2e^-$, which has not yet been observed[1], clearly violates lepton number by two units (like in the case of leptogenesis) and is being intensively searched for. The current best limit for the half-life of the $0\nu\beta\beta$ decay was obtained for ^{76}Ge, $T_{1/2}$>1.9×10^{25} y at 90% C.L. [21]. The decay width of the $0\nu\beta\beta$ is estimated via the relation

$$\Gamma = G_0 |M^{0\nu}|^2 |m_{ee}|^2, \tag{2.16}$$

where G_0 is the phase space factor, $M^{0\nu}$ the nuclear matrix element (NME) and m_{ee} the so-called "effective mass". m_{ee}, which is proportional to the amplitude for this process, is defined as

$$m_{ee} = \sum_{i=1}^{3} U_{ei}^2 m_i, \tag{2.17}$$

with U_{ei} being the coefficients in the first line of the MNSP matrix in Equation (2.2), m_i the individual neutrino masses.

Figure 2 shows m_{ee} in dependence of the lightest neutrino mass (typically m_3 or m_1, depending on the normal or inverted hierarchy) [22, 23]. The same figure also depicts the ranges that can be achieved with the current $0\nu\beta\beta$ decay experiment GERDA and the regimes (in grey) that are

[1] There is a claim by a subgroup of the Heidelberg-Moscow collaboration[20], but the results are controversial and still have to be confirmed by other experiments.

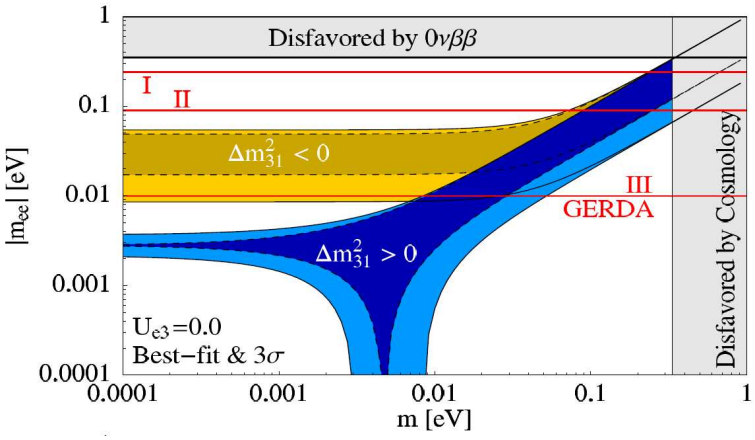

Figure 2: The effective mass m_{ee} as function of the smallest neutrino mass m. The θ_{13}-dependent matrix element was set to $U_{e3} = 0$. 3σ ranges are depicted for the NH (blue) and IH (yellow) hierarchy. For the dark blue and dark yellow regions only the Majorana phases were modulated, while in the light regions all oscillation parameters were modulated within 3σ (taken from [23]).

excluded from previous $0\nu\beta\beta$ experiments and from cosmological limits on the sum of neutrino masses.

If neutrinos are Majorana particles, then it can be demonstrated that the neutrino mass matrix contains two states: $(m^D)^2/m_R^M$ and m_R^M with m^D being the Dirac mass term and m_R^M being the Majorana mass term, R stays for right-handed chirality. Assuming m^D being of the order of the other fermions and m_R^M large enough, one can obtain neutrino masses that are comparable with the expected values for ν_e, ν_μ and ν_τ. In other words, the neutrino mass scale would turn out to be inversely proportional to the scale of its origin. This so-called *see-saw mechanism* [29] is the most prominent explanation for the smallness of the neutrino masses. Thus, the confirmation of the Majorana character of neutrinos would also be a crucial test for the *see-saw mechanism*.

2.1.3 Own analysis: potential of near-future neutrino mass experiments

Together with A. Merle and W. Rodejohann I performed a statistical analysis of the interplay among near-future neutrino mass experiments [23]. In this study, we combined the information of different neutrino mass observables that will be obtained in future $0\nu\beta\beta$ decay experiments, cosmology and direct searches for neutrino mass including realistic uncertainties. Especially the "theoretical" uncertainty for the mass derived from $0\nu\beta\beta$ decay, originating from the highly non-trivial calculations of the nuclear matrix element (NME) was taken into account in the total uncertainty budget as follows:

$$\sigma(|m_{ee}|) = (1+\zeta)(|m_{ee}| + \sigma(|m_{ee}|_{exp})) - |m_{ee}|, \tag{2.18}$$

where ζ parameterizes the NME error and $\sigma(|m_{ee}|_{exp})$ the experimental error.
Here, we consider only the inverted mass hierarchy (IH), which is entirely covered (as shown in Figure 2) by the sensitivity regions of the envisioned three phases (I-III) of the $0\nu\beta\beta$ decay experiment GERDA. Given the case that the effective mass m_{ee} would lie in the IH region, an

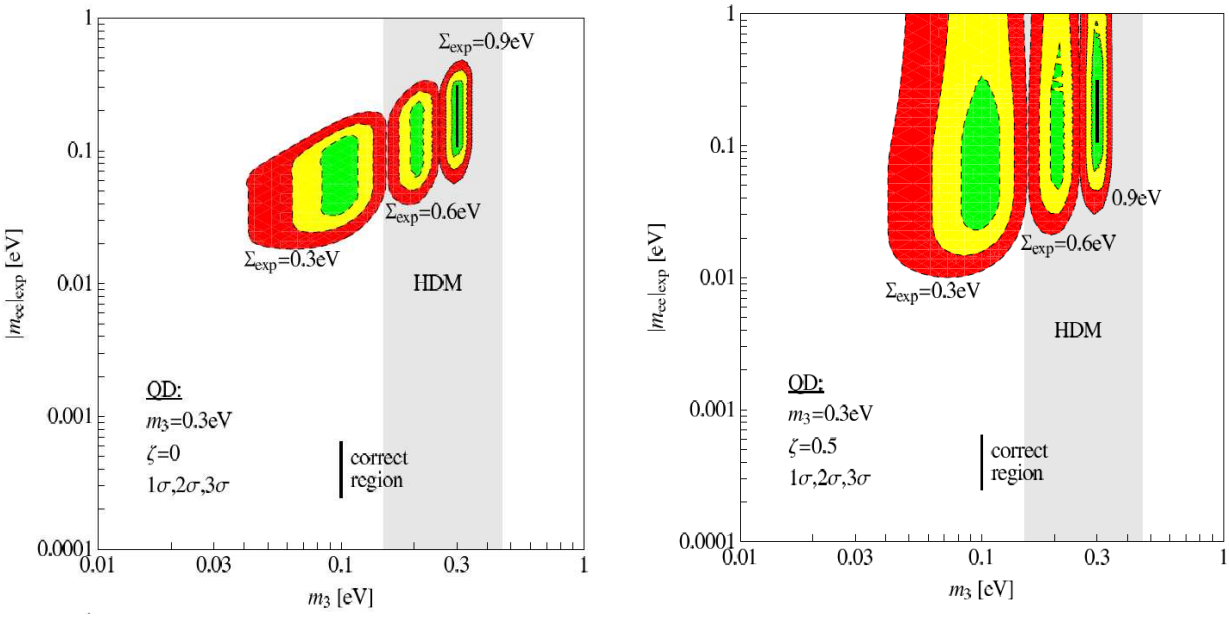

Figure 3: Combining the neutrino mass information from near-future $0\nu\beta\beta$ decay experiments, cosmology and direct search for neutrino mass: 1σ, 2σ and 3σ regions in the classical plane m_3-$|m_{ee}|$. The contour regions with solid lines used the realistic value Σ=0.9 eV, while those with dashed lines assumed 2 incorrect cosmological measurements Σ=0.6 eV, 0.3 eV. The coefficient ζ describing the uncertainty in the calculation of the Nuclear Matrix Element increases from the left (ζ=0) to the right panel (ζ=0.5).

observation of m_{ee} would still be affected by the "theoretical" NME error and would possibly allow the lightest neutrino mass to vary over a larger region. By taking into consideration other neutrino mass observables the parameter space can be restricted.
For this purpose we considered the sum of neutrino masses, which is obtained from cosmological observations

$$\Sigma = m_1 + m_2 + m_3, \tag{2.19}$$

and the kinematic neutrino mass from direct searches for neutrino mass

$$m_\beta = \sqrt{\sum_{i=1}^{3} U_{ei}^2 m_i^2}. \tag{2.20}$$

Cosmology is expected to probe values of Σ down to the 0.1 eV range [27]. A conservative upper limit obtained so far from the WMAP 5-year data is 1 eV. On the other hand, the upcoming experiment KATRIN has a 5σ discovery potential of 0.35 eV for m_β [28].
We investigated three realistic situations assuming "true values" for the different neutrino mass observables. For the case that is presented here we assumed: m_3=0.3 eV, $|m_{ee}|$=0.11-0.30 (variable due to the two Majorana phases), m_β=0.3 eV and Σ=0.9 eV. Different subcases were numerically investigated for different values of ζ. The results from the statistical analysis for two subcases of ζ are depicted in Figure 3. The true values of m_3 and $|m_{ee}|$ are marked by the vertical black lines. The scenario can be reproduced rather accurately by the three neutrino mass observables, since all of them provide non-trivial signals. In the case that the NME error becomes larger, the value of

m_3 would still be precise, while that of $|m_{ee}|$ evidently increases.
Figure 3 also contains scenarios (dashed lines) in which a wrong value for the cosmological observable Σ was deduced; there are many models in literature which lead to erroneous values for Σ.
Further details about this analysis including more subcases and possible constraints on the neutrino mass can be found in [23].

2.2 Solar physics

Our Sun is unique amongst stars in that a large number of its physical properties are known with a high precision. The close distance to the Sun allows a precise measurement of its radius, its mass, its energy spectrum, its luminosity including periodical modulations and its rotation. Moreover, geological surveys of planets and interplanetary material like meteorites have revealed rich information about the age, stability and composition of the Sun.
From the astrophysical point of view the Sun is a main-sequence star which is an ideal candidate to prove our ideas of the internal structure of stars. A well understood and tested model can be transferred to other types of stars and to their evolution. This emphasizes the need to collect information starting from the photosphere and going down to the core of the Sun and to test theoretical predictions.

2.2.1 The Standard Solar Model

So-called Standard Solar Models assume the Sun to be spherically symmetric, ignoring rotation and the magnetic field. For this case the stellar structure can be expressed by means of four equations. They include the conservation of mass [25, 26]

$$\frac{dm(r)}{dr} = 4\pi r^2 \rho(r) \tag{2.21}$$

the hydrostatic equilibrium which balances the radiative pressure against gravity

$$\frac{dp}{dr} = -\rho(r)\frac{Gm(r)}{r^2} \tag{2.22}$$

the energy transport with temperature at a given point

$$\frac{dT}{dr} = \nabla \frac{T}{p}\frac{dp}{dr} \tag{2.23}$$

and the energy production

$$\frac{dL}{dr} = 4\pi r^2 \left[\rho\epsilon - \rho\frac{d}{dt}\left(\frac{u}{\rho} + \frac{p}{\rho}\frac{d\rho}{dt}\right)\right] . \tag{2.24}$$

Here r denotes the distance from the solar center, p is the pressure, m is the mass within a radius r, ρ is the density and T the temperature. G is the gravitation constant. L stands for the flow of energy per time through an intermediate sphere of radius r, ϵ is the rate of nuclear energy generation per unit mass and time, u corresponds to the internal energy per unit volume. The

temperature gradient is given by $\nabla = d \ln T / d \ln p$ and is determined by the energy transport mode. In case of radiation $\nabla \equiv \nabla_{rad}$ is given by the equation:

$$\nabla_{rad} = \frac{3}{16\pi\sigma c G} \frac{\kappa p}{T^4} \frac{L(r)}{m(r)} \tag{2.25}$$

herein c is the speed of light in the medium, σ the Stefan-Boltzmann constant, κ the opacity defined via the mean free path of a photon $\lambda = 1/(\kappa\rho)$. In regions where the adiabatic transport of energy becomes dominant in comparison to radiation, the layers become unstable and the energy is transported mainly by convection. In the case of the Sun, the convection zone starts at $\sim 0.71 R_\odot$. Close to the surface the convection is mixed with turbulence which can be solved in terms of 3D- and time-dependent hydrodynamics. At the surface it manifests itself in form of granulation and super-granulation.
Since the main aim of solar models is the description of the stellar evolution over the entire lifetime of the Sun, an additional equation is strongly required which models the change of elemental abundances in our Sun due to nuclear reactions. For hydrogen it is expressed via

$$\frac{\partial X}{\partial t} = R_H + \frac{1}{r^2 \rho} \frac{\partial}{\partial r} \left[r^2 \rho \left(D_H \frac{X}{r} + V_H X \right) \right] \tag{2.26}$$

with R_H being the rate of change in hydrogen abundance, D_H the diffusion coefficient and V_H the settling speed. Equations for other elements X_i are similar.
With these ingredients and with the estimations of the starting conditions {p, T, L, X_i, ρ} the description of the stellar structure can be calculated numerically. The scheme is the following [32]: A SSM takes as constraints the age of the Sun (4.57×10^9 y; so-called "zero-age"), the radius ($R_\odot = 6.9598 \times 10^{10}$ cm), the luminosity ($L_\odot = 3.8418 \times 10^{33}$ erg s^{-1}), several cross section factors for the nuclear interactions and abundances of the heavier elements (e.g. C, N, O, Ne, Mg, Si, S, Ar, Fe). Free parameters are the initial helium abundance and convective energy transport parameters. Then, the implemented model is simulated for equidistant time intervals. At the end of each step the Equations (2.21-2.24) and the abundances are recalculated and used as input for the next time interval calculation. The successful simulation must match the physical properties of the Sun at present time like the radius, abundances and luminosity. In addition, predictions about neutrino fluxes from the nuclear reactions, the speed of sound and the density profiles etc. are made, which can be tested with direct measurements or compared to helioseismological observations (see Section 2.2.3).
A new calculation of the standard solar model using the best current input parameters is released, which is typically denoted by the initials of the authors and the year of publication. For the determination of the chemical abundances, the same convention is in use.

However, SSM calculations are affected by uncertainties in the initial boundary conditions like the opacity and by the complexity of the included microscopic physics, of diffusion and of thermodynamic processes.
The most remarkable uncertainty is related to the chemical abundance, which is one of the input parameters for the Standard Solar Models. Spectroscopic measurements of meteorites and especially of the solar photosphere are used for the estimation of the abundances. The standard values were established by Grevesse and Sauval using photospheric observations in 1998 (GS98) [33]. In 2005 Asplund, Grevesse and Sauval (AGS05) released an improved estimation by using a 3D hydrodynamical model of the solar photosphere instead of the classical 1D simulation for the first time[34]. It also includes the relaxation of the assumption of local thermodynamical equilibrium (LTE) and improvement in the atomic and molecular data. The new model led to a better

description of the observed shapes of the spectral lines including widths, shifts and asymmetries. At the same time the abundances of elements like C,N,O and Ne decreased significantly. This led to a better agreement between the composition of the Sun, solar type stars, OB stars, H-II regions and the interstellar medium in the solar neighborhood.
The most recent determinations of the solar abundances were published in 2009, reconfirming the low metallicity scenario. Results from solar photosphere studies (AGSS09) are reported in [35] and from meteoritic studies in [36].
The implications of the new low metal abundances on Standard Solar Models and their predictions are discussed in Section 2.2.3.

2.2.2 Solar fusion reactions and solar neutrinos

The energy produced in the core of the Sun results from the nuclear fusion reactions of hydrogen into helium. The overall reaction is given by

$$4p \rightarrow {}^4\mathrm{He} + 2e^+ + 2\nu_e \qquad \mathrm{Q_V} = 26.729\,\mathrm{MeV} \tag{2.27}$$

In the Sun and in stars with a mass below $\sim$1.3 $\mathrm{M}_\odot$ the energy is mainly released via the so-called proton-proton chain (*pp* chain). In larger and in late-stage stars the central core temperature is large enough to allow a second type of fusion reactions to become dominant: the carbon-nitrogen-oxygen cycle (CNO cycle). In case of the Sun with a core temperature of $T_C \sim 1.5{\times}10^7$ K the CNO cycle is expected to contribute only $\sim$1.5% to the total energy generation according to calculations of the SSM [37]. The way the energy is released directly determines the resulting total energy spectrum of the solar neutrinos. Obviously, the main contribution to the total neutrino flux originates from the *pp* chain. Nonetheless, the neutrinos from the CNO cycle are of great importance, since the CNO fusion reactions are highly sensitive to the temperature gradient and to the internal solar structure. So both energy production mechanisms are useful to test SSM predictions.
The following two paragraphs discuss both mechanisms, focusing on those fusion reactions which also release neutrinos.

The *pp* chain The hydrogen burning in the Sun occurs mainly within the *pp* chain. The *pp* chain is typically divided into three branches. This is shown in Figure 4. At the beginning of the *pp* chain there is the fusion of two protons (*pp*-I branch). This is favored by the fact that the quantum mechanical probability P for an atom of atomic number A_1 to tunnel through the Coulomb-barrier of another atom of atomic number A_2 is proportional to $P\ \alpha\ \exp(A_1 \cdot A_2)$ and thus maximal for two hydrogen atoms. However, the nucleosynthesis of hydrogen under solar core conditions is relatively slow. There are two possibilities for hydrogen burning into deuterium:

$$p + p \rightarrow d + e^+ + \nu_e \quad (E_\nu \leq 0.42\,\mathrm{MeV}) \tag{2.28}$$

$$p + e^- + p \rightarrow d + \nu_e \qquad (E_\nu = 1.44\,\mathrm{MeV}) \tag{2.29}$$

Both reactions produce neutrinos. The neutrinos are generally named according to the particles involved in the fusion process. The *pp* neutrinos represent the largest solar neutrino flux. The endpoint energy is at 0.42 MeV. The *pep* neutrinos are mono-energetic with an energy of 1.44 MeV. The flux of *pep* neutrinos is $\sim$400 times weaker than that of the *pp* neutrinos due to the fact that

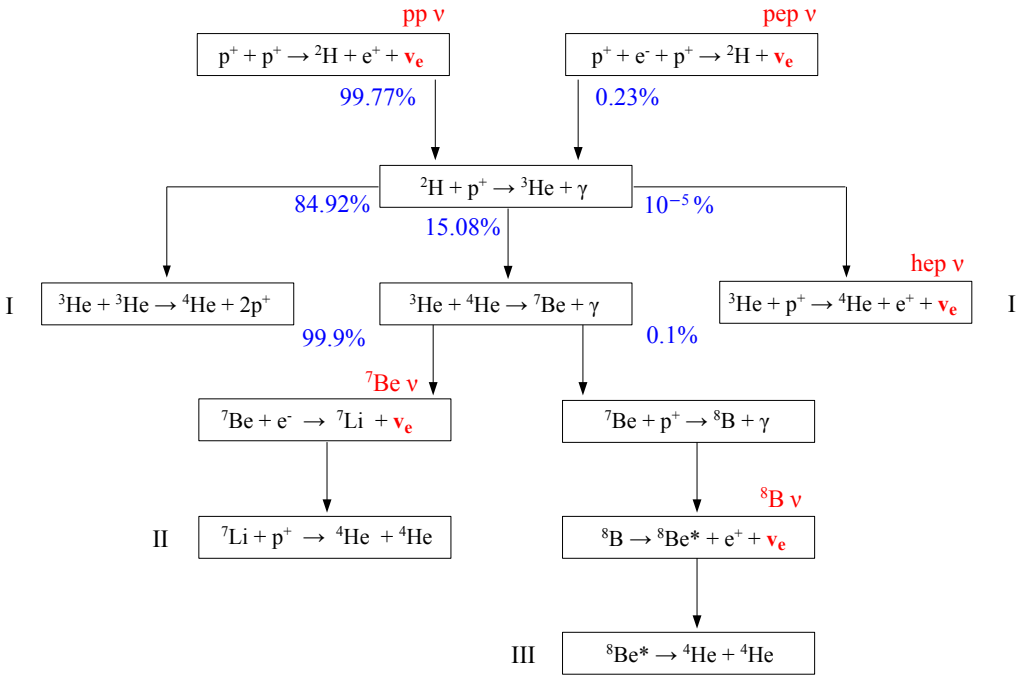

Figure 4: Representation of the solar fusion reactions in the *pp* chain

not two but three particles have to interact at the same time. Nevertheless, taking into account that both reactions have an almost identical matrix element, both neutrino fluxes are strictly correlated. Thus a measurement of the *pep* neutrinos can constrain the *pp* flux. Moreover, *pep* neutrinos can test the MSW effect in the transition region between matter and vacuum dominated regime expected in the interval around 1-3 MeV (see Figure 1). The generated deuterium nuclei undergo fusion processes with protons to ^{3}He nuclei. As depicted in Figure 4 the created ^{3}He nuclei can undergo three different fusion processes. One of these reactions releases the so-called *hep* neutrinos

$$^3\mathrm{He} + p \rightarrow {}^4\mathrm{He} + e^+ + \nu_e \quad (E_\nu \leq 18.8\,\mathrm{MeV}) \tag{2.30}$$

The *hep* neutrino flux is the weakest compared to all other solar neutrino fluxes but at the same time the highest energetic neutrino type. Reactions ^{3}He+^{3}He $\rightarrow$ ^{4}He+2p and (2.30) terminate by releasing ^{4}He atoms which do not fuse further, while the reaction ^{3}He+^{4}He $\rightarrow$ ^{7}Be+γ ends in two different branches *pp*-II and *pp*-III. Within the *pp*-II branch the ^{7}Be nuclei undergo first an electron capture:

$$^7\mathrm{Be} + e^- \rightarrow {}^7\mathrm{Li} + \nu_e \quad (E_\nu = 0.38\,\mathrm{MeV}; 0.86\,\mathrm{MeV}) \tag{2.31}$$

under emission of the mono-energetic ^{7}Be neutrinos at the energies 0.38 MeV and 0.862 MeV. The released ^{7}Li atom undergoes a proton capture releasing two ^{4}He atoms and 17.35 MeV energy. The

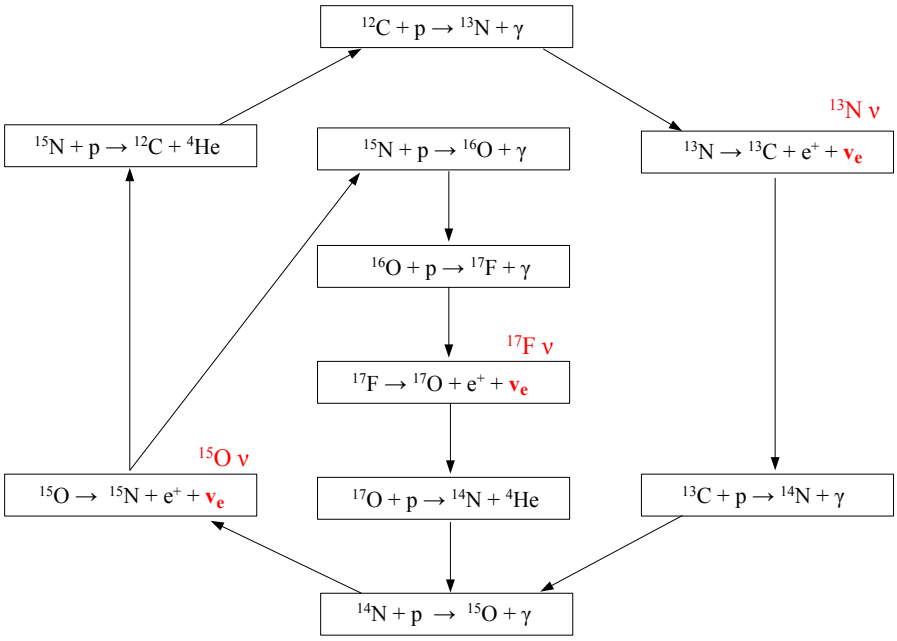

Figure 5: Representation of the solar fusion reactions in the CNO cycle. It is subdivided into a main (outer) loop called CN cycle and a secondary (inner) loop, the NO cycle.

third termination channel (*pp*-III) is suppressed for temperatures below $T_C = 2.5 \times 10^7$ K. In the Sun the probability is ≈0.1%. Within the *pp*-III branch the ^{7}Be atoms undergo a proton capture. The generated ^{8}B nuclei finally undergo a β^+-decay under release of ^{8}B neutrinos:

$$^{8}\mathrm{B} \rightarrow 2\,{}^{4}\mathrm{He} + e^{+} + \nu_e \quad (E_\nu \leq 14.6\,MeV) \tag{2.32}$$

The CNO cycle The CNO cycle represents a second fusion mechanism that burns hydrogen into helium. The elements C, N, O act as catalysts. Due to the high Coulomb barriers of the mentioned elements the CNO cycle plays a secondary role in the actual energy production of the Sun. Only at high central temperatures (T_C >2×10^7 K for M≥M$_\odot$) and high C,N,O abundances the CNO cycle becomes dominant. The cycle is depicted in Figure 5. It consists of a main and a secondary loop. They include three reactions emitting neutrinos which are commonly referred to as CNO neutrinos. The two reactions of the main cycle (CN cycle) releasing neutrinos are given by:

$$^{13}\mathrm{N} \rightarrow {}^{13}\mathrm{C} + e^{+} + \nu_e \quad (E_\nu \leq 1.20\,\mathrm{MeV}) \tag{2.33}$$
$$^{15}\mathrm{O} \rightarrow {}^{15}\mathrm{N} + e^{+} + \nu_e \quad (E_\nu \leq 1.73\,\mathrm{MeV}) \tag{2.34}$$

The ^{13}N neutrinos have a continuous energy spectrum with an endpoint energy of 1.199 MeV. In case of the ^{15}O neutrinos the endpoint energy is at 1.732 MeV.

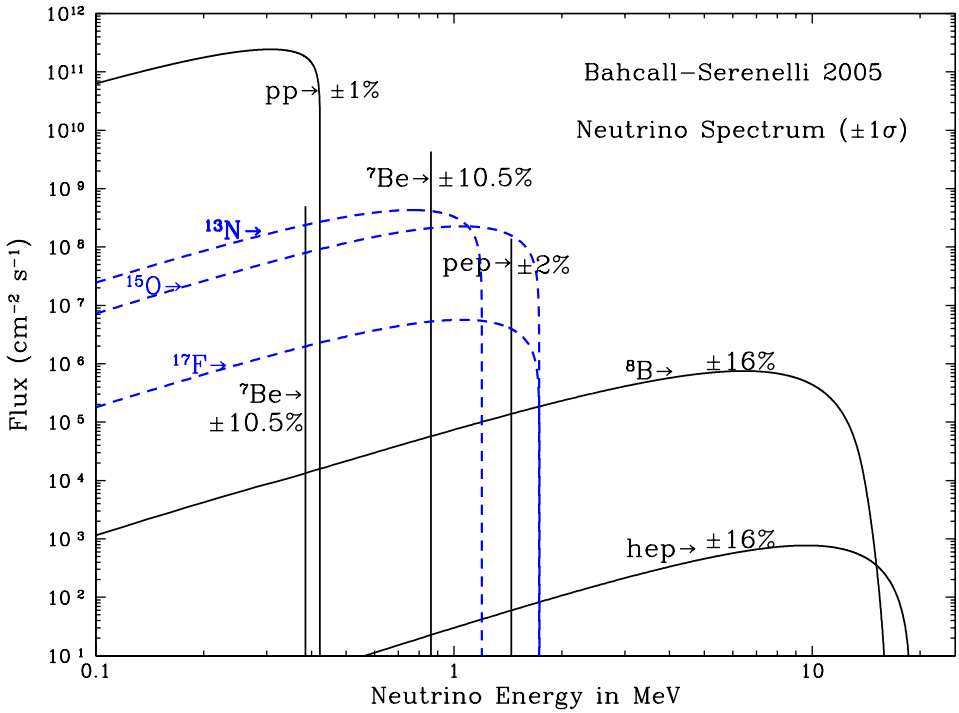

Figure 6: The predicted solar neutrino energy spectrum according to the BS05(GS98,OP) standard solar model [39]. The neutrino fluxes are given for a distance of 1 AU from the Sun. The units are $\mathrm{cm}^{-2}\mathrm{s}^{-1}\mathrm{MeV}^{-1}$ for continuum neutrino sources and $\mathrm{cm}^{-2}\mathrm{s}^{-1}$ for mono-energetic neutrino sources. The fluxes from the *pp* chain are drawn in black, those from the CNO cycle in blue.

The reaction $^{14}\mathrm{N}+\mathrm{p} \rightarrow {}^{15}\mathrm{O}+\gamma$ acts as the bottleneck of the cycle. Because of the higher Coulomb-barrier of ^{14}N compared to e.g. the carbon isotopes, the time scale for a successful ^{14}N fusion reaction with a proton is $\tau = 3.6 \times 10^8$ y. For ^{15}N the mean reaction time is reduced to $\tau = 2 \times 10^4$ y, since the reaction is mediated by the strong force.
At even higher core temperatures (T_C >2.5×10^7 K for M≥M$_\odot$) the NO cycle becomes relevant. The NO cycle contains the β^+-decay of ^{17}F, which also releases neutrinos with an endpoint energy of 1.738 MeV in the following reaction:

$$^{17}\mathrm{F} \rightarrow {}^{17}\mathrm{O} + e^+ + \nu_e \quad (E_\nu \leq 1.74\,\mathrm{MeV}) \tag{2.35}$$

Predicted solar neutrino fluxes The solar neutrino energy spectrum predicted by the Standard Solar Model BP05(GS98,OP) is depicted in Figure 6. It is based on calculations by J. Bahcall and collaborators using the best available physics and input data up to 2005 [39]. The high abundance of heavy elements (GS98) and the radiative opacities from the Opacity Project (OP) [40] were implemented. The expected fluxes of neutrinos from all solar fusion reactions are given at the average distance of the Earth from the Sun corresponding to one astronomical unit (AU). The total flux is 6.6×10^{10}/(cm^2·s) making the Sun an intense source of low energetic (<15 MeV) neutrinos.

Neutrino flux	GS98	AGS05	AGSS09	AGSS09$_{ph}$	Unit [cm^{-2}s^{-1}]
pp	5.97	6.04	6.03	6.01	10^{10}
pep	1.41	1.44	1.44	1.43	10^{8}
hep	7.91	8.24	8.18	8.1	10^{3}
^{7}Be	5.08	4.54	4.64	4.79	10^{9}
^{8}B	5.88	4.66	4.85	5.22	10^{6}
^{13}N	2.82	1.85	2.07	2.15	10^{8}
^{15}O	2.09	1.29	1.47	1.55	10^{8}
^{17}F	5.65	3.14	3.48	3.7	10^{6}

Table 3: Predicted solar neutrino fluxes at a distance of 1 AU from the Sun. Column 2 shows the calculated values based on the high metallicity composition (GS98) [33]. Columns 3 and 4 (AGSS05, AGSS09) use the revised chemical compositions based on (1) photospheric measurements for volatile elements (C, N, O, Ne, Ar) [34, 35] and (2) CI chondritic meteoritic values for the remaining elements [36]. Column 5 (AGSS09$_{ph}$) uses only the latest released photospheric results [35]. (taken from [38])

The most updated calculation of the solar neutrino fluxes was published in 2009/10 by A.M. Serenelli [38]. The first calculated SSM(GS98) uses the old, photospherically estimated high metal abundances. For the newest SSMs the latest estimations of metal abundances from photospheric results published in 2005 [34] and 2009 [35] and from meteoritic results [36] were combined. In the following these SSMs are denoted as (AGS05) and (AGSS09). Additionally, a SSM based only on the latest estimated photospheric metal composition was calculated (AGSS09$_{ph}$).
The results are reported in Table 3. Since the elements O, Ne, Si, Fe are significant contributors to the opacity in the radiative interior of the Sun, the new reduced abundances decreased the central temperature T_C by ∼1%. This had an impact especially on the CNO, ^{8}B and ^{7}Be neutrino fluxes, which are proportional to T_C^{14}, T_C^{18} and T_C^{8}, respectively [45]. The arisen differences of the calculated neutrino fluxes between the high and low metallicity scenarios are 24-44% for the CNO-cycle, and in case of ^{8}B and ^{7}Be neutrinos the fluxes decreased by 21-11% and 10-5%, respectively. The impact of this change will be discussed in Section 2.2.3.
In addition, there is another constraint on solar neutrino fluxes. The standard solar model, which predicts the solar neutrino fluxes, has to match the actual solar luminosity. Assuming that all fusion reactions are known and included in the model, the actual solar luminosity $L_{\odot}^{\gamma}$ (energy released from the surface of the Sun in terms of photons) should be directly related to the total neutrino flux expressed in the overall reaction (2.27). This is the so-called *luminosity constraint*. However, while neutrinos escape the solar interior instantaneously at relativistic speed, photons undergo scattering processes reaching the photosphere only after a period of t_D ∼10^5 y. This leads to two time-shifted images of the Sun. Only if the fusion rates were stable over t_D, the photon luminosity $L_{\odot}^{\gamma}$ and the neutrino luminosity $L_{\odot}^{\nu}$ should coincide [43]:

$$\frac{L_{\odot}^{\gamma}}{4\pi(\mathrm{AU})^2} = \sum_i \beta_i {\Phi_i}^{\nu} \tag{2.36}$$

where β_i is the averaged released energy in the fusion reaction i emitting neutrinos with i={*pp*, *pep*, CNO, ^{8}B, ^{7}Be} and ${\Phi_i}^{\nu}$ the neutrino flux from the reaction i. Testing whether $L_{\odot}^{\gamma}/L_{\odot}^{\nu} \equiv 1$ is actually true has been one of the major goals of recent solar physics research. In this context, flux normalisation constants f_i defined as the ratio of measured to predicted values for single neutrino components i are introduced. Since *pp* neutrinos represent the majority of the total solar neutrino

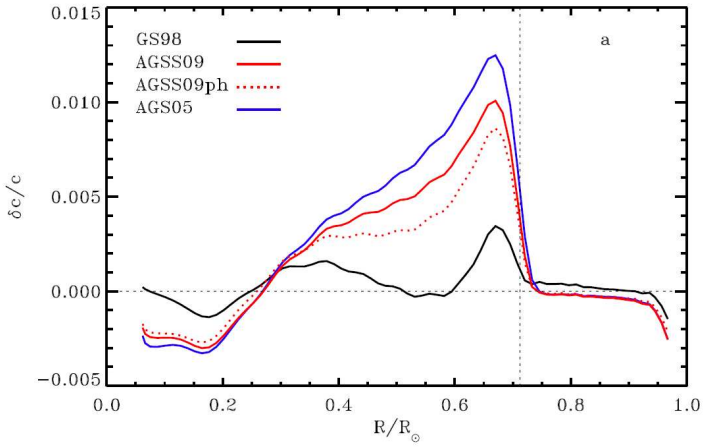

Figure 7: Relative differences of the speed of sound, $\delta c/c = (c_\odot - c_{model})/c_{model}$, between standard solar models and helioseismological results [38].

flux (∼90%), a precise measurement of f_{pp} can test the luminosity constraint hypothesis. The best limit so far was set by the Borexino collaboration in combination with the results obtained in the Gallium and Chlorine experiments gaining $f_{pp} = 1.005^{+0.008}_{-0.020}$ [44].

2.2.3 Helioseismology

Helioseismology is the study of solar oscillations originating from acoustic waves in the solar interior. In the 1960s, periodic oscillations on the solar surface were observed for the first time in local Doppler velocity measurements of the rotating Sun with periods of ∼300 s and a lifetime of several periods. It was found that these oscillations can be interpreted as acoustic modes of pulsation of the entire Sun, representing a superposition of millions of standing waves with amplitudes of an individual mode of the order of few cm s^{-1}. The frequencies of these modes have been determined to an accuracy of better than 1 part in 10^5 [24]. In the 1970s, major theoretical advances in their understanding were made by establishing a new SSM-independent approach of the description of the solar interior. A detailed review of the experimental and theoretical progress in the field of helioseismology over the past 25 years can be found in [25] and references herein.

The observed solar oscillations have extremely small amplitudes and thus can be described as linear perturbations of a hydrodynamical system. Assuming that the time scale for the energy exchange is much longer than the pulsation period, the oscillation motion can be calculated essentially by a linear adiabatic approximation [25]. According to this approximation, low-degree modes can penetrate the interior of the Sun, whereas high-degree modes which are easier to detect remain captured in the outer solar layers. Thus, helioseismological analyses provide only limited information about the solar core ($R<0.05R_\odot$). On the other hand, the adiabatic approximation breaks down near the stellar surface ($R>0.95R_\odot$), where the thermal time scale becomes very short. Within these limitations however, helioseismology makes highly precise predictions.

Recent controversies between the SSM and helioseismology Both, helioseismology and the standard solar models (SSM), which do not include helioseismological constraints, can be compared using four predicted quantities: the surface helium mass fraction Y_S, the depth of the

convective envelope $R_{CZ}/R_{\odot}$ and the quadratic mean[2] of the relative differences of the speed of sound and density profiles denominated with $\delta c/c$ and $\delta\rho/\rho$.
Helioseismology obtains highly precise values for $Y_S = (0.2485 \pm 0.0035)$ and $R_{CZ}/R_{\odot} = (0.713 \pm 0.001)$ [46]. Herein R_C is measured by a clear discontinuity in the speed of sound due to the change in the temperature gradient. The GS98 standard solar model calculated in [38] predicts the correct boundary of the transition of the convective zone and a value Y_S similar to helioseismological data with a maximal deviation of 1.8σ. In contrast, standard solar models based on the recent determinations of solar metal abundances (AGS05, AGSS09, AGSS09$_{ph}$) largely disagree with the results from helioseismological data [38, 39, 42]. By taking into account the uncertainty from helioseismology only, the discrepancy in $R_{CZ}/R_{\odot}$ is 15σ and in Y_S it is 5.5σ.
A similar trend is found for the relative differences of the speed of sound and the density profiles $\delta c/c$ and $\delta\rho/\rho$. The values estimated from SSMs based on the new low metal abundances are ∼5 times worse than the GS98 models. This is shown for the profile of the speed of sound in Figure 7. The new "solar abundance problem" is of second order compared to the original "solar neutrino problem". However, the recently arisen discrepancies are a hint that the stellar interior of our Sun is not yet completely understood. Many attempts have been made so far, but no satisfying solution has been found [39, 47, 48, 46, 49]. The best agreement is obtained by increasing the opacity below the convective zone and the diffusion rates with suitable factors. But the required changes of 15% are larger than the accepted uncertainties in radiative opacities for the solar interior[3], and the surface helium abundance of the models is still too low. Moreover, models with a high metallicity in the interior and a low one in the external convective zone, which include rotation-induced mixing, do not converge with the profile of the seismic speed of sound [50].

The newly arisen problem in solar physics emphasizes the important role of the measurement of the solar neutrino fluxes with high precision. Especially the measurement of the CNO neutrinos will help to throw light on the current "solar abundance problem". This is one of the goals of the present and upcoming solar neutrino experiments: Borexino, which has been collecting data since May 2007, and SNO+, which is planned to become operational in 2013.

2.3 Borexino: physics goals and first results

Over the last 40 years, solar neutrinos have been detected via two methods. First, radiochemical techniques have been used to detect the flux at higher energies via ^{37}Cl (Homestake [51, 52, 53]) and at low energies via ^{71}Ga (SAGE [54], GALLEX/GNO [55, 56, 57]). However, the detection is not real-time and only the integrated neutrino flux above a certain threshold was measured. Individual components could not be disentangled. Direct spectroscopy including real-time detection and directionality of the neutrinos have been accomplished by Cherenkov detectors (KamiokaNDE [58], SuperKamiokaNDE [59, 60], SNO [61, 62]), but were limited to the high-energy neutrino flux above ∼3.5 MeV.

Borexino is the first experiment that can directly observe sub-MeV neutrinos down to ∼0.2 MeV in real-time. The key technical ingredient is the detection medium, a scintillator liquid of ultra-low radioactivity, which results in low background rates but also to a high scintillation light output leading to a good energy resolution. The detection reaction used is electron-neutrino scattering, where the energy of the recoil electrons is measured (for more details see Section 3.1.2). Since the scintillation light is emitted isotropically, it is not possible to deduce the directionality of the incident neutrinos. The simulated pure neutrino spectrum expected in Borexino is depicted in

[2] The quadratic mean corresponds to the root mean square (rms) of the mean of the squares of the values.
[3] The differences between opacities estimated by the OPAL code (Lawrence Livermore National Laboratory) and by the international collaboration *Opacity Project* do not rise above 2.5%.

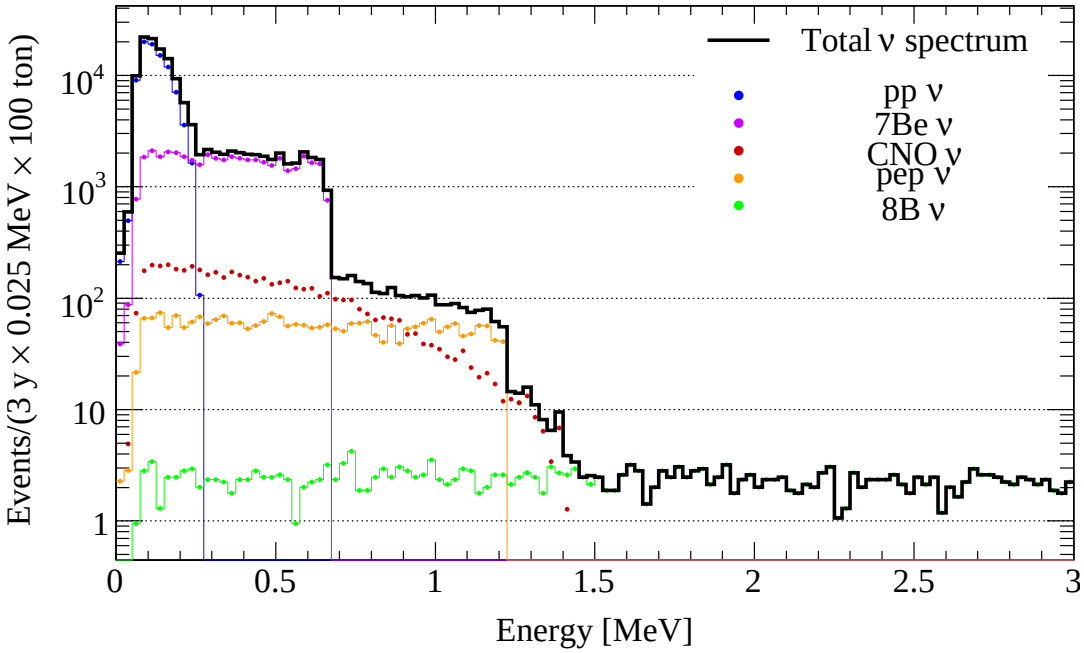

Figure 8: Simulation of the recoil energy spectrum for different solar neutrino types interacting in Borexino, assuming a 3-year lifetime exposure and a target mass of 100 tons. The neutrino fluxes were obtained using the MSW-LMA solution. The simulation was performed within the Borexino software framework *Echidna cycle 11* using the physics simulator `G4BX` and the electronics simulator `BXELEC` (see Section 3.2.2).

Figure 8. For comparison, a typical Borexino recoil energy spectrum from data is shown in Figure 9.
This section discusses the physics goals of the experiment. A full description can be found in [82]. The main results obtained since start of the experiment on May 16, 2007 are also pointed out and summarized in Table 30 in Appendix A.2. For more details see the references cited herein.

Solar neutrinos: The main goal of the Borexino experiment is the real-time spectroscopy of the solar ^{7}Be neutrino flux. The mono-energetic ^{7}Be neutrinos are characterized by a Compton-like continuum with an edge at 0.677 MeV (see Figure 8). The energy threshold at ∼0.2 MeV is given by the high rate of ^{14}C (β^-, Q=0.156 MeV) decays within the organic liquid scintillator. The best value obtained so far for the interaction rate of ^{7}Be neutrinos with the target material in Borexino is R(^{7}Be)=49 events/d/100ton) ± 6%(stat.) ± 8.5%(syst.) [65]. The survival probability P_{ee} = 0.56 ± 0.10 (1σ) deduced herein is in agreement with the vacuum dominated MSW-LMA oscillation scenario and consistent with P_{ee}=0.541 ± 0.017 from the global fit of all previous solar and reactor neutrino experiments[4]. The non-oscillation scenario was rejected at a 4σ level. The total uncertainty budget of the R(^{7}Be) is dominated by systematic effects. Thus, several calibration campaigns with radioactive sources have been carried out in the last two years (see Section 3.4.1) in order to reduce the systematic error and to achieve a sub-5% measurement of the ^{7}Be neutrino flux in the near future.

Borexino has also succeeded to measure the ^{8}B neutrinos flux above 3 MeV which is the lowest threshold so far. This threshold is imposed by the presence of 2.6 MeV γ rays from the external background in Borexino (compare with Section 5.1.2). The measured rate above 3 MeV is

[4] the survival probability is equal to 1 minus the oscillation probability; see Section 2.1.1.

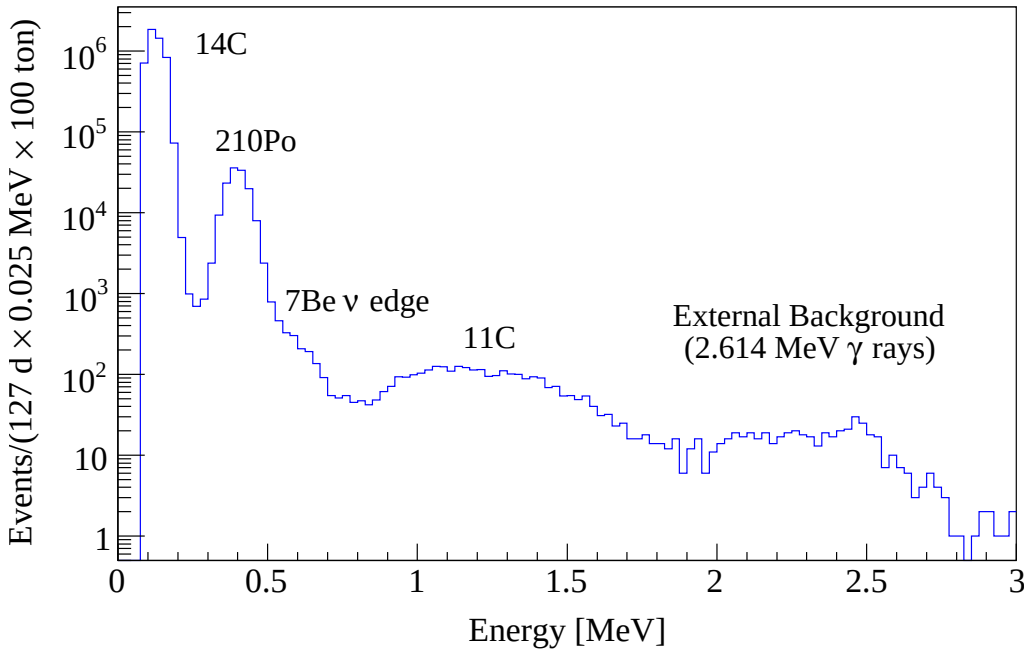

Figure 9: Measured Borexino recoil energy spectrum for a target mass of 100 tons with an energy threshold at 0.1 MeV. The ^{7}Be neutrino shoulder around 0.7 MeV is visible. Most of the main background components, i.e. ^{14}C, ^{210}Po, ^{11}C and the external background (mainly 2.6 MeV γ rays) have a clear signature.

R(^{8}B)=0.217 events/d/100ton $\pm$ 0.038%(stat.) $\pm$ 0.008% (syst.) [15] and the matter-dominated survival probability is P_{ee}=0.29 $\pm$ 0.10 (1σ). This is in agreement with the expected theoretical value as shown in Figure 1 and the non-oscillation scenario was rejected at 4.2σ.
Borexino also explored the constraint of the flux normalization constants f_{pp} and f_{CNO} already introduced in Section 2.2.2. By combining the Borexino results with those of previous radiochemical experiments new best values/limits were obtained. By including the *luminosity constraint* $f_{CNO} < 3.80$ (90% C.L.) was obtained. Translated into solar energy production, the CNO contribution to the solar neutrino luminosity becomes <3.3% (90% C.L.).
A direct detection of the solar *pp*, *pep*, CNO and *hep* neutrinos with the Borexino detector is still missing. The problems related to the detection of these neutrino fluxes are that they are either too weak (*hep*) or affected by larger background components (*pp*, *pep*, CNO) which require a greater effort in extracting the neutrino signal (compare with Figures 8 and 9). Even though the expected *pp*-neutrino rate is high (∼550 events/d/100ton), *pp*-neutrinos have a low endpoint energy and the resulting detection window in the recoil electron spectrum is strongly affected by ^{14}C ($\lesssim$0.20 MeV) and ^{210}Po ($\gtrsim$0.27 MeV) decays. The feasibility of the measurement of the *pep* and CNO neutrinos will be discussed in Section 2.4.

The Borexino collaboration is also studying temporal solar neutrino flux variations at low energies. These include three effects: annual, seasonal and day-night. The expected annual 7% effect is due to the eccentricity of the Earth's orbit proportional to $1/R^2$ and is independent of physics or astrophysics. The day-night or seasonal variation would be a sensitive and direct probe of flavor conversion in a major part of the allowed neutrino mixing and mass parameter space.

Antineutrinos: Another goal of the Borexino experiment is the detection and identification of antineutrinos ($\overline{\nu}_e$). The detection reaction is the inverse β decay $\overline{\nu}_e + p \rightarrow e^+ + n$.

Two sources for antineutrinos are geo-antineutrinos and reactor-antineutrinos. Geo-antineutrinos are produced in β-decays of naturally occurring radioactive isotopes in the Earth and represent a unique probe of the radionuclide heat generation in the interior of our planet. According to the *Bulk Silicate Earth* (BSE) geochemical model in [66] a detection rate of $R_{geo}=(2.5\ ^{+0.3}_{-0.5})$ events/y/100ton is expected in Borexino. On the other hand, reactor-antineutrinos at a rate of (5.7±0.3) events/y/100ton are expected from the 194 nuclear plants distributed across Europe, however, at higher energies.
The measured rate $R_{reactor}=(4.2\ ^{+1.7}_{-1.4})$ events/y/100ton is consistent with the expectation assuming an antineutrino oscillation scenario.
Concerning the geo-antineutrinos a first observation was reported by KamLAND [137]. However, Borexino is the first experiment that has been able to observe geo-antineutrinos with a high statistical significance. The measured rate is $R_{geo}=(3.9\ ^{+1.6}_{-1.3})$ events/y/100ton (1σ) and the null-hypothesis, i.e. $R_{geo}=0$ events/y/100ton, was rejected at 99.997%. The hypothesis of a geo-reactor at the Earth's core with a typical power of 3-10 TW was also investigated and an upper bound for a 3 TW geo-reactor could be set at 95% C.L. [68].
Another source of antineutrinos could be the Sun. A weak antineutrino flux arising from the ν_e conversion could follow the interplay of flavor oscillations and spin flavor precession induced by solar magnetic fields and Majorana neutrinos with sizable electric or magnetic moments. So far, Borexino obtained an upper limit on the transition probability of the solar $\nu_e \rightarrow \overline{\nu}_e$ of $<1.3\times10^{-4}$ (90% C.L.) [72].

Nuclear and elementary particle physics The extremely high radiopurity of the large volume organic liquid scintillator in Borexino also allows to look for rare processes and forbidden transitions. First, Borexino has searched for a non-zero neutrino magnetic moment μ, which might exist given the fact that neutrinos are massive. The presence of $\mu > 0$ would manifest itself in an enhanced cross section at lower energies for neutrino interactions with the scintillator and lead to an increased rate in the energy spectrum at lower values. Borexino obtained $<5.4 \times 10^{-11}\ \mu_B$ (90% C.L.) which is currently the best experimental limit [65].
Secondly, Borexino has looked for possible forbidden transitions in ^{12}C nuclei that violate the *Pauli exclusion principle* (PEP). The transitions of nucleons from the P shell to the already filled $S_{1/2}$ shell resulting in non-Paulian nuclei $^{12}\tilde{C}$ were searched for. The β decay to a non-Paulian nucleon in the final state $S_{1/2}$ has also been discussed. By obtaining upper limits on the lifetimes for different processes the limits can be converted into relative strengths of non-Paulian transitions to normal ones. The variable $\delta^2 = \tilde{\lambda}/\lambda$ is introduced, where $\lambda = 1/\tau$ is the unit time probability (rate) of forbidden ($\tilde{\lambda}$) and normal transitions (λ). Borexino obtained new best limits for different forbidden transitions in ^{12}C nuclei including γ, β, and nucleon emission. The corresponding limits δ^2_γ, δ^2_β and δ^2_N are reported in Table 30 in the Appendix A.2.

Supernova detection Borexino also has the potential of detecting stellar core collapses, which are expected to occur ∼3 times per century in our galaxy. A supernova at 10 kpc distance releasing a binding energy of 3×10^{53} ergs is expected to induced more than 150 events above Borexino's quoted energy threshold (∼0.2 MeV) within tens of seconds [73].
According to standard supernova theory [74, 75], the prompt neutrino signal, which precedes the electromagnetic signal by hours or even by days, can provide an early alert to the astronomical community leading to unprecedented observations with optical telescopes of the very early turn-on of supernova light curves. Moreover, the duration of the neutrino bursts (width of the neutrino pulse at the neutron star) allows to find an upper limit for the electron neutrino mass [76].
In July 2009, Borexino joined the *SuperNova Early Warning System* (SNEWS) collaboration [77],

whose other members are SuperKamiokande, SNO, LVD and IceCube.

2.4 Challenge for the *pep* and CNO neutrino analysis with Borexino

The main focus of the present dissertation lies in the study of the not yet directly measured *pep* and CNO neutrinos and of the background components that affect these neutrino signals.

The *pep* and CNO neutrinos are of major importance for several reasons.
In terms of neutrino oscillations one has to note the energy-dependent survival probability P_{ee} of these neutrino components. The P_{ee} of *pep* and CNO neutrinos lies directly in the transition region between the matter- and vacuum-dominated regime according to the MSW-LMA oscillation scenario expected to be between 1 MeV and 3 MeV (see Figure 1). The *pep* neutrinos are monochromatic with 1.44 MeV energy resulting in a characteristic Compton-like edge at 1.22 MeV in the ν_e-e scattered energy spectrum. The CNO neutrinos have energies up to 1.73 MeV. Hence, in case of their detection, Borexino would be the first experiment to provide measurements in all three oscillation regions.
Moreover, the *pep* neutrinos are directly correlated with the dominant *pp* fusion reactions which release the *pp* neutrinos. Thus, a measurement of the *pep* neutrinos would also constrain the flux of the *pp* neutrinos.
CNO neutrinos play a key role in astrophysics, since the CNO cycle becomes dominant in stars with core temperatures above $T_C > 2\times10^7$ K for $M \geq M_\odot$. CNO neutrinos are also important in the age estimation of globular clusters [78], pivotal in setting a lower limit for the age of the universe. Additionally, the measurement of the solar CNO neutrino flux would help in solving the recently arisen "solar abundances problem" (see Section 2.2.3). According to the newly calculated lower chemical composition (AGSS09), one expects effectively 24-44% less neutrinos from the CNO cycle compared to previous estimates.

The expected interaction rates of *pep* and CNO neutrinos in an organic liquid scintillator as used in Borexino are 2.0 events/d/100ton and 7.1 events/d/100ton, respectively, if the old high metallicity scenario (GS98) [33] is assumed. If the newly calculated low metallicity (AGSS09) [35, 36] composition is used as input for the SSM, the rates are 2.0 events/d/100ton and 5.1 events/d/100ton. Note that these rates are integrated over the entire energy spectrum.
At lower energies, the detection of the solar *pep* and CNO neutrinos is limited by the Compton-like edge at 0.667 MeV of the energy spectrum from recoil electrons scattered with the mono-energetic solar ^{7}Be neutrinos. Taking into account the detector resolution and focusing only on the detection of the *pep* neutrino line, an energy window lying within [0.8,1.3] MeV is defined. Within this observation window the detection of solar *pep* and CNO neutrinos depends on three fundamental prerequisites:

- **Internal background from long-lived radioisotopes** An intrinsic ^{238}U and ^{232}Th contamination of the scintillator at a 10^{-17} g/g level, coupled with a ^{40}K contamination of 10^{-15} g/g would produce ∼0.6 background events/d/100ton in the observation window. Also, contamination from long-lived radon daughters out of secular equilibrium with ^{238}U (in particular from ^{210}Bi which has a spectral shape similar to that of the CNO neutrinos) must be reduced below 1 events/d/100ton in the energy region of interest. The achieved radiopurity in Borexino and the evolution of the concentrations of several intrinsic background components in the first three years of data collection will be discussed in Sections 3.3 and 4.3.7.

- **External background** Long-range γ rays emitted from the construction materials in the outer parts of the detector and from the surrounding can penetrate the buffer layers and reach

the scintillator. One possibility is to reject events detected in outer parts of the scintillator by defining a so-called *fiducial volume* (see Section 3.1.2). For reference, in Borexino the reduction of a target mass of 100 tons to 60 tons contained in spherical centered *fiducial volumes* would reduce the external background by almost 90%, the neutrino signal by 40%. Conversely, the extension to a larger target mass in order to have a larger statistics of neutrino-events would implicate an increased presence of external background events. This will be investigated in Chapter 5.

- **In-situ production of muon-induced radioisotopes** Muons and muon-showers crossing the Borexino detector can undergo interactions with the carbon atoms of the organic scintillator and produce unstable short- and long-lived radioisotopes. The long-lived radioisotope ^{11}C is by far the most dangerous contaminant for the detection of *pep* and CNO neutrinos in Borexino. The rate depends on the depth of the underground location of the experiment. A first rate estimation of muon-induced radioisotopes was experimentally determined in a target experiment (NA54) on a muon beam at CERN [173]. As Borexino has already shown, ∼10 events/d/100ton lie in the observation window of the *pep* and CNO neutrino signal. There is a veto mechanism based on the detection of threefold coincidences that allows to identify and reject this background with a high efficiency. Due to its fundamental importance, the *threefold coincidence* (TFC) method is introduced separately in the next paragraph.

The threefold coincidence method The *threefold coincidence* (TFC) method was originally introduced by M. Deutsch in 1996 [79]. He suggested that ^{11}C decays could be detected and rejected on an *event-by-event* basis exploiting the neutron emission in the reaction:

$$\mu\ (+\mu \text{ showers}) + {}^{12}\text{C} = \mu\ (+\mu \text{ showers}) + {}^{11}\text{C} + n \tag{2.37}$$

Following this process, the tagging of ^{11}C candidates can occur by linking the following three signals:

- **Prompt muon signal:** Detection of a muon or a muon shower crossing the detector. A muon-trigger opens a neutron-triggergate for the search of subsequent neutron capture events following the creation of radioisotopes like ^{11}C.
- **First delayed signal:** Neutrons that are emitted in the reaction (2.37) are thermalized and finally captured with a characteristic mean capture time of $\tau \sim 254$ μs on hydrogen (see Section 4.2.6) resulting in the formation of a deuterium nucleus

  $$n + \text{H} \rightarrow \text{D} + 2.223 \text{ MeV} \tag{2.38}$$

  The emitted characteristic 2.223 MeV γ rays are instantaneously absorbed. They represent the first delayed signal after the muon. They have a strong time correlation with the parent muon and are spatially close to the track of the muon and to the decaying ^{11}C nuclei. Note that the reconstructed position of the absorbed γ energy is described as an energy-weighted "center of gravity".
- **Second delayed signal:** ^{11}C atoms, which are created along the muon track, undergo β^+decays with a mean lifetime of τ=29.4 min

  $$^{11}\text{C} \rightarrow {}^{11}\text{B} + e^+ + \nu_e + 0.960 \text{ MeV} \tag{2.39}$$

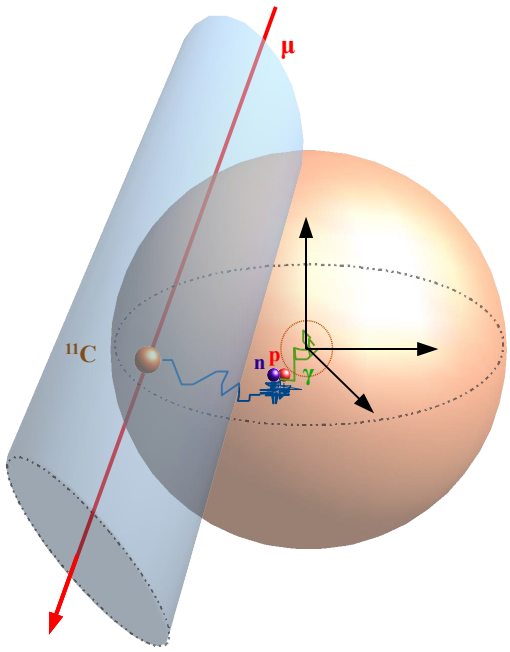

Figure 10: Schematic representation of the *threefold coincidence* (TFC) method. The method is described in the text.

The total energy released in the detector by the decay and the instantaneously following positron annihilation is between 1.02 and 1.98 MeV. Herein, the β^+ spectrum is typically shifted to lower energies due to quenching effects of the scintillator. In the case of the Borexino scintillator, the ^{11}C β^+ spectrum begins at ∼0.84 MeV already (see Section 4.3.4).

After each muon-induced neutron detection, the TFC method defines a set of potential ^{11}C candidates within a time delay *dt* from the detected muon/neutron and inside a sphere of radius *dr* placed around the barycenter of the 2.223 MeV γ rays. Note that, due to the random character of the TFC method, not only real ^{11}C decays are tagged, but also events (including neutrinos) which accidentally fulfill the TFC tagging conditions. In the following, a TFC tagged event is referred to as "^{11}C candidate". Obviously, by selecting ideal TFC space and time cuts (leading to a larger fraction of real ^{11}C decays than of accidental coincidences), the ^{11}C candidates can be discarded and increase the *pep* and CNO neutrino signal-to-background ratio.

However, the success of the TFC method depends on several conditions:
Firstly, the ^{11}C production events by muons and muon showers have to release at least one neutron. Among eight considered ^{11}C production channels induced by muons and muon-showers two of them, ^{12}C(p,d)^{11}C and ^{12}C(π^+,π^0+p)^{11}C, do not release neutrons and escape the TFC method. These channels are referred to as "invisible channels". According to FLUKA simulations the "invisible channels" contribute to ∼5% of the total ^{11}C production [80].
Secondly, the minimization of the detector mass-time fraction lost to the cuts implementing the TFC and the achievement of a high efficiency in the ^{11}C suppression have to be optimized. The TFC method can be improved by exploiting not only the muon detection but also the muon track information. The reconstruction of muon tracks leads to the definition of a cylindrical volume around the track itself. By intersecting the cylindrical volume with the spherical one from neutron

capture detection, ^{11}C atoms can be identified with unchanged efficiency, while less accidental coincidences are tagged reducing the fraction of data loss. This advanced development of the TFC method is depicted in Figure 10.
The third condition is connected with the performance of the detector. A high muon and neutron detection efficiency (see Sections 4.2.2 and 4.1.2), a good position reconstruction of the 2.223 MeV γ rays (see Section 4.2.5), no convection of the scintillator and a reliable muon track reconstruction (see Section 4.1.3) are required.

The TFC method has already been implemented in the Borexino Counting Test Facility (CTF) which is the prototype detector installed closed to the main detector itself at *Laboratori Nazionali del Gran Sasso* (see Section 3.1). The CTF with 3.73 tons of active mass of the Borexino-like scintillator demonstrated the feasibility of tagging ^{11}C using the TFC method [81]. The application of the TFC method in Borexino, which has a $\sim$70 times larger active volume than in the CTF, is investigated within this thesis (see Section 4.3).

3 The Borexino experiment

3.1 Description of the detector

Borexino is a large-volume liquid scintillator detector of ultra-high radioactivity purity capable of detecting neutrinos and antineutrinos from the Sun, from supernovae, from the Earth ("geo-neutrinos") and from nuclear plants. The novel approach consists of detecting these neutrinos with high statistics, in *real-time* and in the sub-MeV energy region.
The original design proposed by R. Raghavan in 1987 foresaw a detector for charged and neutral current interactions of the solar ^{8}B neutrinos on scintillator molecules containing the boron isotope ^{11}B. This 1000 tons scintillator volume detector named "Borex" was intended to have a prototype experiment "Borexino" containing 300 tons of scintillator. It turned out that this detector could also be sensitive to lower energy regions down to $\sim$0.2 MeV, allowing the direct detection of the solar ^{7}Be neutrino flux for the first time. This is actually the primary goal of the Borexino experiment as pointed out in the proposal in 1991 [82]. The key requirement for the success of Borexino was the identification of an ultra-pure scintillator and further reduction of the background levels in the detector components. Since commonly used screening techniques like γ ray spectroscopy, mass spectroscopy and neutron activation analysis do not reach such sensitivities, a prototype called *Counting Test Facility* (CTF) was installed and operated starting in 1995. High sensitivity and purity levels could be obtained: the concentrations in ^{238}U and ^{232}Th were found to be of the order of 10^{-16}g/g, on the other hand the ratio of ^{14}C/^{12}C was of the order of 10^{-18} corresponding to $\approx$30 Bq/100 ton of scintillator. These results were a milestone since they proved the feasibility of reaching the radiopurity levels required from the neutrino physics program of the large-scale detector Borexino. CTF allowed to also study the light propagation [83] and pulse shape discrimination [104] in large-volume scintillator detectors. CTF was not designed for the detection of neutrinos, but allowed to study cosmic-ray induced backgrounds, several rare processes and forbidden decays [85, 86, 87]. Since the start of data acquisition with Borexino in 2007, the CTF has been used for testing ongoing operations in Borexino (see Section 3.4.1).
The Borexino detector was built close to the CTF in Hall C of the underground-based *Laboratori Nazionali del Gran Sasso* (LNGS), Assergi, Italy, in order to shield the target mass against cosmic-ray induced backgrounds. The shielding of the Gran Sasso dolomite massif above Hall C is around 1.4 km thick, corresponding to 3800 meters of water equivalent (m w.e.). Thanks to this overburden, the cosmic-ray flux is reduced by six orders of magnitude, leading to a residual cosmic flux of $\sim$1.2 particle/h/m^2. The layouts of the experiments in Hall C, the Borexino detector, its prototype CTF and the OPERA detector are shown in Figure 11.

3.1.1 Conceptual design of the Borexino detector

The Borexino detector was designed to reach the extremely low background levels required in the experiment. As depicted in Figure 12, a series of large volumes of liquid buffer provides a graded shielding against the external background to the scintillator in the center of the detector. Additionally, cosmic radiation can be vetoed.
The Borexino detector is divided into two subcomponents: the Inner Detector (ID) and the Outer Detector (OD). They are introduced in the following paragraphs. A detailed description of the entire detector is given in [88] and [89].

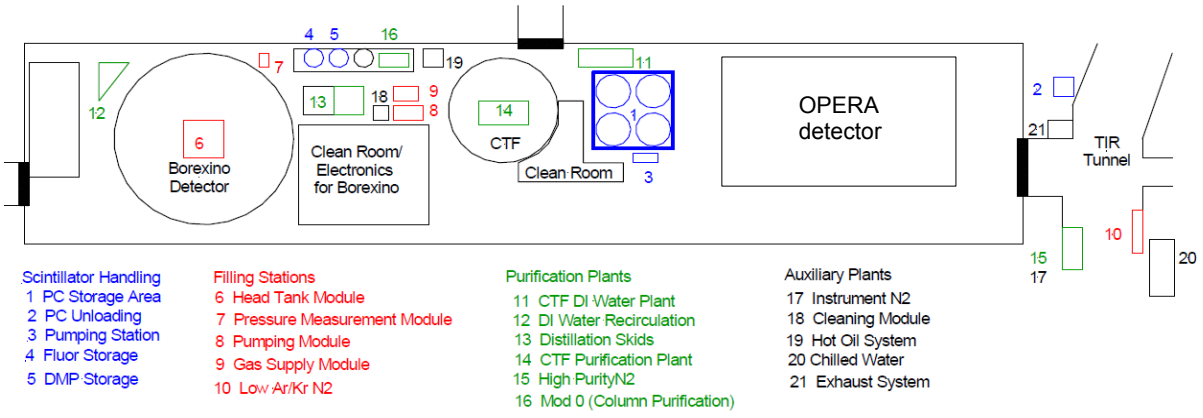

Figure 11: Layout of Hall C at LNGS. The Hall C is 100 m long, 20 m high and 20 m wide. The Borexino experiment occupies approximately 60% of the area, the OPERA experiment the residual 40%. The receiving and unloading of the scintillator for Borexino is done in the entryway (TIR tunnel), while all other operations, storage, purification and cleaning are performed in the subsystems around the Borexino detector (modified picture taken from [97]).

Inner Detector The Inner Detector (ID) contains 278 tons (315 m^3) of scintillator in its central core. This amount is ∼70 times higher than the amount used in the Borexino prototype CTF (see Section 3.1). The liquid scintillator solution is made of ultra-pure PC as a solvent and of the fluor PPO (2,5-diphenyloxazole, $C_{15}H_{11}NO$) as a solute at a concentration of 1.5 g/L (0.17 % by weight). The scintillator is embedded in an almost spherical 125 μm thick nylon vessel (Inner Vessel (IV)) with a radius of R_{IV}∼4.25 m. The nylon is UV-transparent, leak-tight and has nearly the identical index of refraction as the scintillator. The IV is surrounded by 890 tons (1350 m^3) of buffer liquid. The buffer liquid consists of ultra-pure PC (pseudocumene; 1,2,4-trimethylbenzene $C_6H_3(CH_3)_3$) with a small amount (originally 5 g/L; see Section 3.4.1) of the light quencher DMP (dimethylphtalate; $C_6H_4(COOCH_3)_2$). The buffer liquid is used for two reasons. Firstly, the buffer absorbs a large amount of scintillation light produced by environmental radiation and by the outer components of the ID. These detector components have a non-negligible intrinsic radioactivity in ^{232}Th, ^{238}U and ^{40}K, which would otherwise induce a high trigger rate of events that the data acquisition system would not be able to process. Secondly, in order to reduce the diffusion of radon from the outer detector components, the buffer liquid was separated into two shells by a second spherical concentric nylon vessel of radius 5.50 m. The nylon vessel structure is supported by Tensylon ropes and belts to guarantee a stable position of the buffer and scintillator fluids, of which the densities differ only by $\lesssim 1/‰$). Convection within the fluids is suppressed by keeping a constant temperature gradient of ≈4°C, in which the temperature decreases from the top to the bottom of the detector.

An unsegmented Stainless Steel Sphere (SSS) with radius R=6.85 m contains the organic liquids and the mechanical support for 2214 8” PMTs (ETL 9351). The PMTs are in direct contact with the buffer liquid. They are uniformly distributed over the surface and face the center of the detector. 1843 of the PMTs are equipped with light concentrators, leading to a more efficient scintillation light collection [92]. The total coverage is 33%. The 371 PMTs without concentrators can be used to study the background induced by the PMTs and to help identify muons passing close to the PMTs.

Several laser calibration subsystems were installed in order to measure and adjust the gain and

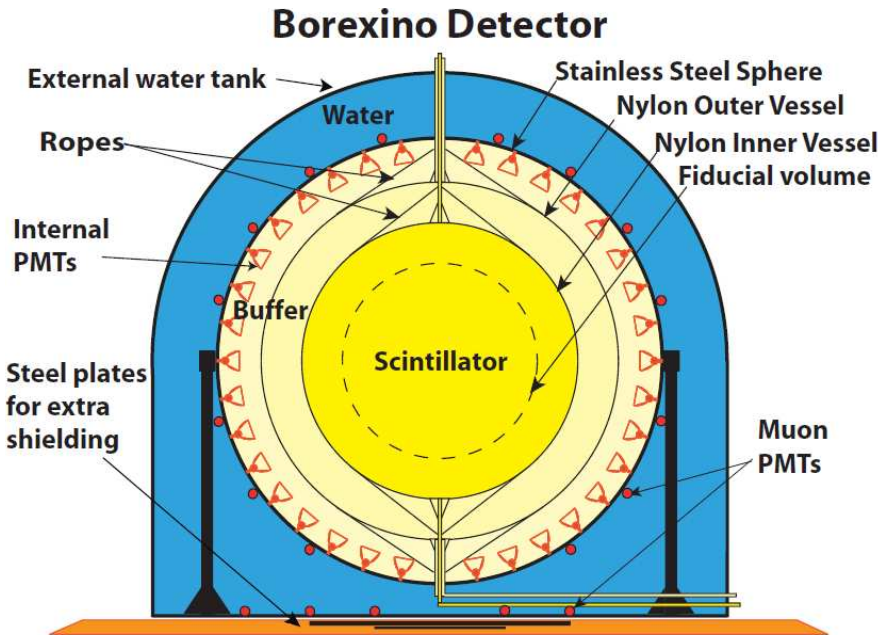

Figure 12: Section view of the Borexino Detector, consisting of the Water Cherenkov Outer Detector and an Inner Detector containing the buffer and scintillator liquids.

pulse time of each PMT. Quartz fibers transport light from the laser of a given wavelength to the light concentrators inducing single photoelectron signals.
Moreover, a CCD camera system consisting of seven calibration cameras, on which fish-eye lenses are mounted, was installed on the SSS. With an illumination of 1200-2400 Watt from eight quartz halogen lamps, photos can be taken from different positions. This allows to monitor the Inner Vessel shape and the position of radioactive sources during internal calibrations of the detector [93]. A photo of the Inner Detector taken with one of the CCD cameras during an internal *off-axis* calibration is shown in Figure 17.

Outer Detector The Outer Detector (OD) is a domed steel tank with 16.9 m of height and 18.0 m of diameter and it contains the Stainless Steel Sphere including the Inner Detector. The OD is filled with 2100 tons of ultra-pure deionized water. On the one hand, this water tank (WT) serves as a passive shielding for the Inner Detector against environmental radiation. On the other hand, it allows to detect Cherenkov light generated by cosmic-ray muons and muon showers crossing the detector. The Cherenkov light detection is performed by 208 fully encapsulated photomultiplier tubes (PMT) which are installed on the outer surface of the Stainless Steel Sphere and on the floor of the Water Tank. Highly reflective Tyvek sheets cover the surfaces of the OD in contact with the water in order to improve the light collection. A special OD calibration system was also installed to synchronize the OD PMTs and to measure their characteristics. Further details are reported in references [89, 90, 91] and in Section 4.1.

Purification plants An efficient solar neutrino measurement with the Borexino detector required a careful selection of all integrated materials with lowest impurity levels possible, severe precautions

during the construction and the procurement and filling of purified scintillator[5].
As shown in Figure 11, several auxiliary systems for the purification and circulation of the scintillator, buffer solution and water were built around the Borexino detector.
Most of the systems, tanks and pipings were extensively measured for ^{222}Rn emanation. The water for the OD was purified by reverse osmosis deionization and nitrogen stripping. Before the filling of the ID the PC was purified. Since PPO has a high melting point (70°C), PPO cannot be purified directly. Instead, a highly concentrated "master solution" of PC with 140 g/L of PPO was prepared and cleaned separately from PC. The purification consisted of: (1) water extraction (removal of ionic particles), (2) distillation at 80 mbar and 92°C (removal of non-ionic impurities including dust particles), (3) N_2 stripping using *Low Argon/Krypton Nitrogen* (LAKN: Rn<8 μBq/m^3, Ar<0.012 ppm, Kr<0.02 ppt (for details see [95]) and (4) ultra-fine filtration.
A detailed description of the commissioning of the complex purification plants of Borexino and of the filling procedure in 2006-2007 can be found in [96, 97].

3.1.2 Detection principle and optical properties of the scintillator

Elastic neutrino-electron scattering The neutrino detection reaction in Borexino relies on the pure leptonic process of elastic neutrino-electron scattering given by

$$\nu_i + e^- \rightarrow \nu_i + e^- \tag{3.1}$$

The neutrino-electron scattering reaction is sensitive to all neutrino flavors ν_i with i={e,μ,τ}. However, only ν_e can interact via the charged and the neutral current, while $\nu_{\mu,\tau}$ exclusively interact via the neutral current. This leads to different energy-dependent cross sections for ν_e and $\nu_{\mu,\tau}$ in the used scintillator. Assuming a zero neutrino magnetic moment, the differential cross section is given by [98]

$$\frac{d\sigma}{dE_e} = \frac{G_F^2 m_e^2}{2\pi}\left[(g_V + g_R)^2 + \left(1 - \frac{E_e}{E_\nu}\right)^2 + \frac{m_e E_e}{E_\nu^2}\left(g_A - g_V^2\right)\right] \tag{3.2}$$

where G_F is the Fermi constant, g_A and g_V the axial and vectorial coupling constants, E_e the recoil energy of the electron and E_ν the energy of the incident neutrino. In case of ν_e-e scattering one obtains $g_V = 1/2 + 2e^2/g^2$, $g_A = 1/2$, in case of $\nu_{\mu,\tau}$-e scattering g_V and g_A become $g_V = -1/2 + 2e^2/g^2$, $g_A = -1/2$. Herein, g is the weak coupling constant and e the elementary charge unit. As a consequence, the cross section $\sigma(\nu_e)$ is larger than $\sigma(\nu_{\mu,\tau})$. At 667 keV, the Compton-like edge of the recoil energy spectrum of electrons scattered with the mono-energetic 862 keV ^{7}Be neutrinos, the ratio of $\sigma(\nu_e)/\sigma(\nu_{\mu,\tau})$ is approximately 4.

Then, the total interaction rate R for neutrino electron scattering can be calculated via

$$R = N_e \int_0^{E_\nu} \phi(q)\left[P_{ee}(q)\int_0^{E_{e,M}} \frac{d\sigma_e(q,t)}{dt}dt + (1 - P_{ee})\int_0^{E_{e,M}} \frac{d\sigma_e(q,t)}{dt}dt\right]dq \tag{3.3}$$

[5]The scintillator was produced at *Polimeri Europa* in Sardinia, Italy. A special loading station was constructed allowing clean isotanks in a N_2 atmosphere. The isotanks were then shipped directly to the experimental site at LNGS within one day and unloaded using a custom-made pumping station. This rapid delivery limited the exposure of the freshly produced PC to cosmic radiation, thereby minimizing the production of cosmogenic ^{7}Be in the PC [94].

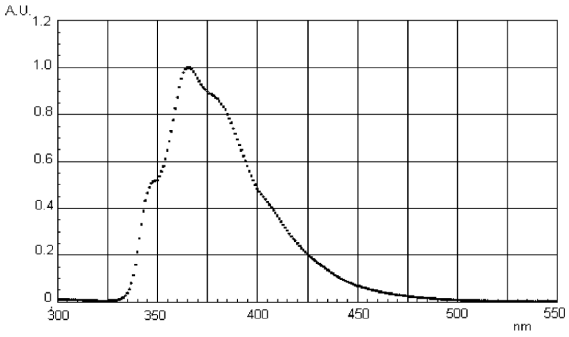

Figure 13: PC plus PPO (1.5 g/L) emission spectrum (in arbitrary units) versus wavelength given in [nm].

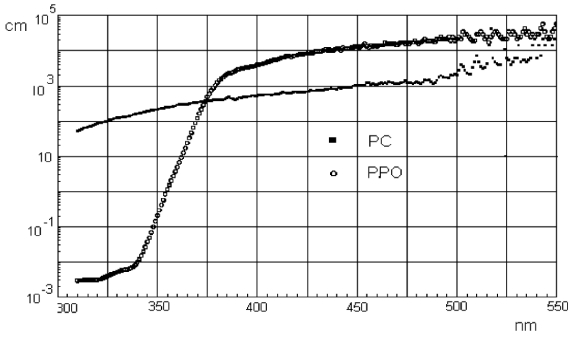

Figure 14: Attenuation length (in [cm]) of PC and PPO (1.5 g/L) versus wavelength given in [nm].

Herein, N_e is equal to the electron density in the target material, $E_{e,M}$ the maximum recoil energy of the electrons, ϕ(q) is the average neutrino flux at 1 Astronomical Unit (distance between Sun and Earth) expressed as a function of the energy q. Moreover, P_{ee}, the survival probability of solar ν_e, and $(1 - P_{ee})$, the survival probability of the combined solar $\nu_{\mu,\tau}$, are used (see Section 2.1.1).

Scintillation light in Borexino Incident charged particles (e.g. recoiled electrons in scattering processes with neutrinos, β and α particles) losing energy in the PC+PPO medium lead to the ionization and excitation mostly of the PC molecules which are present in larger quantities with respect to PPO ones. The PC excited molecules transfer their energy to the PPO ones and the radiative decay of the PPO excited molecules from the first excited state to the ground state is responsible for the observed fluorescence.
The PPO concentration in the PC has been optimized in order to reach:

- Maximum light yield: the maximum energy transfer efficiency from PC to PPO. Compared to pure PC, the light yield S for Borexino was increased by factor ∼20 for β-like events, leading to an emission of ≈10,000 photons per deposited MeV. This induces ≈500 photoelectrons/MeV in all PMTs of the Inner Detector. The obtained energy resolution scales approximately with $5\%/\sqrt{E[MeV]}$ [44].
  On the other hand, the light yield S is reduced by non-radiative energy dissipation typically referred to as *quenching effects*. Quenching effects are due to ionisation and mutual deexcitation of two excited molecules. Quenching is energy-, particle- and density-dependent. A commonly used model is that of Birks [99, 100]. It assumes that the specific fluorescence dL/dx is proportional to the specific energy loss dE/dx of the primary particle, if the quenching can be neglected. If quenching is considered, a correction must be applied, which is assumed to be also proportional to dE/dx. The Birks formula is given by

$$\frac{dL}{dx} = S\frac{\frac{dE}{dx}}{1 + k_B\frac{dE}{dx}} \tag{3.4}$$

  where S is the light yield and k_B the empirically defined Birks parameter.

- Wavelength shifter: the emission spectrum of PPO matches the PMT sensitivity, which lies around [350,500] nm, more closely than PC. Figure 13 depicts the final emission spectrum of PC+PPO in the concentration used for the Borexino scintillator.

- Self-absorption of PPO: The fluorescence light is attenuated by the PPO itself at lower wavelength values $\lesssim$360 nm (see Figure 14). The PPO quantum efficiency to re-emit this light is ∼80%, leading to an absorption after few iteration steps or at least to delayed arrivals of the photons on the photo-cathodes of the PMTs. Hence, the fluor concentration has to be balanced between the highest possible light yield and the fastest emission (see next point). The obtained absorption and scattering mean free length at 420 nm (close to the PMT quantum efficiency peak) are 7.8 m and 6.6 m, respectively. For 460 nm the mentioned mean free lengths are 8.2 m and 11.1 m [101]. This leads to a very transparent medium suitable for a large volume detector like Borexino.

- Fastest time response: A fast de-excitation of the PPO molecules comparable with the time jitter of the PMTs (few ns) allows to reconstruct the position of point-like events in the scintillator using the *time-of-flight* (TOF) information of the isotropically emitted photons. This is discussed in Section 3.2.1.
  The ability to reconstruct the positions of events from data in offline modus is commonly used to define a so-called *fiducial volume* (FV). This virtual volumetric software cut is a powerful tool to reject events reconstructed outside a given region in the scintillator. For instance, the *fiducial volume* commonly used for the ^{7}Be neutrino analysis is a concentric spherical volume with a nominal radius of 3.07 m and a z cut of ±1.67 m within the scintillator. The radial cut rejects efficiently events with a deteriorated energy reconstruction and external background events originating from the outer detector components. The z cut rejects the increased number of events close to the poles of the nylon vessels, where nylon and steel endcaps were mounted to supported the Tensylon ropes and belts which guarantee a stable position of the buffer and scintillator fluids (see Section 3.1.1).
  Another useful application of the position reconstruction algorithms is the tagging of background coincidences in space and time within the scintillator. This will be demonstrated in Chapter 4.

- α/β discrimination: As each particle type may create a different ratio of singlet and triplet states, the characteristic scintillation pulse shapes vary with the incident particle. Figure 15 shows the typical pulse shapes for α and β particles in a Borexino-like scintillator [102]. Based on these results powerful pulse shape discrimination techniques can be defined. The implementation of this characteristic pattern is accomplished e.g. by the *Optimum Gatti's method* [103], which is widely used in Borexino analyses.
  In the following the average time function of the α and β current pulses at the output of the photomultiplier are denoted with $\bar{\alpha}$(t) and $\bar{\beta}$(t). Further, the number of photoelectrons emitted for individual random waveforms in the arbitrary short time intervals Δt_i, into which the duration of the signals can be divided, are defined as α_i and β_i. Then, the particle identification Gatti parameter G for α and β particles is obtained through the following weighted sums [104]:

$$G_\alpha = \sum_i P_i \beta_i \quad \text{and} \quad G_\beta = \sum_i P_i \alpha_i \tag{3.5}$$

  where the weights P_i are expressed as follows

$$P_i = \frac{(\bar{\alpha}_i - \bar{\beta}_i)}{(\bar{\alpha}_i + \bar{\beta}_i)} \tag{3.6}$$

  From Equations (3.5) and (3.6) it follows that the weights P_i are positive for $\bar{\alpha}$(t) being higher than $\bar{\beta}$(t) and vice versa.

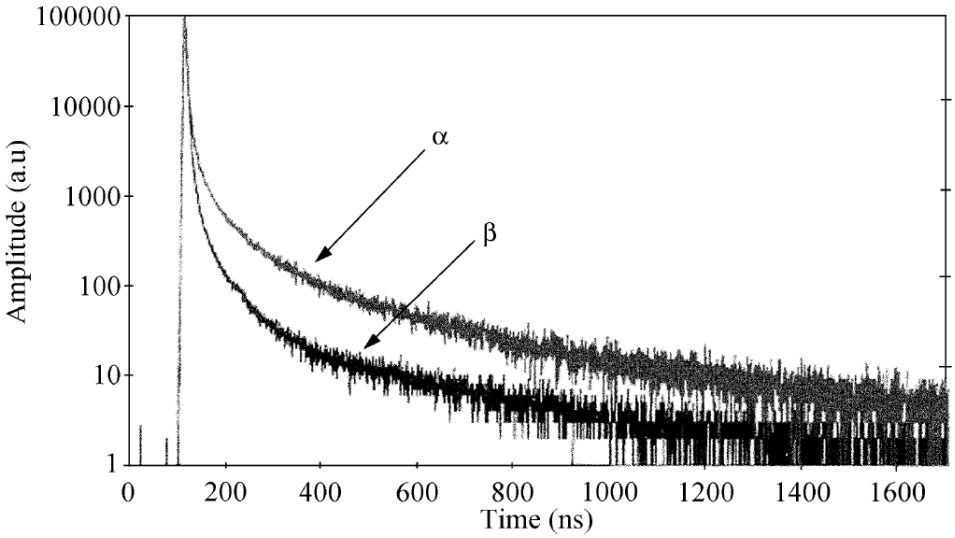

Figure 15: Time evolution of the light emission in a Borexino-like scintillator mixture of PC+PPO for α- and β-like events (taken from [102]).

3.1.3 Signal processing and event generation

Electronics chain and event generation The reconstructed information of an event detected with the Borexino detector relies on the time of arrival and the number of photons reaching the PMTs. This statement is valid for both scintillation light events (in the Inner Detector) and Cherenkov light events (in the Inner and Outer Detector).

In case of the Inner Detector (ID), the signals from the PMTs are collected by custom-made *front-end boards* (FEB). Each of the 14 Inner Detector electronics racks placed in the Borexino electronics room typically holds 14 FEBs. Each FEB contains 12 channels from 12 different PMTs. The FEBs disentangle the incoming DC high voltage signals from the AC signals. Moreover, the FEBs extract the time information, produce the analogue sum of 12 channels per board and prepare the digitalisation process. The digitalisation of the signals is performed by the so-called *laben boards* (LB)[6]. There are 20 LBs in each electronics rack, whereas each LB processes 8 channels. Thus, in total there are 280 LBs. The LBs prepare the signals from the incoming channels for the trigger system. If the Borexino main trigger system (*Borexino Trigger Board* (BTB)) detects more than 25 hit PMTs within a time interval of 60 ns, a trigger signal is generated. It is sent back to the *Power PC modules*, which are also installed on the VME crates. Then, the triggered *Power PC modules* start with the event-building. Finally, the preprocessed subparts of an event are assembled by a main PC, which creates the full event.
The above described main electronics circuit is accompanied by several auxiliary systems:
The *adder/scaler modules* have two functionalities. First, the *adders* provide the total analogue sum of all sums generated by the FEBs. This sum is used as input signal for the Flash ADC systems, that search for Supernova signals or try to detect neutrons following muon events more efficiently[7]. On the other hand, the *scalers* provide *real-time* information about the trigger rate induced by each single FEB. This allows the monitoring of the status of operating PMTs and the

[6]The name "laben" derives from the company LABEN S.p.a. (Milan, Italy), which produced the boards.
[7]The neutron detection systems in Borexino are reviewed in Section 4.2.2.

early detection of arising problems with single PMTs[8].

The Outer Detector (OD) electronics is similar to those used for the ID. However, due to the lower number of PMTs, the signal from each channel is decoupled and directly sent to so-called *charge-to-time-converters*. Subsequently, the total charge collected by the PMTs is calculated. Since the OD PMTs have to deal with much smaller amounts of light than the ID PMTs, the trigger threshold of the corresponding *Muon Trigger Board* (MTB) is set equal to six PMTs hit within 150 ns. Further details about the signal processing chain of the OD can be found in [90, 91, 89].

Trigger types There are different trigger types in Borexino which define subclasses of events. By adopting the nomenclature used in the Borexino data analysis framework *Echidna* (see Section 3.2.1), the following trigger types are distinguished: A trigger induced by neutrinos, γ rays, α and β decays in the ID is typically of `trigger type 1`. The gate length of one such trigger event is 16 μs. The events are sometimes referred to as "neutrino-like". Furthermore, muons induce a trigger in the MTB of `trigger type 2`. If the muons also cross the Inner Detector, they are attributed to a `trigger type 1` event. Finally, muon-induced neutrons are handled as events of `trigger type 128` (see Section 4.2.2). Beside the natural sources there are artificial signals generated by the BTB itself. These signal are used for the calibration of the PMTs to measure their gain, their sensitivity region and their dark noise. Signals from the lasers of wavelength λ=355 nm, 394 nm, 266 nm are referred to as `trigger types 4,8,16`, respectively. Calibration signals dedicated to the time alignment of the PMTs are of `trigger type 32` and random trigger events used for the determination of the dark rate are of `trigger type 64`.

3.2 Data analysis tools

3.2.1 Data reconstruction codes

Data reconstruction codes and modularity in Echidna Before physics analyses can be performed, the raw data files have to be processed in *offline* modus, where the physics parameters of the events are computed.
In 2004, the Borexino collaboration started to develop a common software tool named *Echidna*. This code is written in the object-oriented programming language C++ (as a single language) and uses the analysis platform `ROOT` [105] provided by CERN. The *Echidna* code contains an infrastructure and a number or modules for event processing. The infrastructure manages e.g. the communication with the database (reading, writing) and of the initialization and running of the modules.
The modules are persistent objects of a specific class that are designed to extract information from a given detector segment (`trigger, laben, muon, fadc, neutron, mctruth, track, tags`) at a given sublevel and to process it. The resulting event will be richer in information than in the previous stage. A simplified scheme of the event structure levels is depicted in the left panel of Figure 16. The following modules are executed in particular [90]:

1. Precalibration: The precalibration modules reconstruct the hit time of all PMTs for a given calibration event. This is used for the definition of the time alignment of all other events. Moreover, the charge information and the relative single photoelectron (SPE) peak position

[8]Flashing PMTs are most problematic. One possible reasons for flashing PMTs is water vapor that enters into the usually evacuated bulb of the PMTs via microscopic ruptures and induces continuous discharges and emission of light that can lead to a chain reaction affecting neighboring PMTs.

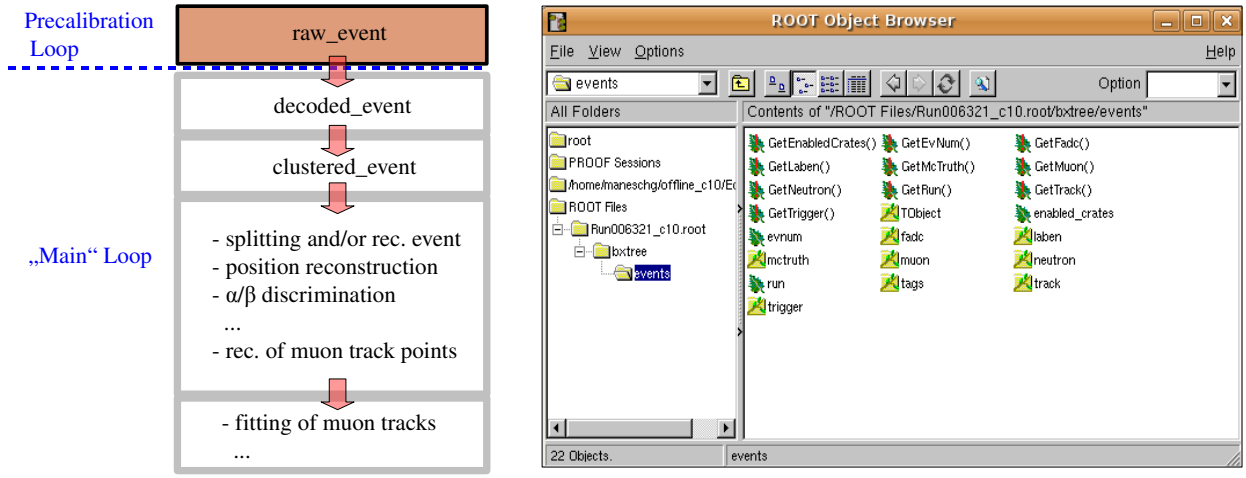

Figure 16: Event reconstruction levels (left) and the `ROOT` tree structure (right) implemented in the framework of the Borexino toolkit *Echidna*.

are estimated. Finally, the GPS time (starting from January 1, 2001) is calculated from the signals recorded by a GPS receiver unit.

2. Decoding: For all detector segments there are decoding modules which lead to a first reconstruction level of the events. In case of the Inner Detector (referred to as `laben`), two main tasks are carried out:
(i) decoded hit time: it takes into account time corrections relative to the grey counter (i.e. internal clock) installed on the *laben boards*.
(ii) decoded hit charge: it is calculated according to $Q_{dec} = (P - B)/s$, where P and B are the peak and base sampling of the PMT pulse and s is the peak position of the SPE.

3. Clustering: Looking at the hit time distribution in a trigger gate of 16 μs, the physical pulse is superimposed to the PMT random hits. In some cases, more than one physical peak from fast coincidences (for example ^{212}Bi-^{212}Po coincidences; see Section 3.3) can appear in the trigger window of the same event. The clustering module groups the hits belonging to the same physical event into so-called *clusters*. The clustering is done by scanning the time distribution of the decoded hits in 16 ns bins. The conditions for the start of a cluster are:
(i) the bin content exceeds the dark noise level by at least 3σ,
(ii) at least 20 hits are found in the first 48 ns,
(iii) the integral of all hits exceeds the trigger threshold (typical BTB: 20 hit PMTs) by 80%.
The end of a cluster is set when the hits of a bin reach the dark noise fluctuation level again. Two subsequent physical events that are too close in time and do not fulfill the last condition are referred to as *pile-up*'s. Splitting algorithms can be used to disentangle such events (for more details see [90]).

Energy reconstruction The identified clusters are examined by further modules which deduce a large number of physical quantities. In this paragraph, only few are discussed.
Some of the modules reconstruct the energy of the clusters. There are two possibilities to express the energy information. The first energy variable is given by the charge information Q_{pe}, where all ADC values from all hit PMTs are collected. The unit is 1 photoelectron [pe]. 1 MeV deposited in the center of the detector corresponds roughly to ~510 pe. Q_{pe} is typically normalized and

expressed by the reconstructed charge variable Q_{pe} as follows:

$$Q_{rec} = 2000 \cdot \frac{Q_{pe}}{N_{pmt}} \tag{3.7}$$

with N_{pmt} being the number of PMTs that operate during a run. At the beginning of data acquisition in May 2007, most of the 2214 mounted PMTs were operational. However, after start of data collection several of the PMTs stopped working, especially in the lower hemisphere of the detector. During data collection, PMTs might be also switched off by subcomponents of the electronics. The normalization factor 2000 is a Borexino-internal arbitrarily chosen value. The energy unit after normalisation is denoted by 1 normalized photoelectron [npe]. Note that the normalization does not take into account the spatial distribution of the operating PMTs during a run, but only its total number. So it is clear that this rescaling does not account for possible geometrical effects.
Additionally, at energies below ∼1 MeV the light yield is not proportional to the deposited energy due to quenching effects (see Section 3.1.2). However, the calibration of the energy scale using a neutron source ^{241}Am^{9}Be (see Figure 18) has also demonstrated that the charge variable grows almost linearly above ∼2 MeV. In the region between 2 MeV and 9 MeV one can parametrized the number of normalized photoelectrons Q_{rec} by $Q_{rec} = a \cdot E + b$, with a=(459±11) npe/MeV and b=(115±38) npe [69].

The second possibility to express the energy of a cluster is the number N_{hits} of hit PMTs. The unit is [hits]. An energy of 1 MeV deposited at the detector center corresponds to ∼350 hits. In analogy to Equation (3.7), the N_{hits} variable can be normalized introducing the reconstructed variable N_{rec} with the unit [nhits]. At higher energies the probability, that a single PMT is hit more than once, increases[9]. By taking into account the binomial probability of such multiple hits and applying the normalisation to 2000 alive PMTs one obtains[10]:

$$N_{rec} = -2000 \cdot \ln\left(1 - \frac{N_{hits}}{N_{pmt}}\right) \tag{3.8}$$

The N_{nhits}^{corr} variable is well-suited for analyses of events, of which scintillation light deposited in the detector lies below ∼1 MeV. Above this value the charge variable Q_{npe} is more adequate, because it has a wider dynamical range and follows an almost linear behavior at least above ∼2 MeV up to ∼9.3 MeV (see Figure 18). An exception is made for muon-induced neutron events: when a muon crosses the scintillator, it produces a large amount of scintillation light. This affects the electronics and thus deteriorates the charge information, while the N_{nhits} and N_{nhits}^{corr} variables remain reliable (more details in Section 4.2.3).

Position reconstruction One module reconstructs the vertex position (i.e. the light barycenter) of a point-like event from the hit time distribution. There are several algorithms in *Echidna* used for the calculation of the vertex position. The algorithms are referred to as *Milano*, *Dubna*, *Moscow* and *LNGS* according to the Borexino groups which developed them. For instance, the well-tested *Milano* algorithm, which was also used in the CTF, is based on the minimization of the following log-likelihood function:

[9] As reference: the photons from a 2.2 MeV scintillation event hit ∼750 PMTs, where ∼15% are hit twice.
[10] The formula is defined for an event in the center of the detector; events close to the transition region between the scintillator and the buffer are affected by border effects.

$$\mathcal{L}(t_0,\vec{r}) = \prod_{i}^{N_{hits}} \text{PDF}\left(t_i - t_0 - \frac{d_{0,i} \cdot n_{eff}}{c}\right) \tag{3.9}$$

where $d_{0,i}$ (and t_i) is the distance (and the *time-of-flight* of the fastest unscattered photons) from the light barycenter of the event to the i$^{\text{th}}$ hit PMT, N_{hits} is the number of hit PMTs and $\vec{r}$ is the position of the barycenter and t_0 the time of the event. The *probability density function* (PDF) corresponds to the simulated PPO emission curve. The constant c denotes the speed of light in vacuum and n_{eff} is an empirically determined effective index of refraction which takes into account all other effects not accounted for in the reconstruction algorithm. This includes optical (e.g. Rayleigh scattering) and electronical (e.g. multiple photoelectron occupancy) effects. The multiple electronics effect is created by the fact that the Borexino electronics record the time of each photoelectron by introducing a dead time of 145 ns after each hit for each PMT. At larger energies the effect becomes more dominant.
Taking into account all of these effects, the resolution of the position reconstruction can be estimated. For the high-energy 2.2 MeV γ rays emitted from a ^{214}Bi source (see Section 3.4.1) the spatial resolution was found to be (13±2) cm in x and y, and (14±2) cm in z [15]. The spatial resolution is expected to scale with $1/\sqrt{N_{PMT}}$. This was also confirmed by examining the spatial resolution of ^{14}C, which was found to be (41±6) cm [44, 88].

By subtracting the *time-of-flight* of each photon from the barycenter to the i$^{\text{th}}$ hit PMT one obtains the emission time spectrum. This is used to define the event type (α-, β-like) according to pulse shape discrimination criteria. One method is the Gatti parameter expressed via the Equations (3.5) and (3.6).

Development of Echidna, Mach4 and MOE Since the beginning of data collection in May 2007, the *Echidna* code has been continuously improved and new modules have been added. Every module is assigned to at least one maintainer, who has to implement, debug and test new scheduled tasks. After a given test phase of typically several months, the modules are merged and the resulting code is "frozen". This terminates a development cycle. The officially released version is denoted by *Echidna cycle N*, with *N* being the number of the cycle. The analyses presented in this thesis are based on several *Echidna* versions. They will be cited in the introduction of each analysis in the following sections.
In 2007, the US-American Borexino collaborators from Princeton University and Virginia Polytechnic Institute and State University set up a second analysis tool called *Mach4*. That way the Borexino collaboration had the opportunity to perform the physics analyses with two independent codes. The advantage of this procedure was a permanent cross-check of the results.
In 2009/2010, the two codes *Echidna* and *Mach4* were merged in a new code named *Mach4-Over-Echidna* (MOE). The primary objective has been to exploit the synergy effect by using both codes. In addition, small discrepancies of calculated physical parameters of single events can be compared. Such small differences can arise at different levels of the data reconstruction codes due to the application of different methods and cut selections.

3.2.2 Simulation tools

The `G4BX` and `BXELEC` simulation tools The Monte Carlo code originally developed for Borexino was `GENEB` [107]. It was programmed by the Italian Borexino group in Milan and is based on the

EGS4 code [108]. A second, more powerful simulation framework tool named *Bxmc* based on GEANT4 [109, 110] has been developed and continuously improved (see Section 3.4) and is now widely used by the Borexino collaborators. A detailed description of the Monte Carlo code and the energy reconstruction algorithm is in preparation by the Borexino Monte Carlo working group.
Bxmc consists of the following parts:

- Particle generation and propagation in the Inner Detector: The Monte Carlo code G4BX generates and propagates particles in the Borexino detector until they reach the photocathodes of the PMTs. Several particle generators can be selected. The decay of radionuclides is typically simulated by the *Radioactive Decay Module* (RDM) which is based on the ENSDF tables. Each generated particle is propagated individually within the fully modelled Inner Detector of Borexino. All materials used for the construction of the detector are included in the simulation.
  The simulation takes into account the production of the scintillation and Cherenkov light, the propagation and the energy loss mechanisms for light and for all other particle types. Each secondary electron in a γ-induced Compton-electron cascade is affected by energy-dependent ionisation quenching, which amplifies the distortion in the γ energy scale. The quenching of the scintillation light is described by the Birks formalism (see Section 3.1.2). To some extent the code also uses a Borexino internal database containing values from laboratory measurements [83] of the characteristic absorption and reemission time of the scintillation light in the scintillator mixture used.
  The output of this simulation can be directly converted into a ROOT-file. At the same time it is used as input for the electronics-chain simulation.

- Electronics-chain simulation: The simulation tool BXELEC simulates the entire electronics chain starting from the photocathode of the PMTs. The trigger threshold, the SPE of each operating PMT, the time delays and the charge information loss within the electronics chain are included.
  In order to simulate a real data set, BXELEC can also adopt the exact pattern of operating PMTs and DAQ/electronics settings during the period of interest.

- Data reconstruction: The data reconstruction tool *Echidna* uses the output of the electronics chain simulation to reconstruct the events according to the procedure described in Section 3.2.1.

3.3 Achieved background levels in Borexino

The uncertainty of a neutrino rate measurement depends on the collected statistics, on the knowledge of the detector response and on the neutrino-to-background ratio. As pointed out in Section 2.4, there are three subgroups of background components: (1) the intrinsic contamination of the scintillator due to impurities, (2) the external background and (3) cosmogenic induced backgrounds (muons/muon showers, muon-induced neutrons and radioisotopes). The latter two groups will be analyzed in Chapter 4 and 5, respectively. The intrinsic contamination of the scintillator is presented in this section.

Intrinsic contamination of the scintillator The background levels achieved in the initial phase of the experiment are summarized in Table 31 of Appendix A.2. Most of the background components have met or even surpassed the specifications. In terms of radiopurity, the lowest ever measured levels of natural contaminants from uranium and thorium have been established. On the

contrary, some background components have shown a higher rate than expected.
The main components of the intrinsic contamination of the scintillator are:

- ^{14}C: Organic liquid scintillators intrinsically contain a high concentration of ^{14}C (β^-, Q=0.156 MeV, τ=8267 y) which is produced by the hadronic component of the cosmic radiation or via neutron-induced reactions underground. The typical ^{14}C/^{12}C ratio is 10^{-12}. The PC scintillator for Borexino was obtained from a crude mineral oil with a ^{14}C/^{12}C ratio of $\sim 10^{-18}$. This corresponds to a rate of ∼30 decays/s/100ton. The probability for two ^{14}C decays to occur simultaneously is relatively high, which leads to a *pile-up*. Due to the finite detector resolution and the *pile-up*, the ^{14}C spectrum ends at ∼0.2 MeV (see Figure 9). This energy marks the lower threshold for all Borexino physics analyses. Since the spectral shape factors of ^{14}C and its *pile-up* are not well known, this energy region is sometimes excluded in global spectral fit analyses.

- ^{238}U decay chain: A representation of ^{238}U and its daughter nuclides is given in Figure 89 of Appendix A.3. In Borexino, the concentration of ^{238}U cannot be measured directly. Instead, the fast ^{214}Bi-^{214}Po delayed coincidences are measured: ^{214}Bi decays (β^-, Q=3.272 MeV) to ^{214}Po, ^{214}Po (α, Q=7.833 MeV, τ=164.3 μs) to ^{210}Pb. Then, the ^{238}U concentration is deduced from the number of counted ^{214}Bi-^{214}Po coincidences assuming secular equilibrium, which however, might be not the case. Assuming secular equilibrium the Borexino collaboration measured a concentration of $(1.6\pm0.1)\times10^{-17}$ g/g [44], which is by one order of magnitude lower than the specification. It is worth noting that the ^{214}Bi-^{214}Po coincidences provide good reference distributions for particle- and energy-dependent α/β discrimination variables like the Gatti parameter (see Section 3.1.2).
  The most prominent ^{238}U daughter nuclide in Borexino is ^{210}Po. It was probably introduced with the PPO. α particles from ^{210}Po decays (α, Q=5.41 MeV, τ=138 d) are quenched by a factor of ∼13, therefore the ^{210}Po peak is located at ∼0.3 MeV. The non-presence of ^{210}Pb proves that the secular equilibrium within the ^{222}Rn subchain is largely broken. The ^{210}Po rejection strategies are waiting for its decay and the efficient α/β discrimination. Thus, the ^{210}Po peak has not be problematic for the ^{7}Be neutrino analysis. However, it is worth to note that the ^{210}Po rate increased several times due to detector operations (see Section 3.4).
  A second troublesome contaminant which is visible in the Borexino energy spectrum might be attributed to the ^{238}U daughter nuclide ^{210}Bi. ^{210}Bi decays (β^-, Q=3.272 MeV) to ^{210}Po. Since it is not clear if the contaminant is indeed ^{210}Bi the background will be referred to as "^{210}Bi-like". The energy spectrum of the observed ^{210}Bi-like contaminant is very similar to the CNO neutrino spectrum. This makes a disentanglement of the CNO neutrino signal from the ^{210}Bi-like contaminant very difficult. Thus, a common fit component CNO+^{210}Bi is typically used. Like ^{210}Po, the rate of the ^{210}Bi-like contaminant gradually increased over time (see Section 4.3.7).

- ^{232}Th decay chain: A representation of the decay sequence of ^{232}Th is given in Figure 90 of Appendix A.3. The concentration of ^{232}Th in the scintillator is estimated via the determination of ^{212}Bi-^{212}Po delayed coincidences: ^{212}Bi decays (Q_β=2.254 MeV; Branching ratio (BR): 64.06%) to ^{212}Po, ^{212}Po (τ=432.8 ns) to stable ^{208}Pb. Assuming secular equilibrium, the concentration of ^{232}Th turned out to be $(6.8\pm1.5)\times10^{-18}$ g/g [44]. This is more than one order of magnitude below the specification.

- ^{85}Kr: This man-made radioisotope is the most problematic contaminant for the solar ^{7}Be neutrino analysis, since the rate and the spectral shape of ^{85}Kr are similar to those of the ^{7}Be neutrinos. ^{85}Kr is released into the atmosphere as a fission product from nuclear reactions in nuclear reactions and from nuclear fuel reprocessing plants. In the atmosphere in Central

Europe an activity of ∼1.5 Bq/m^3 was measured [111]. ^{85}Kr (Q=0.687 MeV, τ=15.52 y) decays via two channels: (1) β-decay into the ground-state of ^{85}Rb (BR: 99.566%) and (2) β-decay into the meta-stable state of ^{85m}Rb which decays (τ=1.464 μs) to ^{85}Rb under emission of a characteristic 0.514 MeV γ ray (BR: 0.434%). The ^{85}Kr content was measured via the second decay mode. The best estimation of the ^{85}Kr activity is (30±5) event/d/100ton. This result is in agreement with the value obtained from the spectral fit analysis of ($25\pm3_{stat}\pm2_{syst}$) events/d/100ton [44]. This value is 3-4 times higher than the specification, even though the value is two orders of magnitude lower than in air. The ^{85}Kr contamination of the scintillator was probably introduced by a small air leak during the initial filling operations.

- Other contaminants: Naturally occurring contaminants like ^{39}Ar, ^{40}K, ^{87}Rb, ^{113}Cd and ^{115}In might also be present in small non negligible concentrations in the Borexino scintillator, but they were not yet measurable. In few cases, a weak guess or an upper limit can be defined. Since ^{85}Kr was probably introduced by an air leak, ^{39}Ar could also be present, however, its activity in air is typically two orders of magnitude lower than the ^{85}Kr activity.
  The concentration of ^{40}K in the organic liquids could also be non negligible for the solar neutrino analyses. ^{40}K (β^-, Q=1.311 MeV, τ=1.842×10^9 y) has two decay modes: (1) In the first mode ^{40}K decays to ^{40}Ca (BR: 89.28%); (2) in the second mode ^{40}K undergoes an electron capture to the excited state of ^{40}Ar*. Then ^{40}Ar* de-excites under emission of a characteristic 1.46 MeV γ ray. The energy released in both decay channels is hidden by the ^{7}Be- and the *pep*/CNO neutrino energy window and by the ^{11}C peak. So far, an upper limit of <3×10^{-16} g/g for the ^{40}K concentration could be determined.

3.4 Detector stability and operations on the detector

3.4.1 Operations on the scintillator

The background analysis of the first months of data collected in Borexino revealed that the achieved concentrations of uranium and thorium in the scintillator were one order of magnitude lower than anticipated (see Section 3.3). In order to maintain these radiopurity levels, the mechanical and thermal conditions of the scintillator should have been kept stable. At the same time, the Inner Detector should have been kept hermetically sealed. However, over the last ∼3.5 years the Borexino collaboration had to perform several operations on the detector to counteract arising problems and to perform calibration campaigns. The following paragraph gives a brief overview over these operations.

Tempering of the scintillator In the summer 2007, the scintillator started to cool down, decreasing the volume of the scintillator contained in the Inner Vessel (for details see [93]). Additionally, the water dissolved in the scintillator began to condense on the Inner Vessel nylon, such that it became opaque. To solve this problem, the water distillation plant was reactivated. Thus, water from the Outer Detector could be heated while circulating. That way, heat could be transferred to the Inner Detector and the haze disappeared.
In the beginning of 2008, the water loop was restarted in order to counterbalance the considerable change in air temperature in Hall C, that induced a movement of the Inner Vessel. The fluctuating air temperature was caused by the large amount of heat generated by the operating magnets of the neighboring OPERA experiment. A better ventilation system in Hall C solved the problem.
Finally, the water loop was used to obtain the optimal temperature gradient of the organic liquids to completely suppress convection processes in the scintillator.

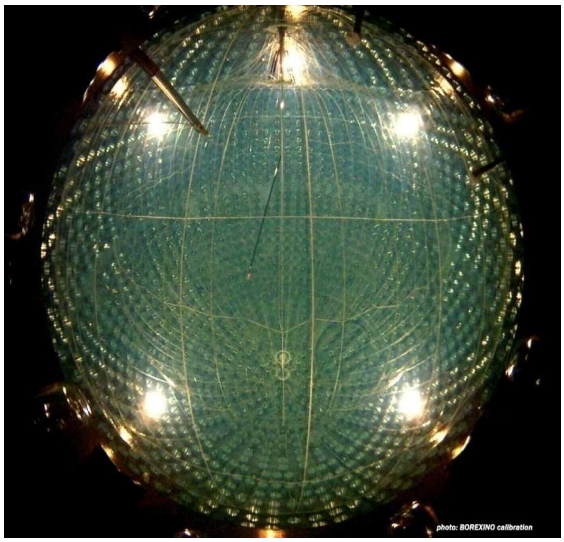

Figure 17: CCD image of the Inner Detector during an *off-axis* calibration campaign. The calibration arm with the red laser light close to the source is well visible.

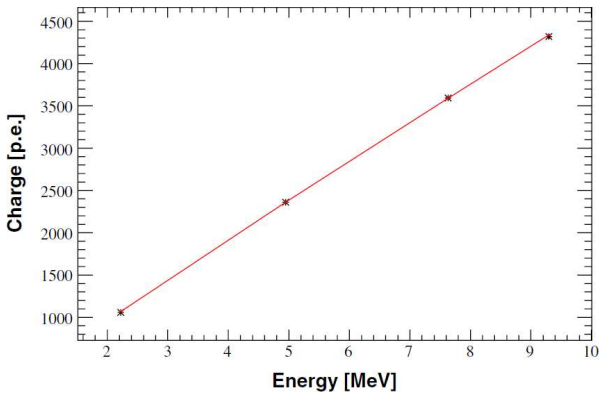

Figure 18: Energy scale of the charge variable: The dots are the measured γ peaks from ^{241}Am^{9}Be neutrons captured on H(2.223 MeV), C(4.945 MeV), ^{56}Fe(7.631 MeV) and ^{54}Fe(9.298 MeV). The red line corresponds to the MC prediction for γ rays generated in the detector center [15].

Removal of DMP from the buffer and refilling operations In spring of 2008, the shape of the Inner Vessel started to change. In August 2008, it was discovered that the scintillator was leaking into the buffer at a spot in the upper hemisphere of the Inner Vessel. This was confirmed by the determination of the chemical composition of extracted buffer samples, but also by the increased number of reconstructed events in the buffer. The leak rate was 1.5 m^3/month [93].
In order to stop the leak, the Borexino collaboration decided to reduce the buoyancy force between scintillator and buffer by reducing the DMP concentration in the buffer (see Section 3.1.1). Until the summer of 2009, the concentration was gradually decreased from 5 g/L to 2 g/L, which finally stopped the leakage. The leak rate was estimated to be <0.5 m^3/month. In November 2010, the Borexino calibration group studies of the Inner Vessel volume confirming this trend.
In order to reestablish the original spherical form of the Inner Vessel, a certain amount of new scintillator had to be prepared. A first charge was inserted into the Inner Vessel in October 2008 and a second one in June 2009.

Calibration campaigns The Borexino detector design has foreseen the possibility to perform a wide range of different calibration types. There is an internal and an external calibration system. The internal calibration system allows to place radioactive/artificial sources within the Inner Vessel. The sources are inserted into the scintillator from a clean room (CR4) on the top of Borexino, where the detector can be opened. In case of the external calibration system, a source is transported through the Water Tank via a tube system and deployed right behind the Stainless Steel Sphere. The preparation for an internal calibration has started prior to the beginning of data collection in May 2007. Because of the achieved high radiopurity of the scintillator, the calibration program was postponed, since a calibration has the potential to contaminate the detector. When the aforementioned leakage was discovered, the internal calibration became more urgent. For that reason, a series of calibration campaigns was planned and carried out in autumn 2008 and in the first half of 2009. A detailed description of the calibration campaigns in the Inner Detector of Borexino is described in [93].
In October 2008, the first internal calibration campaign was performed, in which the sources were

only placed along the z-axis (*on-axis*) perpendicular to the point of insertion. From January to February 2009, the Borexino calibration team used a calibration arm for the first time. Even though its surface is 35 times larger than that of the *on-axis* insertion rods, which increases the possibility to contaminate the scintillator, it allows to scan *off-axis* the interior of the Inner Vessel. The calibration arm consists of several rods which are coupled but still free to move *off-axis* like an "arm" via a tether tube made of Teflon. A source can be fixed on a special coupler mounted on the end of the deployment system. To locate the source, a fiber optic cable transmits a red laser light to a diffuser bulb mounted close to the source. This is shown in Figure 17. The third calibration campaign was performed in June to July 2009, in which the sources were deployed both *on-* and *off-axis*.
In total, ∼300 positions in the Inner Vessel were scanned using different calibration sources: γ emitters (^{139}Ce, ^{203}Hg, ^{85}Sr, ^{54}Mn, ^{65}Zn, ^{60}Co, ^{40}K), β-emitters (^{14}C, ^{214}Bi), the α emitter ^{214}Po and the neutron emitter ^{241}Am^{9}Be. Data were taken for a total of 35 days of lifetime.

As part of the present thesis a first external calibration was performed in July 2010. For this purpose a custom-made ∼5 MBq ^{228}Th source has been produced and deployed at 6.85 m distance from the center of the detector. This distance corresponds to the radius of the stainless steel sphere. Two positions, one in the upper and one in the lower hemisphere of the detector, were measured. Data were collected for a total of 9 days of lifetime. Since the external calibration is non-invasive, a contamination of the scintillator and other detector components was avoided. A detailed description of this calibration is given in Section 5.3.

Purification campaigns Even though Borexino has reached highest radiopurity levels and the internal calibrations of the detector did only introduce a very small contamination, the collaboration decided to try to even further reduce the concentrations of ^{85}Kr, ^{210}Po and ^{210}Bi which impede the first direct measurement of the *pp* and CNO neutrinos. Thus, new purification campaigns of the scintillator have been considered. Several possibilities are available: (i) sparging with *Low Argon/Krypton Nitrogen* (LAKN) [95], (ii) nitrogen (LAKN) sparging and water extraction, (iii) distillation. Several tests in the CTF were carried out in March 2010 to purify the filling system/pipings and to study backgrounds still present after refilling of the purified scintillator batches [112]. Finally, option (ii) was selected. The first purification campaign was carried out from July to October 2010, in which the full scintillator volume was circulated three times. A second purification campaign is ongoing (since January 2011). At the moment of writing the efficiency of the first purification campaign is under extensive study.

3.4.2 Duty cycle calculation

The following section is dedicated to the study of the achieved duty cycle in Borexino. A period of 1180 days (May 16, 2007 - August 8, 2010) has been analyzed. For the calculation of the duty cycle only data were considered, which passed the Borexino validation procedures and were not calibration data. The reduced duty cycle (commonly referred to as "lifetime") over the entire period is shown in Figure 19.
In 2007, the overall lifetime was ∼65%. It has a reduced value due to the initial instabilities of the DAQ-system and frequent failures of electronics subcomponents. In November/December of 2007, an electronics maintenance campaign was carried out which stabilized data acquisition. In addition, a new trigger system for the detection of muon-induced neutrons was installed.
In the period between January 2008 and August 2010 the calculated lifetime was ∼73%. If the 44 days of internal and external calibrations of the detector are not considered, the fraction of lifetime

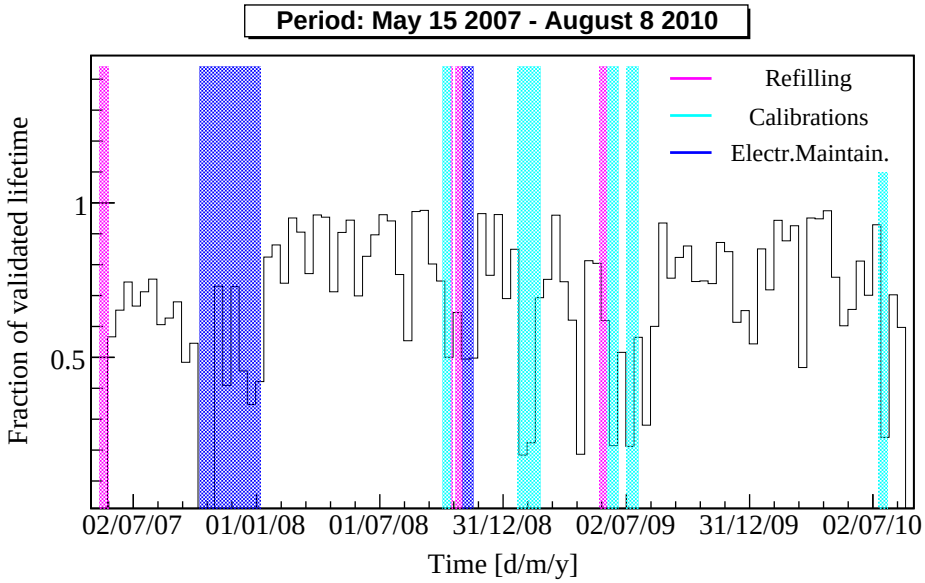

Figure 19: Calculated fraction of lifetime of the acquired and validated data in Borexino. Electronics maintenance campaigns, refilling operations and calibration campaigns are marked in different colors. The latter two were described in Section 3.4.1.

increases to ∼76%. Auto-restart failures and extraordinary hardware problems contributed to ∼10% loss of DAQ-time. Refilling operations themselves did not introduce a loss of lifetime, since the DAQ system could continue to collect data without interruption. However, the frequent imaging of the Inner Detector to monitor the shape of the Inner Vessel in the time after the leak introduced a ∼10% loss of lifetime. Other exceptional events such a blackout in August 2008 and the strong earthquake on April 4, 2009 fortunately did not affect the performance of the detector and induced only few % of lifetime loss.

4 Analysis of muon-induced backgrounds

4.1 Prompt muon signal

4.1.1 Introduction

Even with all the care taken to avoid natural radioactivity, radon diffusion and other intrinsic contaminants, Borexino is still subject to a non negligible cosmic-ray background. The origin and the properties of cosmic-rays in the atmosphere and underground are widely described in literature (see [113, 114, 115] and references herein).

Muons and atmospheric neutrinos are the most frequent particles (compared to e.g. neutrons, protons, e^+, e^-, π^+, π^-) that reach the sea level. Both particle types can penetrate deep into the subsurface. Within the rock, secondary muon-induced electromagnetic and hadronic showers can occur. The higher the muon energy, the deeper muons can penetrate the rock. The mean muon energy at sea-level is $\approx$4 GeV [115]. At the LNGS experimental site, which is covered by a $\sim$1.4 km thick barrier of dolomite stone corresponding to 3800 meters of water equivalent (m w.e.), the mean muon energy is $\approx$310 GeV (extrapolation from [116]). Furthermore, the muon rate is reduced by six orders of magnitude from $\approx$1 μ/min/cm^2 [115] to $\sim$1.2 μ/hour/m^2 [117, 118]. In the case of the Borexino detector, this residual muon flux translates to about 10000 events/d in total. Approximately half of them cross the Inner Detector, generating background signals. Since the rate of observable neutrino events in the innermost 100 tons of the Borexino scintillator is $\sim$50 events/day, the detector was equipped with a muon veto system which was designed to reach a muon detection efficiency higher than 99.98%.
However, not only the muons and muon showers (denoted in the following sections by "muon events") have to be rejected. Borexino must also handle two other types of muon-related background events. Muons and particles in muon showers may collide with atomic nuclei in the detector, producing hadrons such as pions and neutrons. The secondary neutrons randomly propagate through the scintillator and are then mainly captured by protons. These neutron capture processes emit 2.223 MeV photons which can be used to tag the neutron event (see Section 4.2.2). The atomic nuclei which interact with the muon/muon shower particles under emission of nucleons may become radioactive. These muon-induced radioisotopes have different lifetimes and are produced at different rates. The detection and the rejection techniques of these radionuclides are discussed in Section 4.3.

The present section covers the detection and the characterization of prompt muon signals.
Section 4.1.2 reviews the muon detection techniques and their efficiencies achieved so far with the Borexino detector. The section includes an estimation of the average muon rate in Borexino.
Furthermore, several sections are dedicated to the muon track reconstruction, to which several contributions have been made within this thesis. The array of PMTs in the Outer and Inner Detector of Borexino can spatially resolve the *time-of-arrival* of the Cherenkov and scintillation light caused by the muons. In case of the Outer Detector, the charge collected by the single PMTs can be used as well. With this information, muon track points can be reconstructed and a global fit can be performed (Section 4.1.3). As already pointed out in Section 2.4, the muon track is useful for e.g. a more effective rejection of radioisotopes like ^{11}C. In order to apply the muon track reconstruction, the reliability of the algorithms has to be demonstrated first. Several tests had to be carried out, two of them are presented in this work. The radial distribution of the muon tracks is investigated in Section 4.1.4. It is expected to grow linearly with the distance from the detector center. Subsequently, the angular distribution of the cosmic-ray muons is examined in Section 4.1.5. This distribution should follow the geomorphological shape of the overburden above

the experimental site. Additionally, one can look for the spatial distribution of the neutrons or the radioisotope following a muon event. The particles should be located around the track of the parent muon event. Tests concerning the spatial distribution of the neutrons will be described in Section 4.2.5 about the analysis of the muon-induced neutrons.
All analyses presented in this section have been performed within *Echidna cycle 12* (see Section 3.2.1).

4.1.2 Muon detection and muon rate estimation

Muon detection principles Several muon identification techniques are applied in Borexino. A physical hardware system and several software-based offline methods are available. This section gives a brief overview of these methods and analyzes their performance.

- **Outer Detector:** The Outer Detector, which is composed of 208 outward-looking PMTs and Tyvek reflection foil (see Section 3.1.1), detects muon events with a high efficiency. There are two types of tags related to the OD. The first one is the *muon trigger flag* (MTF), a hardware trigger in real-time. It is generated when at least six PMTs are hit within a time interval of 150 ns. A second tag is generated by a software-based offline method, which searches for PMT groups that are triggered by the same muon event and which are spatially separated at the same time (*muon clustering flag* (MCF)).

- **Light concentrators in the Inner Detector:** Along their path through the detector, muons deposit ∼2 MeV/cm. Within the scintillator, an energy of up to ∼2 GeV can be deposited. This energy is far above the energy of any other physical event. The collected charge information typically reaches the saturation level. Nevertheless, these high-energy muon events are used to define very pure muon data sets that can be used for special tests.
  Muons that only graze the interior of the Inner Detector generate a lower amount of scintillation light which is comparable to the emitted Cherenkov light. Such muons can mimic neutrino events. For this reason, 371 PMTs of the Inner Detector were not equipped with light concentrators to make them more sensitive to tangential muons. The so-called "Deutsch parameter" D which was named after Martin Deutsch can be introduced. This parameter corresponds to the ratio of the rate of the photoelectrons (pe), that are collected by the PMTs without concentrators, versus the rate of pe, that are collected by all PMTs. It is higher for Cherenkov events in the buffer than for point-like events in the scintillator. The method was studied in Monte Carlo simulations [119] and in Borexino data [120]. The "Deutsch parameter" has not yet been included in the recent version of the software *Echidna cycle 12*.

- **Pulse shape discrimination:** Since Cherenkov and scintillation light are produced along the entire muon trajectory, the PMTs are radiated over a broader time interval than in the case of a point-like event. This leads to different time distributions of the photons collected by the PMTs. As a consequence, it should be possible to distinguish muons from point-like events by looking at their pulse shapes.
  The following two variables are normally used in the Borexino analyses: the *cluster mean time* t_m and the *cluster peak time* t_p. The variable t_m corresponds to the mean delay time for arriving photons, measured from the very first PMT hit. The variable t_p corresponds to the rise time until the maximum of the hit time distribution is reached. Also t_p starts from the first hit PMT. In Figure 20, the variable t_m is plotted versus t_p for point-like events and for two types of muon events. The latter ones are (1) muons crossing the buffer and the

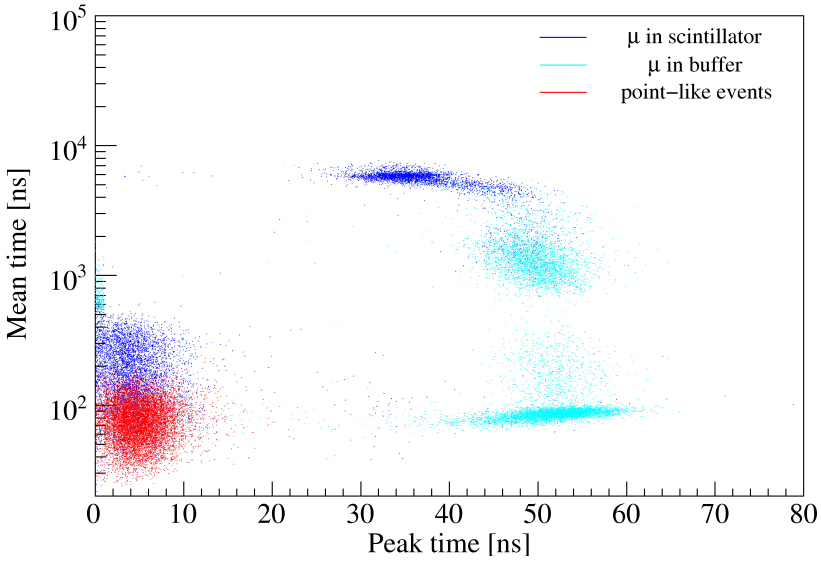

Figure 20: Discrimination of muon events from point-like events via pulse shape analysis. Explanations are given in the text.

scintillator and (2) muons crossing only the buffer[11]. Each sample contains 10,000 events. Point-like events such as neutrino interactions fill the region given by $t_m \lesssim$150 ns and by $t_p \lesssim$30 ns.

In the case of muons there are five subgroups. A first group of muons crossing the scintillator populates the region $t_m \gtrsim$3000 ns. The large mean time is due to the high amount of muon-induced scintillation light. This causes PMT after-pulses that take several μs to attenuate (see also Figure 28). The rise time of $t_p \sim$(35-45) ns is also consistent with the *time-of-arrival* required by the first scintillation light wavefront to hit all PMTs (see Section 4.1.3). A second and a third subgroup with $t_p \gtrsim$30 ns are muons which only cross the buffer. They produce a lower amount of scintillation light compared to the first muon group. Hence, the PMT afterpulses and consequently also t_m are reduced. The rise time t_p of $\sim$(40-65) ns is also consistent with the *time-of-arrival* of the scintillation light wavefront. Two more groups of events that were identified to cross both the scintillator and the buffer populate the region above the point-like events. The rise time t_p is very short; equal to or even smaller than the rise time for point-like events, but the mean time t_m is longer.

Several Borexino collaborators studied the t_p and t_m as function of the energy in terms of the number of PMTs hit. The obtained information was combined with the Gatti parameter (see Section 3.1.2) in order to reject retriggers on PMT afterpulses for the definition of an *Inner Detector Flag* (IDF).

Note that the pulse shape discrimination technique could also consider information about the spatial distribution of the time pattern (i.e. *time-of-arrival*) of PMT hits. The time pattern is expected to be asymmetric due to the characteristic shape of the muon-induced light wavefront (see plots in Figure 21). It is also expected that the PMTs in the northern hemisphere of the detector are illuminated first, since most of the muons enter from the top.

[11]The global tracker in Section 4.1.3 is used to perform the selection. The maximum distance from the detector center to a muon crossing the scintillator is equal to R_{IV}=4.25 m. This corresponds to the nominal radius of the Inner Vessel.

The efficiency determination of the available muon tags is a non-trivial task. The Borexino collaboration used different data samples to determine the efficiencies of the muon identification techniques based on the three tags MTF, MCF and IDF which were introduced in the previous paragraph. A list of all obtained efficiencies was recently reported in [89].
The main result is that the combined muon identification efficiency from all three aforementioned muon identification criteria is at least 99.992% (at 95% confidence level).

Muon rate and muon flux estimation A data set covering a period of 358 days and a total lifetime of 288 days was used for the calculation of the average muon rate in Borexino. The three muon identification criteria introduced in the previous paragraph were used.
The rate of the identified muons crossing the spherical Inner Detector is $\sim$4350 μ d^{-1}. By setting the cross section for the incoming muons equal to the two-dimensional projection of the Inner Detector sphere, the average muon flux Φ_μ(BX) becomes $\sim$1.23 μ m^{-2} d^{-1}. This value is slightly higher than the results obtained by previous experiments located at the LNGS. The LVD experiment obtained Φ_μ(LVD)=(1.19$\pm$0.01) μ m^{-2} d^{-1} [118] and the MACRO experiment Φ_μ(MACRO)=(1.16$\pm$0.03) μ m^{-2} d^{-1} [117].

The Borexino collaboration is currently studying the seasonal variation of the cosmic-ray muon flux. The muon flux is expected to show a positive correlation with the seasonal change of temperature in the Earth's atmosphere, i.e. the higher the temperature, the higher the muon flux underground. The reason is that the density of the air decreases and fractionally more pions/kaons decay to muons before interacting. In the northern hemisphere of the Earth the minimum is typically reached in January and the maximum in July.
So far, several experiments have measured the seasonal variation of the muon flux: MACRO [121], AMANDA [122], MINOS [123], IceCube [124] and LVD [118]. The LVD data cover eight years which is the longest period compared to the other experiments. The average amplitude of the modulation observed in LVD is 1.5%.

4.1.3 Muon track reconstruction

General considerations Borexino is not only able to detect muons crossing the detector but also to reconstruct their trajectories. In principle, both the Outer Detector (OD) and the Inner Detector (ID) allow to define several entry and exit points.

The analysis tool *Echidna* includes several modules which have been designed for the reconstruction of the muon track points. The algorithms for the reconstruction of muon track points were developed and implemented by M. Wurm [91, 89].
For the reconstruction of the OD muon track points, the information from the Cherenkov light generated by the muons is used. Relativistic muons which travel faster than light in a dielectric medium with an index of refraction $n > 1$ generate Cherenkov light. This light is emitted at a fixed vertex angle $\beta = \arcsin(\frac{1}{n})$. For water the refraction index is $n = 1.333$ and the vertex angle $\beta \approx 49°$. The OD tracking algorithms search for PMTs that are grouped in circles/ellipses and detect Cherenkov light within a time interval of few ns. For the PMTs of such groups, the charge and the hit time are determined. Based on this information, the charge barycenters are calculated. Within their uncertainties the charge barycenters agree with the muon track points.
For the reconstruction of the ID muon track points, the algorithms use the *time-of-arrival* of those photons that are generated by muons crossing the ID. The entry point is determined by the fit of the *time-of-arrival* distribution of the first hit PMTs in the ID. The calculation of the exit point is more complex. The algorithm defines a loop that searches for the symmetry plane which divides

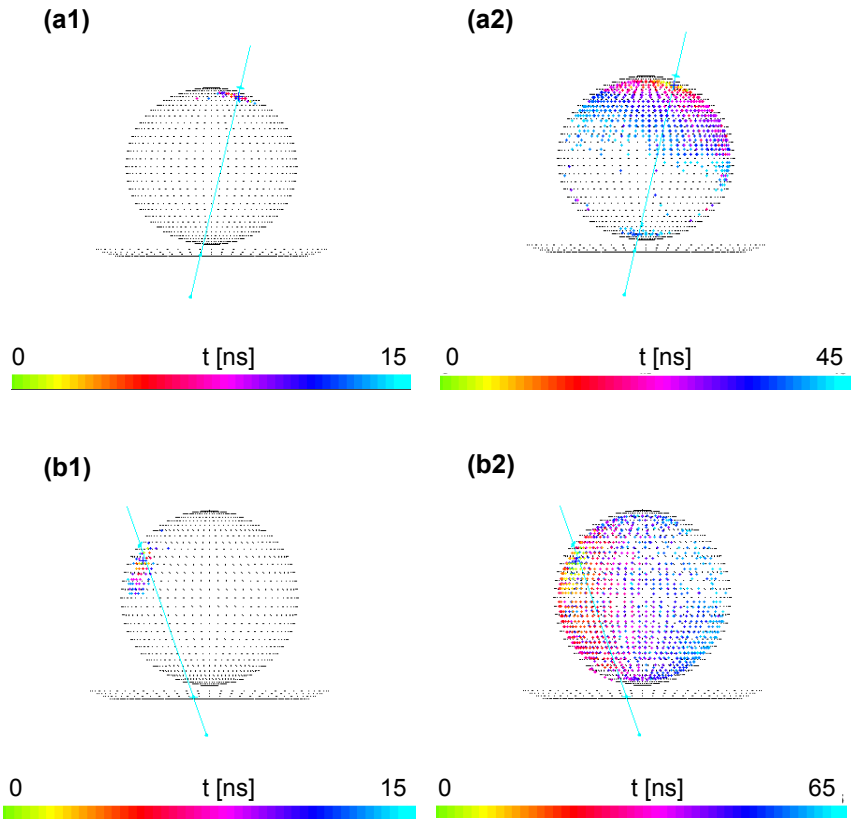

Figure 21: Propagation of the light wavefront generated by muons crossing the Inner Detector of Borexino. Two time sequences of two muons crossing the detector in (a) ∼1 m (Run 5928; ID 2896) and in (b) ∼4.5 m (Run 6007; ID 11793) distance from center of the Inner Detector. The *time-of-arrival* of the photons which trigger PMTs for the first time, is color-coded. (The original design of the visualization tool was written by M. Wurm, TUM.)

the time distribution of the hit PMTs into two mirror images. Both the entry and the exit point are located in this plane. A second loop analyzed the time distribution of the hit PMTs that are placed along the symmetry plane. Discontinuities in the time pattern correspond to the exit point of a muon. However, discontinuities disappear in cases in which the muons are too close to the ID border. An alternative algorithm of the reconstruction of the ID exit point is presented in the following paragraph.

Propagation of the muon-induced scintillation and Cherenkov light This section focuses on the study of the shape of the light wavefront induced by a relativistic muon, which crosses the Inner Detector (ID) of Borexino. Depending on the entry and exit point of the muons the generated light wavefronts have different intersections with the spherical detector. The objective is to use this information for the calculation of the time when a given PMT is hit by a photon of the propagating wavefront for the first time (*time-of-arrival*). Then the procedure is inverted, i.e. the entry point of the muon and the *time-of-arrival* of the wavefront on the PMTs are used to determine the exit point.

The *time-of-arrival* of photons on the inner surface of the ID has been studied for a set of recorded

muon events. The only parameter that was modulated was the distance of the muon tracks from the detector center. The panels in Figure 21 show two time sequences for two individual muons (a) with ∼1 m and (b) ∼5 m distance from the detector center.
In the first case (a), the muon enters from the top of the Inner Detector (panel (a1)). The PMTs around the entry point are triggered in sequence according to a concentrically propagating wavefront. The relativistic muon travels through the detector almost at the speed of light in vacuum c=29.9792 cm ns^{-1}. The diameter of the ID is $d = 1350$ cm. After a time $dt = d/v \approx$45 ns (panel (a2)), the first PMTs in the lower hemisphere of the ID are triggered. They are hit by photons generated by the escaping muon in close proximity to the mentioned PMTs.
In the second case (b), the muon crosses the Inner Detector tangentially. The PMTs placed on the opposite side to the entry point are hit only after ∼(60-65) ns. This time corresponds to the *time-of-arrival* of photons which are emitted close to the entry point and propagate in the Borexino scintillator at the speed of light. The refraction index in pseudocumene is n=1.5048 [125]. Then the speed of light c' in the medium becomes $c' = \frac{c}{n} \approx$19.9 cm ns^{-1}. For a distance of $d = 1350$ cm, a photon needs $dt = d/c' \approx$70 ns. This value is in good agreement with the observed *time-of-arrival* in data.

Based on these observations, it is possible to deduce the most probable shape of the wavefront generated by a single muon. The wavefront can be described by a two-component scenario.
First, the relativistic muons generate Cherenkov light in the scintillator/buffer. The Cherenkov light is emitted instantaneously and at the fixed angle $\beta = \arcsin(\frac{1}{1.506}) \approx 42°$. The resulting coherent wavefront is conical and moves at the same velocity as the muon.
Second, scintillation light is generated by the muon within the scintillator and in smaller amounts also in the buffer. When the muon has passed a given point C, it takes ∼1 ns until the molecules of the scintillator begin to emit scintillation light. The spherical scintillation light wavefronts generated along the muon track superimpose. The overall wavefront consists of (i) a spherical part and (ii) a conical part which confines with the spherical one. The conical part has the same shape and almost the same velocity as the Cherenkov light cone. The shape of the entire wavefront is depicted in Figure 22.

The exit point of muon tracks in the Inner Detector V.V. Kobychev and the author of this thesis developed an algorithm which describes the propagation of the aforementioned light wavefront in time.
The first part of the algorithm describes the *time-of-arrival* t' of the wavefront at the arbitrarily chosen point H on the inner surface of the detector. In this case, the entry point A and the exit point B of the muon track are assumed to be known. Then t' can be calculated via

$$c\,t' = c\,t_A + \left|(\vec{r}_A - \vec{h}) \times \frac{\vec{v}}{c}\right| \sqrt{n^2 - 1} - (\vec{r}_A - \vec{h}) \cdot \frac{\vec{v}}{c} \tag{4.1}$$

The constant t_A is the time when the muon enters the detector, the vectors $\vec{h}$, $\vec{r}_A$ and $\vec{r}_B$ denote the PMT position H and the entry and the exit points A and B. The velocity vector of the muon is given by $\vec{v} = c \cdot (\vec{r}_B - \vec{r}_A)/\,|(\vec{r}_B - \vec{r}_A)|$.
In reality, the exit point B is unknown, while the time pattern of the hit PMTs and the entry point are known. In that case, Equation (4.1) should be inverted. This is the aim of the second part of the algorithm. Since Equation (4.1) is not a vector equation, it is not possible to deduce the three components of the vector $\vec{r}_B$. However, it is possible to estimate the angle ϕ between $(\vec{r}_A - \vec{h})$ and $\vec{v}/c$. There are two solutions:

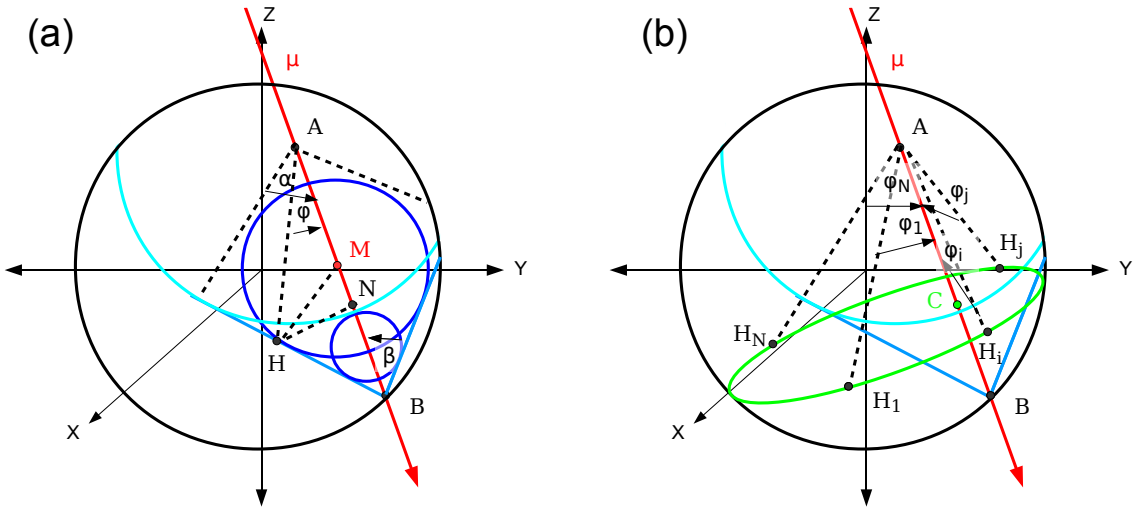

Figure 22: Propagation of the Cherenkov and scintillation light wavefront generated by a muon entering the detector in point A and leaving it in point B. The left plot is used for the calculation the *time-of-arrival* t' of the wavefront at the point H. The right plot is required for the estimation of the muon track direction and its exit point.

$$\phi_{1,2} = \arcsin\left(\frac{c\,(t' - t_A)}{n\,\left|(\vec{r}_A - \vec{h})\right|}\right) - \arcsin\left(\pm\frac{1}{n}\right) \tag{4.2}$$

If $\phi_{1,2}$ are calculated for a large number of points on an arbitrarily chosen circle along the Inner Detector surface, it is possible to deduce a point C lying on the muon track. Moreover, point C lies in the plane in which the circle was placed (see right plot in Figure 22). Thus, C is normally not equal to the exit point B. A series of circles can be defined to get an arbitrary number of points along the muon track intersection with the detector.

A detailed description of the algorithm is given in Appendix A.1.

Global fit of the muon track Muon events with at least three successfully reconstructed muon track points $\vec{p}_i$, $i = 1,2,3,(4)$ can be fitted by a 3D straight line. In principle, this can be done by introducing four parameters defining a vector equation $\vec{l} = \vec{p}_0 + t \cdot \vec{s}$. Herein, $\vec{l}$ is the fit line vector, $\vec{p}_0$ a vector parallel to $\vec{l}$ starting from the center of the coordinate system, $\vec{s}$ an offset vector and t a variable scalar. Then, the perpendicular distance vector (residual) $\vec{r}_i = \vec{g} - \vec{p}_i$ has to be calculated for all muon track points. The χ^2-function, which has to be minimized, is the sum of all squares of the residuals $\vec{r}_i$. The usual way is to set the gradient of the χ^2-function equal to zero in order to find the best fit parameters.

However, the uncertainties of the muon track points that were reconstructed from the Borexino data are described by vectors, which are normally not perpendicular to the straight line $\vec{l}$ and which are correlated. This makes the calculation of the regression line more complicated.
In order to take into account the uncertainties of the reconstructed muon track points $\vec{p}_i$, the 3D

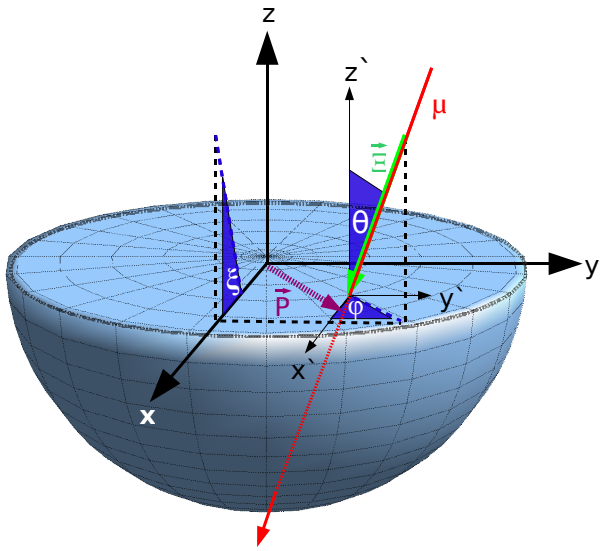

Figure 23: Estimation of the position of a muon track in the reference frame of the Borexino coordinate system. Each reconstructed muon track can be expressed in terms of (1) its distance to the detector center (impact parameter), (2) the zenith angle θ and (3) the azimuth angle ϕ. In addition, the direction of the muon can be defined.

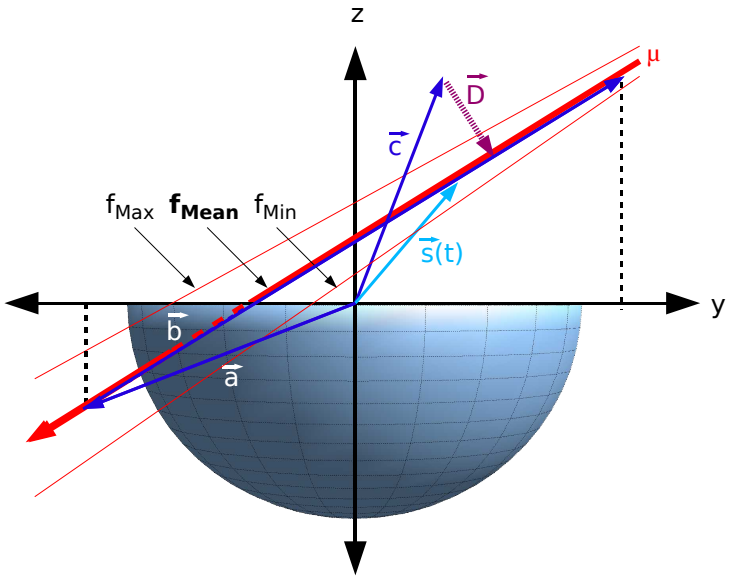

Figure 24: Calculation of the distance of the reconstructed muon track from a given point $\vec{c}$ within the detector. Determination of the distance of muon-induced events like neutrons and radioisotopes from the fitted track of the parent muon.

straight line fit was disentangled by projecting the points into the planes xy and xz. Two 2D regression lines were obtained:

$$\begin{aligned} y &= f(x) = \alpha + \beta x \\ z &= g(x) = \gamma + \delta x \end{aligned} \tag{4.3}$$

The global fit of the muon track was implemented in an appropriate module within the Borexino software tool *Echidna* (see Section 3.2.1). The module name is `track`. Among all modules present in *Echidna*, only this one contains information from both the Inner (module `laben`) and the Outer Detector (module `muon`).
The `track` module includes several subroutines. First, the reference coordinate system is rotated once (twice around two axes) by 45° in case that a muon track is too close to one (two) planes. Second, the reliability of each fit pair is calculated according to $\chi^2 = (\chi^2_{\alpha\beta} + \chi^2_{\gamma\delta})/\text{ndf}$. Herein, ndf stems for the number of degrees of freedom. If four muon track points are successfully reconstructed the following procedure is applied: if $\chi^2 > 3$, the fit is repeated four times, permutating three out of four points. The three points leading to the best fit are finally selected.

The `track` module uses the fit parameters to also calculate variables that can be used to test the radial and angular distributions of the muon tracks. These studies are presented in Section 4.1.4 and 4.1.5. The azimuth angle ϕ which lies in the xy plane is defined by:

$$\phi = \begin{cases} \arctan\beta & \text{if } x_i \leq x_o \\ \arctan\beta + \pi/2 & \text{if } x_i > x_o \end{cases} \tag{4.4}$$

Herein, x_i and x_o are the x-coordinates of the entry and exit points. The zenith angle θ is calculated by introducing the auxiliary vector $\vec{\Xi}$ and the auxiliary angle ξ as depicted in Figure 23. Herein, $\xi = \arctan\delta$ and $\vec{\Xi} = \left(\cos^{-1}\phi, \sin^{-1}\phi, \tan\xi \cdot \cos\phi\right)$. The angle θ then becomes:

$$\theta = \arcsin\left(\frac{\tan\xi \cdot \cos\phi}{\sqrt{1/\cos^2\phi + 1/\sin^2\phi + \tan^2\xi \cdot \cos^2\phi}}\right) \tag{4.5}$$

The distance vector $\vec{D}$ of the muon track from a point $\vec{c}$ of interest is also calculable via the `track` module. The point of interest can be the center of the detector or the reconstructed position of a muon-induced neutron/radioisotope. In the first case, $\vec{D}$ is denoted with *impact parameter* vector. As shown in Figure 24, two auxiliary vectors are defined: $\vec{s}(t) = \vec{a} + t \cdot \vec{b}$ and $\vec{h}(t) = \vec{c} - \vec{s}(t)$, where $t \in [0,1]$. In that case, $\vec{D}$ has to fulfill the following condition:

$$\vec{h}(t) \cdot \vec{b}\,|_{t=t_0} \stackrel{!}{=} 0 \quad \Leftrightarrow \quad \left(\vec{c} - \left(\vec{a} + t \cdot \vec{b}\right)\right) \cdot \vec{b}\,|_{t=t_0} \stackrel{!}{=} 0 \tag{4.6}$$

This scalar equation can be expressed by means of the parameter t_0 as follows:

$$t_0 = \left(\frac{\vec{c} \cdot \vec{b} - \vec{a} \cdot \vec{b}}{\left|\vec{b}\right|^2}\right) \tag{4.7}$$

4.1.4 Analysis of the radial distribution of cosmic-ray muons

Muon-induced energy deposition and radial distance of muons Muons crossing the Inner Detector of Borexino produce a large quantity of scintillation light. The analysis about the pulse shape discrimination of muon- and point-like events in Section 4.1.2 distinguished two main populations of muons: on the one hand, muons crossing the buffer and the scintillator, on the other hand, muons grazing only the buffer layers. For muons crossing the scintillator, long mean times t_m were observed. Long mean times are related to long afterpulses. Long afterpulses are induced by large amounts of scintillation light. Therefore, one expects the spectra of the energy, that was deposited by muons crossing the scintillator and the buffer, to be different as well. This assumption has been investigated. The results are shown in the panels (a1) and (b1) of Figure 25 for the charge variable (unit: photoelectrons (pe)) and for the number of hit PMTs (unit: hits). The two energy variables are plotted versus the impact parameter of the reconstructed muon tracks.
As expected, muons crossing the scintillator generally induce a value in charge and in hit PMTs that is much higher than for buffer muons. The charge variable is fully saturated. The saturation level lies at ∼16800 pe. The number of hits induced by muons crossing the center of the detector is also very high around 14000 hits. This means that the PMTs were hit multiple times according to the Binomial probability. However, the hit variable seems to be not saturated. The number of hits decreases for muon tracks with an increasing value of the *impact parameter*. The *impact parameter* is defined as the distance between the muon track and the center of the detector. For the buffer muons, the hit variable drops down to a value below ∼7000 hits. These observations suggest introducing an energy threshold at 16500 pe and 7000 hits as an additional discrimination criterion for the two main muon populations.

A first test of the muon track reconstruction is performed by looking at the radial distribution of the impact parameter of muon tracks (panels (a2) and (b2) of Figure 25). Since the incoming muons see only the two-dimensional projection of the spherical detector, one expects a linear increase of the number of reconstructed muon tracks with the radius R. The measured distribution is depicted in panels (a2) and (b2). Muons crossing the scintillator and the buffer are separated by the two possible energy cuts that were introduced above.
It turns out that tracks belonging to muons going through the scintillator mostly fulfill the expectation. Only in few cases the tracks are mis-reconstructed outside the scintillator (see also (b1)). In addition, Table 4 shows that the muon tracks are reconstructed with a high efficiency; the rate of reconstructed muon tracks is comparable to the expected muon rate crossing the Inner Vessel.
In contrast, muons crossing the buffer seem to be often mis-reconstructed. This is caused mainly by the difficulty for the muon track algorithms to establish reliable entry and exit points. Since the reconstructed points are closer together, the fit parameter errors from the global fit also become larger. Moreover, as figured out in Table 4 the global fit of tracks belonging to muons crossing only the buffer does not converge in ∼11% of the cases.

Impact on muon-induced backgrounds The results obtained above are important for several analyses about muon-induced backgrounds.
Firstly, the reliably reconstructed tracks of muons crossing the scintillator can be used to examine the position reconstruction of muon-induced neutrons and cosmic radionuclides. Muon-induced neutrons propagate instantaneously within the scintillator. Muon-induced radioisotopes are expected to rest close to the tracks of the parent muons provided that convection processes are negligible (working hypothesis). Nevertheless, particles of both types are expected to be distributed homogeneously around the muon tracks if the position reconstruction was successful. This powerful technique will be applied exemplary for neutrons in Section 4.2.5.

Volume crossed by muons	Muon rate $[\mu\ \mathrm{d}^{-1}]$	Measured rate of muons with reconstructed global track $[\mu\ \mathrm{d}^{-1}]$
Inner Detector (R<6.85 m)	∼4350 (m)	∼4030
Inner Vessel (R<4.25 m)	∼1675 (e)	∼1660
fiducial volume (R<2.0 m)	∼370 (e)	∼390

Table 4: The expected rates for muons (e) crossing different volumes in Borexino are calculated by scaling the cross sections of the spherical volumes of radius R. The reference muon rate (m) for the entire Inner Detector was measured in Section 4.1.2. The rate of measured muons, for which the global track fit was successfully reconstructed, is given in the third column.

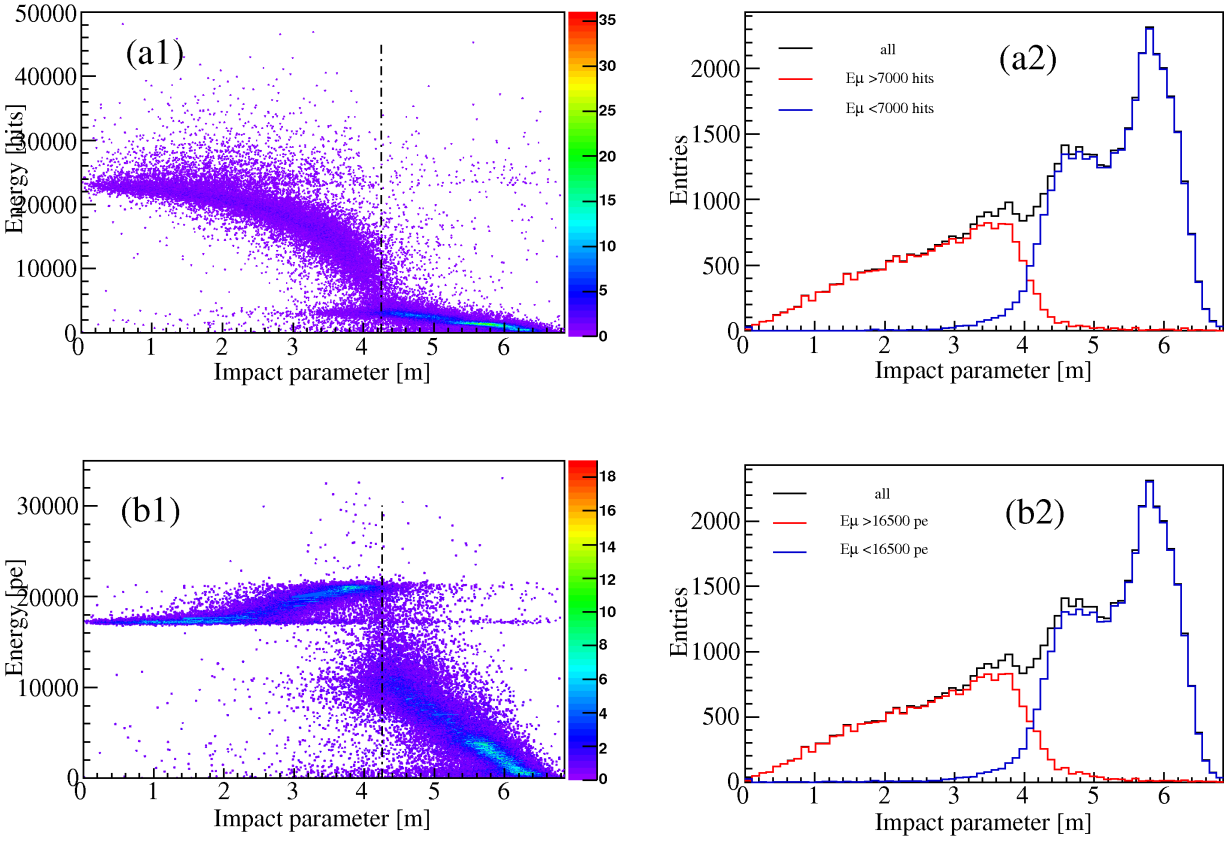

Figure 25: Relation between the muon-induced energy deposition and the distance of reconstructed muon tracks from the detector center. The distance is denoted by the *impact parameter*. Muons crossing the scintillator contained in the Inner Vessel (R<4.25 m) generally deposit a higher amount of energy than muons only going through the buffer (4.25 m < R < 6.85 m). This statement is valid for both energy variables in terms of charge (unit: photoelectrons (pe)) and number of hit PMTs (unit: hits). As shown in panels (a2) and (b2), the radial distribution of the reconstructed *impact parameters* is mostly reliable for muons crossing the scintillator. In the case of buffer muons, the number of mis-reconstructed tracks is notably higher.

Secondly, one can introduce a new boundary condition for the identification of cosmogenic radioisotopes. A real muon-induced radioisotope detected in the scintillator must have a parent muon which crossed the scintillator and thus deposited a large amount of energy. On the other hand, a potential radioisotope candidate which was associated with a muon crossing only the buffer, cannot be of cosmogenic origin. It is either a real neutrino event or a non muon-induced background event.

4.1.5 Analysis of the angular distribution of cosmic-ray muons

A second test and application of the muon track reconstruction is the determination of the angular distributions of incoming muons. The structure of the rock overburden covering the LNGS is quite irregular. The topographic profile of the Gran Sasso mountains above the LNGS is characterized by large differences in the rock thickness for a given direction. Details about the geomorphological profile can be found in [126]. The chemical composition of the rock is essentially calcareous, but mixed up in a non-homogeneous manner with other materials, such as aluminium, silicon, magnesium and organic compounds (sometimes referred to as "Gran Sasso rock") [127]. All of these inhomogeneities should imprint on the muon angular distribution.

The cosine distribution of the zenith angle θ (see Equation (4.5)) measured with the Borexino global tracker is shown in panel (b) of Figure 26. The maximum lies between 0.80-0.85. The entire distribution and its maximum are in rather good agreement with the measurements performed with the MACRO detector (see [128] and references herein). This detector is located at the LNGS in Hall B only ∼100 m away from the Borexino detector. In case of the MACRO result, the maximum of the distribution lies around 0.90-0.95.
The Borexino $\cos(\theta)$ distribution of muon tracks intersecting the scintillator (red line) is almost event-free around $\cos(\theta)\approx 0$. In contrast to this result, a large number of muon tracks only intersecting the buffer layers (blue line) are close to the horizontal plane. These tracks can be regarded as mis-reconstructed.

The distribution of the azimuth angle is depicted in panel (a) of Figure 26. The azimuth angle ϕ defined in Equation (4.4) using the Borexino internal coordinate system was shifted by 65°, i.e. $\phi \rightarrow \phi' = 295° - \phi$, in order to match the curve measured by the MACRO experiment. Muon tracks which cross the scintillator and those which cross only the buffer were treated separately. In general, the curves follow the angular thickness of the rock overburden. Again, the ϕ' distribution is in good agreement with the curve measured by the MACRO experiment. However, the Borexino data show a peak around 295° due to a not yet solved artefact of the global tracker algorithm. The effect is especially visible for buffer muons. In the case of muons crossing the scintillator, the effect is almost negligible.

The main conclusion from the tests performed in this section and in Section 4.1.4 is that the muon track reconstruction is efficient and works reliably, but only for muons crossing the scintillator. This result is especially important for the analyses of muon-induced radioisotopes, which will be discussed in Section 4.3.

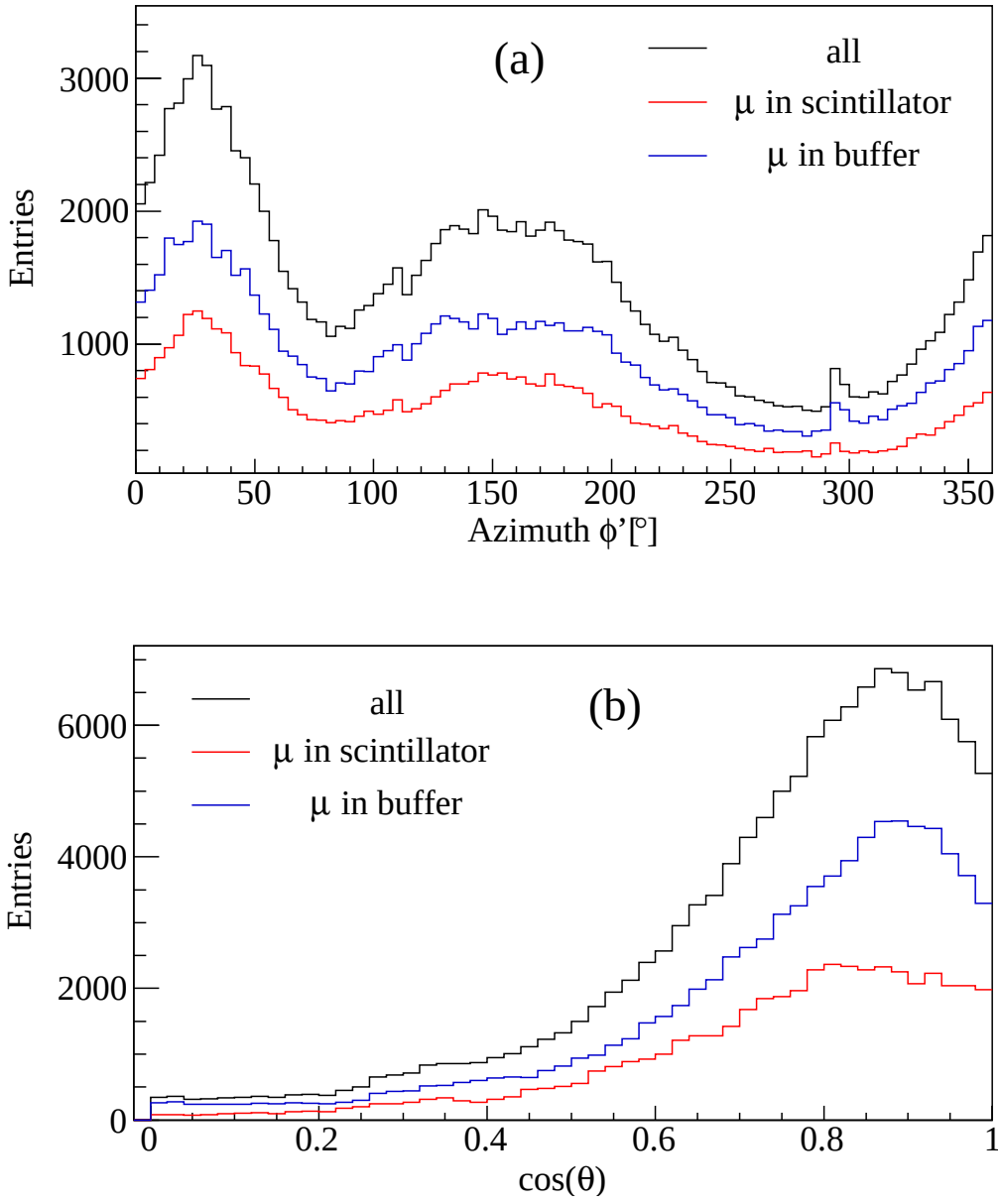

Figure 26: Angular distributions of cosmic-ray muons. The azimuth angle ϕ' and the cosine of the zenith angle θ are in good agreement with the measurements carried out within the MACRO experiment [128]. Inconsistencies at $\cos(\theta)\approx 0$ and at $\phi'=295°$ mainly affect muons that only cross the buffer layers.

4.2 Neutrons

4.2.1 Introduction

Neutrons represent a special type of background in Borexino and they are emitted in different processes. Due to the emission of characteristic γ rays when neutrons are thermalized and captured in the scintillator, neutrons can be used to tag coincidental background signals.
The neutrons to which Borexino was exposed so far are emitted from natural and artificial sources and they have different initial energies. Neutrons can be divided into five categories: (i) neutrons induced by cosmic-ray muon events, (ii) neutrons induced by CNGS-beam muons[12], (iii) neutrons from an ^{241}Am^{9}Be calibration source, (iv) neutrons from inverse β decays induced by reactor and geo-antineutrinos and (v) high-energy neutrons from U/Th spontaneous fissions and (α,n) reactions in the rock and in the detector materials.
The present section focuses on the analysis of neutrons induced by cosmic-ray muons, since they produce a large amount of radioisotopes in the scintillator.
First, the detection of the neutrons following muon events in Borexino is discussed (Section 4.2.2-4.2.3). Neutron events are classified and neutron rates are estimated (Section 4.2.4). Then the radial distribution of neutrons in Borexino and their distance from the parent muon track is determined (Section 4.2.5). Finally, muon-induced neutrons are compared to neutrons from an ^{241}Am^{9}Be calibration source which was inserted into the detector during the calibration campaigns (Section 4.2.6). This comparative study includes the analysis of the propagation and capture time of neutrons in the Borexino scintillator. The results are of interest for rejection techniques such as the *threefold coincidence* (TFC) method that aims to tagging coincidences between muon-induced neutrons and unstable radioisotopes. The study also allows to deduce information about the scintillator and about the intrinsic properties of neutrons, such as their initial energy. This again gives an insight into the mechanisms which release the observed neutrons (see Sections 4.2.7 and 4.2.8).

4.2.2 Detection of muon-induced neutrons in Borexino

Neutron detection with the Borexino Main DAQ system After the beginning of data collection in May 2007 it was soon recognized that the detection efficiency of muon-induced neutrons in Borexino is greatly reduced. This is mainly related to the fact that the muons crossing the scintillator produce large amounts of scintillation light, causing a relatively long recovery time of the read-out and of some sub-components of the electronics. It was found that [130]:

- neutrons are lost: The scintillation light of a muon generates afterpulses of the PMTs which often introduce retriggers in the following ∼10-15 μs. The original trigger design vetoed the third out of three triggers occurring in a short time sequence. Thus, the neutrons were often lost.
- the read-out of the DAQ software is limited: originally, only 25 hits per 12 PMTs per event were allowed. By comparison, a 1 MeV scintillation event typically induces ∼350 hits, distributed over all 2214 PMTs of the Inner Detector. The original setting is sufficient for a neutrino-like event of several MeV energy or for a neutron, but not for a muon. The read-out

[12]The CNGS neutrino beam is part of the OPERA experiment in Hall C (see Figure 11) and is produced at CERN [129]. The beam mainly consists of ν_μ neutrinos with an energy optimized for the appearance of ν_τ neutrinos. Charge current interaction of ν_μ in the rock layers close to the LNGS can produce muons which also become visible in Borexino.

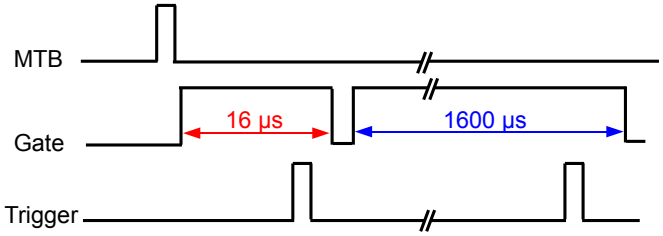

Figure 27: Schematic representation of the neutron detection in Borexino: (150±50) ns after each muon event, a special trigger of gate length 1600 μs is opened for the detection of muon-induced neutrons.

of the hits attributed to a muon takes several μs to get rid of them, thereby losing hits from possible subsequent neutron events.

- the charge of the deposited energy in neutron events is poorly reconstructed: The Front End Boards act as Digital Analog Converters (DAC) and provide (1) a fast linear signal used to measure the *time-of-flight* and the number of hit PMTs and (2) a slow integrated signal used to measure the collected charge. The scintillation light of a muon creates a huge pulse in the Front End Boards. Due to AC coupling, this huge pulse is followed by a large voltage overshoot. While the linear signal recovers within few μs, the integrated signal takes several 100 μs to recover. Thus in terms of energy the charge variable `pe` (photoelectrons) is not reliable, whereas the `hits` variable (number of hit PMTs) is reliable.

An upgrade of the trigger system and of the read-out software was performed in the second half of 2007 [131]. It solved the first two of the aforementioned problems, but the third has not been solved yet (see Section 4.2.3).
In order to overcome the problem of neutron detection, the internal logic of the Borexino Trigger Board (BTB) was modified and a custom-made timing setup was installed: When a neutrino-like event of `trigger type 1` is registered by the Inner and Outer Detector (i.e. a muon signal), a second trigger gate is opened by a new `trigger type 128` (see Section 3.1.3) (150±50) ns after the end of the muon event [89]. This trigger looks for muon-induced neutrons. The gate length of a neutron trigger is 100 times larger than the gate length of a normal trigger event, namely 1600 μs. This time interval corresponds to approximately 6 times the expected neutron capture time on protons in the Borexino scintillator. The scheme of both trigger types is depicted in Figure 27, whereas two examples for a muon and a subsequent neutron event with different multiplicity are shown in Figure 28.
The improved neutron trigger, including the position and the energy reconstruction of the neutrons, has been operational since December 15, 2007. The ID number of the first run with the new setting is 6562.

Clustering and definition of a neutron event Muon-induced neutrons in Borexino are measured indirectly by means of detecting characteristic γ rays. These γ rays are emitted after neutron captures on hydrogen (2.22 MeV γ rays) and on carbon nuclei (4.95 MeV γ rays) and they are detectable if a sufficiently large fraction of their energy is deposited within the scintillator. Sophisticated clustering algorithms have been developed. They search for such peaks in the recorded neutron trigger events in offline mode. The found clusters are commonly referred to as "neutron clusters" and include the characteristic γ rays, but also accidentals like ^{14}C decays. In the case

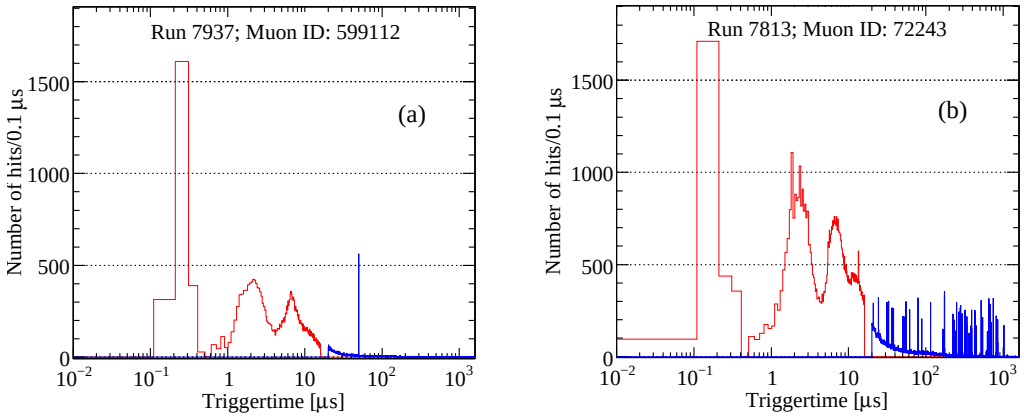

Figure 28: Two examples of muon (red) and neutron (blue) detection: The neutron event in panel (a) has a single-cluster, whereas the event in panel (b) has 54 clusters, i.d. multiplicity M_n=54. The muon events typically show several larger afterpulses. The muon event in panel (b) preceding the neutron event shows two narrow peaks on the first and one peak on the second afterpulse, which are probably related to neutron captures. The possibility of clustering neutrons within the muon trigger gate is under study.

of neutrons, the energy and the position of the light-barycenter of the characteristic γ rays are reconstructed. Note that the reconstructed positions neither correspond to the neutron emission point nor to the neutron capture point (see Figure 37).
As shown in Figure 28, one single muon crossing the detector might produce several neutrons within the active volume and thus several neutron clusters within one neutron trigger. The Borexino trigger logic groups all neutron clusters following a single muon to a so-called "neutron event". The number of neutron clusters in a single neutron event corresponds to the "neutron-multiplicity" M_n. A "single-cluster neutron event" has a multiplicity M_n=1 and "multiple-cluster neutron event" a finite value above M_n >1. Note that neutron events with a high multiplicity are sometimes referred to as "neutron bursts".

Neutron detection efficiency A high neutron detection efficiency is essential for the tagging of cosmogenic radioisotopes. The new neutron trigger has led to a high efficiency, but there are still situations where neutron clusters are poorly reconstructed (see Section 4.2.5) or not detected at all: Neutrons captured during Main DAQ interruptions are not available for the tagging of radioisotopes that decay at the beginning of the following runs. Neutrons emitted from muons crossing the outer parts of the scintillator might be captured in the buffer liquid and become undetectable, whereas the cosmogenic radioisotopes decay within the scintillator. Neutrons captured when the muon trigger gate (the first ∼16 μs after neutron emission) is still open can be hardly disentangled from the muon signal and are not reconstructed by the present algorithms.
Auxiliary neutron detection systems have been installed to improve once more the neutron detection of the Main DAQ system and to test its total efficiency: (1) a two channels 500 MHz FADC board system operated by the Borexino Princeton group, (2) four FADC boards (CAEN V1731) by the Borexino Genoa group [132] and (3) 34 Fast Wave Form Digitizing 400 MHz, 8 bit VME boards (CAEN V896) by the Borexino group at the Kurchatov Institute, Moscow [133]. These hardware architectures allow to estimate the total efficiency of the Main DAQ system and to register neutrons during run interruptions of the Main DAQ system.
An absolute overall detection efficiency of muon-induced neutrons in Borexino has not yet been established. By comparing the Princeton system with the Main DAQ system it turned out that the

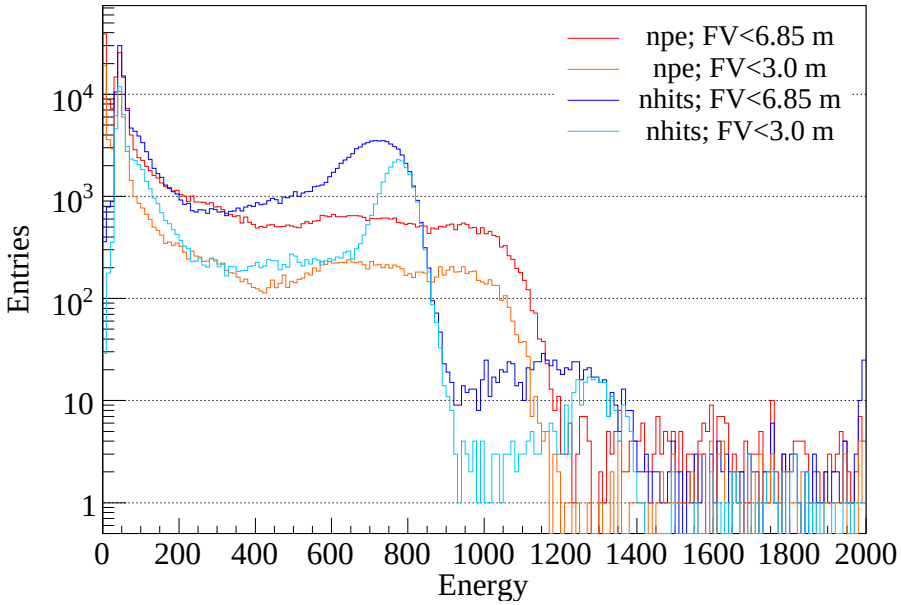

Figure 29: Energy spectrum of the neutron clusters detected in Borexino. The energy is expressed in units of normalized photoelectrons (npe) and normalized number of hit PMTs (nhits) (see legend). The unit of the energy scale is color coded. The charge variable does not show a clear peak of 2.22 MeV γ rays at ∼1060 npe from neutron capture on protons, whereas the variable of hit PMTs has a peak at the expected position ∼775 nhits. The subsample of neutron clusters lying within a *fiducial volume* of 3.0 m radius is also shown, where border effects between scintillator and buffer at ∼4.25 m from the center of the detector are suppressed.

Main DAQ is only ≈92% efficient [134]. In the following studies, only information from the Main DAQ neutron system is used and an absolute efficiency of 92% is assumed.
Finally, the possibility to detect neutron clusters within the muon event is under study and seems to be promising, at least for the time interval from ∼8 μs to 16 μs after the start of the muon trigger [135].

4.2.3 Analysis of the reconstructed energy of muon-induced neutron clusters

The present subsection is dedicated to the study of the energy reconstruction of muon-induced neutron clusters. The effects impairing the energy information are analyzed. This analysis is important for the separation of neutron clusters that originate from real neutron captures and from accidental background events.
The study was performed in the framework of *Echidna cycle 12*. A data set covering a period of 843.8 d (Jan 13, 2008 - Aug 7, 2010) for a total of 662.1 d of lifetime was used.

Muon-induced electronics effects: The new `trigger type 128` allows to detect neutrons with a high efficiency, however, the energy reconstruction of the neutron clusters is still sometimes affected by the large amount of scintillation light generated by muons crossing the scintillator:

- **Deterioration of the charge variable:** As already mentioned in Section 4.2.2, the muon-induced scintillation light bursts cause large voltage overshoots in the electronics of the detector. These do not allow the reconstruction of the charge variable (unit: `pe` photoelectrons)

of the neutron clusters. Only the number of hit PMTs (unit: `hits`) is mostly reliable. This is shown in Figure 29, where the measured energy values E_m for the two variables were normalized according to Equations (3.7) and (3.8). Then, the spectra of the normalized charge and hits variables were compared. The 2.22 MeV peak from neutron captures on protons is expected at ∼1060 npe and ∼775 nhits in the energy spectra of both variables, respectively. Only in case of the `nhits` variable the peak is clearly visible, whereas the `npe` variable is more deteriorated.

- **Empty boards:** Muons can saturate the *laben boards* (LB) (see Section 3.1.3), losing the signals from several hit PMTs. These boards behave like empty boards and lead to a reduced value of the reconstructed energy of the neutron clusters, making their detection more difficult or even impossible. Out of all effects presented in the following sections, this effect has the strongest impact on the reconstructed energy of the neutron clusters. For this reason, the dependencies of the number of empty boards N_{eb} on other properties of the neutron clusters and of the parent muons have been studied. The results are depicted in Figure 30 and explained in the following paragraph:
  Muons crossing the scintillator (within 4.25 m from the center of the detector) cause a large number of empty boards up to N_{eb} ∼200 (maximal number of LBs is 280), while N_{eb} is ∼50 for muons crossing the buffer. This is shown in panel (a1), where the impact parameter is the distance of the muon track from the center of the detector. Red points are neutron clusters where the algorithms failed to reconstruct the track of the parent muon and the impact parameter was set to zero.
  Since the scintillation light of muons crossing the scintillator always saturates the electronics (∼18000 pe; see panel (a2)), it is not possible to say whether a muon or muon shower with larger energy deposition in the detector induces a larger N_{eb}. However, panel (b1) gives a hint that a muon/muon shower followed by a high multiplicity neutron event is accompanied by a higher N_{eb}. For a neutron multiplicity M_n >100 it is found N_{eb} >100. As shown in panel (b2), this is true within the entire scintillator, independent of the muon impact parameter.
  For a higher N_{eb} (and thus for a higher M_n), the reconstructed value of the `nhits` variable of the neutron clusters is generally reduced (see panel (c) and Figure 28). Moreover, the Gatti parameter (see Section 3.1.2) of the γ rays, which should lie around -0.03 (β-like), is rarely reliable for N_{eb} >50 (see panel (d)).

  The distribution of events in panel (c) is used for the correction of the reconstructed energy E_{rec} of the `nhits` variable: For each bin on the N_{eb}-axis, the mean value of all entries has been calculated. The distribution of all mean values was fitted by the analytical function $f(a,b,c,N_{eb}) = a + b \cdot (N_{eb} - c)^2$. Using the best-fit values for a,b,c, the corrected energy value E_{corr} is given by:

$$E_{corr} = E_{rec} \frac{1}{1 + \alpha(N_{eb}^2 - \beta N_{eb})} \tag{4.8}$$

  where $\alpha(a,b,c)$=2.1796×10^{-5} and $\beta(c)$ = 3.98×10^2. The unit for the corrected normalized number of hit PMTs is denoted by `nhits_corr`.
  As shown in the right panel of Figure 31, the correction given in Equation (4.8) leads to a better separation of the clusters that are either induced by neutron captures or accidentally by low-energy background events (mostly below <100 nhits_corr).

Intrinsic detector effects: Several intrinsic detector properties also cause a deterioration of the `nhits` variable of the muon-induced neutron clusters.
A first effect, which was already introduced in the previous paragraph in Equation (3.7), is given

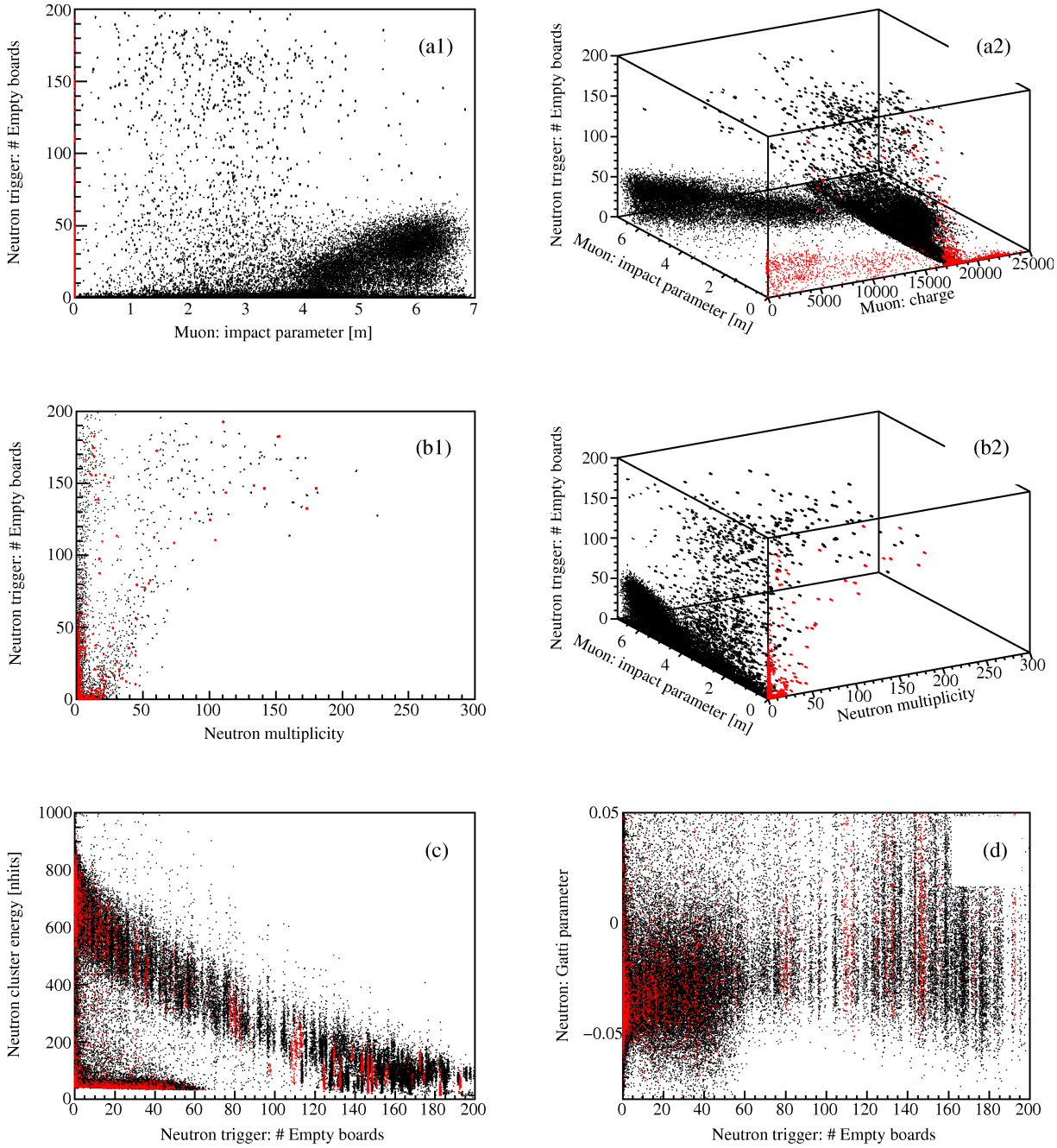

Figure 30: Reconstructed energy of neutron clusters in relation to the number of empty boards N_{eb} during neutron triggers. Dependencies on other variables of the neutron cluster and of the preceding muons are shown. Explanations are given in the text. The depicted graphs only contain a subsample (288.6 d of lifetime) of the main data set for better visualization.

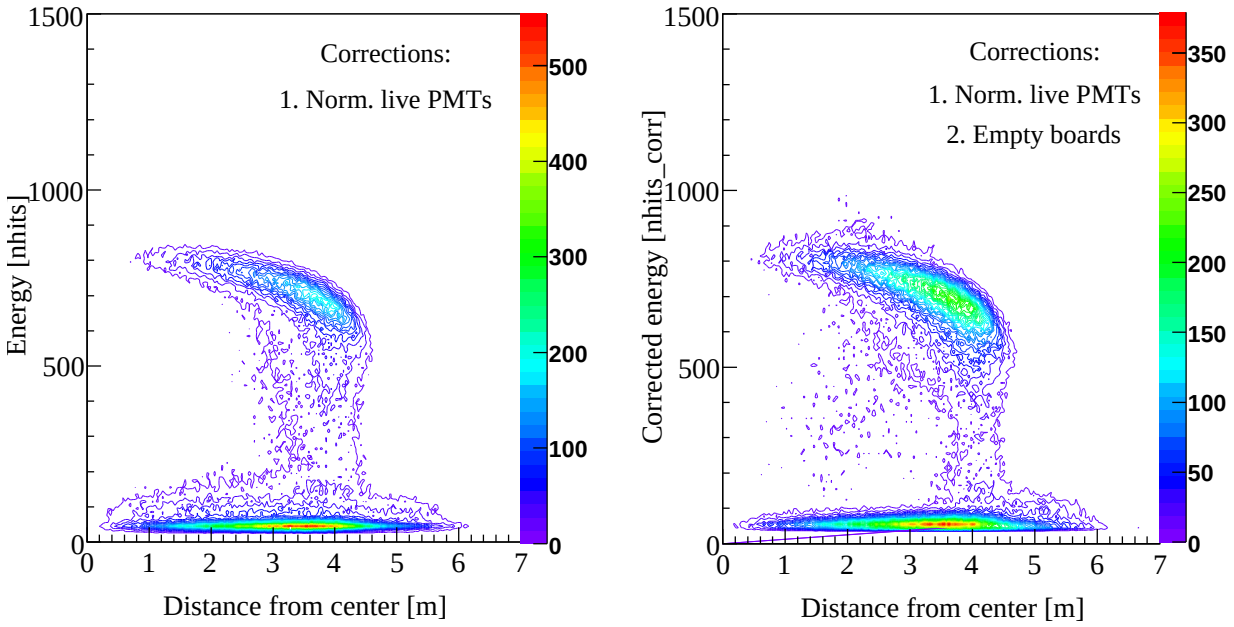

Figure 31: Normalized neutron cluster energy vs. distance from the detector center. The energy deposited in the scintillator decreases close to the Inner Vessel which separates the scintillator from the buffer layers. The empty boards correction in Equation (4.8) is applied in the right panel, showing a better separation of low energy neutron clusters, which were mainly induced by accidental background events (Binning: x-axis: 4 cm/bin; y-axis: 1 nhits/bin (left), 1 nhits_corr/bin) (right)).

by the number of alive PMTs during a run. However, this correction does not take into account the geometrical distribution of the working PMTs. Indeed, the number of dead PMTs in the southern hemisphere is larger than in the northern hemisphere of the detector. This leads to a North-South asymmetry in the energy reconstruction. Compared to the empty boards problem, this effect is of secondary order.
Secondly, the energy of the γ rays emitted in neutron capture processes close to the border of the Inner Vessel (at 4.25 m from the center of the detector) can be partly absorbed in the buffer. This means that the reconstructed energy decreases the closer one gets to this transition region. This is demonstrated in both panels of Figure 31.
Thirdly, the probability that a PMT is hit multiple times increases with the deposited energy of the event. It is described by a binomial distribution. A correction including this effect would also be radial dependent due to geometrical effects (coverage of PMTs, absorption of light in the buffer). Since the following analyses do not require an exact conversion of the Borexino internal `nhits` energy scale into MeV units, a correction of this effect is not applied.

4.2.4 Neutron rate and neutron multiplicities

As already shown in Figure 28, a single muon crossing the Borexino detector can induce a large number of neutrons within the scintillator. This section is dedicated to the study of the neutron rate in the entire detector and to the neutron multiplicities induced by cosmic-ray muons and muon showers. The CNGS muons (see Section 4.2.1) and their correlated neutrons were excluded (71110

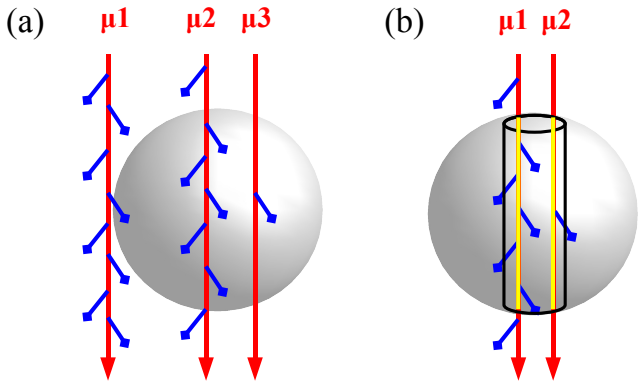

Figure 32: Estimation of the neutron rate in Borexino induced by muons/muon showers: (a) Definition of the multiplicity M_n of a neutron event: the muons $\mu 1$ and $\mu 3$ are followed by a single neutron cluster event, $\mu 2$ by a neutron event with M_n=5. (b) Estimation of the average number of neutrons produced by a muon per unit path length: only muons with a track passing close to the detector center are used in order to avoid border effects.

muon events present in the used data set of 662.1 d of lifetime)[13]. The section concludes with some consideration about the average number of neutrons that are produced by cosmic-ray muons per unit path length.

Neutron rate To estimate the neutron rate, the time profile of neutron clusters from all neutron events is plotted and fitted with an exponential function and a constant term[14]. The latter one describes the contribution from accidental events which are assumed to be homogeneously distributed over the entire neutron trigger gate. With the present DAQ settings and the clustering algorithms 25% of all detected neutron clusters turn out to be accidentals. The resulting background-free neutron rate in the entire Inner Detector (R<6.85 m; mostly within the Inner Vessel (R<4.25 m) which contains the scintillator) is $R_{n,tot}$=276 neutrons/d. In a spherical concentric *fiducial volume* of radius R<3.0 m (∼100 tons of scintillator), the total rate is $R_{n,tot}$=103 neutrons/d.
Table 5 distinguishes between neutron rates induced by neutron events (i) of a given multiplicity M_n and (ii) within different *fiducial volumes*. The number of neutron events for a given multiplicity M_n up to 10 can be directly deduced from the table. For neutron events with M_n >10, the average rate is ∼4.4/d.

It should be noted that the variable M_n is a function of the uniformity of the detector, of the muon track length crossing the detector and of the neutron trigger gate interval. As shown in panel (a) of Figure 32, a muon ($\mu 1$) generating many neutrons in the buffer, but depositing only a single neutron in the active volume, is handled like a muon ($\mu 3$) which propagates through the entire scintillator and interacts with one ^{12}C atom under emission of a single neutron. In these two cases, the multiplicity is equal to one. By taking this into account, ∼62% of all single neutron clusters reconstructed in the Inner Detector are accidental clusters (corresponding to ∼96% of the

[13]The CNGS neutrino beam is operated in supercycles of few tens of seconds. Each supercycle contains 2-4 subcycles. During a subcycle there are two fast extractions of 10.5 μs and 50 μs. The *time-of-flight* of the extracted neutrinos for the distance of 730 km from CERN to LNGS is ∼2.4 ms. Since the CERN and Borexino clocks are synchronized, CNGS muons can be identified easily in Borexino (see [89]).

[14]One fit parameter of the exponential term corresponds to the neutron capture time. Its determination is presented in more detail in Section 4.2.8.

	Inner Detector R<6.85 m				*fiducial volume* R<3.0 m			
M_n	R_n [cl/d]	R_b [cl/d]	$R_b/(R_b+R_n)$ [%]	$R_n/R_{n,tot}$ [%]	R_n [cl/d]	R_b [cl/d]	$R_b/(R_b+R_n)$ [%]	$R_n/R_{n,tot}$ [%]
all	276.4	90.9	24.7	100.0	102.8	39.7	27.8	100.0
1	53.6	87.2	62.0	19.4	13.8	37.2	73.0	13.4
2	24.3	2.1	8.0	8.8	6.9	0.8	10.7	6.7
3	15.8	0.1	0.9	5.7	4.7	0.1	1.6	4.5
4	11.5	0.1	0.8	4.2	3.5	0.1	1.3	3.4
5	8.6	0.1	0.7	3.1	2.7	0.1	2.0	2.6
6	7.7	0.1	0.7	2.8	2.7	0.1	1.8	2.6
7	7.0	0.1	<0.7	2.5	2.2	0.1	3.0	2.1
8	6.1	<0.1	<0.7	2.2	2.1	<0.1	<1.0	2.1
9	5.5	<0.1	0.4	2.0	1.7	<0.1	2.2	1.7
10	5.1	<0.1	0.9	1.9	1.6	<0.1	2.9	1.6
>10	132.0	0.4	0.3	47.7	61.7	0.6	1.0	60.0

Table 5: Rates of neutron clusters induced by neutron captures in the scintillator/buffer (R_n) and by accidental background events (R_b) for neutron events of multiplicity M_n. The rates are given in clusters/day [cl/d]. The rates were measured within (i) the entire Inner Detector (R>6.85 m) and (ii) within a *fiducial volume* with radius R<3.0 m.

accidentals present in neutron events of all multiplicities). The residual ∼38% of single neutron cluster events are induced by real neutron captures and represent ∼19.4% of all detected neutrons. Double neutron cluster events contribute to ∼2.3% of all background events and to ∼8.8% of all neutrons. High multiplicity neutron events with M_n >10 are almost background free and contribute to 47.7% of all neutrons observed in Borexino. For comparison, in the LVD experiment which is located at the LNGS like the Borexino experiment, the high multiplicity neutron events caused by hadronic and electromagnetic cascades contribute to more than >60% of all observed neutrons [136].

High multiplicity neutron events A muon that crosses the Inner Vessel (R<4.25 m) of Borexino and that is followed by a neutron event generates ∼2.3 neutrons on average. Nevertheless, neutron events with multiplicities up to several hundert clusters have also been observed. The neutron event with the highest multiplicity detected by Borexino in the used data set of 662.1 d of lifetime had M_n=244 (Event ID: 157013, Run: 9977). Table 32 in Appendix A.4 summarizes the 150 neutron events with the highest multiplicity.
An insight into the production mechanism of such neutron bursts can be obtained by looking at the properties of the parent muon/muon showers and of the neutron clusters themselves. Showering muon events produce a large amount of scintillation light and typically a large number of neutrons. The scintillation light bursts first induce large afterpulses, as shown in Figure 28, which make a disentanglement of neutron clusters more difficult. In addition, the large amount of scintillation light induces an increased number of empty boards, leading to a reduced number of hits of the neutron clusters. The energy (Section 4.2.3), but also the position reconstruction (Section 4.2.5) of the clusters tend to deteriorate.
Finally, the emitted and detected particles are effectively neutrons. This can be seen from the capture time distribution of these clusters which is compatible with that of single neutron cluster events.

Average neutron production by muons per unit path length The estimation of the average number $\overline{N}$ of neutrons which are produced in Borexino by muons per unit path length is of fundamental importance. The value of $\overline{N}$ depends on the (i) medium which a muon crosses, (ii) the incident muon energy $\overline{E}_\mu$ and on (iii) the muon flux Φ_μ. In the case of Borexino, the medium is an organic liquid scintillator/buffer, the mean muon energy $\overline{E}_\mu \approx$310 GeV (see Section 4.1.1) and the muon flux becomes $\sim$1.23 μ m^{-2} d^{-1} (see Section 4.1.2). This means that $\overline{N}$ is characteristic for a given detector at a given experimental site. Prior to Borexino, $\overline{N}$ was estimated by seven other experiments at different locations with an overburden of 25 m w.e. up to 5200 m w.e. (see references in [137]). For the LVD experiment which is located at the LNGS like Borexino and which is also filled with a liquid scintillator, one gets $\overline{N} = (4.38 \pm 0.53) \times 10^{-4}$ neutrons/(muon g cm^{-2}) [136][15]. By combining the results from the seven experiments, an almost linear trend-line of $\overline{N}$ versus $\overline{E}_\mu$ was deduced. Therefore, it is possible to predict the expected value $\overline{N}$ for the Borexino experiment. This is a unique possibility to estimate an absolute neutron detection efficiency of all hardware systems integrated in Borexino (see Section 4.2.2). Moreover, the experimental results have turned out to be approximately two times higher than the values simulated by the most updated versions of the Monte Carlo codes FLUKA [139] and GEANT4 [109]. For an organic liquid scintillator detector located at the LNGS experimental site, one expects $\overline{N}_{MC} \approx 2.6 \times 10^{-4}$ neutrons/(muon g cm^{-2}) from the FLUKA simulation and $\overline{N}_{MC} \approx 2.4 \times 10^{-4}$ neutrons/(muon g cm^{-2}) from the GEANT4-based simulation [137, 140, 141]. In this paragraph, the author of this thesis presents a road map for the estimation of the average number $\overline{N}$ for the Borexino detector:

1. Selection of muons: Only muons with successfully reconstructed tracks and those which have a small distance from the detector center (e.g. <1 m) are considered. By selecting only muons with a small distance from the center, border effects between scintillator and buffer can be avoided. Among these muon events, only a small percentage is followed by a neutron event. The total number of muon events of that category is denoted by N_μ. The not considered muons where the muon track reconstruction failed are taken into account by the efficiency $\epsilon_{mt,\mu}$.

2. Mean muon track length within the scintillator: for all considered muons, the part of the tracks intersecting the spherical Inner Vessel (R<4.25 m) has to be estimated. The obtained mean value is denoted by $\overline{L}_\mu$. Including the density ρ=0.88 g/cm^3 of the scintillator, the average muon path length is expressed by $L =< \overline{L}_\mu \cdot \rho >$.

3. Estimation of the number N_n of neutrons: All neutron clusters that were induced by the above selected muons and that are not accidentals are counted. The total number N_n includes neutron clusters from neutron events of all multiplicities. Then one can assume that all neutrons emitted along the muon track intersections with the scintillator are captured inside it.
   Three efficiencies are still needed: $\epsilon_{tg,n}$=0.94 takes into account neutrons that have been captured in the scintillator before the neutron trigger was opened; $\epsilon_{mt,n}$ considers neutrons that were not counted, since they belong to muon events with a non-reconstructed track; $\epsilon_{abs,n}$ is the absolute efficiency of all hardware systems and clustering algorithms used for the neutron detection in Borexino.

The neutron cluster and muon event selection procedure is depicted schematically in panel (b) of Figure 32. These cuts allow to estimate the mean traveling path $< L_\mu >$ of the muons with a small uncertainty and to detect most of the neutrons that are emitted along these track intersections

[15] In the original publication from 1999, the LVD collaboration published $\overline{N} = (1.5 \pm 0.4) \times 10^{-4}$ neutrons/(muon g cm^{-2}); but this value was only related to neutrons with energies higher than 20 MeV [138].

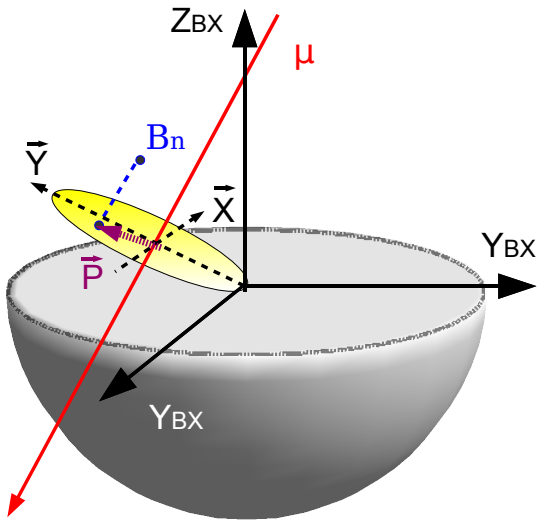

Figure 33: Scheme of the algorithm used to study the reliability of the position reconstruction algorithms for muon-induced neutrons. Note that the projection vector $\vec{P}$ has to be calculated separately for each of the muon-induced neutron in the used data set. For more details see the text.

within the scintillator. It is expected that neutrons emitted along the tracks of the aforementioned muons are predominantly captured within the scintillator. For example, neutrons emitted in single-neutron cluster events are absorbed at >98% level within a distance of 2 m from the point of emission (see Section 4.2.6).
Finally, $\overline{N}$ can be calculated according to the formula:

$$\overline{N} = \frac{N_n \cdot \epsilon_{mt,\mu}}{N_\mu \cdot L \cdot \epsilon_{tg,n} \cdot \epsilon_{mt,n} \cdot \epsilon_{abs,n}} \tag{4.9}$$

4.2.5 Position reconstruction and lateral distribution of neutrons

In the present paragraph, the position reconstruction of muon-induced neutron clusters is investigated. Unlike events that are not preceded by a muon event, the position reconstruction (PR) algorithms might encounter difficulties in reconstructing the positions of neutron captures. This could occur due to the aforementioned electronics problems which persist after a muon has crossed the detector.
There is a large interest in knowing the reliability of the position reconstruction algorithms under these conditions. On the one hand, a correct position reconstruction of muon-induced neutrons is an essential ingredient for tagging techniques like the *threefold coincidence* (TFC) method (compare with Section 2.4). This technique is based on the correct association of neutrons with ^{11}C decays in space and time. On the other hand, the determination of the lateral distribution of the captured neutrons around their parent muon tracks is of interest for Dark Matter detectors and other experiments and for testing simulation programs like FLUKA.

Reliability of the position reconstruction The general idea of the present analysis is to use the distances between the reconstructed position of neutron clusters and the reconstructed muon tracks to study the quality of the position reconstruction (PR) algorithm. As shown in Figure 33 a plane is defined for each single muon by the distance vector $\vec{Y}$ of the detector center to the muon track and by the vector $\vec{X}$, which is perpendicular to $\vec{Y}$ and to the muon track leading to an orthogonal basis. The vector $-\vec{Y}$ is directed to the center of the detector. Then the reconstructed positions of the neutron clusters B_n are projected into the $\vec{X}\vec{Y}$-plane. The projection vector is denoted by $\vec{P}$. If the PR algorithms were successful, the neutron cluster distribution should have a maximum around $(\vec{X},\vec{Y})_M$=(0;0) cm, where the muon tracks cross.
The study was performed separately for neutrons of different multiplicity M_n in order to recognize effects which might arise with a different M_n. Besides the variation of the neutron multiplicity and the muon track information, other parameters like the maximum distance of the muon tracks from the detector center and the minimal energy of the neutron clusters were modulated.

The results obtained for single neutron cluster events (M_n=1) are reported here. The selected neutron clusters have to belong to muons whose muon track can be reconstructed and whose distance from the detector center is lower than R<6.85 m. The distribution of these neutron clusters around their muon tracks is depicted in panel (a1) of Figure 34. The non-uniform oval distribution which is not concentric around the expected maximum is introduced by the finite size of the active volume of Borexino: neutrons emitted by muons crossing the outer parts of the detector are only detected if they propagate inwards (in $-\vec{Y}$ direction) to the detector center and are captured in the scintillator.
The maximum of the distribution has been fitted and found to be around $(\vec{X},\vec{Y})_M$=(0;8) cm, which demonstrates that the reconstructed neutron cluster positions are shifted slightly inwards to the detector center. Panel (a2) of Figure 34 shows the distance distribution of the selected neutron clusters from the detector center, which was fitted by a volumetric function convoluted with the detector response. This also demonstrates that the positions of a smaller fraction of clusters tend to be reconstructed further inwards. However, it turns out that these clusters are mainly the accidental ones induced by ^{14}C decays. An energy cut of the neutron clusters at 100 nhits_corr as suggested by Figure 31 efficiently removes the isotropic component around the maximum shown in panel (a1). It is also found that the muons which are followed by these accidental ^{14}C events cross mainly the buffer and not the scintillator.

For neutron multiplicities M_n>1 the background component becomes increasingly smaller (see Table 5), which facilitates the study of the position reconstruction. A global inwards shift of the distances of neutron clusters as shown in panel (a1) of Figure 34 for M_n=1 is observed for all multiplicities. Up to M_n=9, the inwards shift of the maximum is between ∼4 cm and ∼22 cm. For neutron events with multiplicity above M_n >9, which occur ∼4.9 times per day in Borexino, the shift of the maximum increases rapidly. All clusters from neutron events with multiplicities M_n >9 are shown in panel (b1) of Figure 34. The average shift is ∼2.5 m. This means that not only the energy information of high-multiplicity neutron events is poorly known (see Section 4.2.3), but also the position reconstruction is no longer reliable.

Lateral distribution of neutrons The lateral distance distribution $\Phi(d)$ of cosmic-ray induced neutrons around the tracks of their parent muons has been studied. The analysis is based on the same sample of muon tracks that was used for the estimation of the average neutron production by muons per unit path length (see Section 4.2.4). The muon tracks of this data set have a maximum distance of 1 m from the detector center. Therefore, cosmic-ray induced neutrons are detected as long as their distance d from the tracks does not exceed ∼3.5 m. Neutrons propagating over a longer distance are mostly absorbed in the buffer and thus they cannot be detected. This would

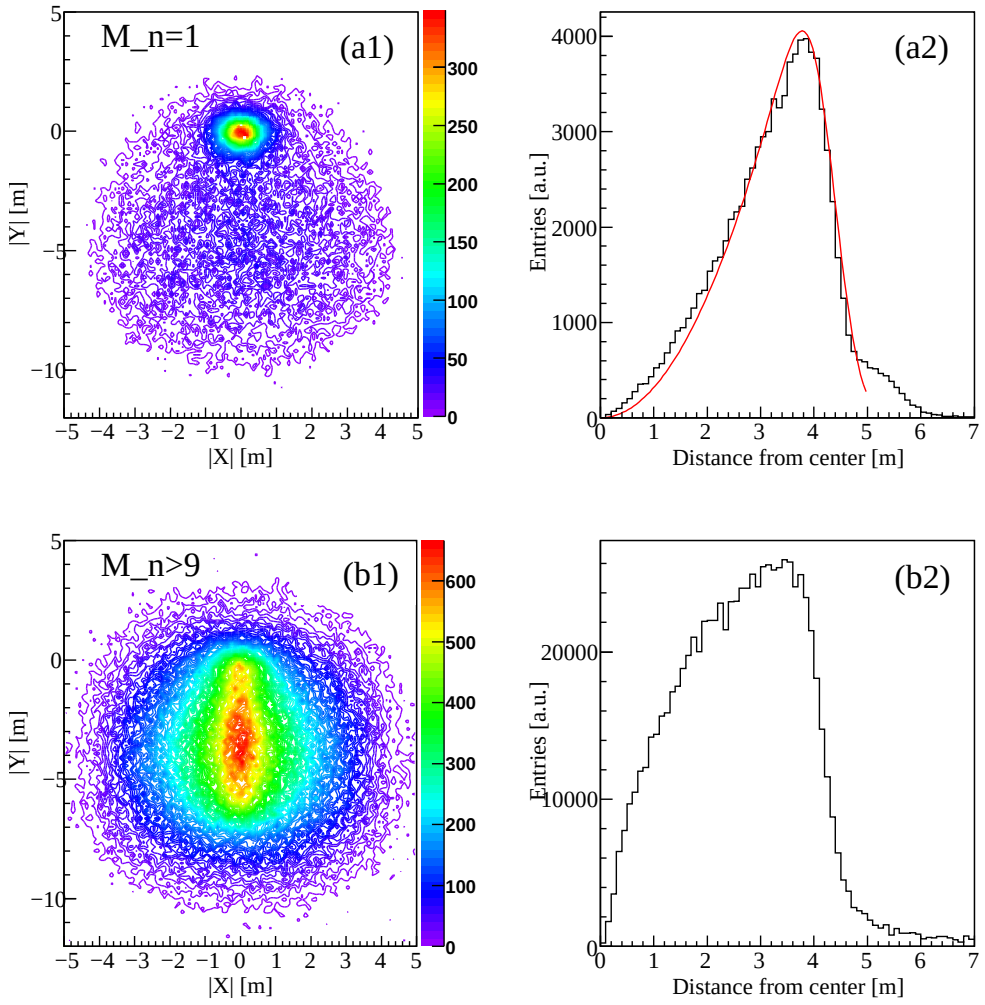

Figure 34: Position reconstruction of neutron clusters detected after cosmic-ray muon events: Single neutron cluster events and neutron events with M_n>9 are shown. Panels (1) show the distance of the neutron clusters from the tracks of the parent muons, panels (2) show the distance of the neutron cluster positions from the detector center.

induce a reduced number of neutrons in the $\Phi(d)$ distribution.
The results are depicted in Figure 35. The number of neutrons per bin only contains the statistical error. Single neutron cluster events (M_n=1) and neutron events with multiplicities up to M_n<10 are shown separately. Neutron events with higher multiplicities are not considered due to the degenerated position reconstruction of the clusters (see previous paragraph). The inwards shifts of the neutron cluster positions for M_n=1 and M_n<10 are 3 cm and 7 cm, respectively. The uncertainty of the muon track reconstruction is in the range of ∼30 cm. The shown distributions have not been corrected for these effects, since they become negligible with increasing distances.
The $\Phi(d)$ distribution for M_n=1 decreases faster than the one for M_n <10. This indicates that neutrons emitted in higher multiplicity events have higher initial energies. Figure 35 also shows the $\Phi(d)$ distribution obtained in the LVD experiment [138] and in the most updated FLUKA simulation [137]. There is a rather good agreement between the LVD and the Borexino result for M_n<10. However, a direct comparison cannot be drawn in the present analysis, since the LVD as well as the FLUKA results include neutrons of all multiplicities, also the ones produced in muon showers.

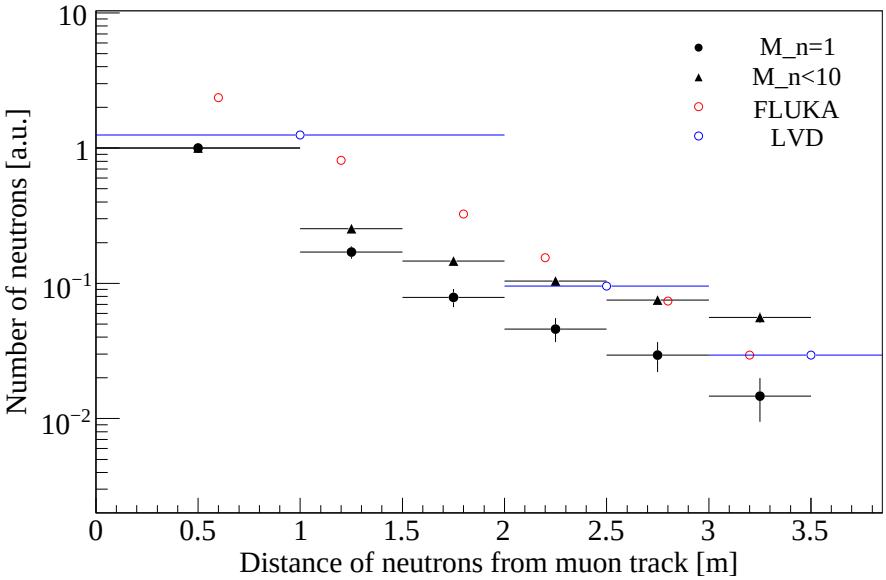

Figure 35: Lateral distance of neutrons from the primary tracks of cosmic-ray muons. Borexino neutron events of multiplicity M_n=1 and M_n<10 are shown separately and compared to the results of the FLUKA simulation in [137] and of the LVD experiment [138]. Only the statistical uncertainty was taken in account for the Borexino results.

The $\Phi(d)$ distribution is a function of the incident muon energy and of the medium in which the neutrons propagate. However, the present analysis impede the estimation of the real propagation length of the neutrons. The first reason is that the neutron emission point is not known. Secondly, the above measured distances d are defined between the light barycenters of the characteristic γ rays, which are emitted in the neutron capture processes, and the closest point to the reconstructed muon track. The muon track itself is affected by fit parameter uncertainties.
The following Section 4.2.6 is dedicated to a more detailed study of the propagation processes of neutrons in the Borexino scintillator.

4.2.6 Propagation of neutrons in the Borexino scintillator

Microscopic description of the propagation and capture time of neutrons The Borexino scintillator is a material rich in carbon and hydrogen which act as moderator and absorber of neutrons propagating through it.
The slowing down of fast neutrons in the scintillator to thermal energies is dominated by several energy loss mechanisms, mainly inelastic and elastic scattering processes [142, 143].
Firstly, inelastic scattering takes place if the target nucleus which the neutron scatters on has the capacity of changing into excited states. It follows that hydrogen nuclei are excluded from this process. Secondly, elastic scattering only occurs if the neutron energy is larger than or equal to the energy amount required to reach the first excited state of the target nuclei. Under this condition, the neutron can form a compound nucleus with the target nucleus. Then the neutron is usually re-emitted with a lower energy, leaving the nucleus in an excited state. Note that in few cases high energetic neutrons can also be captured under emission of an α particle and of a characteristic γ ray (Example: ^{12}C(n,α)^{9}Be with E$_\gamma$ = 1.75 MeV).
Elastic scattering processes can be described by the relation between the incident and the final neutron energy in the laboratory system for a collision of a neutron with a nucleus of mass number

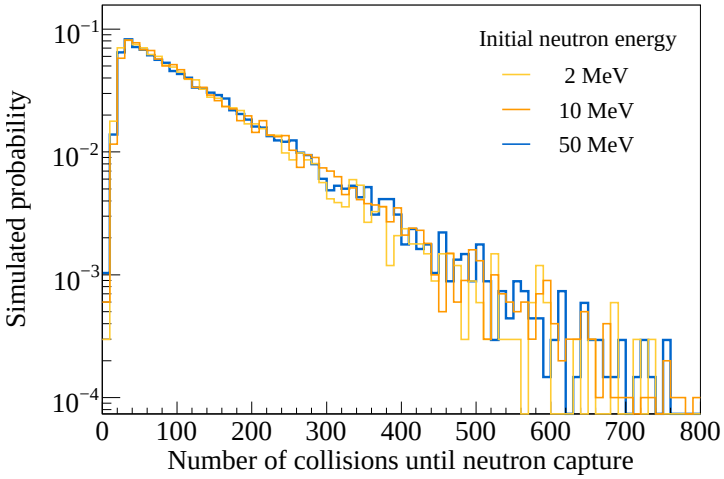

Figure 36: Number of collisions of neutrons with atoms in the Borexino scintillator before they are captured. The simulation was carried out with the simulation tool *MaGe* based on *Geant4* (version 4.9.2.p01).

A [142]:

$$E_a = E_i \cdot \frac{A^2 + 1 + 2 \cdot A \cdot \cos(\theta)}{(A+1)^2} \tag{4.10}$$

where E_i is the neutron energy before the collision process, E_a the energy after the collision, θ the scattering angle in the CMS-system. The maximum energy loss is obtained for central collisions ($\theta = \pi$) when the target nucleus is assumed to be at rest. In this case, neutrons can lose all of their energy in a single elastic collision with hydrogen and 28.4% of the initial energy scattering with ^{12}C nuclei.
After reaching thermal energies below 1 eV the neutrons walk randomly and can be scattered both down and up, i.e. the neutrons can also gain energy ("up-scattering"). Finally, the neutrons will reach thermal equilibrium with the scintillator. At thermal energies, the cross section for neutron capture on protons largely increases, that for ^{12}C is two orders of magnitude lower.

The capture time τ of neutrons in a moderator and absorber like the Borexino scintillator can be divided into two parts:
The first component, denoted with τ_a, is the time interval between the emission of neutrons and their thermalisation. During this phase, the high energetic neutrons lose significant fractions of their initial energies E within few elastic and inelastic collisions and within a very short time: For neutrons with an initial energy of several MeV, the typical time interval between collisions ranges from 10^{-9} s to 10^{-6} s [144].
The second component τ_b covers the time between the beginning of the thermal diffusion of the neutrons and their absorption in the medium. At these energies, the time interval between two collisions during the second phase is of the order of 10^{-6} s [145]. Depending on the composition, density and temperature of the medium, the neutrons can undergo several hundreds of collisions before being captured. Simulations of neutrons of different energies propagating through a scintillator as used in Borexino were carried out. Then the number of collisions until the neutrons are captured were counted. The results are shown in Figure 36. The mean values range between 121 and 128 collisions for 2 MeV to 50 MeV neutrons. The slight increase is due to additional collisions during the first slowing down phase.

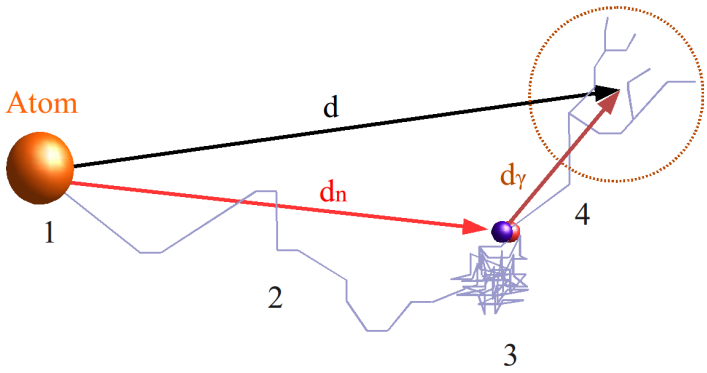

Figure 37: Schematic view of a fast neutron propagating through the Borexino scintillator: (1) Emission of a fast neutron from an atom via an arbitrary mechanism. (2) Slowing down of the neutron to thermal energies; (3) Neutron capture under emission of a γ ray of a specific energy; (4) Propagation and absorption of the γ ray including the reconstructed light-barycenter.

Based on these considerations, it becomes clear that mainly τ_b contributes to the total capture time τ and that its measurement does not reveal any information about the initial neutron energy. The capture time τ can be described by the theoretically deduced formula [146]:

$$\tau^{-1}(\mathrm{T}) = \left(\sigma_H \cdot \nu_H(\mathrm{T}) + \sigma_C \cdot \nu_C(\mathrm{T})\right) \cdot v_n(\mathrm{T}) \tag{4.11}$$

Herein, σ_H and σ_C are the neutron capture cross sections of hydrogen and carbon at thermal energies, ν_H and ν_C the hydrogen and carbon densities of the medium at the temperature T. The variable $v_n(\mathrm{T})$ corresponds to the neutron velocity at thermal energies and is equal to $v_n(\mathrm{T})$=2200 m/s at room temperature T=20°C.
If the temperature in a medium increases, $v_n(\mathrm{T})$ also increases and ν_H as well as ν_C decrease. As a consequence, τ will increase. Since σ_H is approximately two orders of magnitude larger than σ_C, one also expects a correlation between τ and the density of hydrogen ν_H in an organic medium: the larger ν_H, the smaller τ.

The following paragraphs analyze how the Borexino scintillator affects high-energy neutrons propagating through it. The study is restricted to muon-induced neutrons and to neutrons from an ^{241}Am^{9}Be source and will include measurements of the characteristic capture time, of the propagation length and of the initial energy of the two cited neutron classes.

Modelling of the neutron propagation in the Borexino scintillator Whereas the neutron capture time τ mainly depends on the hydrogen density ν(H) of the used organic scintillator, the propagation length d_n of neutrons through a given scintillator mainly depends on the initial energy E_i of the neutrons. This information is contained in the Borexino data, however, it is restricted to a certain class of events. Figure 37 illustrates the propagation distance d_n of the neutrons and the distance the Borexino detector is able to measure. Borexino allows to measure the variable d, which is the distance between the point of neutron emission and the light barycenter of the characteristic γ rays (commonly referred to as "neutron clusters", see Section 4.2.2) following the neutron capture on protons; d is the vectorial sum of the neutron propagation distance d_n and the gamma propagation length d_γ. The point of neutron emission is determined by a prompt de-excitation of the nucleus emitting the neutron (in case of the ^{241}Am^{9}Be source) or by a delayed decay of the nucleus (in case of muon-induced neutrons).

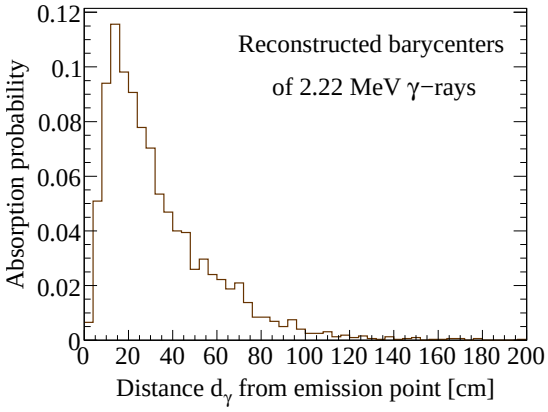

Figure 38: MC simulation of path travelled by 2.22 MeV γ rays in the Borexino scintillator.

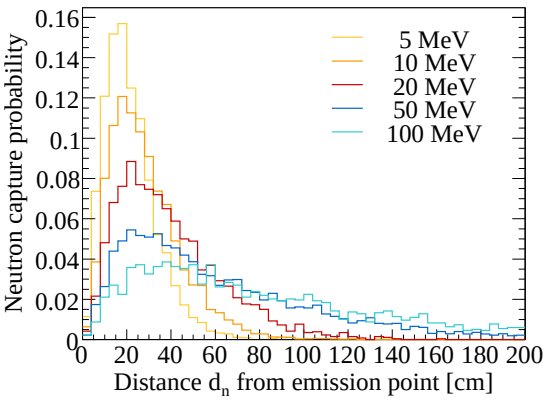

Figure 39: MC simulation of path travelled by neutrons of different energies in the Borexino scintillator.

The estimation of the propagation length of the neutrons and of their initial neutron energy requires the determination of the neutron distance d_n. For this purpose, a model based on a three-step Monte Carlo simulation was developed that enables one to disentangle d_n from d_γ and d:

1. **Simulation of the distance** d_γ: the paths of 10,000 2.22 MeV γ rays travelling through the Borexino scintillator were simulated. The Borexino simulation tools `G4BX` and `BXELEC` (*Echidna cycle 12*) were used. These tools allow to reconstruct the light-barycenter of the absorbed 2.22 MeV energy and to take into account the detector resolution like in normal Borexino data. The normalized distribution of the simulated distances d_γ is shown in Figure 38.

2. **Simulation of the distance** d_n: The travelling path d_n of neutrons from a given emission point to a neutron capture point was simulated with the *Geant4* based simulation tool *MaGe*[16]. This program code was used because it allows to select particles of different types and energies and to define geometries and materials of experimental set-ups with a high flexibility.
   The travelled distances of neutrons with mono-energetic and continuous energy distributions $\Phi(E)$ were simulated. Figure 39 depicts the propagation distance d_n for mono-energetic neutrons of 5, 10, 20, 50 and 100 MeV.

3. **Vectorial combination of** d_γ **with** d_n: The distances d_γ and d_n were randomly combined assuming an isotropic emission of the 2.22 MeV γ rays. The simulation was performed using the generator of random numbers `TRandom3` in the framework of the *ROOT* analysis tool. Pairs of (d_γ; d_n) from the obtained distributions shown in Figure 38 and 39 are randomly selected. The angles ϕ and θ were also randomly generated in the range [0,π) and [0,2π), respectively. Then d was calculated from $d = \sqrt{d_1^2 + d_2^2 + d_3^2}$ where:

$$\begin{aligned} d_1 &= d_\gamma \cdot \cos(\theta) \cdot \sin(\phi) + d_n \\ d_2 &= d_\gamma \cdot \sin(\theta) \cdot \sin(\phi) \\ d_3 &= d_\gamma \cdot \cos(\phi); \end{aligned} \tag{4.12}$$

   The cumulative distributions of the total propagation length d obtained for different mono-energetic neutron fluxes are depicted in Figure 40.

[16] Simulation package from the Joint GERDA and Majorana collaborations

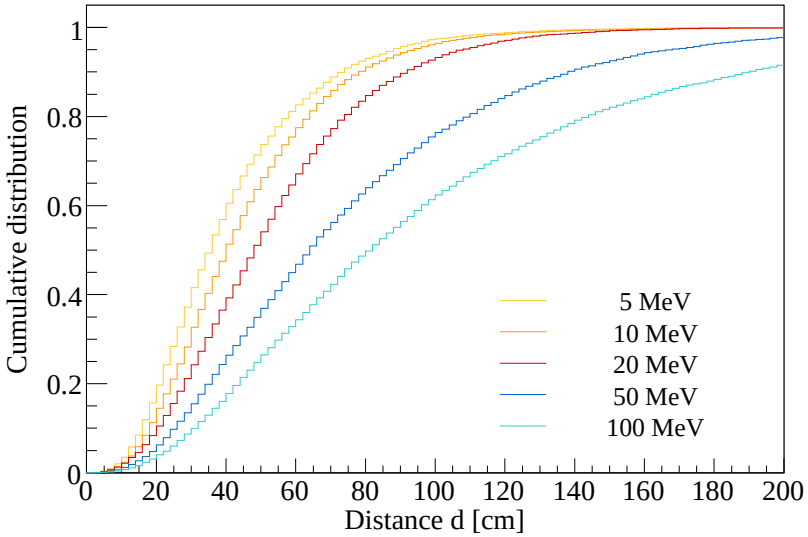

Figure 40: Cumulative distributions of simulated distances d for neutron events detected in Borexino. Several initial neutron energies are simulated. The distance d is the vectorial sum of the path travelled by the neutron and by the subsequent γ ray emitted isotropically in a random direction.

4.2.7 Analysis: Propagation of neutrons from an ^{241}Am^{9}Be source

Neutron production mechanisms in an ^{241}Am^{9}Be source During the second and third internal calibration campaigns in Borexino (see Section 4.3.1) the collaboration also carried out a calibration with a ∼9.8 Bq ^{241}Am^{9}Be neutron source.
To access the full information from the ^{241}Am^{9}Be source calibration data, the neutron production mechanisms are briefly reviewed. The neutron production is based on the decays of ^{241}Am→ ^{237}Np+α in a low-Z elemental matrix, in this case composed of an oxide-^{9}Be-mixture. Five neutron types are produced mainly via (α,n) reactions. The primary reactions are:

$$^{9}\mathrm{Be}(\alpha,n_0)^{12}\mathrm{C}_{g.s.} : \Delta E(n_0) = [5.5,11.0]\,\mathrm{MeV} \tag{4.13}$$
$$^{9}\mathrm{Be}(\alpha,n_1)^{12}\mathrm{C}^{*(1)} : \Delta E(n_1) = [1.7,6.4]\,\mathrm{MeV} \tag{4.14}$$
$$^{9}\mathrm{Be}(\alpha,n_2)^{12}\mathrm{C}^{*(2)} : \Delta E(n_2) = [0.2,2.9]\,\mathrm{MeV} \tag{4.15}$$

$$^{9}\mathrm{Be}(\alpha,\alpha\, n_b)^{8}\mathrm{Be} : \Delta E(n_b) < 2.0\,\mathrm{MeV} \tag{4.16}$$
$$^{9}\mathrm{Be}(\alpha,n_b)3\alpha : \Delta E(n_b) < 2.0\,\mathrm{MeV} \tag{4.17}$$

The measured neutron yield is around 65-80 neutrons/10^6 α particles [147, 148].
The neutron energy spectrum for ^{241}Am^{9}Be has been calculated by several authors as in [147, 149, 150]. The spectrum in Figure 91, Appendix A.5, is taken from [150] and shows the separated contributions from different branches. Neutron fluxes n_0, n_1 and n_2 dominate. Multibody break-up neutrons n_b contribute considerably below 1 MeV. However, the fraction of neutrons with energies below 1.5 MeV contributes only 15% to the total neutron flux. The neutron mean energy is E=4.05 MeV [201]. The ^{241}Am^{9}Be neutron energy spectrum measured in [148] can be found in Figure 92 in Appendix A.5.
Even though the neutrons are fully absorbed in the scintillator, Borexino does not measure the

neutron energy spectrum, but two categories of events which are correlated in space and time. These are:

- **Prompt signals**: These events are generated instantaneously when neutrons leave the source. Firstly, $^{12}C^{*(1)}$ nuclei de-excite with a relaxation time of $\tau \sim 6\times10^{-14}$ s [154], releasing 4.439 MeV γ rays (Branching ratio (B.R.): 100%). The 7.66 MeV excited state of $^{12}C^{*(2)}$ decays predominantly by α emission.
  A second type of prompt signals is represented by high-energy γ rays emitted from recoil protons in the calibration source holder, which is made of lead and Delrin® (acetal resin from DuPont^{TM}).
- **Delayed signals:** These events are generated instantaneously after neutron capture on hydrogen/carbon atoms or other materials in the vicinity of the calibration source. Characteristic γ rays are emitted after the neutron capture: 2.22 MeV for hydrogen atoms, 4.95 MeV for carbon atoms. For neutron captures on Fe, Ni, Co, Cu, Cr, Mn contained in the stainless steel of the insertion calibration arm, the γ energies go up to approximately 9 MeV.

Data selection The described signature composed by prompt and delayed signals allows to search for coincidences in the Borexino data. To tag such coincidences, the following cuts have been applied:

- Only events that are neutrino-like and that are no muons are selected. Their reconstructed positions must be within a spherical *fiducial volume* with radius R<3.5 m.
- The first event (prompt signal) of the coincidence must not have more than two clusters, the second event (delayed signal) not more than one cluster.
- The maximum time window for a candidate coincidence is 2600 μs; this corresponds to $\sim$10 times the expected capture time of neutrons in pseudocumene. It is obvious that coincidences within a time interval $\geq$1300 μs are mainly accidental.
- No other events in a time interval of 2600 μs prior to and after the coincidence are allowed. For each tagged coincidence, the reconstructed distance ΔR_C and the time interval Δt between prompt and delayed signal is recorded. For a known source position, also the distance ΔR_S between source and delayed signal can be defined.

Analysis of the energy spectra of the $^{241}Am^{9}Be$ source The energy spectra of the prompt and delayed signals from coincidences with $\Delta R<7$ m are shown in Figure 41.
The spectrum of the prompt signals contains γ rays from recoil protons (break up channel), a 4.4 MeV peak from the de-excitation of ^{12}C nuclei in the source and a broad peak around 4-7 MeV which stems from the combination of both signals. The peak at 8.8 MeV originates from the superposition of two 4.4 MeV γ rays. At 2.22 MeV there is also a contribution from delayed signals that were able to accidentally pass the data selection cuts for prompt signals as defined in the previous paragraph.
The energy spectrum with the delayed signals contains the peaks of the characteristic 2.22 MeV, 4.94 MeV and 7.64 MeV γ rays released immediately after the neutron capture on protons, on ^{12}C nuclei and on ^{56}Fe atoms contained in the stainless steel of the insertion arm which was used during the calibration campaigns in Borexino.
The peaks in the $^{241}Am^{9}Be$ energy spectra observed in Borexino can be used for several analyses:

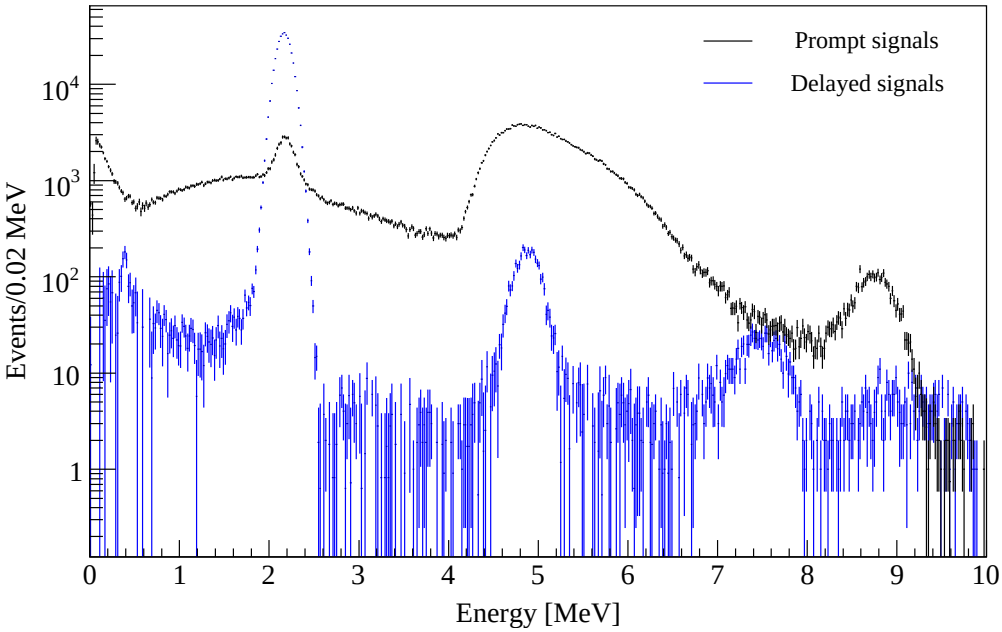

Figure 41: Energy spectrum of prompt and delayed signals of the ^{241}Am^{9}Be source registered by the Borexino detector. The data were collected in February 2009 and the source was placed close to the center of the detector.

- **The energy scale in Borexino**: The exact peak positions allow to estimate the energy scale for the charge variable and the energy resolution up to ∼9 MeV. The measured light yields for the 2.22 MeV and 4.94 MeV γ rays at the center of the detector are (1062±1.0) photoelectrons (pe) and (2361±1.3) pe, respectively. A. Derbin et al. (Borexino collaboration) performed an accurate analysis of the energy scale also including the peaks at higher energy: one peak at 8.88 MeV originates from the instantaneous emission of two 4.44 MeV γ rays when ^{12}C atoms within the ^{241}Am^{9}Be source de-excite; several more superimposed peaks around 7.64 MeV stem from delayed signals emitted by neutron capture on the stainless steel [155]. It turned out that the energy (by means of the collected charge) scales almost linearly in the energy interval from ∼2 MeV up to ∼9 MeV (see Figure 18). Thus, after normalisation of the charge variable according to Equation (3.7) one can express the energy scale in MeV units as follows:

$$Q_{rec}\,[MeV] = -0.02(1) + 0.00209(1) \cdot Q_{rec} \tag{4.18}$$

  This conversation has already been applied to the energy spectra shown in Figure 41.

- **Neutron capture cross section**: The count rates of the delayed signals of 2.22 MeV and 4.94 MeV γ rays from neutron capture on hydrogen and carbon atoms can be used to estimate the ratio λ=σ(H)/σ(C) of the neutron capture cross sections of these two elements. Note that the accidental 2.22 MeV γ rays present in the prompt energy spectrum also have to be taken into account to calculate the total 2.22 MeV γ rays count rate. Assuming a linear background beneath the peak regions of 2.22 MeV and 4.94 MeV, the result is λ=123±3. Using the literature values of the cross sections σ(H) = 0.3326 barn and σ(C) = 0.0035 barn [157] and the chemical composition C_9H_{12} of pseudocumene, which is the main Borexino scintillator component, one calculates λ ∼127. The measured value obtained from the

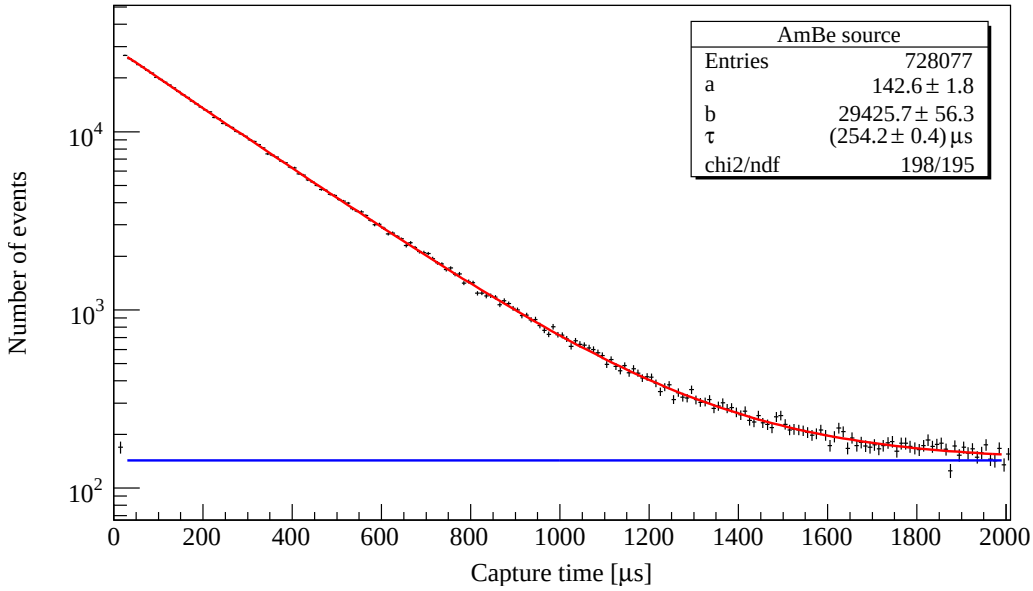

Figure 42: Estimation of the capture time of neutrons from an $^{241}Am^{9}Be$ source in the Borexino scintillator. The maximum distance of 2 events from a coincidence is $\Delta R<2$ m. The amount of accidental coincidences still present in the data set is 6%.

Borexino data is in very good agreement with the expected one.

Estimation of the capture time of neutrons from an $^{241}Am^{9}Be$ source The present analysis aims at using the $^{241}Am^{9}Be$ calibration data to precisely determine the capture time of fast neutrons propagating through the Borexino scintillator. The study was performed in *Echidna cycle 12*.
In order to exclude possible systematics, three different data sets were selected. They are composed of data acquired for different source positions (at the center and up to 4 m from the center of the detector) and during different time periods (February 2009 vs. July 2009). Details are given in Table 6.

For each data set, the following procedure was applied: The coincidences between prompt and delayed signals were selected according to the data selection described in the second last paragraph. The time intervals between prompt and delayed signals lead to a time profile distribution, which can be fitted by the function $f(t) = a + b \cdot e^{-t/\tau}$. The accidental coincidences contribute to a flat background whose area in the time interval [0,2000] μs is denoted by B. The area below the exponential curve without B is denoted by A. This allows to define the ratio $\zeta = B/A$.
Then, a subsample of coincidences was chosen whose delayed events have a given distance $< R_S$ from the source position. For this subsample, the time profile was fitted in different intervals ΔT. It is worth noting, that the source position was estimated by evaluating the CCD camera images and the maximum of the spatial distribution of the events. The reconstructed positions from the CCD camera images have an overall uncertainty of ± 2 cm. However, a general shift of approximately 4 cm in the -z direction was observed between the position reconstruction algorithms and the CCD camera images (see Table 6). This discrepancy is under study and is important for the reduction of the systematical uncertainty which is also important for the current ^{7}Be neutrino analysis aiming at a total error below 5%. However, since the z-shift is common to all reconstructed event positions, the relative distances are still correct and do not affect the present analysis.

Data set	1	2	3
Period	February 2009	June 2009	July 2009
Runs	9701,3,4,5,8,10,11	10490-93	10689-91,10701-13
Position [cm]:			
CCD cameras	(7.6,-7.0,0.9)	(267.2,-27.3,116.4)	(1.9,2.3,400.8)
LNGS code	(6.9,-7.3,-3.6)	(268.2,-28.3,112.5)	(1.5,2.8,397.5)
Capture time [μs]:			
ΔR<7 m	256.8 $\pm$ 2.0	256.2 $\pm$ 1.5	254.3 $\pm$ 1.4
ΔR<2 m	254.5 $\pm$ 0.6	255.4 $\pm$ 1.0	253.6 $\pm$ 0.9

Table 6: Comparison of data sets from three different calibration campaigns in 2009 using an ^{241}Am^{9}Be source. The source positions were estimated by CCD cameras and using position reconstruction algorithms applied to data. The measured capture times from the different data samples are in agreement and follow the same behavior: for a clean subset of coincidences with few accidental ones (i.e. smaller distance between prompt and delayed signal), the value converges versus $\sim$253.5 μs.

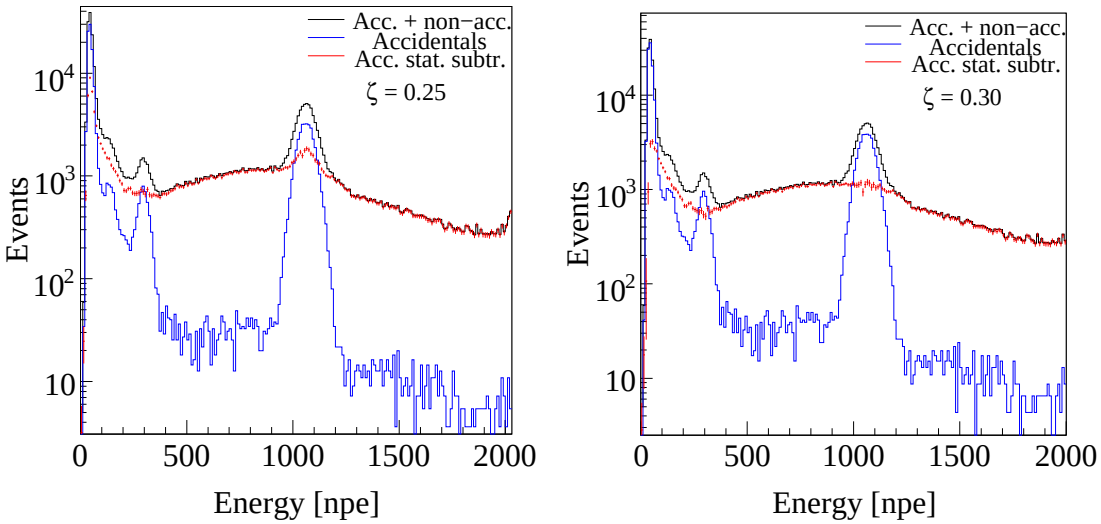

Figure 43: Prompt and delayed energy spectrum of the ^{241}Am^{9}Be source in Borexino. The prompt energy spectrum is affected by accidental delayed events. These background events are statistically subtracted. Their amount is equal to the background present in the time profile of the tagged coincidences, where the fraction is denoted by ζ. A correct estimation of the neutron capture time τ and of ζ leads to a correct statistical subtraction of the energy spectrum.

The first estimation of the neutron capture time was done for a distance cut R_S <2.0 m between the source and the reconstructed position of the delayed signal. As the cumulative distribution in Figure 44 will demonstrate, this cut is ideal since it contains the delayed 2.22 MeV γ rays from almost all neutrons (>99%) that were emitted from the source and captured around it. A smaller distance cut would not take into account all emitted 2.22 MeV γ rays, on the other hand, a larger cut would only add more accidental background events.
The time profile of events from the first data set turns out to have a fit value τ which is constant for different fit ranges ΔT. For the largest range ΔT=[20,2000] μs, the value of τ is (254.2±0.4) μs (χ^2/ndf=198/195). The fit is shown in Figure 42. The ratio ζ is ∼0.06, i.e. the percentage of accidental coincidences, is low at 6%.
The time profiles of the coincidences from the other two data periods/other source positions led to similar capture time measurements as shown in Table 6. By combining all three measurements one obtains

$$\tau = (254.5 \pm 1.8)\ \mu s \tag{4.19}$$

In order to exclude systematical effects that have not yet been considered, the measurements were repeated for delayed events with a distance R_S <7.0 m from the source. The neutron capture time τ is sensitive to the fit range ΔT. This is illustrated by means of the first time period when the source was deployed in the center of the detector: In case of ΔT=[100,1000] μs, one obtains τ=(253.9±1.2) μs (χ^2/ndf=110/87) and ζ=0.30, for ΔT=[200,2600] μs the capture time is equal to τ=(260.7±0.8) μs (χ^2/ndf=268/237) with ζ=0.26.
To constrain the estimated value for the neutron capture time in the Borexino scintillator, an independent measurement was carried out. It is based on the fact that the measurement of the variable ζ from the time profile corresponds to the percentage of accidental events visible in the prompt energy spectrum. If the variable ζ (und thus τ) was estimated correctly, a statistical subtraction of the same fraction of delayed events from the prompt energy spectrum should purify the prompt energy spectrum. The application of this new method is shown in Figure 43. Indeed the value ζ=0.30 leads to a correct subtraction of accidental events in the prompt energy spectrum. Hence, the correct value of τ has to be close to 254 μs as already previously found.

Propagation distance and initial energy of neutrons from an ^{241}Am-^{9}Be source The method in Section 4.2.6 is applied in the case of neutrons emitted from the ^{241}Am-^{9}Be source. It is a good opportunity to test the method, since the energy spectrum and the mean energy of the neutrons from the ^{241}Am-^{9}Be source are well known.
For a given source position, the delayed signals from neutron captures on hydrogen and carbon were tagged according to the coincidence method described in Section 5.4.1. Then the distance of the delayed signals from the source position was calculated and the resulting cumulative distribution plotted with 10 cm bin size. The uncertainty in the distance determination was estimated to be ±5 cm, which corresponds to the maximum deviation of the position reconstruction from the calibration reference positions at a distance of R=4 m from the detector center. The distribution is shown in the left panel of Figure 44.
To compare the cumulative distributions from data and from the simulations of mono-energetic neutrons, a χ^2 fitting function was defined. It takes into account the uncertainties of the x- and y-coordinates of the data points. The perpendicular distances from the data points to the simulated curves were estimated. The resulting χ^2 map is shown in the right panel of Figure 44. From the minimization one finds that among mono-energetic neutron distributions the one with an initial energy of (5±1) MeV leads to the best fit. Neutrons from an ^{241}Am-^{9}Be source have a mean energy of 4.05 MeV [158]. The fit result is in good agreement with this value assuming that the ^{241}Am-^{9}Be neutron energy spectrum would be purely mono-energetic. Simulating the real continuous energy

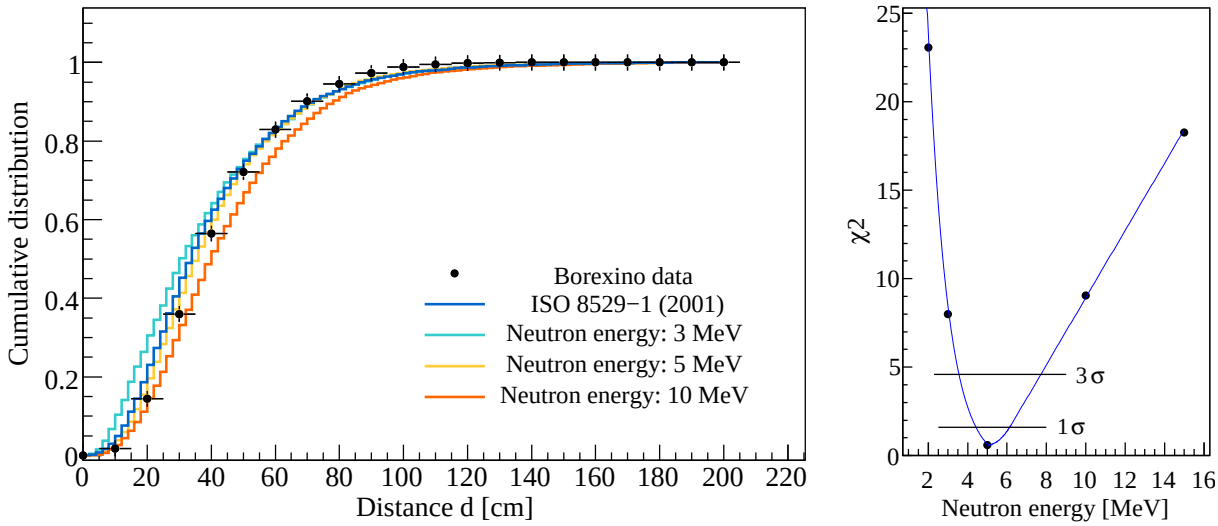

Figure 44: Cumulative distribution of the distance d of neutron events from an ^{241}Am^{9}Be source: the data is in agreement with neutrons with an initial energy of (5±1) MeV. This is consistent with the mean energy deduced from the ^{241}Am^{9}Be source used in the norm ISO 8529-1 (2001) [201]. For reasons of comparison, simulations of mono-energetic neutron classes with an energy of 3 MeV and 10 MeV are also shown.

spectrum of the ^{241}Am-^{9}Be source with energies up to 11 MeV (see norm ISO 8529-1 (2001) [201]), the fit leads to a reduced χ^2-value close to 1. This result proves that the model, which is based on simulations and aims at extracting the initial energy of neutrons from their propagation length, is reliable.

4.2.8 Analysis: Propagation of muon-induced neutrons

Estimation of the capture time of muon-induced neutrons The estimation of the capture time τ of muon-induced neutrons is presented in the following paragraph. For this purpose, the data set defined in Section 4.2.3 covering a total of 662.1 d of lifetime is used.

Even though muon-induced neutrons might have an initial kinetic energy which is higher than that of neutrons from the ^{241}Am-^{9}Be calibration source, one expects a value for τ which is in agreement with the value obtained for the ^{241}Am-^{9}Be source in Section 4.2.7. This is expected, since the capture time of MeV neutrons is almost independent of their initial energy.
In contrast to the neutrons emitted from the ^{241}Am-^{9}Be source, muon-induced neutrons are emitted simultaneously to the parent muons/muon showers crossing the detector. Hence the time of the prompt muon signals can be used to easily determine the time of neutron emission. A determination of coincidences of prompt and delayed signals as used for the ^{241}Am-^{9}Be source is not required. On the other hand, muons preceding muon-induced neutron events disturbs the electronics affecting the detection of neutron clusters within the neutron trigger gates (see Section 4.2.2). Since the problems induced by muons on the DAQ subcomponents apparently increase with the multiplicity M_n of the neutron events (see Section 4.2.4), the capture time τ of muon-induced neutrons is studied for different M_n. Figure 45 shows single-neutron cluster events (M_n=1) and of multiple cluster neutron events with M_n>10.

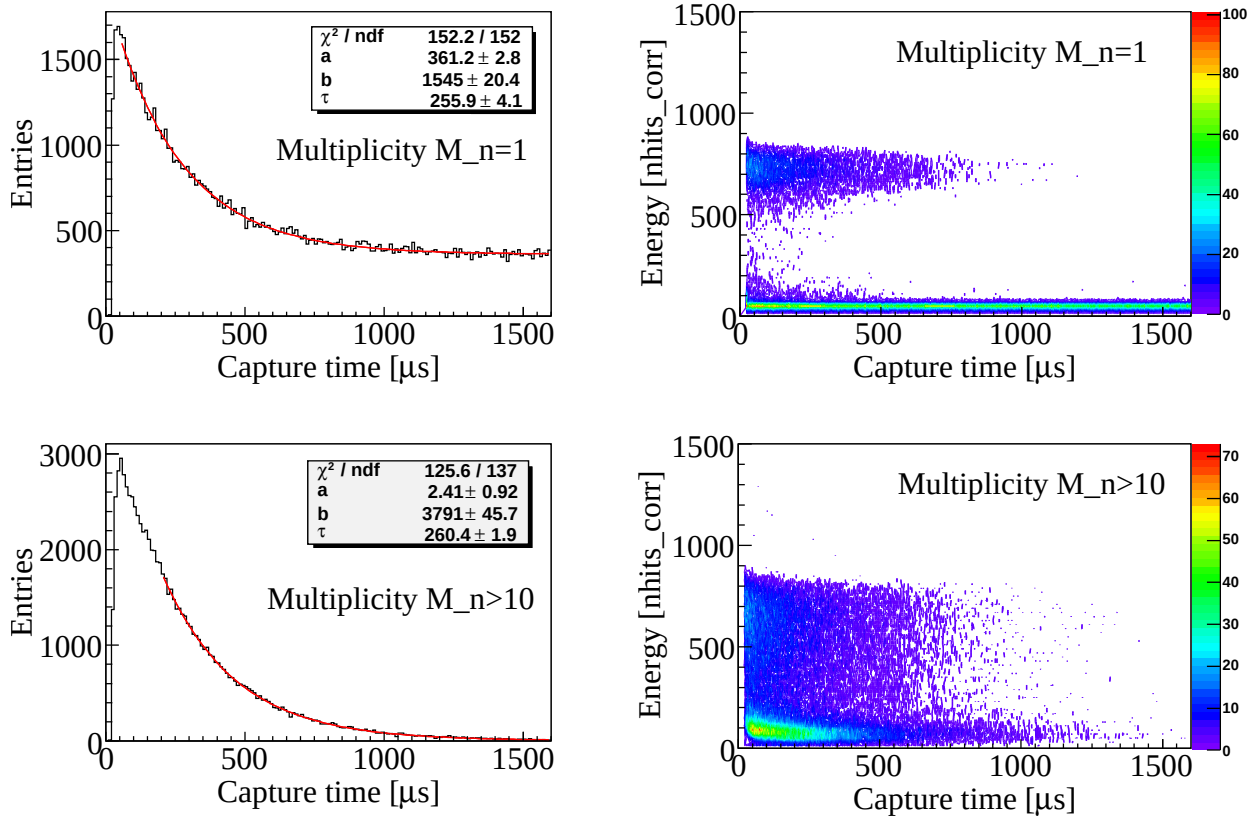

Figure 45: Estimation of the capture time of muon-induced neutrons in the Borexino scintillator. Neutron events with a multiplicity M_n=1 and M_n >10 were observed separately. As shown in the lower right panel, neutron events with the higher multiplicity (M_n>10) have a decreased number of neutron clusters in the initial ∼50-100 μs of the trigger gate. They were not reconstructed by the clustering algorithms and that leads in general to a larger capture time.

In case of M_n=1, the time profile shows a large background component at lower energies around 100 nhits due to accidentals, mainly ^{14}C decays. Assuming that this background is flat, the time profile is fitted by the function $f(t) = a + b \cdot e^{-t/\tau}$. Fitting the time profile within the range ΔT=[50,1600] μs, one obtains τ=(255.9±4.1) μs. The goodness of the fit is very high (χ^2/ndf=152.2/152), but it is also in agreement with the value obtained from the ^{241}Am-^{9}Be source.
In the case of M_n>10, the time profile shows a small background component due to accidentals. However, two other systematical effects appear for M_n>10 (see right lower panel in Figure 45): (i) the reconstructed energy of the neutron clusters is poor and overlaps with that of the accidental events, (ii) the number of reconstructed clusters in the initial phase (the first ∼100 μs) of the neutron trigger gate seems to be reduced. The latter inefficiency leads to larger values for the neutron capture time because it includes the initial phase of a neutron trigger signal. Indeed, fitting the time profile in the interval ΔT=[50,1600] μs leads to τ=(264.8±1.3) μs (χ^2/ndf=159.9/152), whereas the fit in ΔT=[200,1600] μs gives τ=(260.4±1.9) μs (χ^2/ndf=125.6/137). The systematic uncertainty introduced by the effects in point (i) and (ii) is small for M_n=1 compared to the statistical one. Thus, the neutron capture value obtained for M_n=1 will be used taking into account that the total error is underestimated:

$$\tau = (255.9 \pm 4.1)\ \mu s \tag{4.20}$$

Exp.	Material	T	ρ	H/C	ν_H	τ_a	τ_b	τ	Ref.
BX	C_9H_{12} (PC) 1.5 g/l PPO	15	0.876	1.33	5.2			255.9±4.1 254.5±1.8	μ-ind. $^{241}Am^9Be$
	H_2O	20	1.00	20	6.6	6	205	211	[145]
KL	20%: C_9H_{12} (PC) 80%: $C_{12}H_{26}$ 1.52 g/l PPO	11.5	0.780	1.97	6.8			207.5±2.8	[159]
LVD	$C_{<9.6>}H_{<21.2>}$	∼15	0.800	2.21	7.4			187^{+24}_{-19}	[138]
	$C_{30}H_{62}$	20	0.890	2.07	7.8	7	160	167	[145]

Table 7: Measured capture time τ of fast neutrons in different materials and organic mixtures as used for large scale liquid scintillator experiments. The organic compounds C_9H_{12}, $C_{12}H_{26}$ and $C_{30}H_{62}$ stand for pseudocumene (PC), dodecane (DC) and paraffin wax (PW). The unit for the temperature T is [°C], for the density ρ $[g/cm^3]$, for the hydrogen density ν_H $[10^{22}/\mathrm{cm}^3]$ and for the capture time [μs]. In few cases, the time before thermalisation (τ_a) and after thermalisation until the neutron is captured (τ_b) is reported separately. The scintillators used in the experiments Borexino, KamLAND and the Large Volume Detector are noted by BX, KL and LVD.

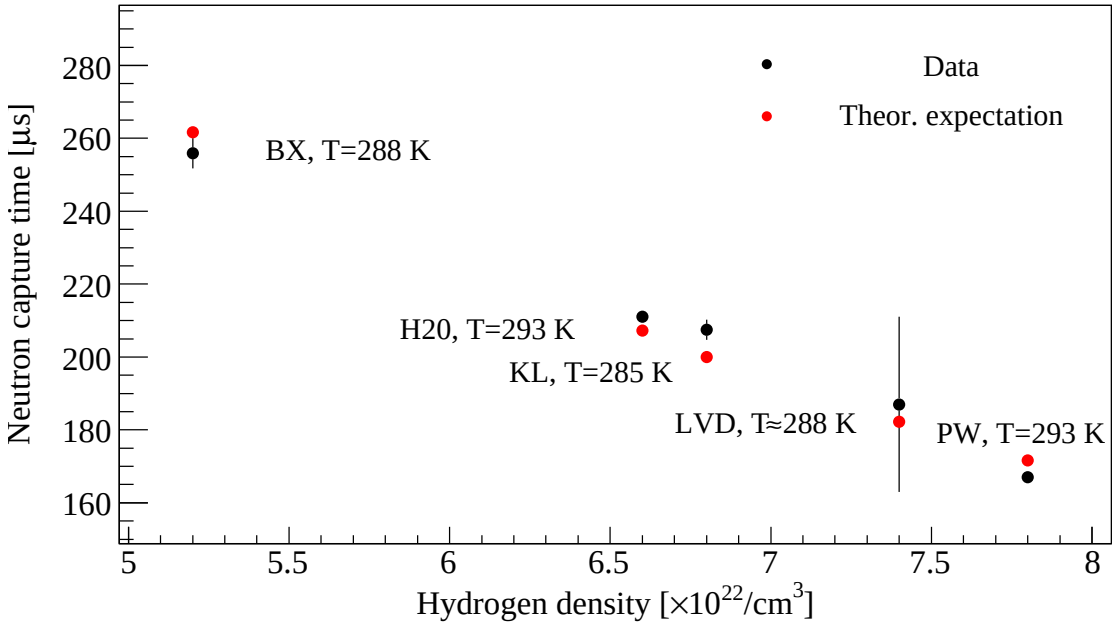

Figure 46: Dependence of the neutron capture time τ from the hydrogen density ν_H in different materials. Measured and theoretically predicted values are compared. For the expected values the temperatures reported in Table 7 were used. Abbreviations are taken from the caption of Table 7.

As pointed out in the introduction of Section 4.2.6, the capture time τ of neutrons in an organic medium depends on the hydrogen density and can be described by Equation (4.11). To test these statements, the value for τ in the Borexino scintillator, which was deduced in the present work and in other organic compounds reported in literature, was compared to the expected values. Table 7 summarizes the experimental results for the scintillators used in Borexino (BX), in KamLAND (KL) and in the Large Volume Detector (LVD) as well as for water and for paraffin wax. As shown in Figure 46, the experimental values for τ decrease almost linearly with increasing hydrogen density. Moreover, the experimental values are in good agreement with the expected values which were calculated according to Equation (4.11) and which took into account the temperature T of the materials.
Finally, Equation (4.11) is used to predict a possible difference $\delta\tau$ in the capture time τ of neutrons released and captured in the upper and lower hemisphere of the Borexino Inner Detector. A temperature gradient of $\sim$5°C has been established in order to prevent convection processes in the scintillator. By only taking this temperature difference and no density differences into account, one expects a value $\delta\tau\approx$3 μs. This corresponds to a $\sim$1% effect and is comparable to the total uncertainty budget of the high-precision measurements of τ presented in this thesis.

Expected production mechanisms of muon-induced neutrons In order to study the production mechanisms of muon-induced neutrons in Borexino, it is useful to recall the dominant neutron-generating processes predicted by simulations for the *Laboratori Nazionali del Gran Sasso* [140, 160]. Assuming that muons with a mean muon energy $\overline{E}_\mu \approx$310 MeV cross the scintillator, hadronic cascades are expected to contribute 75% to the observed neutron yield. The residual 25% originate from photonuclear disintegration processes [160]. The neutrons from these processes are generated in the following way:

1. Photonuclear disintegration: fast muons ("muon spallation") or muon-induced electromagnetic showers give rise to Bremsstrahlung of sufficiently high energy to produce *photo-neutrons* via (γ,n) reactions. These photo-nuclear disintegrations occurring at lower energies (0-50 MeV) exchange virtual/real photons with the nuclei. These interactions can lead to high frequency resonances in nuclei called *Giant Dipole Resonances* (GDR) [161, 162, 163, 164, 165]. At high nuclei-dependent excitation energies, the target nuclei act as strong absorbers of the incident photons mediated between the charged particles and the atoms in the scintillator. The γ-rays induce a highly collective nuclear excitation, in which the bulk of the protons moves in one direction, whereas the neutrons move in the opposite direction. After a given period, the nucleus stops oscillating under the release the excess energy; the nuclei either expel γ rays or evaporate nucleons. The measured photo-absorption cross section for ^{12}C, which is the chemical element of major interest for the present Borexino analysis, is depicted in Figure 93 in Appendix A.5. The resonance frequency of the absorption spectrum is reached at $E_{GDR} \approx$30 MeV. The energy spectrum of the emitted *photo-neutrons* registered in Borexino is expected to resemble that of the absorption spectrum in Figure 93, but shifted to lower energies due to the ^{12}C binding energy of E_B=7.68 MeV acting on each single nucleon.

2. Hadronic spallation: Meson-producing processes involving negative pions are an efficient source of neutrons, since most of them will slow down and stop in the surrounding matter. They are then captured into orbits of pionic atoms and produce neutron pairs by the quasi-deuteron absorption process $\pi^- + d' \rightarrow 2n$ on the central nucleus [166].
Neutrons emitted in photonuclear interactions or in hadronic showers can also collide with atomic nuclei. If the impact in such a nucleon-nucleon interaction is peripheral, several secondary neutrons can escape. If the impact is central, the nuclei are left in an excited state. If

the de-excitation energy is higher than the binding energy, one or more low energy neutrons can be evaporated.

The following study analyzes Borexino data trying to deduce information about the mechanisms that lead to the emission of neutrons in the scintillator.

Propagation distance and initial energy of muon-induced neutrons The present analysis aims at deducing the value of the initial energy of muon-induced neutrons. The same method that was used for the ^{241}Am^{9}Be source (see Section 4.2.7) should be applied, however, there are some difficulties. First, it is difficult to estimate the cumulative distribution of the travelling distances d of the muon-induced neutrons in the Borexino scintillator. In order to estimate d, the point of the neutron emission has to be known. In contrast to the ^{241}Am^{9}Be source, there is neither a known source position nor a prompt signal. Since the neutron emission point is equal to the cosmogenic radioisotope, the *threefold coincidence* (TFC) method can be applied. This method has already been introduced in Section 2.4 and will be discussed in full detail in Section 4.3.
The TFC method associates the barycenters of 2.22 MeV γ rays from neutron captures on hydrogen with the delayed decay signals of unstable muon-induced radioisotopes. The tagging of random coincidences cannot be excluded, but their total amount can be disentangled from the number of real coincidences. In the present study, the distance cut dr between two coincidence events was increased from 0.0 m to 2.0 m in 10 cm intervals. The time interval was kept constant at 120 min. This corresponds to four times the lifetime of ^{11}C (τ=29.42 min), which is the most long-lived cosmogenic radioisotope and the one with the highest production rate. Additionally, several prerequisites have to be fulfilled to avoid the introduction of a bias in the d distribution:

- The produced ^{11}C atoms must be correlated with the correct neutrons: in high neutron multiplicity events, several ^{11}C atoms might be produced. In case of such an ambiguity, the TFC method does not allow to associate the decay of the ith ^{11}C atom with the neutron that was ejected by the i-th ^{12}C atom. As a consequence, a random association would lead to an isotropic d distribution. To avoid this systematic effect, one can only consider muons that are followed by a single neutron ("single-neutron-cluster event").
- No convection on the time scale of two hours: convective drift of ^{11}C atoms in the scintillator within a time scale of several hours has to be much smaller than the distance between the neutron and the radioisotope of interest. This avoids a systematic bias in the d distribution. As a working hypothesis, one can assume that this condition is fulfilled (compare with Section 4.3.4).

The measured cumulative distribution of the travelling distances d of the single-cluster neutron events is depicted in Figure 47. The same figure also contains the curves for different neutron energies simulated according to the model in Section 4.2.6.
From the χ^2 map on the right panel in Figure 47 one deduces that the mean energy of the neutrons belonging to single-cluster neutron events is E$\approx$(22$\pm$3) MeV. This energy lies approximately in the expected re-emission energy region of the GDR in ^{12}C. This is a hint that at least single-cluster neutron events measured in Borexino are mainly produced by photonuclear disintegration processes. On the other hand, hadronic showers might induce the high-multiplicity neutron events observed in Borexino.

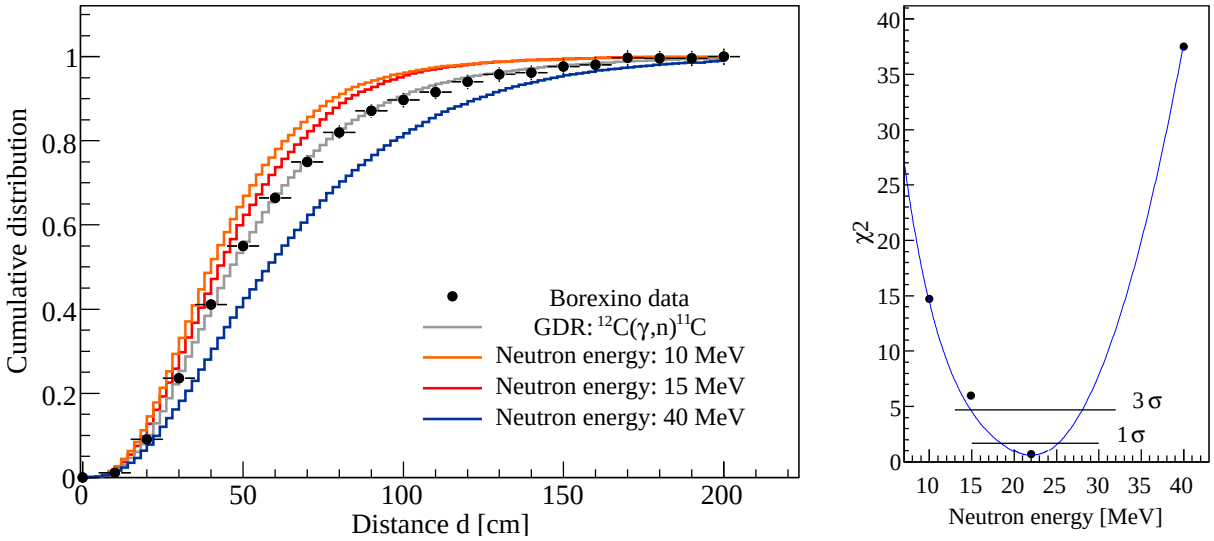

Figure 47: Data versus MC: muon-induced neutrons propagation in the Borexino scintillator. The data were obtained via the TFC method, using only single-neutron cluster events. The initial energy distribution $\Phi(E)$ used for the simulation of the neutron propagation distance d_n corresponds to Figure 93. There is a good agreement between data and MC, if one assumes that the *Giant Dipole Resonance* is responsible for the emission of neutrons from ^{12}C.

4.3 Cosmic-ray induced radioisotopes

In organic liquid scintillator (LS) detectors such as Borexino, high-energy cosmic-ray muons and subsequent showers mostly interact with ^{12}C atoms; giving rise to disintegration and spallation products. These processes do not only lead to the emission of neutrons but also to the generation of radioactive isotopes. These radioisotopes have different production rates, decay modes, lifetimes and Q-values. The most relevant muon-initiated radioisotopes in Borexino are the carbon isotopes $^{11}_{6}$C, $^{10}_{6}$C and $^{9}_{6}$C, the boron isotopes $^{11}_{5}$B and $^{8}_{5}$B, the beryllium isotopes $^{11}_{4}$Be and $^{7}_{4}$Be, the lithium isotopes $^{11}_{3}$Li and $^{9}_{3}$Li, and the helium isotopes $^{8}_{2}$He and $^{6}_{2}$He.
Depending on the production rate and the covered energy range, the decays of cosmic-ray induced radionuclides can mimic different types of neutrino signals. In order to uncover the neutrino signatures in the energy spectrum, different strategies have to be applied. In case of short lifetimes, the radioisotopes can be simply rejected by vetoing the entire detector over a time period of several lifetimes. For longer lifetimes, coincidence techniques like the *threefold coincidence* (TFC) method or pulse shape discrimination criteria have to be developed.
The most critical radionuclide for the *pep* and CNO neutrino analysis is the long-lived ^{11}C isotope. The ^{11}C rate is ∼10 times higher than the expected neutrino rate in the *pep* and CNO neutrino energy window [0.8,1.3] MeV. The identification and rejection of this radionuclide is the major objective of the present section.

Section 4.3.1 presents the expected production rates of isotopes in Borexino generated by muon-initiated spallation and disintegration processes. The following sections focus on the application of the TFC method to the identification and rejection of ^{11}C. The estimation of the ^{11}C rate in a data set of tagged ^{11}C candidates is discussed in Section 4.3.3. In Section 4.3.4, a pure data set of ^{11}C events is localized. Several analyses based on this data set are presented. The rejection strategies of ^{11}C are presented in Section 4.3.5. The optimal TFC cut selection is investigated. The possibility of including the muon track information is discussed. Subsequently, an *event-by-event* subtraction of the ^{11}C events tagged via the TFC method is applied, showing the efficiency of the technique (see Section 4.3.6). Finally, secondary background components are investigated which arive after the ^{11}C subtraction (see Section 4.3.7).

4.3.1 Production of radioisotopes through cosmic-ray muons and showers

Production yield In this paragraph, the production yields of the most important cosmic-ray induced radioisotopes in the Borexino scintillator are presented.
The expected production yield R^{i}_{BX} of the i^{th} cosmic-ray induced radioisotope in Borexino is determined via a direct comparison with KamLAND results in [159]. The KamLAND detector, which contains 1 kton of liquid scintillator, is located under the Ikenoyama, Japan, in a depth of 2700 meters of water equivalent. The muon flux at KamLAND's experimental site is $\Phi_{\mu,KL}$=(5.37±0.41) μ m^{-2}h^{-1} and the mean muon energy is $E_{\mu,KL}$=(260±8) GeV [159]. The adopted extrapolation of the KamLAND rates to the Borexino rates assumes a power-law dependence on the mean muon energy. This is defined by the following equation [172]:

$$R^{i}_{BX} = R^{i}_{KL} \cdot \left(\frac{E_{\mu,BX}}{E_{\mu,KL}}\right)^{0.73} \cdot \left(\frac{\Phi_{\mu,BX}}{\Phi_{\mu,KL}}\right) \tag{4.21}$$

The exponent 0.73 is a weighted mean value of slightly different exponents that are determined for each single radioisotope (see [173] and references herein). The muon flux $\Phi_{\mu,KL}$=(1.19±.0.01) μ

Isotope	Lifetime	Energy [MeV] & decay mode	KL measured rate [events/d/100ton]	BX expected rate [events/d/100ton]	
				full energy range	< 3 MeV
^{12}B	29.1 ms	13.4 (β^-)	5.48±0.15	1.38±0.06	0.157 ± 0.007
^{12}N	15.9 ms	17.3 (β^+)	0.22±0.05	0.06±0.01	0.002 ± 0.001
^{9}C	182.5 ms	16.5 (β^+)	0.38±0.15	0.10±0.04	0.003 ± 0.001
^{8}He	171.7 ms	10.7 ($\beta^-\gamma n$)	0.10±0.05	0.03±0.01	0.003 ± 0.001
^{9}Li	257.2 ms	13.6 ($\beta^-\gamma n$)	0.28±0.02	0.07±0.01	0.005 ± 0.001
^{8}Li	1.21 s	16.0 ($\beta^-\alpha$)	1.56±0.32	0.39±0.08	0.049 ± 0.010
^{8}B	1.11 s	18.0 ($\beta^+\alpha$)	1.07±0.29	0.27±0.07	0.017 ± 0.005
^{11}Be	19.9 s	11.5 (β^-)	0.14±0.03	0.04±0.01	0.003 ± 0.001
^{10}C	27.8 s	3.65 ($\beta^+\gamma$)	2.11±0.18	0.53±0.05	0.52 ± 0.05
^{11}C	29.4 min	1.98 (β^+)	110.6±17.8	27.82±4.58	27.82 ± 4.58

Table 8: Expected rates of radioisotopes in Borexino (BX) induced by cosmic-ray muons and showers. The rates are estimated using an extrapolation of the measured rates in KamLAND (KL) [159] following a power-law proposed in [172]. Except for ^{12}N the fraction of events lying below 3 MeV is taken from [15] for the different radioisotopes.

$m^{-2}h^{-1}$ assumed for the Borexino experimental site is taken from [118]. Furthermore, in Borexino one can assume a mean muon energy of $E_{\mu,KL}$=(310±10) GeV, which is interpolated from [174].

The measured rates in KamLAND and the extrapolated rates in Borexino are reported in Table 8. The expected rates in Borexino below 3 MeV are also listed, they show that the most relevant radionuclide in this energy region is ^{11}C.
The KamLAND collaboration measured the rates for all single nuclides with a data set collected over a period of ∼5.2 years. In contrast, Borexino has collected data over a period of ∼3.7 years so far. Moreover, Borexino has a larger overburden and a target mass that is three times smaller than KamLAND, resulting in a lower collected statistics. The Borexino collaboration has already published several results about the production yields induced by muons and their secondaries [15, 65, 68]. In rare cases, the lifetimes of the radioisotopes are similar and therefore only combined rates were determined. The highest rates were measured for ^{11}C and ^{10}C, namely (25±2(stat.)±2(syst.)) events/d/100ton [65] and (0.50±0.13) events/d/100 ton [15].

The isotope production yields in a Borexino-like liquid scintillator have been studied in an earlier experiment using the CERN Super Proton Synchrotron (SPS) muon beam [173]. The energy dependence of the production of the background nuclei was studied with 100 GeV and 190 GeV incident muons. Some production yields measured with Borexino and KamLAND are found to be inconsistent with extrapolations (based on the power-law in Equation (4.21)) of results from the muon beam experiment. For instance, the ^{11}C production yield deduced from the CERN experiment was underestimated by ∼42% if it is compared with the value measured in Borexino.
A reason for the underestimation of the production yields in the muon beam experiment might be related to hadronic showers which were only partially detected; the scintillator samples were small-sized such that escaping secondary particles did not have the possibility to create more radioactive nuclei.

Production mechanisms for ^{11}C and ^{10}C The most relevant radioisotope ^{11}C is generated by several mechanisms. The study reported in [80] identified eight different production channels. Besides the most common channel ^{12}C(γ,n)^{11}C there are five other reactions ending with a neutron

in the final state. However, two of them, ^{12}C(p,d)^{11}C and ^{12}C(π^+,π^0n)^{11}C, do not emit a free neutron and thus the ^{11}C events cannot be tagged with a technique such as the *threefold coincidence* (TFC) method. These so-called "invisible channels" represent an intrinsic inefficiency and account for ∼4.5% of the total ^{11}C production rate [80, 81].
^{10}C is mainly produced via ^{12}C(γ,2n)^{10}C and ^{12}C(n,3n)^{10}C. Since these production channels have at least two neutrons in the final state, the TFC method can be applied with an even higher efficiency than in the case of ^{11}C.

4.3.2 The threefold coincidence method and classification of ^{11}C coincidences

The basic idea of the *threefold coincidence* (TFC) method has already been introduced in Section 2.4.
After each muon-induced neutron detection, the TFC technique defines a set of potential ^{11}C candidates within a time interval *dt* following the detected neutron/muon event and inside a sphere of radius *dr* around the neutron capture point. The ^{11}C candidates are typically located within a given *fiducial volume*, whereas the position of neutron events can be reconstructed outside this volume. In some analyses, the ^{11}C candidates are associated only with neutron event of a given multiplicity M_n. Hence, ^{11}C analyses based on the TFC method usually modulate the parameters *dt*, *dr*, M_n and the size of the *fiducial volume*.

Classification of coincidences tagged via the TFC method Each coincidence tagged via the TFC method consists of three associated events: (1) the ^{11}C candidate, (2) the neutron candidate and (3) the muon candidate. The ^{11}C candidate is either a real ^{11}C decay or an accidental background event which fulfills the ^{11}C selection criteria. The neutron candidate is either a real γ ray emitted from a neutron capture on a hydrogen or carbon nucleus (see Section 4.2.7) or an accidental event (e.g. a ^{14}C decay). The real neutron is either correctly associated with the related ^{11}C decay or wrongly associated with a non-related ^{11}C decay or with an accidental background signal. The muon candidate is mostly a real muon event (muon or muon shower), but sometimes also a background event. Neutrons are always correctly associated with the parent muon event. As a consequence, if a decayed ^{11}C nucleus is correlated wrongly with a non-related neutron, the ^{11}C atom is automatically correlated with a non-related muon event.

Besides the random character of the TFC method, the reconstructed physical parameters of the associated events might not be reliable. For instance, the reconstructed positions of the ^{11}C and neutron candidates, but also the muon track might be reconstructed wrongly or with a large uncertainty. These circumstances lead to a large number of coincidence types. Figure 48 gives an overview over all possibilities. The quality of the coincidences increases towards the lower left side of the depicted trees. Different analyses require data sets of ^{11}C coincidences of different quality. Three important examples are listed here:

1. Propagation of muon-induced neutrons in the scintillator: The analysis includes the estimation of (i) the distance of neutrons from their point of emission[17], (ii) the lateral distribution of the neutrons from the tracks of their parent muons and (iii) the directionality of the neutrons compared to the muon tracks. These studies require a data set of high quality coincidences, in which real neutrons are associated with the related ^{11}C decays. High multiplicity neutron events must be avoided, since the neutrons might not be associated with the correct decaying ^{11}C atom. This has already been applied in Section 4.2.8.

[17] The neutron emission point is assumed to be equal to the position of the decaying ^{11}C radioisotope.

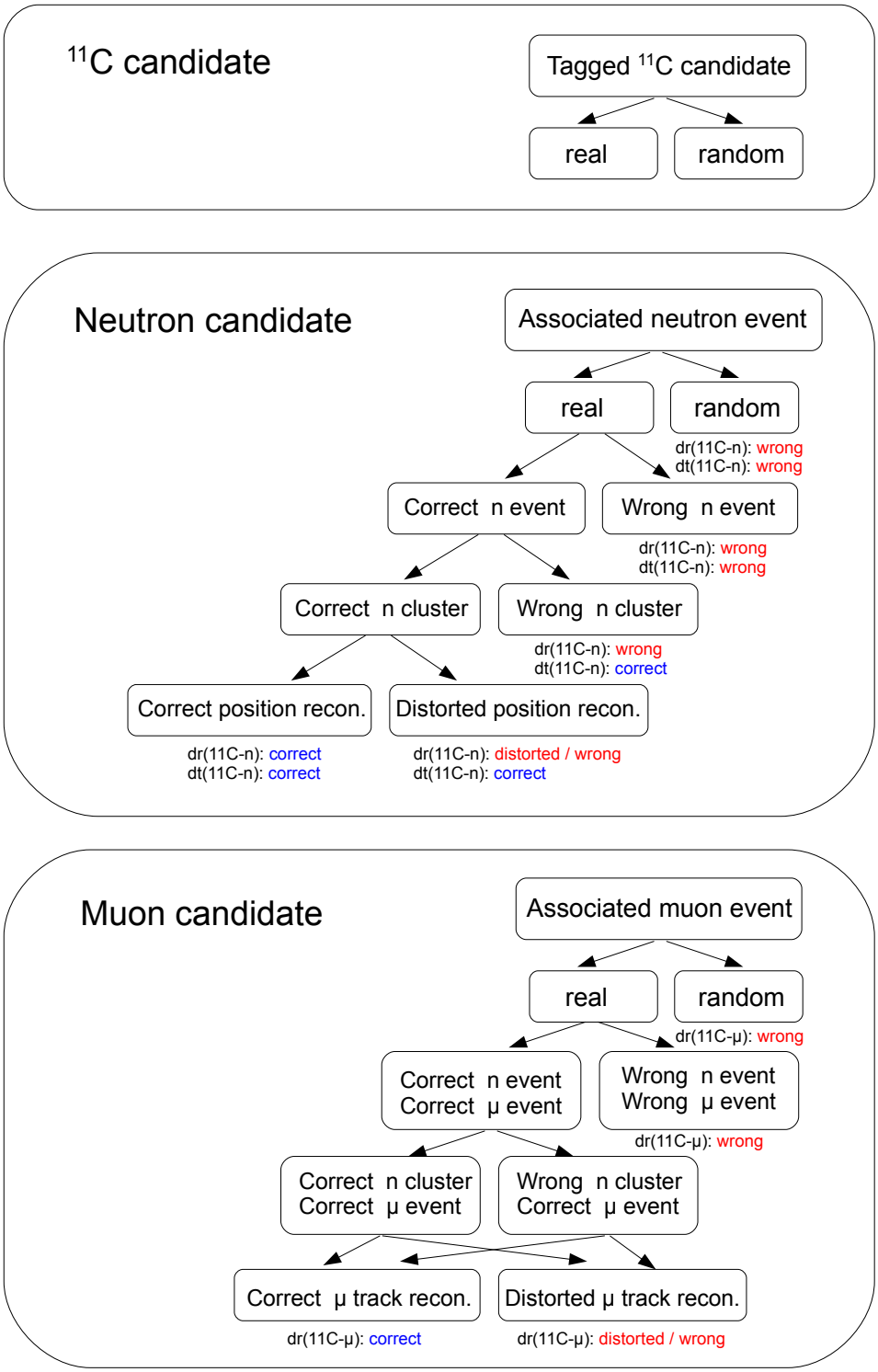

Figure 48: Classification of the ^{11}C candidates tagged with the TFC method. Each event class contributing to the triple coincidences of the primary muons, the spallation neutrons and the β^+ decays of ^{11}C can contain accidental background events. In addition, some reconstructed physical parameters of the events might be not reliable. Consequently, the calculated distance dr, the time interval dt and other related quantities between two associated events might be either wrong or degraded.

2. Estimation of the fraction of real ^{11}C decays in a data set of tagged ^{11}C candidates: The amount of real ^{11}C events is disentangled from random coincidences by looking at the time profile distribution. In this case, it is important that the ^{11}C events are correlated with the correct neutron events to account for the correct time interval. The algorithm is presented in the following Section 4.3.3.

3. Rejection of ^{11}C: The *pep* and CNO neutrino analysis focuses on the maximum possible rejection of ^{11}C. The TFC cuts are optimized to increase the tagging efficiency of real ^{11}C decay with a moderate loss of the "time×mass" fraction. It is not essential if the real ^{11}C decay is associated with a non-related neutron. Only if the TFC method is combined with the muon track information, the related neutron has to be selected correctly, and the neutron position and the muon track have to be reconstructed reliably (see Section 4.1.4).

4.3.3 Procedure for the rate estimation of ^{11}C decays via the TFC method

A fundamental problem in several ^{11}C analyses is related to the precise measurement of the number of ^{11}C decays which are successfully tagged in a given data set via the TFC method.

In principle, the number of ^{11}C decays tagged in a data set can be deduced from the time profile distribution of the measured time intervals δt between the ^{11}C candidates and their associated neutron candidates. One expects that the time profile distribution follows the behavior $\Theta(t) = A\, e^{-t/\tau}/\tau + B$. The first component describes the exponential decay of the ^{11}C atoms, whereas the second component consists of accidental background events and real ^{11}C decays that were wrongly associated with non-related neutron events.
The TFC based algorithm which searches for the time intervals δt has to fulfill one condition: the time interval between each real ^{11}C decay and its related neutron event has to be tagged and counted exactly one time. If a related neutron event has more than one neutron cluster, the time interval δt is counted only one time. A wrong association of real ^{11}C decays with non-related neutron events is allowed. These coincidences only contribute to the accidental background component. A scheme of the search algorithm is shown in Figure 49.
Apart from the correct definition of a search algorithm, one also has to take into account the finite run duration. In Borexino, a run terminates automatically after six hours. After few seconds a new run is started. The 6 hours runs contain several GByte of data which are still manageable in terms of processing time. However, DAQ failures and operations on the electronics and on the detector have notably reduced the duty cycle; in the period between January 2008 and August 2010 the lifetime was estimated to be ∼76% excluding the calibration campaigns (see Section 3.4.2). Muon-induced neutron events might occur during run interruptions, whereas generated ^{11}C atoms might decay at the beginning of the subsequent run. Hence, the TFC method will be less effective at the beginning of a run, especially after longer run interruptions and for coincidences with longer time intervals δt between the neutron and the ^{11}C candidates. As a consequence, both components of the time profile distribution $\Theta(t)$ will be distorted.
In order to consider the effect of the finite run duration, the deformation of the originally constant background component $\vartheta(t) = B$ was investigated. One can assume that all runs have a constant duration length L and all run interruptions the length q. Then, the time profile distribution of the background component can be expressed via:

$$\widetilde{\vartheta}(t) = \begin{cases} N\ (1 - t/L) & \text{for } t < q\ , \\ N\ (1 - q/L) & \text{for } t \geq q \end{cases} \tag{4.22}$$

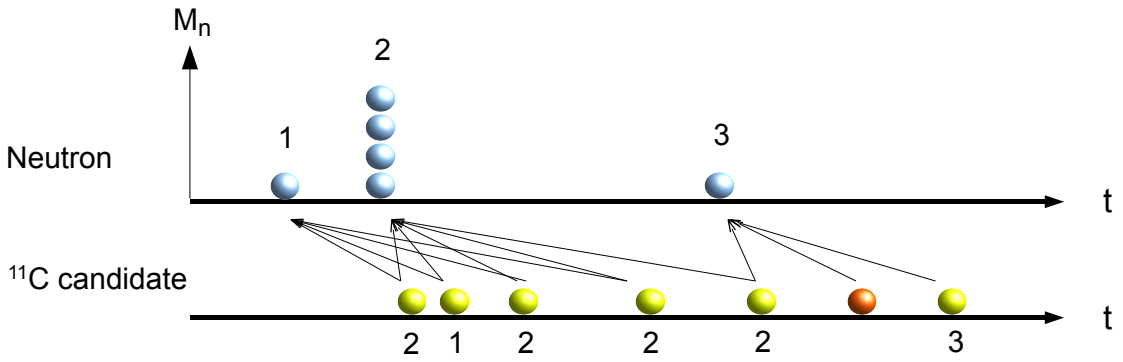

Figure 49: Determination of the time intervals between neutron clusters and ^{11}C candidates required for a correct calculation of the time profile distribution. A TFC event is associated with a maximum number of neutron clusters, but no more than one time with each neutron event. The numbers denote the correct association of real ^{11}C decays (yellow) with the parent neutron events. ^{11}C candidates that are accidental background events are depicted in orange. The multiplicity of a neutron event is denoted by M_n.

The variable N corresponds to a scaling factor. The entire step function $\widetilde{\vartheta}(t)$ is shown in Figure 50, where C is equal to $N(q/L)$ and B equal to $N(1-q/L)$. In reality, L and q are not constant and the discontinuity at $t = q$ is smeared out. Thus, one can approximate $\widetilde{\vartheta}(t)$ via

$$\widetilde{\vartheta}(t) = B\left(1 + \alpha e^{-t/\lambda}\right) \tag{4.23}$$

The constant α corresponds to the constant ratio C/B (see Figure 50). To validate the approximation, a data set was defined that only includes accidental coincidences. This was achieved by applying the TFC method to a class of events with energies outside the ^{11}C energy region. Normally, a sample of ^{210}Po decays or muons is used and associated with the muon-induced neutrons. In the present analysis, a sample of ^{210}Po decays was used. The time profile of α particles from the ^{210}Po decays which were associated with muon-induced neutrons is shown in Figure 51. The exponential function matches the behavior of the background time profile.

The effect of the finite run duration is equal for the background and the exponential time profile components. Thus, the $\Theta(t)$ function turns into:

$$\widetilde{\Theta}(t) = \left(1 + \alpha e^{-t/\lambda}\right)\left(A\,\frac{e^{-t/\tau}}{\tau} + B\right) \tag{4.24}$$

Finally, the introduced procedure is exemplarily applied to given data. The selected TFC cuts are dr<2.0 m and dt<600 min. Following the above mentioned search algorithm, the TFC method is first applied to a class of events lying outside the ^{11}C energy region. This allows to estimate the parameters α and λ which are characteristic for a given data set (Figure 51) and a given *fiducial volume*. Then, the TFC method is applied to the class of events covering the ^{11}C energy region. The obtained time profile distribution is shown in Figure 52. The fit function $\widetilde{\Theta}(t)$ leads to a ^{11}C

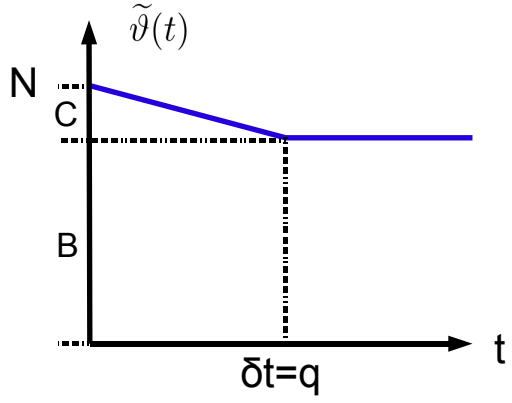

Figure 50: Modelling of the quasi-flat background component in the time profile distribution.

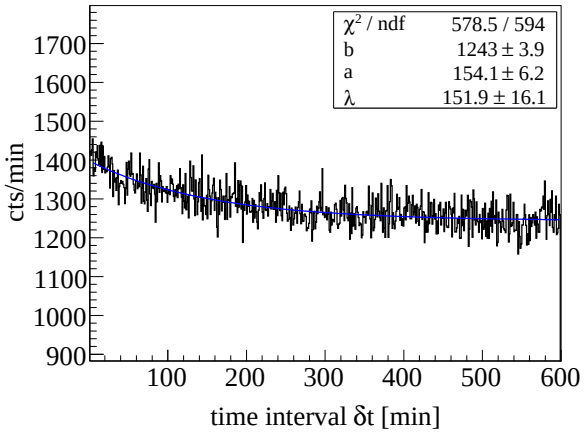

Figure 51: Application of the TFC method to a data set containing only accidental events.

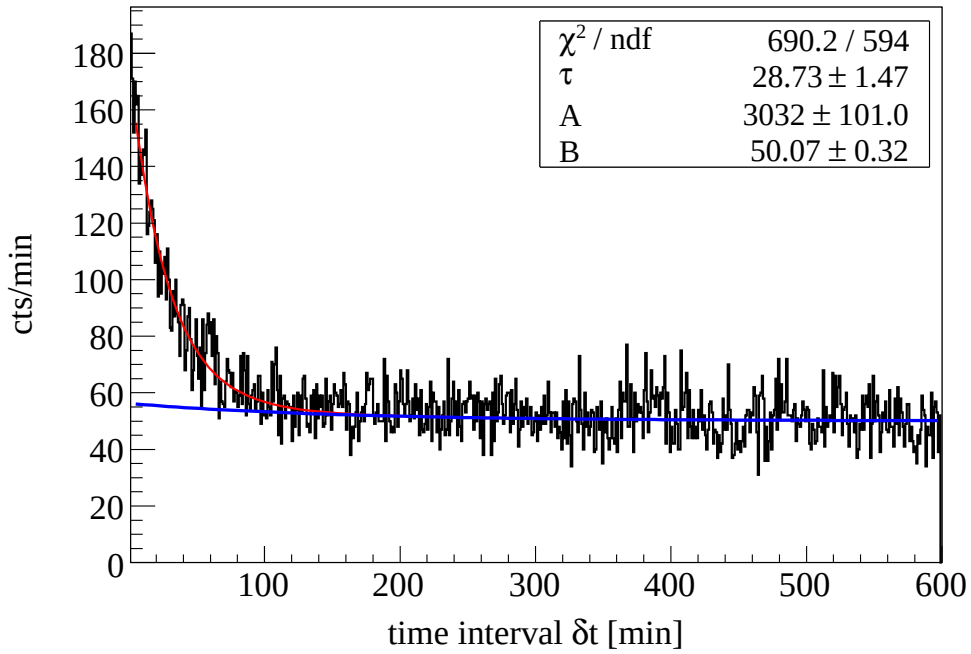

Figure 52: Time profile distribution of ^{11}C candidates tagged via the TFC method. The used TFC distance cut is dr<2.0 m. The selected ^{11}C candidates have energies in the range [0.8,2.0] MeV and are contained within a spherical *fiducial volume* with radius R<3.0 m.

lifetime equal to τ=(28.7±1.5) min. The measured value is in good agreement with the literature value τ_L=29.42 min [175]. This confirms the reliability of the introduced procedure.

4.3.4 Determination and analysis of pure ^{11}C data sets

General considerations In the present section, a data set containing a high percentage of ^{11}C decay events is determined. Such a data set has a wide range of applications, as described in the following:

- Analysis of the *pep* and CNO neutrinos: On the one hand, the spectral shape of the selected ^{11}C events can be used for a statistical subtraction of ^{11}C. This allows to study potential secondary background components that are hidden below the ^{11}C spectrum. On the other hand, the obtained ^{11}C spectrum can be directly used as a fit component in the global spectral fit analysis.

- Study of the energy response in Borexino: The ^{11}C energy spectrum is well-suited to study the scintillation light properties and the energy response of the detector. The gamma quenching and the light yield can be deduced by fitting the energy spectrum with the theoretical β spectrum of ^{11}C convoluted with a Gaussian function describing the detector response. Furthermore, the measured energy spectrum of ^{11}C represents an isotropically distributed calibration source with an energy range between 0.8-2.0 MeV. Besides point-like sources (see Section 3.4.1), the ^{11}C data set is ideal for testing the Borexino Monte Carlo simulation package *bxmc*. This allows a fine-tuning of the implemented parameters and processes.

- Pulse shape analysis: The ^{11}C events are ideal candidates for studying the pulse shape of β^+-like events. The ^{11}C sample determined in this thesis has been widely used by other Borexino collaborators.
  Firstly, the Gatti parameter of the ^{11}C events was studied for the geo-antineutrino analysis (see Section 2.3). In Borexino, geo-antineutrinos are detected via the interaction $\nu_e + p \rightarrow e^+ + n$ by looking at the neutron-positron coincidence.
  Secondly, Borexino collaborators have recently started to study a new pulse shape discrimination criterion to distinguish positrons from other event types. Before a positron annihilates in matter, the positron and the electron can form a bound system that is analogous to a hydrogen atom. This pure leptonic atomic system is called positronium [176]. In the ground state, it has two possible configurations. In the case of parapositronium, which is the singlet state with a total spin equal to zero, the lifetime in vacuum τ_V is ∼125 ps. It decays under emission of two γ rays. Orthopositronium, which is the triplet state with a total spin of electron and positron equal to 1, has a lifetime of τ_V=(142.05±0.02) ns [177]. It decays under emission of three γ quanta. Other decay modes are negligible [178, 179]. The lifetimes τ_M are strongly reduced in matter. In the case of liquid scintillators as used for neutrino experiments, orthopositronium still has a lifetime of several ns [180]. This can induce a significant distortion of the pulse shape which can be used for tagging positrons on an event-by-event basis. The feasibility of this technique has been already demonstrated in simulations and laboratory tests [180].

- Relation between ^{11}C and the parent muons: In the ideal case, the ^{11}C isotopes rest along the muon track where they were generated until they decay. In this case, a position of a ^{11}C decay reconstructed next to the muon track is attributable to the resolution of the position reconstruction or/and to the uncertainty in the muon track reconstruction. However, convection and diffusion could also play a role. Due to the long lifetime of ^{11}C, convection and diffusion

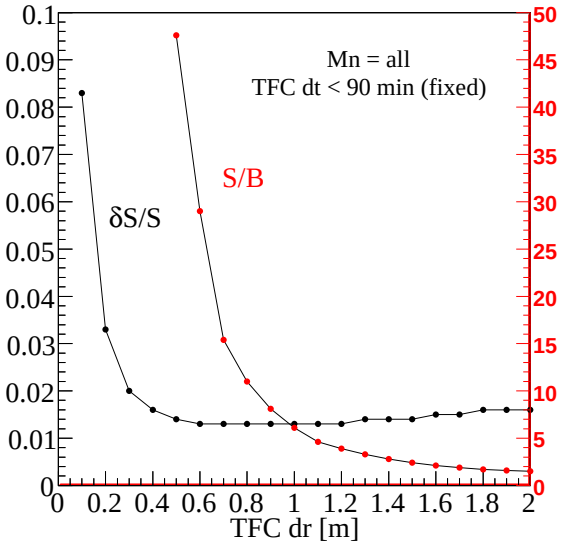

Figure 53: S/B ratio and collected statistics (δS/S) of ^{11}C events in a data set with a lifetime of 281 d. All neutron events (M_n >1) are used for the tagging of ^{11}C coincidences.

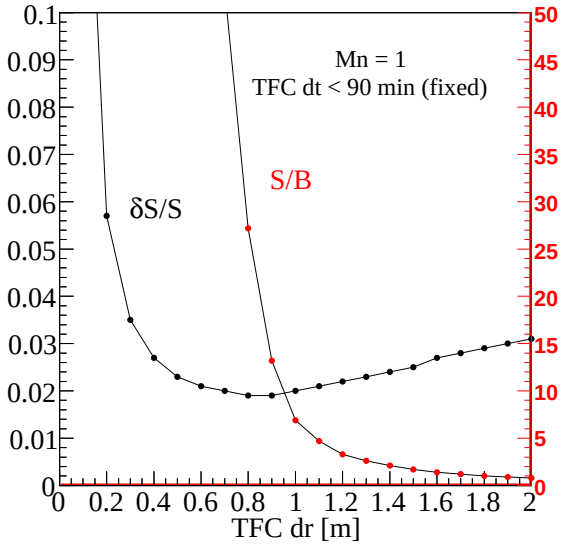

Figure 54: S/B ratio and collected statistics of ^{11}C events in a data set with a lifetime of 281 d. Only single-cluster neutron events are used for the tagging of ^{11}C coincidences.

processes might be able to transport ^{11}C nuclei within the scintillator before their decay. A vertical temperature gradient of ~4°C within the organic liquids in the Inner Detector of Borexino was ideally selected in order to suppress convection. In [159], KamLAND reported a contamination of the detector with ^{222}Rn during a calibration campaign. The measured diffusion velocity around the source device is approximately 1 mm/h. As working hypothesis one can assume a similar diffusion speed of the ^{11}C atoms in the Borexino scintillator. Thus, the effect should be negligible.

Determination of a pure ^{11}C data set The TFC method is used for the determination of a ^{11}C data set with a minimized number of background events. In this context, all events that do not correspond to real ^{11}C decays are regarded as background signals. The numbers of tagged ^{11}C decays and of background events are denoted by S and B, respectively, and their ratio is $R = S/B$. The values of S and B are calculated from the time profile according to the procedure described in Section 4.3.3.

The TFC cuts are modulated in order to obtain a data set of ^{11}C candidates with the maximum value for R and S. However, R and S are anti-correlated and the areas of application have different requirements to the minimal acceptable value for R and S. Thus, also the definition of *figures of merit* will not be uniform.

One important application of the pure ^{11}C data set is the determination of the shape of the ^{11}C energy spectrum. In this case, two criteria should be fulfilled: First, the statistical error δS of S should be minimal, i.e. S as well R should be high. For the calculation of $\delta S/S$, the ^{11}C signal S is expressed via $S = T - B$, where T is the total number of events. By applying the Gaussian error propagation and by using the Poissonian uncertainties of T and B, one obtains:

$$\frac{\delta S}{S} = \frac{\sqrt{T+B}}{S} = \sqrt{\frac{S+2B}{S^2}} = \frac{1}{\sqrt{S}}\sqrt{1+\frac{2}{R}} \tag{4.25}$$

Secondly, the collected statistics in the single bin should contain a low number B of accidentally tagged background events[18]. Since the energy of these events is not known, they would distort the ^{11}C spectrum.

The estimation of a pure ^{11}C data set was performed in *Echidna cycle 9* (see Section 3.2.1) using a data sample of 281 d of lifetime. The time cut parameter of the TFC method was scanned in the range of (0,30) min and (0,120) min. The TFC space cut parameter was scanned in (0,200) cm. In addition, the ^{11}C candidates were associated with (i) only single-cluster neutron events (M_n=1) and with (ii) single- and multiple-cluster neutron events (M_n>0).
The best estimate could be found for a TFC time cut between ∼(60-90) min. The case in which the TFC time cut was set to dt<90 min is briefly discussed. If all neutrons are included (M_n >0) (Figure 53), the ideal TFC distance cut for the above data set of 281 d is dr<50 cm: the ratio R is ∼50 and the collected statistics is S ∼12 events/d/100ton. If only single-cluster neutron events are used for tagging the ^{11}C candidates, the ratio R∼50 is already achieved for dr<70 cm. In this case, the rate is S ∼5 events/d/100ton. This is depicted in Figure 54.

Analysis of the energy spectrum of a pure ^{11}C data set In the present study a fit of the energy spectrum of a pure ^{11}C data set is performed using the convolution $\Phi(E)$ of two analytical functions:

$$\Phi(E) = \int_{-\infty}^{\infty} \frac{dN}{dE}(E) \cdot \Psi(M,E) dE \tag{4.26}$$

The first function $dN/dE\,(E)$ describes the number dN of deposited events in a given energy dE interval corresponding to the β^- spectrum which is defined via [181]:

$$\frac{dN}{dE}(T,Z) = K\,(2m_eT + T^2)^{1/2} \cdot (T + m_e) \cdot (T_0 - T)^2 \cdot C(T) \cdot F(T,Z) \tag{4.27}$$

Herein, m_e is the electron mass, T the kinetic energy of the electron, T_0 the Q-value, Z the effective atomic number and K a norm factor. $F(T,Z)$ is the non-relativistic Fermi function which takes into account the electromagnetic interaction between the β^- particle and the nucleus. $C(T)$ is the spectral shape factor which takes into account secondary effects due to induced weak currents. A comprehensive description of all these terms is given in [14].

The second function $\Psi(M,E)$ takes into account the detector response. It includes the detector resolution which is assumed to be Gaussian. Moreover, the number M of photoelectrons (unit: npe) can be converted into MeV units if one divides M by the light yield (LY). Thus, $\Psi(M,E)$ is expressed via:

$$\Psi(M,E) = \frac{e^{\frac{(E-M/LY)^2}{2\sigma^2}}}{\sqrt{2\pi\sigma}} \tag{4.28}$$

The resolution σ is defined as $\sigma = \sqrt{E/LY}$.
Equation (4.27) describes a β^- spectrum, whereas ^{11}C is a β^+ emitter. The annihilation of the

[18] In Borexino analyses, a binsize of 10 p.e. (≈20 keV) or 10 nhits (≈30 keV) is typically used.

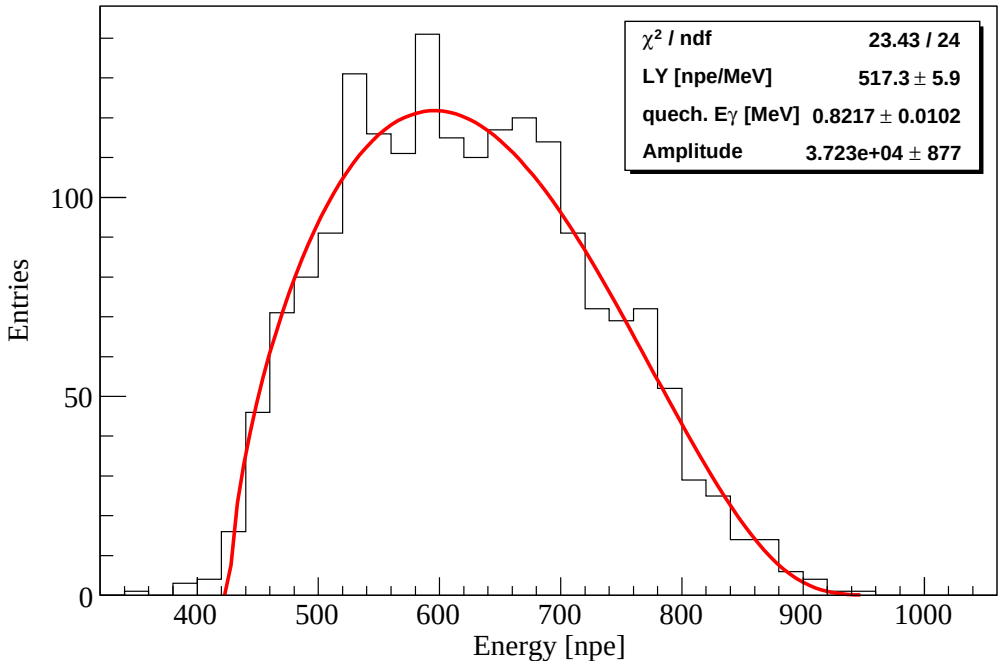

Figure 55: Measured energy spectrum of the muon-induced radioisotope ^{11}C in Borexino. The shown spectrum contains only ∼3% of accidental background events. All ^{11}C events are reconstructed within a *fiducial volume* with a radial cut R<3.067 m and a cut along the z axis, $|z|$ <1.67 m. The fit function $\Phi(E)$ corresponds to the red curve.

positron with an electron into two γ rays of energy E_γ=511 keV leads to a shift of the entire β^- spectrum. The shift is defined by $E \rightarrow E - 2\,q(E_\gamma)$. Herein, $q(E_\gamma)$ is the quenched energy of a 511 keV γ ray in the Borexino scintillator.

The analysis was performed in *Echidna cycle 11*. The analysis is based on different data sets which were selected according to two criteria. The first criterion is related to the percentage of real ^{11}C decays contained in the data set. The second criterion concerns the shape of the *fiducial volume*: two spherical and two non-spherical volumes have been selected. The *fiducial volume* with a radial cut R<3.067 m and a z-cut $|z|$ <1.67 m is typically used for the ^{7}Be neutrino analysis (see Section 3.1.2). The one with a radial cut R<2.8 m and a z-cut -2.4 m< z <2.2 m has been recently proposed for the *pep* neutrino analysis.
The obtained spectra were fitted with the $\Phi(E)$ function based on an implementation by D. Franco. The spectrum containing events in a *fiducial volume* of radius R<3.067 m and z-cut $|z|$ <1.67 m is exemplarily shown in Figure 55. The fit results are summarized in Table 9. The fit parameter values for the light yield LY and for the quenched energy q(E_γ) that were obtained from different data sets agree within their uncertainties. For the selected *fiducial volume*, a radial dependent energy response of the detector is not yet visible. The best fit parameters are obtained for the data set that is used for the ^{7}Be neutrino analysis and contains ∼97% of ^{11}C decays. The light yield is LY=(517±6) npe/MeV and the quenching energy of two 511 keV γ rays is q=(0.822±0.011) (χ^2/ndf = 23.4/24).
Table 33 in Appendix A.4 contains the bin entries of the ^{11}C energy spectrum for the following energy variables: the normalized charge variable (unit: npe) and the normalized number of hits (unit: nhits). The used data set contains ∼97% of ^{11}C decays. The ^{11}C decays are contained within the *fiducial volumes* used/proposed for the ^{7}Be/*pep* neutrino analysis.

^{11}C content in data set	*fiducial volume* radial cut [m]	z-cut [m]	light yield [npe/MeV]	quenched E_γ [MeV]	χ^2/ndf
∼97%	R<3.0	–	514±5	0.826±0.009	18/24
”	R<2.5	–	512±6	0.832±0.011	19/24
”	R<3.067	z< |1.67|	517±6	0.822±0.011	23.4/24
”	R<2.8	-2.4<z<2.2	515±6	0.824±0.010	20/24
∼95%	R<3.0	–	512±3	0.829±0.006	38/24
”	R<2.5	–	509±4	0.836±0.007	34/24
”	R<3.067	z< |1.67|	517±4	0.822±0.006	39/24
”	R<2.8	-2.4<z<2.2	513±4	0.828±0.006	32/24

Table 9: Light properties of the Borexino scintillator. The combined quenched energy of two 511 keV γ rays and the light yield are determined from the spectral fit of data sets containing a high percentage of real ^{11}C decays. Different ^{11}C purity levels and *fiducial volumes* have been selected.

Comparison of the ^{11}C energy spectrum obtained from data and MC The Borexino collaboration pursues the goal of a full reproduction of the acquired data using the Borexino Monte Carlo simulation package *bxmc* (see Section 3.2.2). This would proof that the detector response, including the related systematic effects, is completely understood. The MC code requires the knowledge of the detector energy response to different types of particles. The main parameters are the light yield (LY) and the Birks parameter (k_B) (see Section 3.1.2). The values for these two parameters are determined via the comparison of simulated spectra with measured calibration data. Typically, calibration data from point-like sources deployed into the scintillator have been used for the tuning of the two parameters (see Section 3.4.1). In the present work, the ^{11}C data sample of high purity is used for the estimation of the ideal (k_B,LY) parameter set. In contrast to point-like sources, ^{11}C events are isotropically distributed.
The simulations of ^{11}C events were performed in *Echidna cycle 11*. A parameter scan covering the range [10500;12500] γ/MeV for the light yield and the range [0.011;0.021] cm/MeV for the Birks parameter was carried out.
The comparison of the measured and simulated histograms was performed via a Pearson χ^2 statistic test. Starting from the same number of bins, denoted by r, the formula used looks like a $\chi^2_{(r-1)}$ distribution [182]:

$$\chi^2 = \sum_{i=1}^{r} \frac{(n_i - N \cdot p_i)^2}{N \cdot p_i} + \sum_{i=1}^{r} \frac{(m_i - M \cdot p_i)^2}{M \cdot p_i} = \frac{1}{M \cdot N} \sum_{i=1}^{r} \frac{(M \cdot n_i - N \cdot m_i)^2}{n_i + m_i} \tag{4.29}$$

where n_i and m_i are the number of events in the ith bin of the first and the second histogram; N and M represent the total numbers of events in the first and second histogram, respectively. The probability p_i that a random event belongs to the ith bin is not known *a priori*. Since it was assumed that the hypothesis of homogeneity is valid for all i = 1,...,r, the following expression was used for the maximum likelihood estimator:

$$p_i = \frac{n_i + m_i}{N + M} \tag{4.30}$$

For the uncertainties of the number of entries in each bin, only the statistical error was taken into account.
The χ^2 values of the comparison tests between the measured energy spectrum and 40 spectra,

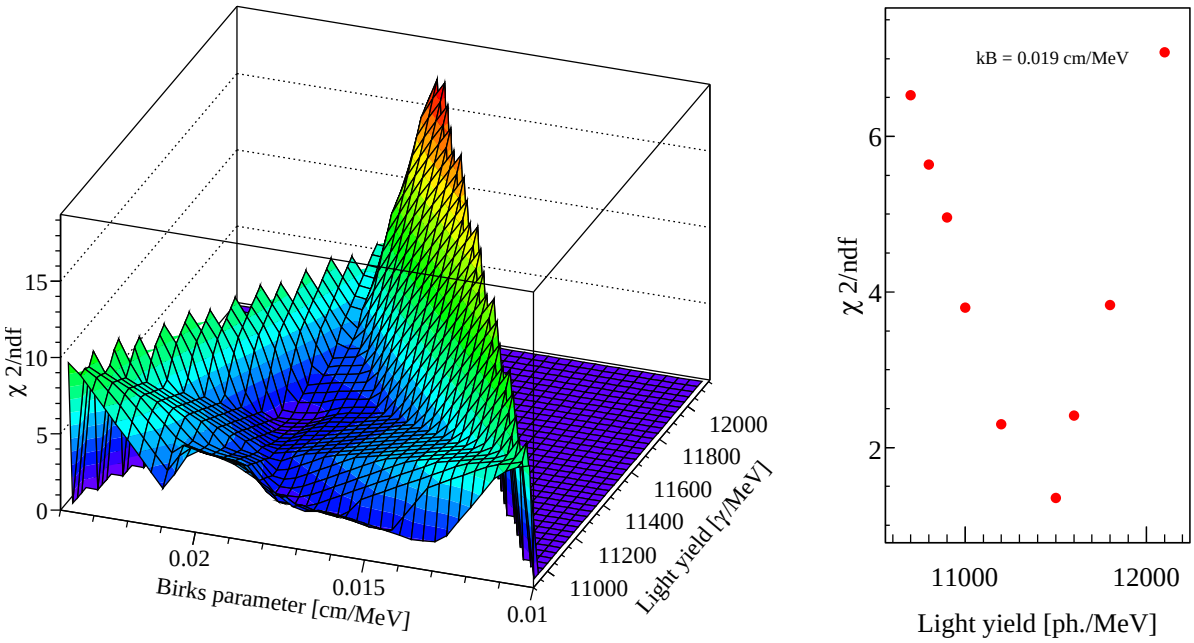

Figure 56: Comparison of the measured ^{11}C energy spectrum with MC simulated spectra, in which both the light yield (LY) and the Birks parameter (k_B) were modulated (left). The right plot is a cross section in which k_B was kept constant at 0.019 cm/MeV and which shows one of the two localized minima.

which were simulated with different (k_B,LY) values, are shown in Figure 56. The χ^2 map contains two local minima, one at (0.020 cm/MeV, 11500 γ/MeV), (χ^2/ndf = 41/37) and a second one in (0.013 cm/MeV, 10900 γ/MeV), (χ^2/ndf = 58/35).

The comparison technique of the simulated and of measured ^{11}C energy spectrum has led to a degenerate result. Besides the two identified minima, further minima might lie outside the region scanned in the present analysis. The real minimum can be estimated, if one of the two parameters k_B and LY can be fixed via an independent measurement. Low-energy γ sources and mono-energetic electrons with energies between few tens and few hundreds of keV would be ideal probes, since the quenching effect is especially sensitive in this region. Even if precise measurements are carried out, MC codes might still lead to different k_b values. This depends on the elaborateness of the implemented physics models and the reference data bases used.

4.3.5 ^{11}C rejection techniques and optimization strategies

Rejection strategies Even though the *threefold coincidence* (TFC) method plays a central role in the removal of ^{11}C decays, several other techniques can be combined with the TFC method to increase the total ^{11}C rejection efficiency. In this work, an extensive chain of filters has been developed, using the package *bxfilter* within the framework *Echidna* (see Section 3.2.1) in order to implement these methods.
Most of the methods implemented in the custom-made filters have been optimized. Auxiliary studies were carried out to investigate the efficiency of the TFC method in different situations. In cases in which the TFC method was found to have a reduced ^{11}C tagging efficiency, alternative techniques were applied.
Furthermore, the filters were optimally arranged. Since the filter in which the TFC method is

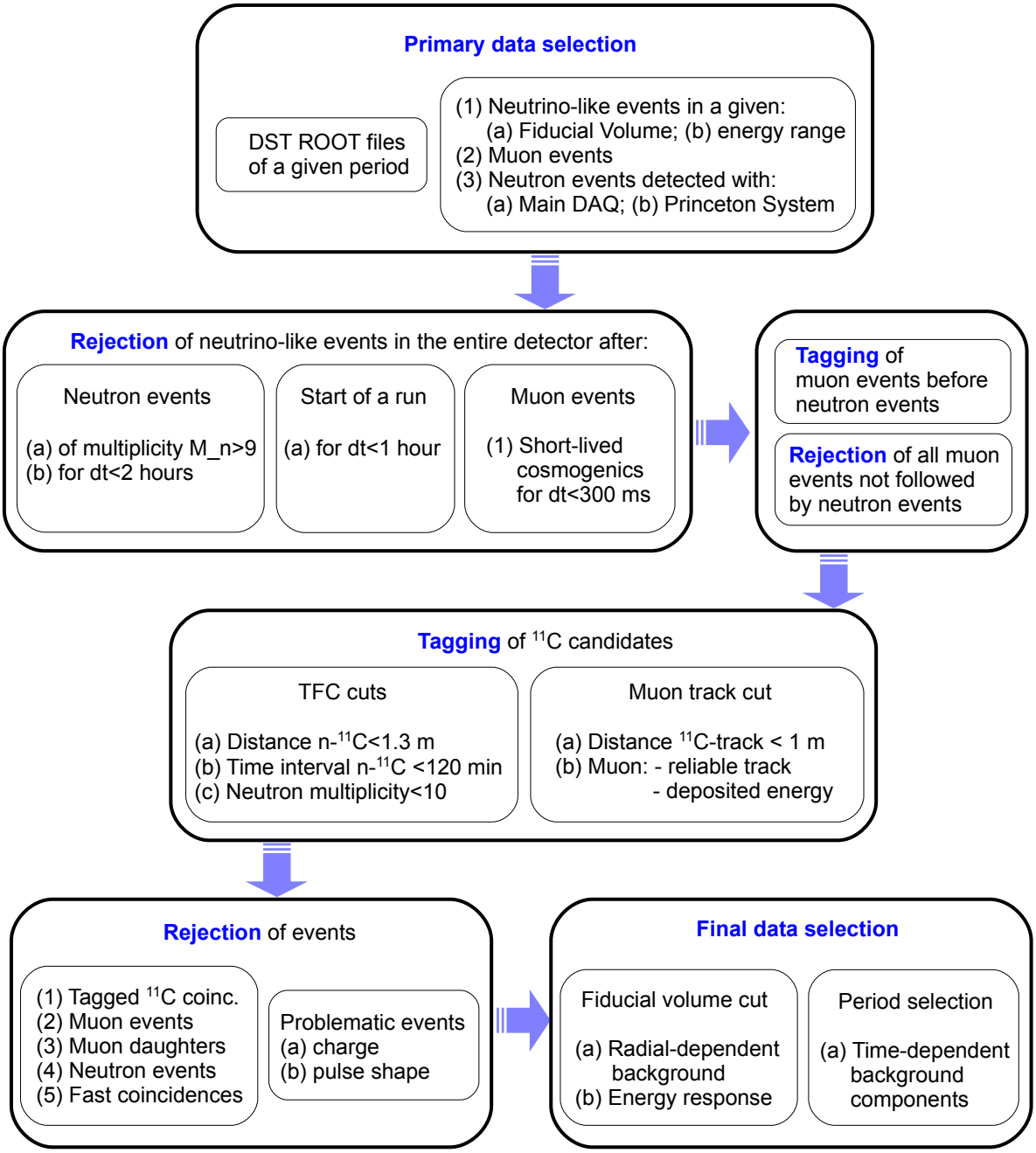

Figure 57: ^{11}C rejection strategy for the *pep* and CNO neutrino analysis. Four stages are designated (from top to bottom): (1) data selection, (2) veto of entire detector and rejection of not needed events, (3) ^{11}C tagging and (4) rejection of tagged ^{11}C events, residual muon events, muon daughters, neutron events, fast coincidences and finally optimization of the data set selection.

embedded requires a long processing time[19], not needed information in data is discarded prior to the application of the TFC-based filter. The reduction of information in data can be (i) either the rejection of entire events or (ii) the rejection of subinformation of events.

An overall strategy for the ^{11}C rejection is depicted schematically in Figure 57. The filters are divided into four stages.
For the primary data selection, the Borexino DST `ROOT` files are used. DST `ROOT` files are smaller and more flexible than the Borexino standard `ROOT` files, since DST `ROOT` files do not contain e.g. the raw hit and decoded hit information of events (compare with Section 3.2.1). In this first stage, a filter extracts all events of interest, i.e. muons, neutrons and neutrino-like events in a given time period from the DST `ROOT` files. Typically, only neutrino-like events that are reconstructed within a given *fiducial volume* and that have an energy in a given energy range are selected. In addition, the information from different hardware systems might be combined to improve the ^{11}C rejection efficiency. This is the case e.g. for muon-induced neutrons (see Section 4.2.2).
In the second stage, a large fraction of events is discarded. A veto of neutrino-like events over the entire detector is applied after neutron bursts (2-hour veto) and after the beginning of each DAQ run (1-hour veto). In both cases, the TFC method has a low efficiency. The reasons for the lowered tagging efficiencies are discussed in the next paragraph. The entire detector is also vetoed after each muon event for 300 ms. This cut allows to reject short-lived radioisotopes without introducing a large loss of statistics. Finally, all muons which are not followed by a neutron event are discarded. The reason is that only muons followed by neutrons are interesting for an advanced TFC method that also makes use of the muon track information (see Section 2.4).
In the third stage, the TFC method is applied. In order to reduce the lost fraction of "time×mass" the reconstructed muon track is/can be included.
Reaching the fourth stage, all TFC-tagged events, all residual muon and neutron events and fast Bi-Po coincidences from the uranium and thorium decay chain are subtracted. Additionally, problematic events with mis-reconstructed physical parameters (e.g. the energy and the Gatti parameter) are carefully identified and rejected. In a final study, sub-periods of the used data set are examined and the *fiducial volume* size is varied. Certain sub-periods might show increased rates of time-dependent backgrounds (see analysis in Section 4.3.7). An adjustment of the initial *fiducial volume* cut might be also applied. At larger distances from the detector center the rate of external background events increases and the energy response of the detector deteriorates. In contrast, a selection of a *fiducial volume* with a smaller radius excludes a large fraction of the collected statistics.

Inapplicability of the TFC method In some cases, ^{11}C decays cannot be tagged via the TFC method. In other cases, the efficiency of the TFC method is drastically reduced. The most important cases are listed below and the possibilities to reject such ^{11}C background events are presented.

1. **Invisible channels** According to simulations performed in [80] (see Section 4.3.1), ∼5% of all ^{11}C nuclei are produced via "invisible" channels without any emission of neutrons. Hence the identification of such ^{11}C decay via the TFC method is impossible. In the following analyses this efficiency will be denoted with ε_{ic} and its value set equal to ∼95%.

2. **Old neutron trigger setup:** As reported in Section 4.2.2, the neutron trigger efficiency was strongly reduced in the initial phase of data acquisition from May 16, 2007 until December 15,

[19] For each found ^{11}C candidate, the TFC filter defines a loop which recursively searches for neutron candidates within a time interval of two hours. All events in-between have to be scanned.

Neutron multiplicity M_n^C	Remaining statistics outside the ^{11}C energy window [%]	Remaining statistics inside the ^{11}C energy region [%]
no cut	100	100
>13	82	59
>11	79	56
>9	75	53
>7	68	49
>5	60	42
>3	42	29
>1	11	8

Table 10: Loss of lifetime when a 2-hour veto of the entire detector after each neutron event with multiplicity M_n^C is applied. The percentages are relative to the original energy spectrum in which no veto has been applied. The statistical errors of the values in the second and third column are $\leq$1% and $\sim$5%, respectively.

Data set		Number	Lifetime	Duty cycle	ε_{br}	^{11}C rate
Beginning	End	of runs	[d]	[%]	[%]	[events/d/100ton]
May 13, 2007	Dec. 15, 2007	635	139.1	65.0	94.9	1.4
May 19, 2007	Jan. 05, 2008	705	148.8	63.4	94.5	1.5
Jan. 06, 2008	Dec. 13, 2008	1320	281.3	82.2	97.4	0.7
Dec. 16, 2007	Jan. 17, 2009	1497	318.2	80.3	97.7	0.7

Table 11: Calculation of the TFC efficiency ε_{br} to tag ^{11}C decays at the beginning of a run. The efficiency is expected to be reduced due to missing neutrons that were generated and captured during run interruptions. The calculation is based on a model that assumes a random distribution of the neutron events in time. The exact sequence of runs vs. run interruptions in a given data set has been implemented. The rate of non-taggable ^{11}C decays refers to the mean value of the expected total ^{11}C rate in Table 8.

2007. Since the neutron trigger efficiency is of fundamental importance for the TFC method, this period will not be treated in the upcoming analyses.

3. **Neutron bursts** In Section 4.2.5 it has been shown that the position reconstruction of neutron clusters deteriorates with an increased neutron multiplicity M_n. Moreover, high multiplicity neutron events are sometimes followed by a large number of ^{11}C decays. To efficiently reject these ^{11}C decays, the entire detector is vetoed for a time interval of 2 hours. However, the veto is only applied if a critical neutron multiplicity M_n^C is exceeded. A special analysis was carried out to find the ideal limit. Table 10 shows the loss of lifetime for a 2-hour veto of the entire detector after each neutron of multiplicity M_n^C. The optimal limit was found to be $M_n^C > 9$. The 2-hour veto leads to a still acceptable lifetime loss of $\sim$25%, whereas the events in the ^{11}C energy window [0.8,2.0] MeV are effectively removed by $\sim$47%. Additionally, below $M_n \lesssim 9$ the position reconstruction of neutron clusters works reliably and thus the TFC method can be applied (compare with Section 4.2.5).

4. **Beginning of runs:** Interruptions of the DAQ do not only cause a distortion of the measured decay timeprofile of ^{11}C as described in Section 4.3.3, but also diminish the efficiency ε_{br} of the TFC method. The reason is that muon-induced neutrons which are generated and captured

during DAQ interruptions are not available for the tagging of ^{11}C decays at the beginning of the following run. This efficiency of the TFC method was investigated with the help of a numerical calculation for real Borexino data sets. For this purpose, the author of this thesis developed a model which foresees the inclusion of the exact sequence of runs and run interruptions present in a given data set. The model assumes that all neutrons are produced in single-cluster neutron events, i.e high-multiplicity neutron events are not included. However, the implemented average neutron rate corresponds to the measured one. The neutrons are distributed randomly over the entire period of the data set. Next, the algorithm calculates the probability that a ^{11}C atom decays within the run interruption or at the beginning of the next run.

A first study has shown that the worst case is reached for run interruptions longer than $\sim$120 min; above this value, the efficiency ε_{br} is stable at approximately 90%. Constant run interruptions of 10 min still reduce the tagging efficiency ε_{br} to $\approx$98%.

Table 11 summarizes the results for four real data sets. Two data sets mainly include runs taken in 2007 in which the duty cycle of the DAQ was rather low around $\sim$65% (see Section 3.4.2). The calculated value of the efficiency ε_{br} is 94.5%. Assuming a ^{11}C rate equal to 27.82 events/d/100ton, which is the expected mean value reported in Table 8, the rate of non-taggable ^{11}C decays becomes $\sim$1.4 events/d/100ton. The other two reported data sets mainly include data acquired in 2008. The duty cycle and the efficiency ε_{br} increase to $\sim$81% and 97.5%, respectively. In terms of non-taggable ^{11}C decays, the latter value corresponds to a rate of $\sim$0.7 events/d/100ton.

There are two possibilities how to deal with this inefficiency of the TFC method: one can either tolerate the inefficiency or apply a veto of the entire detector for e.g. 1 hour at the beginning of each run. The latter option would reject most of the ^{11}C decays, but at the expense of losing statistics. The situation is especially ambivalent for periods after the installation of the new neutron trigger system (see Sections 3.4.2 and 4.2.2), when not only the neutron detection efficiency has been improved, but also the duty cycle of data collection has increased.

Since the main objective of the following analyses will be a maximum rejection of ^{11}C decays, a 1-hour veto of the entire detector will be applied. In the case of data collected in 2008, the calculated value for ε_{br} increases from 0.974 to 0.997 due to the improved duty cycle of the data acquisition system.

Optimisation of the TFC cut selection and estimation of the ^{11}C rate In the following paragraph, the TFC method was applied with the aim of rejecting ^{11}C decays from the energy spectrum. For this purpose, the author of this thesis studied the ideal selection of the TFC cuts. The TFC time cut corresponds to the maximum time interval dt in which a coincidence between a neutron event and a ^{11}C candidate is looked for. The spatial TFC cut is related to the maximum distance dr between both events. TFC cuts that are too large evidently increase the fraction of lost "time×mass". By contrast, ^{11}C events are rejected less efficiently when too small TFC cuts are applied.

The reduction of ^{11}C decays via the TFC time cut is easily calculable; the efficiency is equal to $\epsilon_{dt} = 1 - e^{-dt/\tau}$ with τ=29.42 min. In order to achieve a strong suppression of ^{11}C, the TFC time cut will be set to dt=120 min, leading to ϵ_{dt}=0.984.

In the case of the TFC distance cut dr, a special analysis has been carried out. The analysis was performed in *Echidna cycle 9*, using a data set which covers most of 2008 with a lifetime of 281 days. Vetoes of events in the entire detector as described in the previous paragraph were not applied.

The value of dr was varied in steps of 10 cm in the range between 0 cm and 200 cm. For each

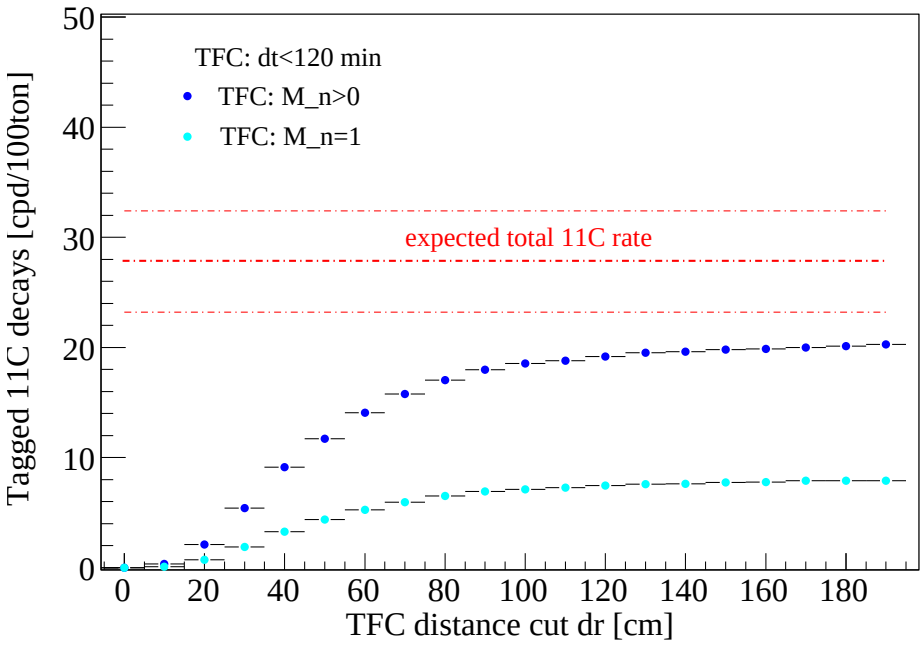

Figure 58: The rate of ^{11}C decays tagged via the TFC method in dependence of the distance cut dr. The rates of ^{11}C decays tagged in association with only single-cluster neutron events (M_n=1) and with all neutron cluster events (M_n>0) are in light blue and dark blue, respectively. The expected ^{11}C rate from Table 8 is also shown, including the 1σ region.

sample containing the TFC-tagged ^{11}C candidates, the amount of real ^{11}C decays was estimated according to the procedure introduced in Section 4.3.3. In a first study, ^{11}C candidates were

Effect/mechanism	Notation	Efficiency
Invisible channels	ε_{in}	0.95
Muon detection	ε_{μ}	>0.99992
Neutron trigger gate: [16,1600] μs	ε_{tg}	0.939
Neutron detection hardware + clustering	ε_{nd}	≈0.92
Neutron loss at the beginning of runs (2008)	ε_{br}	0.975
TFC method: distance cut dr<200 cm	ε_{dr}	$\gtrsim$0.99
TFC method: time cut dt<120 min	ε_{dt}	0.985

Table 12: Efficiencies related to the identification ^{11}C on an *event-by-event* basis, using the TFC method. The values of the dr and dt are the free parameters of the TFC method. The values reported here lead to very high efficiencies, but also to a significant reduction of the exposure.

associated with neutron events of all multiplicities (compare with Section 4.2.2). The dark blue markers in Figure 58 denote the rate of successfully tagged ^{11}C decays as a function of the TFC spatial cut. The TFC time cut was kept constant at 120 min. Several conclusions can be drawn from the obtained cumulative distribution:

1. the saturation level of the TFC distance cut is reached at around 2 m. For dr=190 cm, the efficiency of the TFC method to successfully tag ^{11}C decays is $\varepsilon_{dr} \gtrsim$99%. The corresponding ^{11}C rate is

$$R_{TFC} = (20.3 \pm 0.3) \text{ events/d/100ton}. \tag{4.31}$$

2. Assuming that all efficiencies are known, one can directly estimate the total ^{11}C production rate in Borexino from Equation (4.31). All relevant efficiencies are listed in Table 12. As reported in the mentioned table, the absolute efficiency of the neutron detection (hardware and software) is not well known. For the analysis, only neutrons detected with the Borexino Main DAQ system were used. One can make a conservative assumption that the absolute neutron detection efficiency of the Main DAQ system of Borexino is ≈92%. The percentage of approximately 92% corresponds to the relative difference in efficiency measured with the Main DAQ system of Borexino and with the Princeton neutron detection system [134] (see Section 4.2.2). For the muon detection efficiency ε_μ, an upper limit of 0.99992 was estimated at a 90% confidence level [89]. Taking these limits into account, the corrected ^{11}C rate becomes

$$R_{TFC,corr} \gtrsim 25.9 \text{ events/d/100ton}. \tag{4.32}$$

   This value is in agreement with the expected value reported in Table 8. On the one hand, this result indicates that the contribution from unknown or not well known efficiencies might be small. On the other hand, the efficiencies reported in Table 12 demonstrate the limitation of the TFC method in rejecting ^{11}C decays. The Borexino collaboration currently tries to improve: (i) the neutron trigger gate efficiency by also looking for neutrons in the muon gate (see Figure 28), (ii) the neutron detection efficiency by combining different neutron detection hardware systems and by improving the software clustering algorithms and (iii) the inefficiency due to run interruptions by achieving a better duty cycle.

3. An ideal TFC distance cut for the ^{11}C subtraction from the energy spectrum can be established. For the ^{11}C subtraction presented in the next section 4.3.6, the distance cut will be set equal to dr=130 cm. The ^{11}C rejection efficiency of this cut is ε_{dr} ≈0.96.

In a second study, the ^{11}C candidates were associated with single-cluster neutron events (M_n=1) only. The corresponding cumulative distribution in Figure 58 is marked by light blue dots. Saturation of the TFC tagging efficiency is reached again for dr ∼2 m. For dr=190 cm, the rate of successfully tagged ^{11}C decays is (7.9±0.2) events/d/100ton. This means that almost ∼40% of all ^{11}C decays which can be tagged with the TFC method are associated with single-cluster neutron events.
The cumulative distribution obtained in this second study contains a large fraction of ^{11}C decays that were correctly associated with the related neutron cluster (see Figure 48). Thus, the curve reflects the propagation of neutrons emitted in single-cluster neutron events in the Borexino scintillator. The neutron propagation length from this distribution has already been deduced and discussed in Section 4.2.8.

4.3.6 Applying the ^{11}C subtraction

In this section, the ^{11}C rejection techniques are applied as described in Section 4.3.5 for the purpose of the *pep* and CNO neutrino rate determination in Borexino. The ^{11}C rejection carried out in the present analysis follows the paradigm presented in Figure 57, however, not all intermediate steps (such as the final optimisation of the *fiducial volume* cut) will be performed here.

Definition of a figure of merit In order to describe the performance of the applied ^{11}C rejection cuts, one has to define a *figure of merit*. The statistics contained in the initial data set prior to the application of any cuts is expressed by the total exposure G. G corresponds to the total mass M_0 multiplied by the total lifetime T_0, i.e. $G = M_0 \times T_0$. The mass M_0 corresponds to the target mass contained in a selected *fiducial volume*.
There are different cuts which can introduce a fractional loss of exposure, but not necessarily.
For instance, the rejection of events such as muons and neutrons does not introduce a loss of statistics in the neutrino-like energy spectrum. Events of these types are contained in the data set only for the purpose of tagging neutrino-like background components such as ^{11}C events.
A single cut which rejects all neutrino-like events in the entire *fiducial volume* for a given time interval dT is called a "veto cut". Introducing the variable $a = dT/T_0$, a veto cut reduces the exposure by $dG' = a\,T_0 \times M_0$.
A single cut which removes neutrino-like events only within a sub-volume dM of the *fiducial volume* over a time interval dt reduces the exposure by $dG' = a\,T_0 \times b\,M_0$, with $a = dT/T_0$ and $b = dM/M_0$. One example is the *threefold coincidence* (TFC) cut, which is defined by a distance cut dr as well as a time interval dt between a neutron and a ^{11}C candidate.
Within a data set, the single cuts of a given type are frequently applied. Thus, single cuts might interfere with each other and superimpose the single "time×mass" fractions. As a consequence, the total lost "time×mass" fraction G' in a data set is typically smaller than the sum of the fractions dG' that are induced each time a cut is applied. Hence, the following *figure of merit* F is introduced:

$$F = 1 - \frac{1 - C'}{1 - G'} \tag{4.33}$$

where C' denotes the overall fraction of ^{11}C decays which could be successfully removed after the application of the ^{11}C rejection techniques. The value of C' after the application of a cut is calculated as follows: The remaining statistics in the ^{11}C energy window is estimated, then the expected contribution from solar neutrinos and from the external background is subtracted. The fraction of lost exposure G' can be determined by measuring the reduction of the events in an energy window which lies outside the ^{11}C spectrum. In an ideal case, the *figure of merit* F should converge to 1.

A second criterion has to be introduced which takes into account the statistical error of the final statistics or the expected neutrino signal, since this information is not included in the abovementioned *figure of merit*. For this purpose, Equation (4.25) will be used.

^{11}C subtraction on an event-by-event basis In this paragraph, the author of this thesis perform the ^{11}C subtraction on an event-by-event basis using the *threefold coincidence* method and veto cuts as described in Section 4.3.5. For this purpose a data set of 125.8 d of lifetime covering the period from January 13, 2008 to June 7, 2008 is used. The analysis is carried out in *Echidna* cycle 12. The general rules of the strategy proposed in Section 4.3.5 were followed applying a series of filters to the data set. The energy spectra obtained after the application of the main filters are shown in Figure 59. Equation (4.18) has been used to convert the original normalized charge variable into MeV units.
Muon events dominate the initial spectrum. Only at energies below ∼300 npe the ^{210}Po peak and the ^{14}C beta spectrum are able to exceed this background. After the muon and neutron event subtraction, one obtains the energy spectrum, which contains still all ^{11}C decay events.
Then a 2-hour veto cut was applied after each muon-induced neutron event that has more than nine neutron clusters (neutron multiplicity M_n>9). This cut looses 25% of exposure, but the

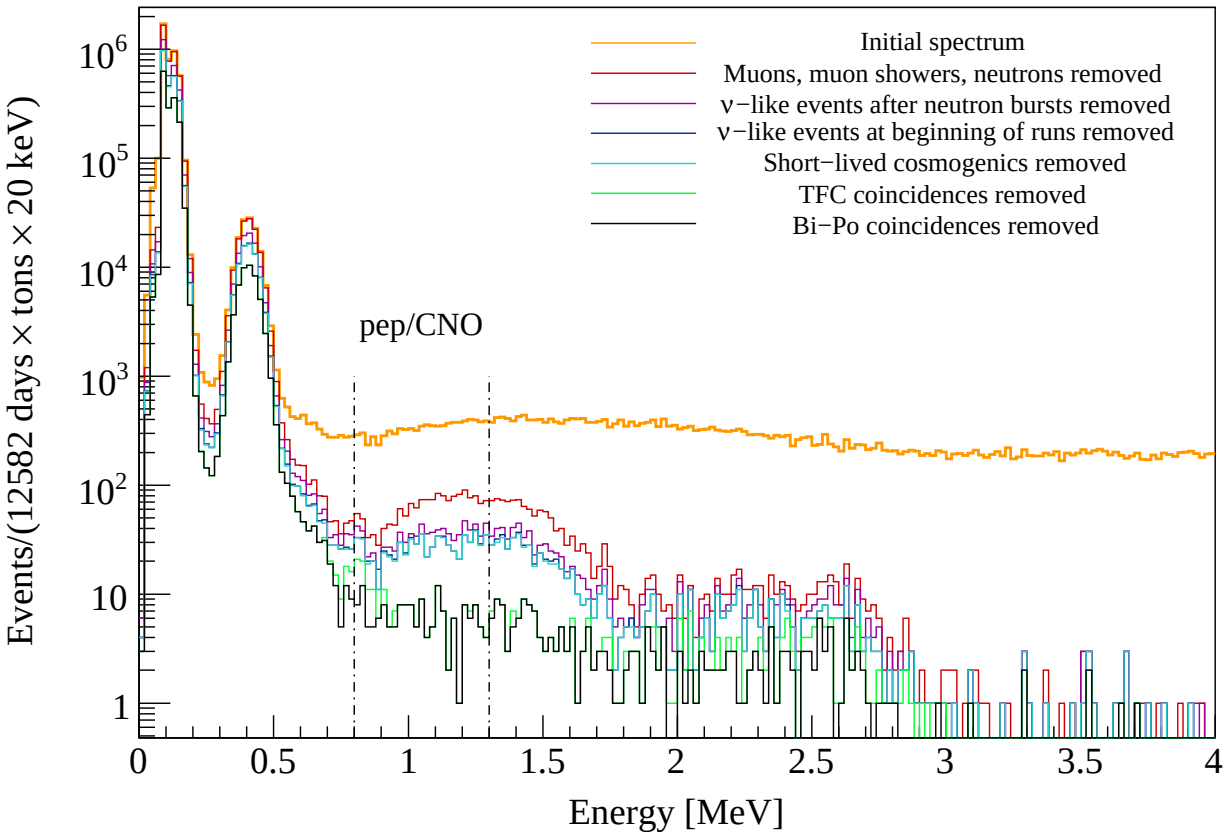

Figure 59: ^{11}C subtraction in a data set of 125.8 days of lifetime in the period from January 13, 2008 to June 7, 2008. The data were processed with *Echidna cycle 12*. The events are contained in a spherical *fiducial volume* with radius 3.0 m. The applied cuts reject: (i) all muon and neutron events, (ii) all neutrino-like events within 2 hours after a neutron event of multiplicity M_n>9, (iii) all neutrino-like events within 1 hour after the beginning of a run, (iv) all neutrino-like events within 300 ms after each muon event for the rejection of short-lived (SL) cosmogenic radionuclides, (v) all neutrino-like events which fulfilled the TFC criteria of a ^{11}C candidate, (vi) the fast ^{214}Bi-^{214}Po and ^{212}Bi-^{212}Po coincidences. The two lines denote the preferred energy window at [0.8,1.3] MeV for the observation of solar *pep* and CNO neutrino signal in Borexino.

Cut	Remaining statistics outside the ^{11}C energy window [%]	Remaining statistics inside the ^{11}C energy region [%]	Removed ^{11}C [%]
no cut	100	100	0
without n bursts	75	51	32
without beginning of run	60	41	34
aftermuons	59	41	34
TFC method	39	8	80

Table 13: The ^{11}C rejection efficiency of different techniques as applied in this analysis are presented and compared with the loss of exposure. These values are used to calculated the *figure of merit* defined in Equation (4.33). Further details are given in the text.

rate of ^{11}C in the resulting spectrum is strongly diminished by 32%. A second 1-hour veto of all neutrino-like events in the entire *fiducial volume* is applied after the beginning of each run. The lost "time×mass" is 15% of the initial exposure, whereas the ^{11}C rate decreases by 2%. A third 300 ms veto is applied after each muon event (compare with the measured muon rate in Section 4.1.2: ∼3 muon events/min) to reject short-lived cosmogenic radioisotopes which also partly affect the *pep* and CNO neutrino window. The 300 ms veto cut implies a 1% loss of statistics, whereas the ^{11}C rate remains constant.
The centerpiece of the ^{11}C subtraction is the identification of ^{11}C decays on an *event-by-event* basis via the TFC method. The used TFC cuts are $dr < 130$ cm for the maximum distance and $dt < 120$ min for the maximum time interval between the ^{11}C and neutron candidates. Neutron events with multiplicities smaller than M_n<10 were considered. The TFC cut implies not only an efficient removal of ^{11}C decays but also of decays of muon-induced ^{10}C decays.
Finally, one more filter is applied to identify and remove the fast Bi-Po coincidences from uranium and thorium. This cut removes especially events in the valley between the ^{7}Be neutrino Compton-like edge and the arising ^{11}C peak. The introduced fraction of "time×mass" is negligible.

The reduction of the exposure versus the ^{11}C rejection efficiency is summarized in Table 13. The *figure of merit* defined in Equation (4.33) becomes F=0.48 after the application of all filters. The total remaining exposure is 39%, whereas the ^{11}C rate is reduced by 80%. Assuming an initial ^{11}C rate equal to 27.82 events/d/100ton, which corresponds to the expected mean value reported in Table 8, the ^{11}C rate is reduced to 5.6 events/d/100ton. In the *pep* and CNO neutrino energy window [0.8,1.3] MeV, the rate of ^{11}C decays is lowered to 3.4 events/d/100ton. The expected rates of *pep* and CNO neutrinos in Borexino are 2.0 events/d/100ton and 7.1 events/d/100ton respectively, if the LMA solution for neutrino oscillations and the old high metallicity scenario (GS98) are assumed (compare with Section 2.4). If the newly calculated low metallicity (AGSS09) composition is used, the rates are 2.0 events/d/100ton and 5.1 events/d/100ton (see Section 2.4). For the low-metallicity scenario, the rate of the combined neutrino signals in the entire energy window is 7.1 events/d/100ton. However, in the observation window of [0.8,1.3] MeV the combined neutrino rate is reduced to ∼2 events/d/100ton. In this case, the ratio ρ between the expected solar *pep* and CNO neutrino rate and the rate of residual ^{11}C events becomes 1:1.7.

Statistical subtraction of ^{11}C In the following analysis, a statistical subtraction of the residual ^{11}C events was performed which are left in the energy spectrum determined in the previous paragraph. A statistical subtraction has the advantage to possibly visualize the *pep* neutrino Compton-like edge, but also to reveal the signature from unexpected background components.

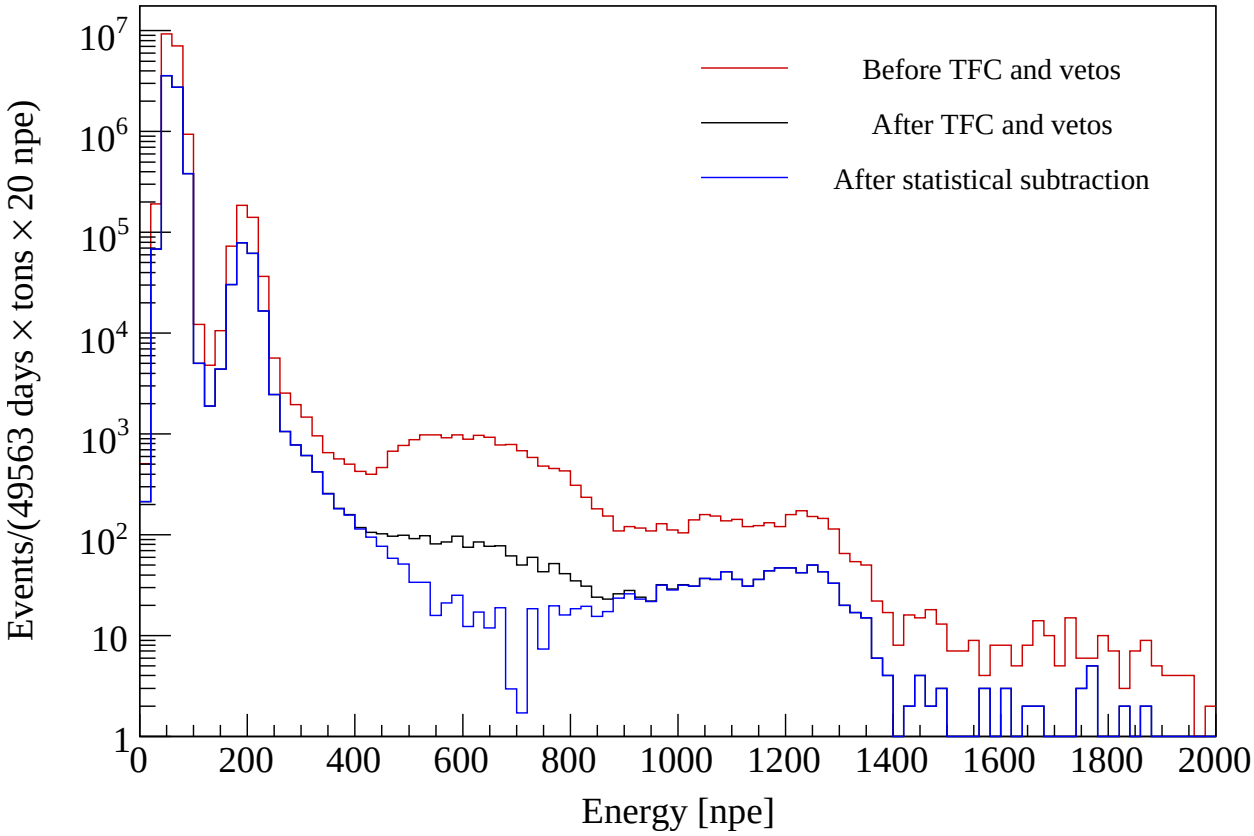

Figure 60: Statistical subtraction of the residual ^{11}C events still present after the application of the threefold coincidence method and other veto techniques (see Figure 59). The used data set was processed in *Echidna cycle 12* and contains 495.6 days of lifetime (period from January 13, 2008 until January 2, 2010).

There are several possibilities to carry out a statistical subtraction. Currently, Borexino collaborators are developing and testing several methods. One procedure which is based on a pulse shape discrimination technique has already been described in Section 4.3.4. Another procedure is based on Boosted Decision Trees (BDT). Both techniques make use of high-purity ^{11}C data sets that are determined by the TFC method.

The procedure adopted in this analysis uses the spectral shape information of the ^{11}C energy spectra which were obtained in Section 4.3.4. These spectra are ideal, since they intrinsically contain the exact detector response. Moreover, the amount of accidental background events is small (3-5%), whereas the collected statistics is still high, i.e. the spectra have several thousand events.
Besides the spectral shape information, one has to calculate the number N' of ^{11}C decays still present in the ^{11}C reduced spectra obtained in the previous paragraph. For this purpose, one needs to know: (i) the percentage ϵ_r of the residual ^{11}C decays, (ii) the total ^{11}C rate R and (iii) the reduced exposure time G'. The value of N' is calculated via $N' = R \cdot G' \cdot \epsilon_r$.
The used values for ϵ_R and G' are given in Table 13. For the ^{11}C rate R, the lower limit reported in Equation (4.32) is used. By using this value, N' will be a lower limit as well. Then, the ^{11}C spectrum of 95% purity reported in Table 9 was used. The area below the ^{11}C spectrum is normalized and scaled by the number N'. Finally, the scaled ^{11}C spectrum is statistically subtracted (bin-per-bin) from the ^{11}C reduced energy spectrum.

Figure 60 reports the energy spectra prior to and after the ^{11}C subtraction. The used data

set covers the period from January 13, 2008 to January 2, 2010. The total lifetime is 495.6 d. The β-like spectrum before any ^{11}C subtraction is depicted in red. The energy spectrum after the application of the TFC method and of several other veto techniques is given in black. The blue curve represents the energy spectrum after the application of the statistical ^{11}C subtraction. Even though some ^{11}C events are still present in the latter spectrum, it allows an insight into the spectral components which are hidden below the ^{11}C peak. Besides the expected solar *pep* and CNO neutrino spectra a second component with a maximum energy at ∼1250 npe (∼2.65 MeV) that penetrates the ^{11}C energy window at lower energies is clearly visible. There might be other background components which affect the *pep* and CNO neutrino energy window. The following Section 4.3.7 aims at individualizing and characterizing such background components.

4.3.7 Other background components besides ^{11}C

The measurement of the *pep* and CNO neutrino rate with the Borexino detector strongly depends on the rejection efficiency of ^{11}C. However, other backgrounds might as well affect the *pep* and CNO neutrino energy window at [0.8,1.3] MeV. For this reason, the author of this thesis examined the residual energy spectrum which was obtained after the application of the event-by-event ^{11}C subtraction (see Section 4.3.6).
There are different ways to identify potential secondary contaminants. One possibility is a partial or complete identification of the spectral shape of a background. A second possibility is to examine the stability in time of the event rate in a given energy region. Convection processes in the scintillator and detector operations (see Section 3.4.1) might have led to increased background levels. Finally, one can investigate the event rate in a given energy region as a function of the *fiducial volume* radius. This allows to recognize possible radial-dependent contaminants.

Isotropically distributed contaminants in the scintillator A first background contribution arises from naturally occurring trace contaminants in the scintillator mixture. Concentrations of the order of 10^{-17} g/g were achieved for ^{238}U and ^{232}Th (see Section 3.3).
In the case of ^{40}K (β^-, Q=1.311 MeV, τ=1.842×10^9 y), the Borexino collaboration has established an upper limit for the ^{40}K concentration which is ≤3×10^{-16} g/g. Assuming a concentration of 10^{-15} g/g for ^{40}K and the measured concentrations of 10^{-17} g/g for ^{238}U and ^{232}Th, these contaminants would contribute to ∼0.6 events/d/100ton within the *pep* and CNO neutrino window [81].
The simulated spectrum of ^{40}K is shown in the left plot of Figure 62. The *full-energy peak* and the β spectrum of ^{40}K affect the *pep* neutrino spectrum. Thus, it might be difficult to disentangle the ^{40}K background from the neutrino signal.

Time-dependent contaminants In this paragraph, potential time-dependent contaminants were examined. Three periods (I-III) are selected: (I) from January 13, 2008 to June 7, 2008; (II) from June 8, 2008 to January 3, 2008; (III) from January 3, 2010 to May 1, 2010. The data were processed with *Echidna* cycle 12.
The ^{11}C subtracted energy spectra for all three periods are shown in Figure 61. The same ^{11}C rejection cuts were applied to the spectra of all selected periods. The spectra only includes events within a spherical *fiducial volume* of radius R<3.0 m and are normalized to 100 d of lifetime. One observes that the event rates in different energy regions have changed in time.

As shown in Figure 61 a first energy window at [150,250] npe includes the ^{210}Po peak.
The high concentration of ^{210}Po in the first period of data acquisition might have been introduced with the PPO contained in the Borexino scintillator (see Section 3.3). Due to a lifetime of τ=138

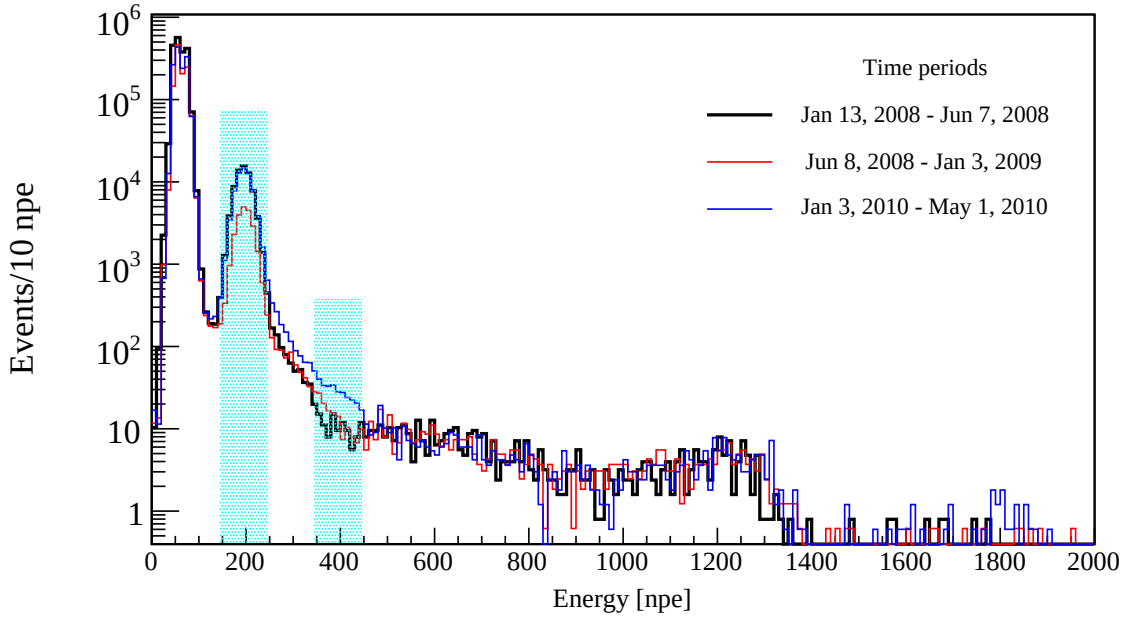

Figure 61: Time-dependent background components in Borexino. Energy windows suitable for the rate study of these contaminants were defined. The rates were observed for three time intervals in the period 2008-2009. The rates from ^{210}Po and ^{210}Bi fluctuate in time. Above the ^{11}C energy spectrum no time variations of potential backgrounds such as ^{214}Bi were observed. Further details are given in the text.

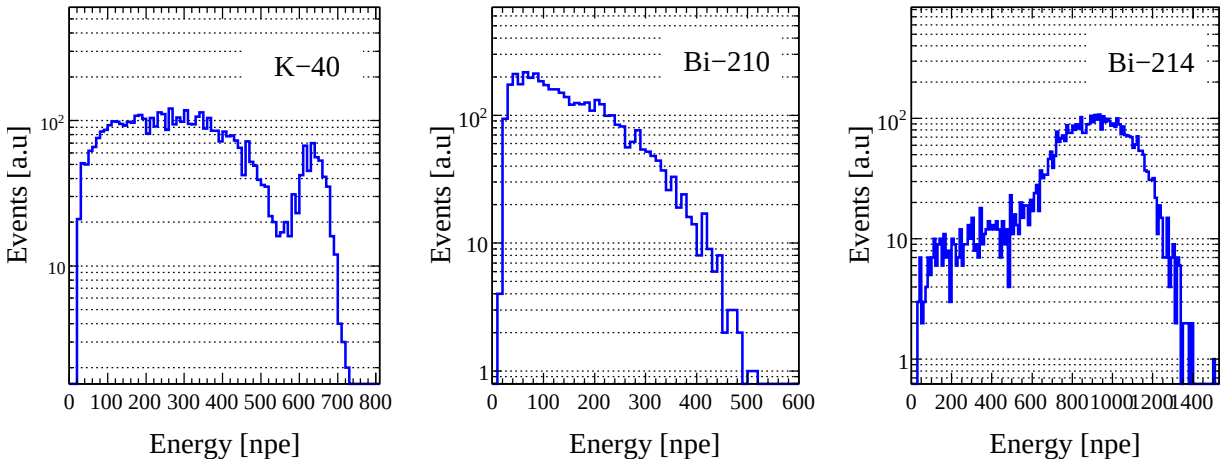

Figure 62: Simulation of the radioactive decays from ^{40}K (left), ^{210}Bi (middle) and ^{214}Bi (right) in a spherical *fiducial volume* of radius R<3 m. The simulations were performed using particle generators which are included in `GENEB` (see Section 3.2.1).

d, ^{210}Po decreases by factor of ∼14 within one year. However, occasional refilling operations have continued to reintroduce ^{210}Po (see Section 3.4).

A second window around [350,450] npe corresponds to the valley between the ^{7}Be neutrino Compton-like edge and the arising ^{11}C energy spectrum. In the periods II and III the rate in the defined energy window increased by ∼33% and ∼95% relative to the first period I. This time-dependent background might be attributed to decays of the radionuclide ^{210}Bi (τ=7.23 d). Assuming that the ^{210}Bi-like contaminant is effectively ^{210}Bi, it should not be problematic due to the short lifetime. However, the concentration of its long-lived parent nuclide ^{210}Pb (τ=32.2 y) might have increased in time and continued to generate new ^{210}Bi atoms.
The β spectrum of ^{210}Bi has been simulated within *Echidna cycle 11* and is depicted in the middle panel of Figure 61. The spectrum has an endpoint energy at 1.162 MeV. Since its spectral shape is similar to the CNO neutrino spectrum (compare with Figure 8), it is not possible to disentangle the background from the neutrino spectrum. Thus, in global spectral fit analyses a single component for ^{210}Bi and CNO is usually used whose weight is a free parameter of the fit. For the period from May 16, 2007 to April 12, 2008, the Borexino collaboration published a combined ^{210}Bi-CNO rate of 23±2(stat)±2(sys) events/d/100ton [44].

For sake of completeness the energy region above the ^{11}C energy spectrum was also examined. One possible contaminant that could appear and change in time is the ^{222}Rn daughter ^{214}Bi (τ=28.7 min). The simulated ^{214}Bi spectrum is shown in the right panel of Figure 62. The event rate was studied in the energy region [800,1400] npe. Within the statistical uncertainty, no temporal fluctuation of the overall event rate has been observed. The constant rate of this high-energy background is related to an external background which is constant in time and originates from the outer detector components. This background will be described in the following paragraph.

Radial-dependent background Especially long-range 2.615 MeV γ rays from ^{208}Tl decays in the outer detector parts constitute a background relevant for the *pep* and CNO neutrino analysis. The radial dependency of this external γ ray background is demonstrated in Figure 63. The used data set covers period I (January 13, 2008 to June 7, 2008). The data set only includes events which are contained in *fiducial volumes* with radii R<3.0 m and R<2.5 m, respectively. In the latter case the spectrum was rescaled for the reduced "mass×time" fraction of 40% compared to the larger volume. For a smaller *fiducial volume* of radius R<2.5 the *full energy peak* at 2.615 MeV (∼1250 npe), but also the Compton continuum, which extends to lower energies decreases. However, they do not disappear completely and might affect the *pep* and CNO neutrino energy window or at least the ^{11}C energy spectrum. Therefore, one has to investigate the optimal treatment of the external background within the *pep* and CNO neutrino analysis. The application of a strong radial cut such as R<2.5 m not only reduces the external background, but also the entire statistics of the data set. For a larger *fiducial volume* radius, the situation is reversed. In both cases the spectral shape of the external background has to be determined.

Motivated by these observations, the author of this thesis started an extensive study of the Borexino external background. The results of this analysis is presented in the following Chapter 5.

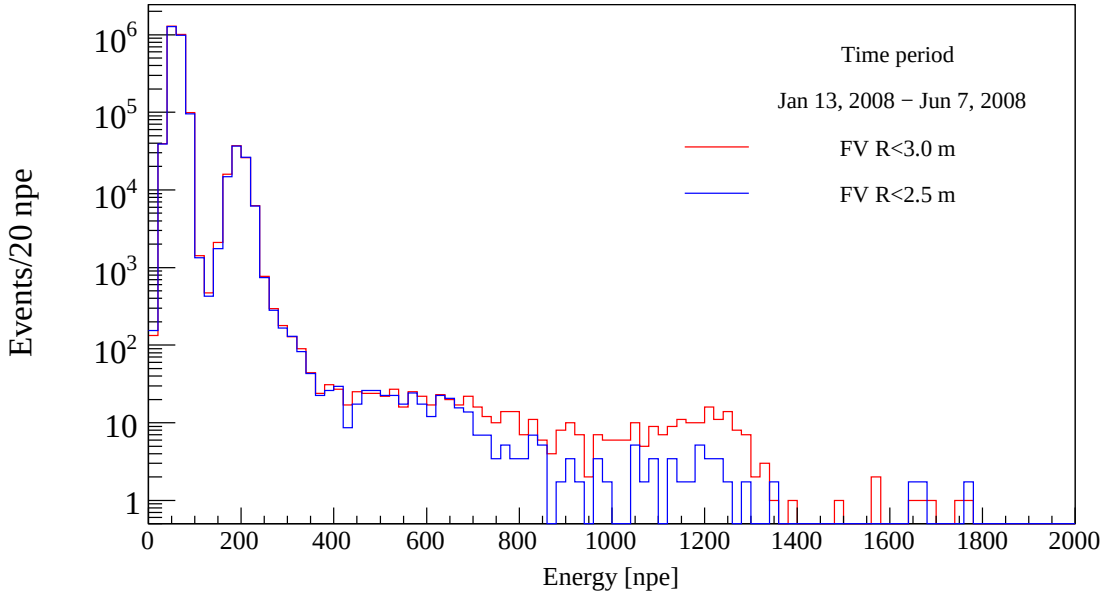

Figure 63: Radial dependence of the external background component. The spectra of events contained in two spherical *fiducial volumes* with radii R<2.5 m and R<3.0 m are compared. The used data set covers the period from January 13, 2008 to June 7, 2008.

5 Analysis of the external background

5.1 Introduction

The analysis in Section 4.3.7 has shown that the external background constitutes a relevant secondary background for the *pep* and CNO neutrino detection in Borexino. The energy spectrum of the external background has a peak around 2.6 MeV and decreases to lower energies. The rate of the events also decreases for smaller *fiducial volumes* but was found to be still visible within a spherical *fiducial volume* with radius R<2.5 m (see Figure 63). 2.615 MeV γ rays originating from decays of the ^{232}Th daughter nuclide ^{208}Tl mainly contribute to the external background. The 2.615 MeV γ rays are the highest energetic photons released from naturally occurring radioactive decays. Radioactive decays and nuclear interactions in the buffer, the photomultiplier tubes (PMT), the light concentrators, the Stainless Steel Sphere (SSS) and from the environment emit highly energetic γ rays and neutrons which can penetrate the buffer layers, producing a signal in the *fiducial volume*. A discrimination of these signals is not possible as opposed to an internal contamination by ^{232}Th. In that case it is possible to look for e.g. fast coincidences from ^{212}Bi-^{212}Po decays.
When studying the external background, it is interesting to know where the γ rays and neutrons are generated and which of them mainly contribute to the observed background in the energy spectrum. This is especially important for estimating the spectral shape of the external background below the clear signature from the 2.615 MeV *full-energy peak*.
The latter one is important for estimating the rate but especially the spectral shape of the external background below the clear signature from the 2.615 MeV *full-energy peak* in dependence of the *fiducial volume* dimensions.
These and other topics related to the study of the external background will be discussed in this chapter.

5.1.1 Origin of the external background

The external background can be divided into two parts, one originating from the rock and one from the detector components.

The environmental γ radioactivity consists mainly of 2615 keV, 969 keV, 911 keV, 583 keV, 238 keV γ rays from the ^{232}Th decay chain and of 2204 keV, 1764 keV, 1120 keV, 1001 keV, 766 keV, 609 keV, 351 keV, 242 keV γ rays from the ^{238}U decay chain (see Figures 89 and 90 in Appendix A.3). 1461 keV γ rays from ^{40}K decays are also emitted. The fluxes of the mentioned γ lines are given in Table 14. For the most energetic and thus most long-range 2615 keV γ rays the total flux on the Outer Detector of Borexino is about 1.5×10^7 $\gamma/d/m^2$ [82]. Passing the $\sim$2 m thick Water Tank the total flux is attenuated by four orders of magnitude. In the following, the count rate expected for different concentric spherical volumes is studied: for a typical *fiducial volume* with radius R<3.0 m, for the *Inner Vessel* (R=4.25 m) and for the entire Inner Detector (R=6.85 m). For the mentioned volumes one expects a total flux of approximately 10^{-2}, 4×10^1 and 10^4 $\gamma/d/m^2$ for the 2.615 MeV γ line, respectively. The total fluxes of all other γ lines are reduced by at least one order of magnitude compared to the 2615 keV γ ray flux [82].
In addition, there are neutrons escaping the rock and neutron-induced γ rays. The main sources of neutrons at LNGS are (α,n) and spontaneous fissions in the rock. The total flux was measured in Hall A and is $(3.27 \pm 0.21)\times10^3$/d/m^2 in the energy range [0,25] MeV [183]. The total number of neutrons impinging on the detector is 1.9×10^3 neutrons/d/m^2. Within the *Inner Vessel* one expects a total flux of $<10^{-8}$ neutrons/d/m^2. The contribution to the background from neutrons generated by spontaneous fission and (α,n) reactions inside the detector is estimated to be negligible due to

Radionuclide	Energy [keV]	Flux from walls (Hall C) [m^{-2} d^{-1}]
^{208}Tl	2615	1.4×10^{7}
^{228}Ac	911	4.8×10^{6}
^{208}Tl	583	4.1×10^{6}
^{214}Bi	1764	1.7×10^{7}
^{214}Bi	1120	1.4×10^{7}
^{214}Bi	609	2.9×10^{7}
^{40}K	1461	3.8×10^{7}
		Flux from walls (Hall A) [m^{-2} d^{-1}]
neutrons	[0,25] MeV	$(3.27\pm0.21)\times10^{3}$

Table 14: Fluxes of γ rays emitted by radioactive elements connected to ^{238}U and ^{232}Th chains and by ^{40}K (from [82]) in the rock surrounding the Borexino detector located in Hall C at LNGS. The flux of neutrons with energies in the region [0,25] MeV is also reported. It is based on a measurement performed in Hall A at LNGS [183].

the low levels of radioactive impurities [82].
When the neutrons entering the detector are thermalized, they can be captured in water and in other detector materials emitting characteristic γ rays with energies up to 10-20 MeV. For a more detailed list of the interaction rates, cross sections and released energies see [82]. The resulting neutron-induced γ ray flux entering spherical volumes with radii R smaller than 3.0 m, 4.25 m and 6.85 m is approximately 10^{-6}, 10^{-4} and 10 $\gamma/d/m^2$, respectively.

The second constituent of the external background originates from the radioactivity contained in the detector materials outside the *Inner Vessel*. Even though all materials were carefully selected all detector components include a finite radioactive contamination. The detector components outside the *Inner Vessel* under investigation are the SSS, the 2214 PMTs, the 1843 light concentrators, the steel end cap of the *Outer* and *Inner Vessel* (OV, IV), the nylon bag, the nylon pipe and nylon end caps between OV and IV and the hold down ropes. Table 15 summarizes the measured mass fractions of ^{238}U, ^{232}Th and ^{40}K of the single components, their total amount of mass and their mean distance from the detector center [184, 185, 92].
Using the values in Table 15, one can calculate the total rate of γ rays of a given energy from a given isotope emitted by a single detector component. In the following discussion we will assume that the natural decay chains are in secular equilibrium. Then, the mass fractions can be expressed in terms of concentrations using the conversion factors: U: 10^{-9} g/g = 12.35 mBq/kg; Th: 10^{-9} g/g = 4.06 mBq/kg; K: 10^{-9} g/g = 31 μBq/kg.
Concerning the count rate of 2615 keV γ rays from the SSS, the PMTs and the light concentrators one gets approximately 2.6×10^{7}, 3.6×10^{7} and 9.6×10^{7} γ/d radiated in 4π, respectively. The count rates of 2615 keV γ rays from all other detector components are 4-6 orders of magnitude lower. This statement is similar for all other γ lines from U and Th assuming secular equilibrium. A second conclusion is obtained by comparison of the count rate from the rocks with those from the SSS/PMTs/light concentrators by going towards the interior of the detector: The count rate of 2615 keV γ rays emitted from the rocks is at least one order of magnitude lower than that from the sum of the aforementioned detector components. This statement is again valid for all other dominating γ lines escaping the rock. Thus, the contribution from the environment to the amount of external γ rays reaching the interior of the detector is of second order.

In a final step the number of γ rays, which are able to cross the *Inner Vessel* (radius R=4.25 m) are estimated by means of (1) their point of emission and (2) their energy. A simple model is used which includes the solid angle covering the *Inner Vessel* as a function of the point of emission.

Detector component	^{232}Th [g/g]	^{238}U [g/g]	^{40}K$_{nat}$ [g/g]	Distance from center [cm]	Mass [kg]
SSS	3×10^{-9}	7×10^{-10}	7×10^{-8}	6.85	7×10^{4}
PMT	3.3×10^{-8}	6.6×10^{-8}	2×10^{-5}	6.55	2×10^{3}
Light concentrators	1.8×10^{-7}	1×10^{-9}	1×10^{-5}	6.45	1.2×10^{3}
PC buffer	1×10^{-15}	1×10^{-15}	1×10^{-12}	4.25-6.85	1.04×10^{6}
O.V. Steel endcaps	2×10^{-9}	1×10^{-9}	7×10^{-8}	5.75	1.5×10^{1}
I.V.-O.V. Nylon pipe	5×10^{-11}	5×10^{-11}	7×10^{-7}	–	4.2
I.V. Nylon endcaps	5×10^{-11}	5×10^{-11}	7×10^{-7}	4.25	1.2×10^{1}
Hold down ropes	5×10^{-11}	5×10^{-11}	1×10^{-6}	4.25	4.5
Nylon bag	4×10^{-12}	$<1.7\times10^{-12}$	1×10^{-8}	–	3.2×10^{1}

Table 15: Detector components contributing to the external background outside the *Inner Vessel*. The mass fractions of ^{232}Th, ^{238}U and ^{40}K, the total mass of the component and its average distance from the center of detector is included [92, 185, 186]. Upper limits are given at 90% confidence level.

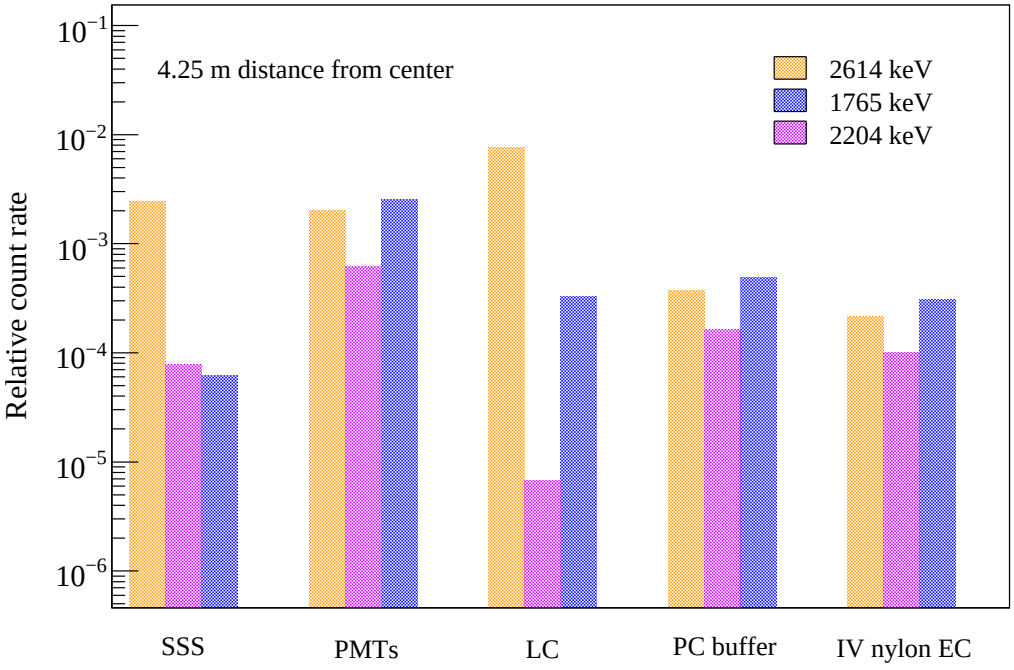

Figure 64: Approximative estimation of the relative count rates of the dominating γ rays from the U and Th decay chains, that are expected at the *Inner Vessel* radius facing inwards the detector. All γ rays originating in the buffer and in the nylon components were assumed to start directly from the *Inner Vessel* border. Components reported in Table 15 that are not shown in the chart have in general lower count rates.

Additionally, the γ rays of the buffer liquid and of the nylon components are assumed to start directly from the *Inner Vessel*.
The approximate rates of the most intense and most long-range γ lines from U and Th daughters are depicted in Figure 64.
The main conclusion is that the dominating component crossing the *Inner Vessel* can be attributed to 2615 keV γ rays. The 2204 keV γ rays originating from ^{214}Bi decays in the PMTs constitute the second highest count rate. However, the rate is by one order of magnitude lower than that from 2615 keV γ rays. The 2615 keV γ rays are emitted mainly from the PMTs, the light concentrators and also from the SSS. Compared to them the contributions from all other detector components are relatively small.

5.1.2 Motivation for an external calibration

Neutrino analyses based on *fiducial volumes* with different radii above R≈(2.0-2.5) m suffer from a lack of knowledge about the total spectral shape from the external background. As previous Monte Carlo simulations have shown [185, 188] the spectral shape is expected to change dramatically with the size of the *fiducial volume*: the larger its radius the larger the probability to encounter Compton-scattered γ rays, which are still able to reach the outer region of the scintillator in the *Inner Vessel*. This leads to an increased Compton continuum below the *full-energy peak* of the 2.615 MeV γ line.
Monte Carlo simulations trying to estimate the spectral shape of the external background with adequate precision encounter the problem of collecting statistics in reasonable CPU time. To solve this problem some codes propagate γ rays in a layer of a certain thickness of material and record the residual energy spectrum and the distribution of the initial direction of γ rays which were not absorbed. These spectra then are used as input for the propagation of γ rays in the next layer etc. This might introduce a bias as well as other secondary effects not yet included in a full Monte Carlo simulation.
The aim of the following work is the exact determination of the external background in Borexino performing an external calibration with an appropriate source. The source of interest should be a 2615 keV γ ray emitter, since these γ rays represent the main external background component entering the *Inner Vessel*. A source of proper activity can solve the problem of statistics and include *a priori* the information of the detector response. A successful measurement with a calibration source also depends on an exact energy and position reconstruction. Hence, the DAQ system exposed to such a highly radioactive source has to be stable during an external calibration.
More analyses benefit from such a measurement:

- Energy reconstruction:
  - Using the spectral shape information of the external background for neutrino analyses (^{7}Be, CNO, *pep*, ^{8}B, anti-neutrinos)
  - Testing the energy uniformity by looking for North/South asymmetries in the detector
  - Supplying an energy calibration point and defining the energy resolution at 2.615 MeV
- Position reconstruction:
  - Definition of the spatial resolution of position reconstruction
  - Periodical monitoring of the position reconstruction stability. This is important to check the validity of the solar neutrino signal time variation measurements such as the annual 7% variation due to the Earth orbit eccentricity
  - Studying of the radial distribution: estimating the external background rejection efficiency

- MC simulation:
  - Comparison of data versus MC calculated spectra for different source positions and tuning of the MC code
  - Using the tuned MC code to perform a simulation of the full external background
- Borexino's participation in the SuperNova Early Warning System (SNEWS)
  - Testing the Borexino trigger system designed for the early detection of close-by supernovae explosions. Moving a strong γ source into the *Inner Detector* instantaneously induces an event rate of several 100 Hz, which mimics a neutrino shower signal from a galactic supernova.
- Background outside the Inner Detector
  - By placing the source within the Water Tank at different distances from the SSS one can study the propagation of γ rays through three media of different composition and density (water, stainless steel, pseudocumene).

5.1.3 The external calibration system

The Borexino detector is equipped with both an invasive internal and a non-invasive external system for the calibration with radioactive sources.
The external calibration system was designed for the purpose of positioning highly active γ sources at the level of the PMTs with a minimal distance of ∼635 cm from the center of detector [188, 189]. The external calibration system was never used before the work here presented. Within the analysis performed in Section 4.3.7 the author of the thesis recognized the importance of the external background for the *pep* and CNO neutrino analysis and carried out an external calibration for the first time. Details are given in Section 5.3.
To insert a γ source into the detector, 61 cm long stainless steel reentrant tubes were installed in the SSS at 14 different positions [189]. The positions are in a vertical plane[20], but not homogeneously distributed. The reentrant tubes are connected via polyethylene tubes going through the Water Tank (WT) and ending on the platform above the WT of Borexino. One organ pipe is located north of the clean room of the internal calibration system, one south of it. The tubes are thick enough to relieve the buoyant forces that they have been exposed from the water in the Outer Detector since 2007. However, several tests in 2009 showed that two out of 14 tubes are no longer tight, i.e. they were submerged in water.
For the placement of a γ source at a given position within the detector the source is inserted into an appropriate source holder made of stainless steel. Its diameter is 9 mm, which is clearly smaller than the inner diameter of 12.3 mm of the organ pipe tubes. The source holder is welded with an electrician's fish tape which allows to move the source through the tube system. Tests in 2009 and 2010 showed that the friction is minimal.
Since the polyethylene tube is non-conductive, the conductivity between the fish tape and SSS/Water Tank can be measured to find out when the source touches the end of the selected reentrant tube. As tested in 2010, the end position of a single reentrant tube can be used as reference point for the definition of other positions within the reentrant tube with high accuracy (± 1 cm). This guarantees the reproducibility of the calibration measurement.

[20] The plane is not parallel to the geographical North-South direction, but almost aligned with the water tank's organ pipes so that they do not interfere with other installations.

5.2 Production and characterisation of an external γ source

In the following section the production and characterisation of a custom-made ^{228}Th source of MBq activity optimized for the Borexino experiment is presented. As head of the project the author of this thesis supervised the production, the characterisation and the transportation of the source and carried out the first external calibration in Borexino. The work included several proposals, technical procedures and radioprotection reports.
The author of this thesis established a scientific cooperation among the following institutes: the Max-Planck-Institut für Kernphysik, Heidelberg (GER), the Paul Scherrer Institut PSI, Villigen (CH), the Institut für Kernchemie, Mainz (GER), the Physikalisch-Technische Bundesanstalt PTB, Braunschweig (GER), the Laboratori Nazionali del Gran Sasso, Assergi (ITA) and the Physik-Institut der Universität Zürich, Zürich (CH) involving several physicists, radiochemists and responsibles of the radioprotection at the different institutes. The work comprised also a close and permanent cooperation with the company Eckert & Ziegler Nuclitec GmbH, Braunschweig (GER), which provided the radioactive material and encapsulated the source.
Together with the PSI collaborators the author of the thesis organized a special meeting at PSI to discuss the plan for the production of the Borexino source and participated in the production of the source at Institut für Kernchemie.
Together with M. Laubenstein and D. Budjas the author of this thesis prepared a γ spectroscopic measurement in order to calibrate the γ activity of the source. The neutron source strength measurement was designed, carried out and evaluated by the PTB collaborators. Their analysis is reported in this section for completeness. Together with A. Ianni the author of this thesis organized the first external calibration campaign in Borexino which was carried out in July 2010.

5.2.1 Requirements to the γ source

The calibration source that was found to be most useful is a ^{228}Th source: ^{228}Th is a long-lived nuclide (τ=2.76 y), ^{208}Tl is one of its daughter nuclides and the emission probability of the 2.615 MeV γ line is 35.6%. The α and β particles emitted by daughter nuclides of ^{228}Th are blocked by the source encapsulation, lower energetic γ rays are absorbed in the buffer. A fraction of β particles can produce Bremsstrahlung photons, but their energy and rate are small compared to the 2.615 MeV γ rays [188]. Moreover, the dimensions of a ^{228}Th source can be kept small enough to fit into the reentrant tubes of the external calibration system.
A ^{228}Th source with an activity of several MBq is needed. Such an activity allows to obtain enough statistics and a good signal-to-noise ratio in reasonable integration time[21]. The LNGS is authorized to handle maximally 8 MBq ^{228}Th. In Table 16, the simulated rates for a 4.8 MBq ^{228}Th source at a distance of R = 6.85 m from the center are compared to the rates from a Borexino run taken under normal conditions without any source.

A ceramic matrix material is typically used in commercial ^{228}Th sources to incorporate the radioisotope. Interactions of α particles from the ^{228}Th chain with low-Z nuclides in the ceramic can produce neutrons. The neutron source strength depends on the activity of the ^{228}Th source and on the chemical composition of the ceramic. Al_2O_3 and $NaAlSiO_2$ are two possible candidates [191]. For these two compositions the neutron source strength was calculated by Tarka et al. [191] using the MCNP code SOURCES 4A [190]. The calculated neutron source strength from a 5.4 MBq ^{228}Th source is 140 s^{-1} and 205 s^{-1} for Al_2O_3 and $NaAlSiO_2$, respectively. In both cases the

[21] Neutrino-like events, i.e. neutrinos, external background, intrinsic contaminants like ^{14}C and ^{210}Po in the scintillator and in the buffer represent a background for the external source calibration. The values given in Table 16 were estimated from normal runs without any source placed in the detector

F.V. radius R [m]	(0.25, 0.8) MeV MC: source [cph]	Data: bkgr [cph]	S/B	(0.8, 3.0) MeV MC: source [cph]	Data: bkgr [cph]	S/B
3.5	16	70	0.23	518	4.8	108
3.0	0.4	61	0.05	44	1.7	26

Table 16: Rates and the signal-over-background ratios for predicted γ rays from a point-like 4.8 MBq ^{228}Th source at 685 cm distance from the center of the detector. The prediction was based on simulations in [188] that were scaled to the the mentioned distance and source activity. As "background" we consider all events that typically occur during a normal run, i.e. neutrinos, contaminants in *Inner Vessel* etc. A data set of 307.7 d lifetime was used for its estimation. Different spherical *fiducial volumes* and energy windows were selected.

expected mean energy of the emitted neutrons is around 1.5 MeV.

Even though a neutron source strength of the order of 100 s^{-1} is not problematic for Borexino, strong limitations for the usage of neutron emitting sources were imposed by LNGS. The reason is a possible perturbation of other experiments at LNGS which e.g. try to directly detect *Dark Matter*. Due to this fact the production of a custom-made ^{228}Th source with suppressed neutron source strength became necessary.
It can be achieved by using materials which suppress (α,n) reactions. For instance, gold has an energy-threshold at 9.94 MeV for (α,n)-reactions, whereas the mean energy of α particles from the ^{228}Th chain is 6.5 MeV. Two possibilities are:

1. Th_2Au: The tetragonal inter-metallic alloy Th_2Au exists [192]. Such an actinide noble-metal system can be produced by arc melting of high-purity constituents under reduced argon atmosphere [193]. The production of such a ^{228}Th source was not explored.

2. ThO_2 on Au: The Universität Zürich, Switzerland, and the Paul-Scherrer Institut, Villigen, Switzerland, have developed a technique where a ThO_2 substrate is included in gold foil. So far, the custom design was pioneered only for weaker sources of ∼20 kBq sources by the two institutes. This technique was selected and adopted for the production of the Borexino ^{228}Th source which, however, has an activity of several MBq (see Section 5.2.2).

A non-commercial ^{208}Bi source could also be produced. ^{208}Bi is an unstable long-lived β^+ emitter (τ=3.65×10^{5}y) which emits purely 2.615 MeV and 0.511 MeV photons, the latter ones from positron annihilation. No neutrons are produced. Production methods of ^{208}Bi are fast neutron activation (energy threshold: 7.5 MeV) at reactor site or application of the Liquid Metal Ion Sources (LMIS) [194]. The production of such a ^{208}Bi source of MBq activity was not explored.

Procurement of a $ThCl_4$ solution The ^{228}Th for the custom-made Borexino calibration source was provided by Eckert & Ziegler Isotope Products Inc., Valencia, California, in the form of thorium tetrachloride dissolved in 1M HCl water solution.
Table 17 summarizes the characteristics of the liquid source in detail.
The ^{228}Th activity of the delivered solution is 5.77 MBq ± 15% (at 1σ; reference date: March 1, 2010) corresponding to 0.19 μg ^{228}Th. Besides ^{228}Th the solution also contains similar amounts of ^{230}Th and of the synthetic radioisotope ^{229}Th. Their contribution to the total activity is negligible (<0.03%).
Additionally, the solution contains 10 μg elemental zirconium. Zirconium was requested as a carrier

Activity	5.77 MBq ±15%	Reference date:	March 1, 2010
Chemical composition	$ThCl_4$ in 1 ml HCl(1 M)		
Carrier	10 μg Zr		
Isotope composition	Nuclide	Weight [%]	Activity [%]
	^{228}Th	34.844	99.9703
	^{229}Th	39.620	0.0295
	^{230}Th	25.238	0.0002
	^{232}Th	0.299	0.0000

Table 17: Data sheet of thorium solution delivered by Eckert & Ziegler Isotope Products Inc. The isotope composition was provided by Oak Ridge National Laboratory.

during precipitation, which is a well-established radiochemical method for the separation of a given radioisotope from other radioactive species. Even though the carrier ions could be removed by placing the thorium tracer and zirconium carrier in 9-12 M HCl and removing the zirconium with anion exchange resin [195], it was not considered within the production of the Borexino source for two reasons: (1) to guarantee maximal transfer of activity from the initial to the final product[22], (2) Zr has an energy threshold E_t=7.95 MeV for (α,n)-reactions, therefore a small contribution from Zr to the neutron source strength of the final product is expected [191].

5.2.2 Production of a custom-made 5.4 MBq ^{228}Th source

Expertise in ^{228}Th source production prior to Borexino The ^{228}Th source for Borexino was build at Institut für Kernchemie, Mainz, Germany.
Prior to the production of the Borexino ^{228}Th source in March 2010, the Swiss institutes Paul Scherrer Institut and the Physik-Institut der Universität Zürich applied the technique to the construction of three ^{228}Th calibration sources for the GERDA experiment starting from ∼20 kBq $ThCl_4$ solutions [191]. The procedure turned out to be highly sensitive to the environmental conditions: applying apparently the same technique the transfer of activity in its final product was ∼100% in 2 cases and only ∼35% in 1 case. In order to avoid an uncontrolled release of activity in case of the MBq ^{228}Th source for Borexino, dedicated tests were performed at the Paul-Scherrer-Institut. The general conclusions were that (a) an electrostatic charge of environment, (b) larger residues of ^{228}Th solution on used equipment and (c) a adding to much heat to the ^{228}Th compounds in the liquid/solid phase have to be avoided.

Experimental setup The ^{228}Th source for Borexino was produced at Institut für Kernchemie, Mainz. The production took place within a glovebox installed in one out of three shielded nuclear radiation containment chambers (so-called *hot cells*) which are connected to an air filter system. The air filter system was required for the collection and controlled release of ^{220}Rn (daughter nuclide from ^{228}Th) to the atmosphere. The instruments, materials and chemicals used within the glovebox for the production of the Borexino ^{228}Th source are listed below and are shown in Figure 65:

- precast 25 μm thick gold crucible and gold envelope; for a single source approximately 6 cm^2 of gold foil are required

[22]The activity of the final source has to be high enough in order to collect enough statistics in the Borexino detector within 1-2 weeks planned for a typical external calibration campaign.

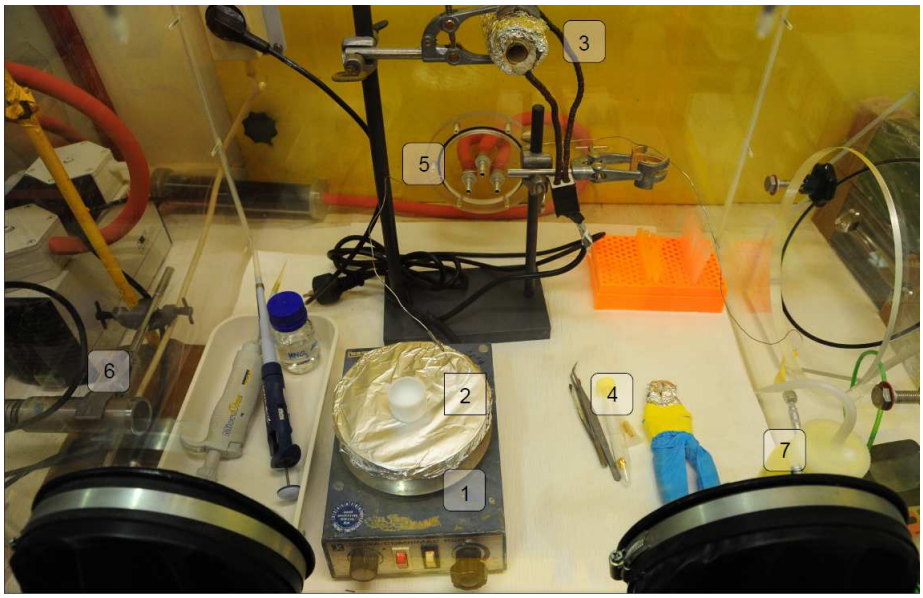

Figure 65: Setup for the production of the test source and of the Borexino source: 1. heater 2. teflon beaker with conical cavity 3. oven 4. precast gold crucible and gold cover 5. connection to air filter system 6. real-time dosimeter 7. distilled water

- heater: used for the chemical conversion of the $ThCl_4$ solution into $Th(NO_3)_4$ and after transfer of $Th(NO_3)_4$ into the gold crucible. The heater was covered with aluminum foil, grounded and connected to a temperature sensor located outside the glovebox.
- Oven: used for the conversion of $Th(NO_3)_4$ into ThO_2
- Pipettes: (a) 5 ml for transfer of $ThCl_4$ solution; (b) 100 μl for transfer of $Th(NO_3)_4$ into the gold crucible; the used polypropylene tips were Tipac C20/TJ from GILSON
- Teflon beaker with conical cavity
- HNO_3 acid
- Distilled Water: used to keep a high humidity within the glovebox, avoiding electrostatic charge of inner surfaces of the glovebox
- Two 5 cm thick lead bricks: installed between the two gloves for radioprotection (not visible in Figure 65)
- real time dosimeter: placed behind glovebox for monitoring the activity in vials, the transfer of activity and the contamination of used instruments.

Procedure The reliability of the setup and of the procedure at Institut für Kernchemie, Mainz, was successfully tested extracting 5 μl from the original 1 ml $ThCl_4$ solution for the production of a test source. Subsequently, the same procedure was applied to the production of the main ^{228}Th source for Borexino. The thermal conditions of the processing steps for both ^{228}Th sources are given in Table 18.
The production steps are:

1. Conversion of $ThCl_4$ into $Th(NO_3)_4$ (Figure 66, top left):
   The $ThCl_4$ solution is pipetted into a teflon beaker with conical cavity, few ml of HNO_3 are added and heated at T∼115°C for ∼3 hours. The following reaction takes place:

$$3\,ThCl_4 + 16\,HNO_3 \xrightarrow{\sim 115°C} [3\,Th(NO_3)_4]_s + [4\,NOCl + 8\,H_2O + 4\,Cl_2]_g \qquad (5.1)$$

   where *s* stands for solid phase and *g* for gaseous phase.
   $Th(NO_3)_4$ is generated and left in a solid state in the teflon cavity, while the remnants nitrosylchloride, water and chloride evaporate. To avoid any loss of activity the teflon beaker was covered with a glass fiber filter. Condensed gas on it did not show any contamination. The residue activity in the glass vial was washed out with HNO_3 several times and added to the $Th(NO_3)_4$ already present in the teflon beaker. The heater was grounded to avoid electrostatic charge.

2. Transfer of $Th(NO_3)_4$ into gold crucible (Figure 66, top right):
   Gold foil of thickness d=25μm was used to form a crucible. 1 ml HNO_3 was added to the $Th(NO_3)_4$ in order to transfer the thorium nitrate to the gold crucible. It was heated at T∼120°C for ∼30 min evaporating the HNO_3. Meanwhile, the teflon beaker was washed out several times.
   In principle, the conversion of $ThCl_4$ into $Th(NO_3)_4$ could occur directly in the gold crucible, which would minimize the number of intermediate steps. However, it was shown [196] that the foldings of the gold crucible have strong capillarity forces moving $Th(NO_3)_4$ to the border of the gold crucible. Moreover, HNO_3 in combination with HCl forms a highly corrosive solution known as *aqua regia* (typically 1M HCl, 3 M HNO_3) which dissolves gold. To prevent a spill the gold foil must be thick enough.

3. Conversion of $Th(NO_3)_4$ into ThO_2 (Figure 66, bottom left):
   The gold crucible is folded but not hermetically. Then, it is inserted into an oven and heated at T∼650°C. At this temperature, residual organic compounds volatilize and the $Th(NO_3)_4$ compounds are broken. $Th(NO_3)_4$ releases NO_2 and O_2 and forms a ThO_2 substrate on the inner surface of the gold foil:

$$3\,Th(NO_3)_4 \xrightarrow{\sim 650°C} [3\,ThO_2]_s + [12\,NO_2 + 3\,O_2]_g \qquad (5.2)$$

4. Folding of gold crucible (Figure 66, bottom right):
   The gold crucible was folded and inserted in a second gold cover. This was folded again several times in order to prevent a loss of activity.

5.2.3 Encapsulation and sealing

The ^{228}Th gold foil was sent to Eckert & Ziegler Nuclitec GmbH for encapsulation and sealing.
A double encapsulation made of 1.4571 stainless steel was selected for the inclusion of the radioactive gold foil. The profile and a photo of the selected encapsulation (type: VZ-3474-002) are shown in Figure 67. The encapsulation is mounted on a screw which allows to fix it with a rod or an appropriate electrician's fish tape if required.
After sealing, several leakage and contamination tests were performed. The results fulfilled the following criteria: the removed activity with a wipe moistened with ethanol is <200 Bq and after immersion of the source in a suitable liquid at 50°C for at least 4 h <200 Bq (ISO classification C.11111). After the arrival of the ^{228}Th source at LNGS an additional wipe test was performed to ensure that the source was unaffected by the transportation. It was found that the upper limit of the activity on the outer surface of the source encapsulation is 10 mBq [197].

Figure 66: Production of the Borexino ^{228}Th source (from left, top, to right bottom): Conversion of $ThCl_4$ into $Th(NO_3)_4$; Transfer of $Th(NO_3)_4$ into gold crucible; Conversion of $Th(NO_3)_4$ into ThO_2; Insertion of gold crucible into gold cover.

Chemical process	Test source (5 μl): 30 kBq	Borexino source 1 ml: 5.77 MBq
Conversion: $ThCl_4 \rightarrow Th(NO_3)_4$	$T_1 = 115°C$ $T_2 = 120°$ C $dt_{1\rightarrow2} = 2h\ 52$ min	$T_1 = 109°C$ $T_2 = 113°$ C $dt_{1\rightarrow2} = 2h\ 45$ min
Transfer of $Th(NO_3)_4$ to gold crucible + HNO_3 evaporation	$T_1 = 116°$ C $dt_1 = 21$ min	$T_1 = 130°$ C $T_2 = 119°$ C $dt_{1\rightarrow2} = 37$ min
Breaking off $Th(NO_3)_4$	$T_1 = 0°$ C $T_2 = 660°$ C $T_3 = 199°$ C $dt_{1\rightarrow2} = 12$ min $dt_2 = 19$ min $dt_{2\rightarrow3} = 15$ min	$T_1 = 0°$ C $T_2 = 645°$ C $T_3 = 230°$ C $dt_{1\rightarrow2} = 37$ min $dt_2 = 20$ min $dt_{2\rightarrow3} = 9$ min

Table 18: Thermal conditions and duration of chemical processes during production of the test source and the Borexino source at Institut für Kernchemie, Mainz.

Figure 67: Photos of the inclusion of the radioactive gold foil into the double encapsulation of the Borexino ^{228}Th source. The profile of the encapsulation is shown on the right, the lengths are given in millimeters. (Images courtesy of Eckert und Ziegler Nuclitec GmbH)

5.2.4 Characterisation of the Borexino ^{228}Th source

Activity transfer from the $ThCl_4$ solution to the final ^{228}Th source The production method of the Borexino ^{228}Th source was based on a chemical-thermal treatment of a $ThCl_4$ solution. For the individual production steps several tools and materials were used, these were partly contaminated. In case of larger residues, they were recollected e.g. by adding new HNO_3 solution to the teflon beaker. Unpredicted losses of activity (e.g. on glovebox walls) due to non-ideal environmental conditions could have significantly reduced the activity of the final source and thus the expected statistics from a calibration in Borexino. In this case, it would have been mandatory to search for the radioactive residues and to reinsert them in the final source. In order to exclude this worst-case hypothesis, several γ spectroscopic measurements were carried out at Institut für Kernchemie in Mainz directly before and after the production of the source: The $ThCl_4$ solution in the original glass vial was measured before the source production. The ThO_2 embedded in gold was measured several times after the source production. For the measurements a High Purity Germanium Coaxial Detector manufactured by Ortec was used. The energy range was set to [40,2000] keV. Its *full width half maximum* is 1.8 keV at the 1.33 MeV γ line from ^{60}Co.
The count rates were calculated according to [198]. Self-absorption effects of the final source were taken into account. The first measurement after the source production showed a deviation of $\sim$25% from the original activity value. A second measurement 8.33 d after the source production showed only a deviation of maximally 9%. Thus, during the first measurement the secular equilibrium of the ^{228}Th decay chain was distorted, whereas it was restored prior to the second measurement.
The main conclusion is that the yield of activity transfer to the final ^{228}Th source is larger than 91% (at 1σ). Even though the result still had a large uncertainty, this interim result was satisfactory, so the custom-made source could be sent to Eckert & Ziegler Nuclitec GmbH for encapsulation (see Section 5.2.3).

Estimation of the absolute activity of the Borexino ^{228}Th source The activity of the Borexino ^{228}Th source after sealing was only known with a large uncertainty. The uncertainty consisted of (1) the $\pm$15 % error (k=1) of the activity of the initial $ThCl_4$ solution, (2) the activity loss on instrumentation (tweezers, cones, vials) during the source production (from 1629 keV γ line:

Nuclide	Energy [keV] [keV]	Branching ratio [%] [%]	Corrected count rate [10^6 events/s]
^{212}Pb	238.6	43.3	2.05 ± 21%
^{208}Tl	538.2	30.4	4.63 ± 11%
	2614.5	35.6	5.41 ± 6%

Table 19: Count rates of three prominent γ lines from the Borexino ^{228}Th source. The count rates were corrected only for the branching ratios of the corresponding γ lines. Thus, the corrected count rates of lower energetic γ rays are suppressed due to self-absorption effects in the source encapsulation. The reference date is March 1, 2010.

<9% (k=1)), (3) the not completely restored secular equilibrium during the first γ spectroscopic measurements and (4) the energy-dependent absorption of γ rays due to the 1 mm thick gold foil and the 1.4 mm thick stainless steel capsule.
Since an accurate estimation of the absolute activity is of interest for several analyses, a dedicated measurement campaign was carried out at LNGS Outside Buildings 209 d after the source production. At this time the broken secular equilibrium was fully restored.
The method was based on a comparison of the activities of the Borexino ^{228}Th source and of a calibrated reference ^{228}Th source by means of γ spectroscopy.
The activity of the reference ^{228}Th source was selected in order to exceed the background of the environment also at a larger distance from the detector, such that both ^{228}Th sources could be treated as point-like sources. For this purpose a calibrated ^{228}Th source with an activity of A_r=297 kBq ± 5% (at 2σ; Reference date: March 1, 2010) was selected.
The used γ spectrometer was a Broad Energy Germanium detector (BEGe) manufactured by Canberra. The energy range of this detector was set to approximately [20,3000] keV and its *full width half maximum* is 1.7 keV at the 1.33 MeV γ line from ^{60}Co and 0.57 keV at the 59.5 keV γ line from ^{241}Am.
For the measurement the ^{228}Th sources were placed one by one in ∼162 cm distance from the detector. At this distance both sources can be assumed to be point-like. One measurement for each of the two ^{228}Th sources and one of the background were carried out. The spectra are shown in Figure 68.
The evaluation was carried out according to [198]. The obtained results are summarized in Table 19. The measured count rates of single γ lines corrected by their branching ratios are not equal due to self-absorption in the source encapsulation. They differ by more than factor of 2 in the range of [238,2615] keV. For the high-energetic 2.615 MeV γ rays a corrected count rate of (5.41 ± 0.30)×10^6 counts/s is obtained (reference date: March 1 2010). Taken into account the activity loss during the source production and the intrinsic attenuation (between 4% and 11% for 2.615 MeV) there is a very good agreement between the final source activity (within the encapsulation) and the initial activity of the $ThCl_4$ solution.

Measurement of the neutron source strength In order to estimate the reduction of produced neutrons from the custom-made Borexino ^{228}Th source compared to those from commercial sources, the source was sent to the Physikalisch-Technische Bundesanstalt (PTB) after sealing to measure the neutron source strength. The measurements and the following analysis were conducted by B. Wiegel and A. Zimbal, PTB.
The measurements were carried out using a spherical helium-3 (^{3}He) neutron proportional gas counter of type SP9 manufactured by Centronic Ltd, Croyden, UK. The gas pressure is 200 kPa. The detector is most sensitive to thermal neutrons (E<1 eV) and is normally used in conjunction

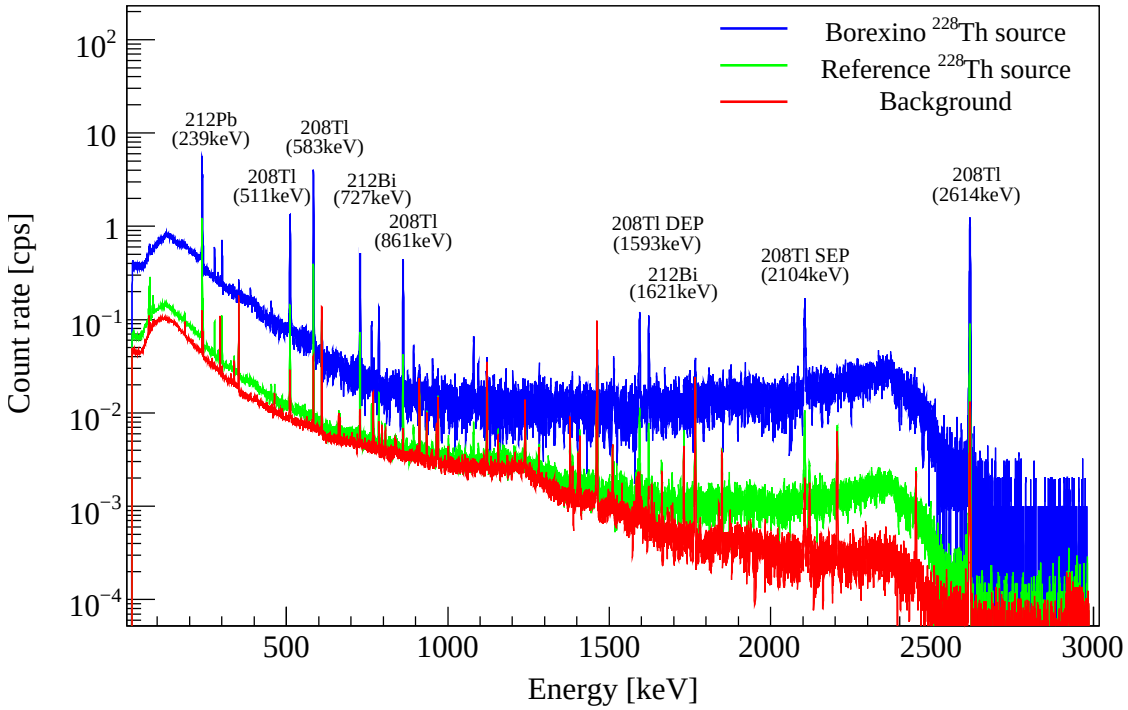

Figure 68: Energy spectrum of the Borexino ^{228}Th source and the ^{228}Th reference source at a distance of ∼162 cm from BEGe detector. The γ rays contributing to the background stem from the environment and intrinsic contamination of the detector. The count rates are expressed in counts per second [cps].

with a moderator material, in this case with a paraffin block of size 50×75×50 cm^3. The detection reaction is based on the interaction of the moderated neutrons with ^{3}He atoms, i.e. ^{3}He(n,p)^{3}H, in which two charged particles are released with a Q-value of 764 keV.
The γ rays entering the detector can also ionize ^{3}He atoms, but with a much lower efficiency than the moderated neutrons. So in principle the SP9 counter is well-suited for γ-n discrimination. However, in case of the Borexino ^{228}Th source the ratio of γ rays to neutrons was expected to be in the range of 10^5 to 10^6. These circumstances required a feasibility study, in which the neutron source strengths under such extreme conditions were measured. For this purpose, the detector was exposed to (a) a 11 GBq ^{137}Cs γ source (alone), (b) to a ^{252}Cs neutron source with neutron source strength of 4×10^5 s^{-1} (alone) and (c) to the combined sources. It was found that the software threshold in the pulse height spectrum had to be increased. Using the new settings it could be demonstrated that the high γ ray activity does not perturb the neutron efficiency of the SP9 counter.
The estimation of the neutron source strength of the Borexino ^{228}Th source was performed in three stages.
First, the SP9 counter was placed alone in the paraffin block in an appropriate holder to measure the background of the setup. The resulting background events, exceeding the aforementioned DAQ settings, are due to high energetic neutrons from cosmic radiation, which cannot be shielded above ground, and intrinsic contamination of the counter itself. The latter contribution accounts for only 2% of the total background [199]. The cosmic induced contribution is anti-correlated to the air pressure: lower neutron fluence rate at high air pressure and vice versa [200]. However, for the present measurement this effect is negligible and thus was not corrected.
In a second step, the energy-dependent efficiency of the experimental setup had to be determined

Reference source (rs)	Reference	E_{mean} [MeV]	B_{rs} [s^{-1}]	c_{rs}	Reference date
^{241}AmBe	[201]	4.05	72829 ± 1736	1806.3 ± 43.1	March 23, 2010
^{241}AmB	[202]	2.61	149570 ± 1081	1706.4 ± 12.3	May 8, 2010
^{252}Cf	[201]	2.13	1131906 ± 16979	2063.6 ± 31.0	May 6, 2010

Table 20: List of used reference neutron sources. The mean energies E_{mean}, the neutron source strengths B_{rs} (unit: number of emitted neutrons per second) and the non-normalized efficiencies c_{rs} are reported.

for the planned source position in the paraffin block at 20 cm from the SP9 counter. This was done by using radionuclide sources of known neutron source strength and different mean energy. ^{252}Cf, ^{241}AmB and ^{241}AmBe were used. These sources have a mean energy of 2.13 MeV, 2.61 MeV and 4.05 MeV, respectively. Their characteristics and the estimated efficiencies c_{rs} for the presented setup are summarized in Table 20. The expected energy spectrum of the Borexino ^{228}Th source was estimated in [191] via the MCNP code SOURCES A4. It was calculated for ThO_2 embedded in gold. The resulting mean energy is 2.41 MeV. The contribution of (α,n) reactions from the 10 μg Zr present in the original $ThCl_4$ solution was estimated to be small. The contribution from the presence of possible iron residues was also regarded as negligible. Looking at the mean energies of the reference sources in Figure 69, ^{241}AmB is closest to the ^{228}Th source. Therefore, the efficiency value c_{rs} obtained for ^{241}AmB was used for the estimation of the neutron source strength B_{Th} of the Borexino ^{228}Th source.

The measurements to determine the neutron source strength of the Borexino ^{228}Th source were conducted out from April 23 to May 4, 2010. The lifetime of all data is 264 hours. The source was again placed in an appropriate holder within the paraffin block at 20 cm from the SP9 counter. Then the neutron source strength B_{Th} was calculated according to:

$$B_{Th} = f_c \cdot c_{AmB} \cdot N_{Th} \tag{5.3}$$

Herein f_c is the correction factor due to the choice of the factor c_{rs}, $c_{AmB} = B_{AmB}/N_{AmB}$ the efficiency factor for ^{241}AmB and N_{Th} the background corrected count rate of the ^{228}Th source. N_{Th} is calculated by $N_{Th} = N_{bgTh}$ - $f_{NTh}N_{bg}$, where N_{bgTh} is the measured count rate of the ^{228}Th source including the background, f_{NTh} is the air pressure correction factor and N_{bg} the background rate. N_{AmB} is calculated analogue to N_{Th}.
The correction factors f_c, f_{NTh} (and f_{NAmB}) were normalized to 1, but are required for the correct calculation of the uncertainty budget according to [203]. As shown in Table 20, the source dependent efficiencies c_{rs} spread about 15%. From a separate uncertainty propagation calculation it was found that f_c=(1±0.121). The anti-correlation of the background count rate to air pressure was not corrected, but an uncertainty of (1 ± 0.072) was assigned to both correction factors f_{NTh} and f_{NAmB}.
The measured count rate of background events is N_{bgTh}=(7.26±0.11)h^{-1} and the count rates from the ^{228}Th and ^{241}AmB sources including the background is N_{Th}=(20.38±0.28)h^{-1} and N_{AmB}=(3.1555 ± 0.0012)×10^5 h^{-1}. By taking into account the total uncertainty budget, the neutron source strength of the Borexino ^{228}Th source was estimated to be:

$$B_{Th} = (6.22 \pm 0.80) s^{-1} \tag{5.4}$$

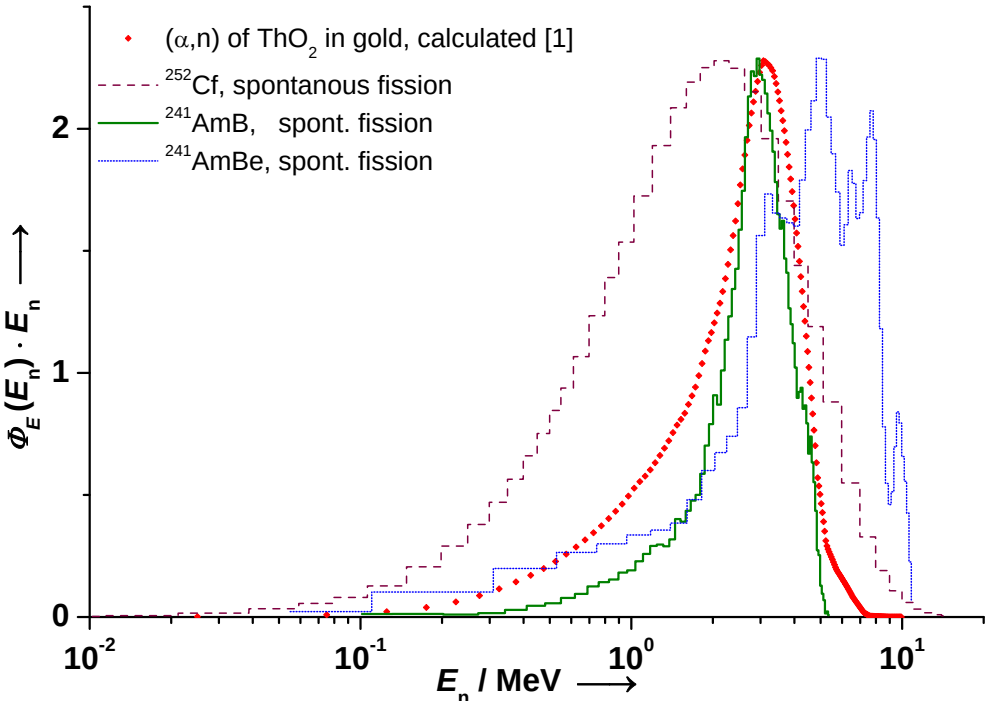

Figure 69: Energy spectra of different neutron sources: the expected Borexino ^{228}Th source spectrum (calculated by M. Tarka) is compared to the reference spectra of ^{252}Cf, ^{241}AmB, ^{241}AmBe (by B. Wiegel and A. Zimbal, PTB).

The uncertainty assigned to f_c and f_{NTh} contributes to 87% and 9% of the total error of B_{Th}. The statistical error of the count rate N_{bgTh} is the third largest contribution at 2.7%.
The neutron source strength was obtained for the reference date April 29, 2010 (00:00 UT) from an 11-day measurement. By scaling back the result to the common reference date of March 1, 2010, the mean value and its uncertainty (1σ) become $(6.60 \pm 0.85)s^{-1}$.

5.2.5 Full characterisation of the custom-made ^{228}Th

The custom-made ^{228}Th source for the Borexino experiment is unique for several reasons:
To our knowledge it was the first time that a custom-made ^{228}Th source of MBq activity was successfully produced beginning with a $ThCl_4$ solution that was chemically-thermally treated in order to include ^{228}Th in a gold foil. The adopted technique was designed to reduce the production of unwanted neutrons that are typically produced in (α,n) reactions in commercial ^{228}Th sources. The adopted procedure showed a high yield in the transfer of the activity of the original solution to the final product.
After the production the Borexino ^{228}Th source was completely characterized in terms of activity, neutron source strength, radiation dose and sealing properties. Table 18 summarizes all results. The activity of the 2.615 MeV γ rays could be determined with a good precision to be 5.41 MBq $\pm$ 6%. The neutron source strength is $6.60s^{-1} \pm 13\%$. This is several times less than from commercial sources based on ceramics compositions. Taking into account the ratio 3×10^5:1 of long-range 2.615 MeV γ rays to emitted number of neutrons, the estimation of the neutron source strength set a milestone in terms of background suppression for ^3He neutron proportional gas counters.
A detailed description of the production and characterisation of the Borexino ^{228}Th source will be

Type:	$^{228}ThO_2$ in gold foil
ID number:	SR-837
Encapsulation:	Type VZ-3474-002; doubled capsule made of 1.4571 stainless steel
Sealing:	ISO classification C.11111
Half life of ^{228}Th:	1.9116 y
Activity:	
$ThCl_4$ solution: A_S	5.77 MBq ± 15% (1σ)
^{228}Th source: relative:	$>0.91 \cdot A_S$ (1σ)
^{228}Th source: absolute:	5.41 MBq ± 6% (1σ) measuring 2.615 MeV
Neutron source strength:	
SOURCES 4A calculation [191]	$\sim$3 s^{-1} Pure ThO_2, E_{mean}=2.41 MeV)
Measurement:	(6.58 ± 0.84) s^{-1} (Ref.: ^{241}AmB, E_{mean}=2.61 MeV)
Dose in 1 cm distance:	
Literature [205]:	10.1 mSv/h (secul. eqlb. assumed; all daughter nuclides included)
Measurements	12.1-14.3 mSv/h (2 dosimeters used)

Table 21: Full characterisation of the custom-made Borexino ^{228}Th source. For reasons of comparison, all values and limits are referred to March 1, 2010. The uncertainties were scaled to this date, using the same factor as used for the mean values.

published in [204].

5.3 First external calibration campaign in Borexino

The first external calibration campaign was performed between July 5 and July 14, 2010. At this time, the emission rate of the long-range 2.615 MeV γ rays emitted from the Borexino ^{228}Th source was $(1.67\pm0.10)\times10^6$ counts/s.
Data were taken for three different positions in the detector. Their coordinates are given in Table 22.
On July 5, 2010 the ^{228}Th source was placed in position N2*. This position is located in the northern hemisphere of the detector inside the buffer at a distance of 50.4 cm from the inner surface of the Stainless Steel Sphere (SSS). At this position, the ^{228}Th source induced a large amount of signals: even though the Borexino Trigger Board (BTB) energy threshold was set to 250 (maximal value: $2^8 = 256$) the trigger rate was still at 150 Hz and $\sim$4.6 GB/h of data were collected.
On July 6, 2010 the signals from the most-exposed PMTs were tested showing no anomaly despite

Position	x [m]	y [m]	z [m]	Positioned in
N2*	3.95	-0.70	4.91	Buffer
N2	4.28	-0.76	5.34	Water Tank
N6	2.57	-0.76	-6.35	Water Tank

Table 22: Positions of the ^{228}Th source during the first external calibration campaign. They are referred to the Cartesian Borexino coordinate system. The uncertainty of the absolute value of the vectors is in the range of few cm.

of the high trigger rate. However, the ^{228}Th source was moved back by (55.1±0.5) cm. This should guarantee a good quality of data, avoid troubles with electronics and the DAQ system and reduce the collection of large amounts of data. In addition, the muon trigger was disabled to achieve a more stable DAQ system[23]. The new position of the ^{228}Th source called N2 is located (4.7±1.0) cm behind the inner surface of the SSS. Figure 71 depicts the positioning of the source in the detector. At this position, the SSS is 8 mm thick and the tube diameter is 12.7 mm. Therefore, the radiation of the ^{228}Th source entering the *Inner Vessel* is slightly collimated. The trigger rate decreased to acceptable 12.4 Hz for a BTB threshold of 250.
In the following days, the BTB threshold was gradually lowered with the purpose of extending the energy range to the lowest possible value. Table 23 reflects the impact of the modified BTB threshold on DAQ.
On July 9, 2010 the ^{228}Th source was extracted from the detector and moved to the southern hemisphere. The new position of the source called N6 is again located (4.6±1.0) cm behind the inner surface of the SSS. Here the thickness of the sphere is 12 mm, the tube diameter 12.7 mm. The trigger rate induced by the ^{228}Th source in position N6 was lower than in position N2 for a given BTB threshold. This is related to the fact that the buffer layer in the southern is approximately 30 cm thicker than in the northern hemisphere of the detector.
On July 12, 2010 the first *Water Extraction Cycle* in Borexino started (see Section 3.4.1). The external calibration campaign continued with two short interruptions of 3 hours and 1 hour to take normal runs 13728 (July 12, 2010) and 13741 (July 13, 2010) for background monitoring. During these runs, the ^{228}Th source was parked in the Water Tank of Borexino inside the external calibration tube system. The distance between the source and the Stainless Steel Sphere was approximately[24] 1-2 m.
On July 14, 2010 the ^{228}Th source was extracted from the detector and stored at LNGS Outside Buildings.

5.4 Analysis of energy and position reconstruction

Before studying the impact of the measured energy spectrum obtained from the external ^{228}Th source on neutrino analyses, it is important to analyze the detector response in terms of energy and position reconstruction. This is the aim of the present section which is divided in four parts: (1) data selection, (2) energy response for different source positions including the energy scale and its resolution, (3) position reconstruction of events for different source positions including the possibility to scan the *Inner Vessel* shape and (4) Monte Carlo simulations.

[23]The Muon trigger (Outer Detector) and the Main DAQ (Inner Detector) are known to interfere, the effect is stronger under extreme conditions such as a high trigger rate. By switching off the muon trigger, the Inner Detector continues to provide an independent flag when a muon crosses the detector, so muons are still tagged.

[24]The position could not be established exactly since the precise location of the polyethylene tubes within the Water Tank is not known.

Figure 70: Representation of the source holder used for the ^{228}Th source during the first external calibration campaign in Borexino. The source holder is made of stainless steel and was welded with a fish tape. The picture on the right shows the source holder after embedding of the ^{228}Th source and before the first insertion into the detector (July 5, 2010). Adhesive foil was used to fix the screw of the source holder.

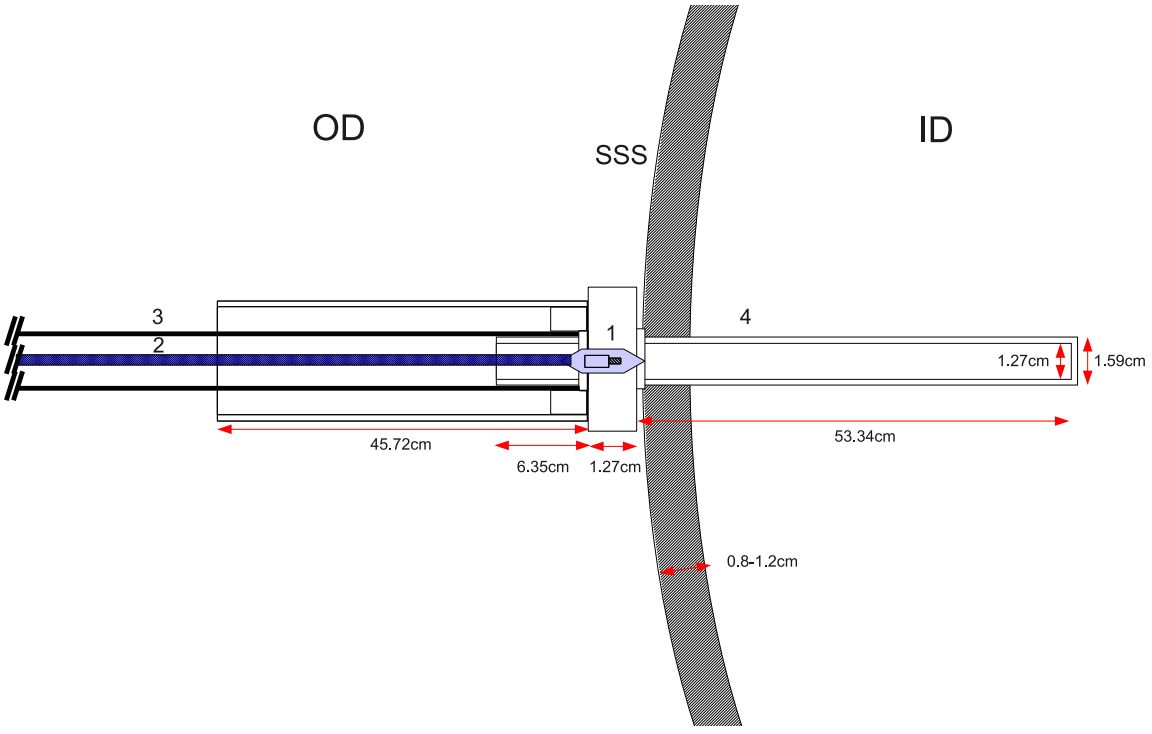

Figure 71: Positioning the ^{228}Th source in the Borexino detector. The source (1) is embedded in a source holder attached to a fish tape (2). Via one out of 14 polyethylene tubes (3) the source can be moved through the Outer Detector (OD) and inserted into the reentrant tube (4). The reentrant tube crosses the Stainless Steel Sphere (SSS) and ends in the outer buffer layer of the Inner Detector (ID).

Position	BTB	Runs	Trigger [Hz]	Rate [10^3 events/h]	File [MB/h]
N2*	250	13561-13609	145	535	4600
N2	250	13610-13636	12.5	49	320
	200	13637-13654	20.5	79	410
	180	13655-13663	24	83	450
	100	13664-13686	26	99	470
N6	200	13687-13688	6	27	150
	100	13689-13699	7.6	63	170
	80	13701-13727	8.5	71	180
		13729-13740	8.5	71	180
		13742-13756	8.5	71	180

Table 23: BTB thresholds during the first external calibration campaign in Borexino. The BTB threshold was gradually decreased in order to access the lowest possible energy without exceeding a predefined trigger rate of ∼30 Hz. The source in position N2 and N6 has the same distance to the center of detector. However, the rate in N6 is lower due to the 30 cm thicker buffer layer in the southern hemisphere of the detector. Screen shots of the Borexino online monitor and of the scalers during source insertion are shown in Appendix A.5.

All data were processed and evaluated within *Echidna cycle 12* (see Section 3.2.1). The most updated position reconstruction algorithm, which was developed by the *LNGS* Borexino group, and the charge variable (unit: photoelectrons [p.e.]) were used (see Section 3.2.1). The charge variable was chosen owing to its larger dynamical range at higher energy values (i.e. above 1-2 MeV) compared to the *number-of-hits* variable. In addition, after applying the analytical correction defined in Equation (4.18) to the charge variable it can be converted into an SI-based energy scale.

5.4.1 Data selection

During the external calibration in Borexino, the detector was exposed to an extraordinary high rate of high-energetic 2.615 MeV γ rays. It was expected that it might affect the DAQ and thus the energy and position reconstruction. This section is dedicated to a systematic study of the quality of acquired data in order to reject problematic runs and to define a reliable data-set of maximal statistics.

General considerations Figure 72 shows the energy spectra of events induced by the presence of the external ^{228}Th source deployed in the position N2. The lifetime of the data-set used is six hours. Only single-cluster events with the pulse-shape variable *mean_time_short* <100 μs were considered. Spectrum (a) contains all events deposited in the *Inner Detector* (R<6.85 m) while spectrum (b) represents only those events that were reconstructed within a spherical *fiducial volume* with radius R<3.5 m. The energy spectra show the expected behavior: The *full-energy peak* of the 2.615 MeV γ rays is accompanied by a Compton continuum at lower energies. The Compton continuum is gradually suppressed the smaller the radius of the concentric spherical *fiducial volume* is. Figure 73 explains this by the fact that the main contribution to the Compton continuum arises from events which were reconstructed in the scintillator and in the buffer layers close to the *Inner Vessel*. The majority of these events are 2.615 MeV γ rays which were able to traverse the buffer shells with only partial energy dissipation. These Compton γ rays are absorbed more frequently than not yet scattered 2.615 MeV γ rays.

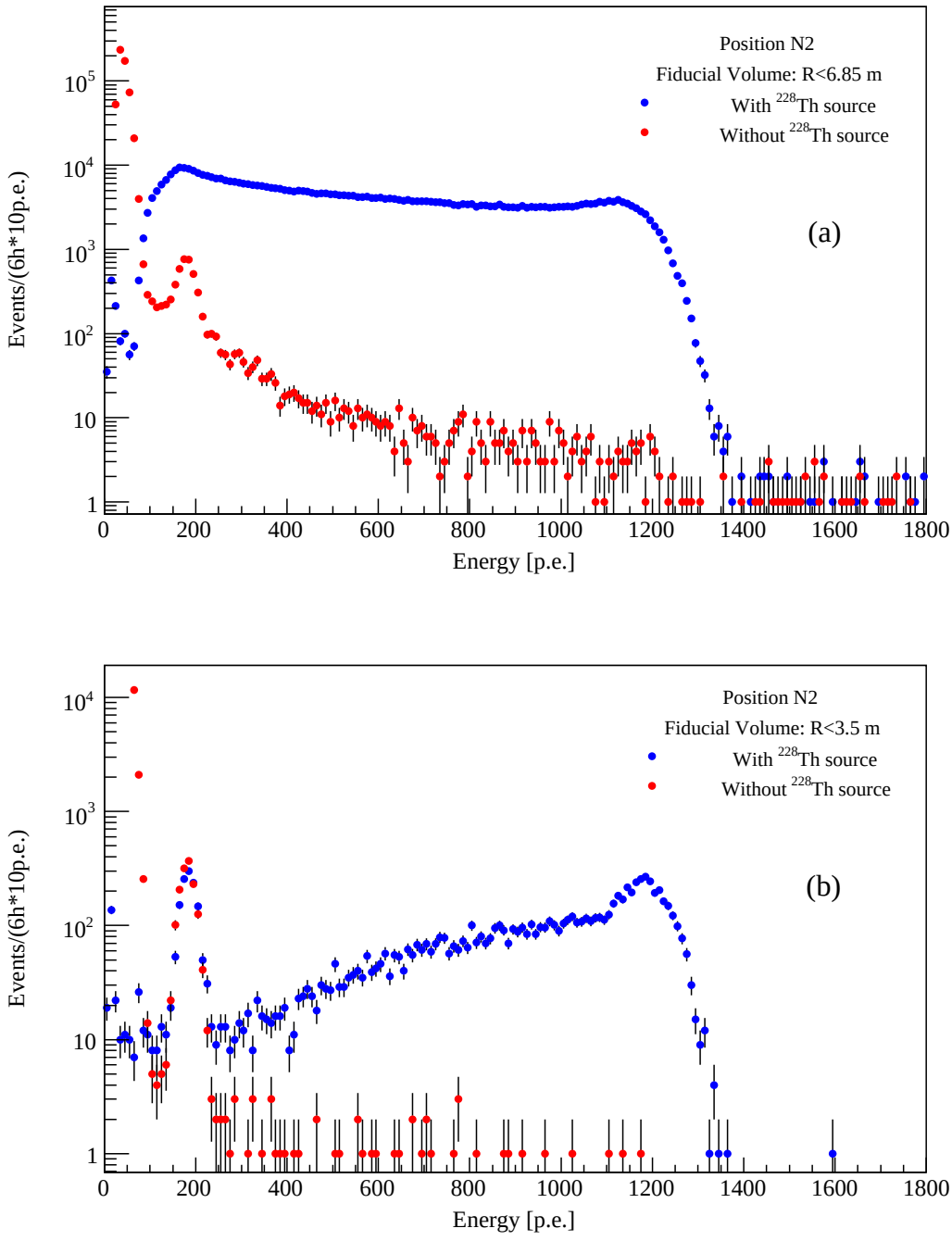

Figure 72: The energy spectrum of the external ^{228}Th source in position N2 is depicted for two spherical *fiducial volumes*. Their radius is R<6.85 m and R<3.5 m. For comparison a normal 6-hour run (♯ 13547) taken on July 4, 2010 (one day before the start of the external calibration campaign) is shown. The events in the normal run include neutrino events, contaminants in the scintillator like ^{238}U, ^{232}Th, ^{14}C, ^{210}Po, ^{210}Bi, the external background and muon-induced signals like ^{11}C. Above the ^{210}Po peak around 200 p.e (∼400 keV) these events represent a small background for the external calibration with the γ source.

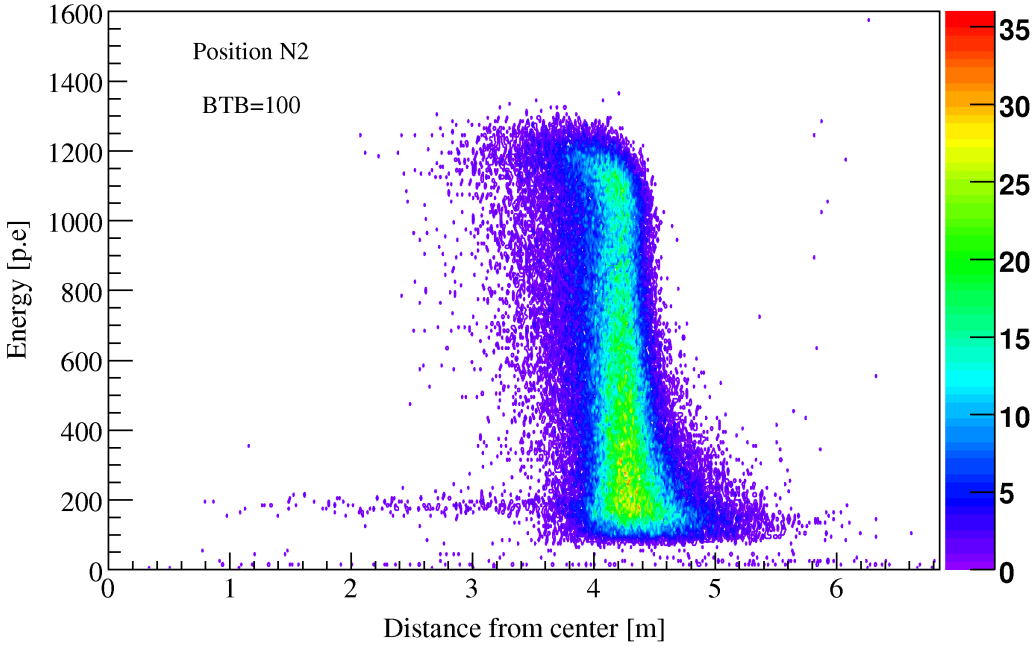

Figure 73: Contour plot of energy versus radial distance of reconstructed events from center of detector. The plot depicts the events from a 1-hour run taken with the Borexino ^{228}Th source in position N2 with a BTB energy threshold equal 100. The binning in distance is 1 cm/bin and in energy 10 p.e./bin. The transition between scintillator and buffer imposed by the *Inner Vessel* occurs at ∼4.25 m.

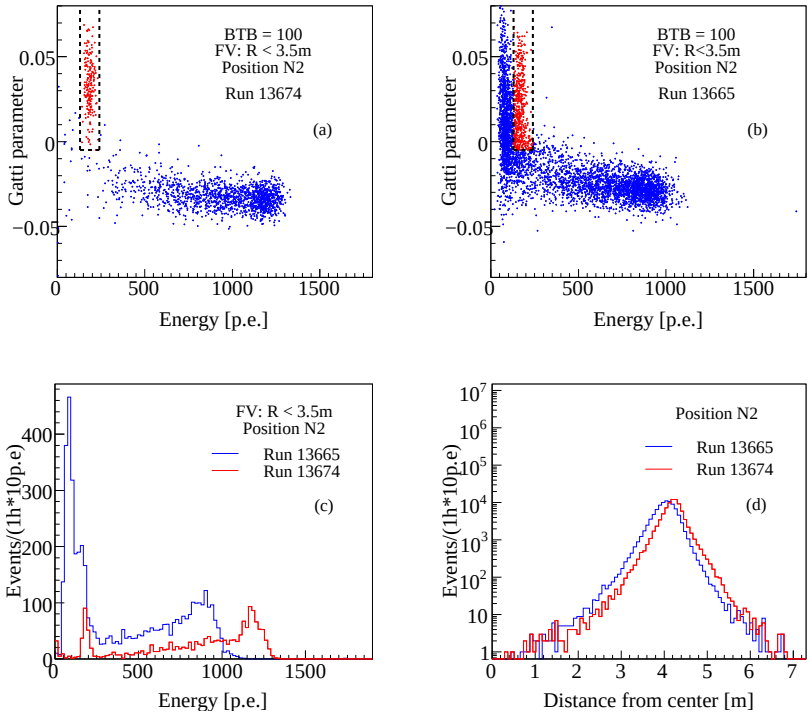

Figure 74: Comparison of one problematic (♯ 13665) and one non-problematic run (♯ 13674) taken with the ^{228}Th source in position N2. The energy spectra, the Gatti parameter and the radial distribution are compared in order to distinguish them.

The energy spectra shown in Figure 72 terminate at smaller energies around ∼100 p.e. owing to the BTB trigger threshold set to 100. The edge is not sharp. However, the spectra also show events below this edge in the region below ∼30 p.e. These events are present in the entire *Inner Detector* as shown in Figure 73 and they can be attributed to noise events.
Additionally, the energy spectra in Figure 72 depict a characteristic peak arising around 190 p.e which is attributable to ^{210}Po. It is the only background that is clearly visible besides the events induced by the external γ source. Contrary to expectations, the presence of the ^{210}Po peak turns out to be useful for the present analysis. As shown in panel (a) of Figures 74-76, the Gatti parameter of the α-like ^{210}Po events clearly separates these events from the β-like events induced by the ^{228}Th external source. On the one hand, a change of the ^{210}Po can be used as an indicator for problematic runs. On the other hand, the ^{210}Po peak can be rejected with a high efficiency for *fiducial volumes* with radii R≤3.5 m by applying the following software cut:

$$\Delta E = [130{,}240]\,\text{p.e. with Gatti parameter} \geq -0.005 \tag{5.5}$$

Exclusion of problematic data The extraordinary situation for the detector and for the DAQ system exposed to the high rate of γ rays from the external ^{228}Th source might have led to a wrong energy and/or position reconstruction of events in the collected data. The following study aims at individualizing possible "problematic runs" in the calibration data. For this purpose, all runs taken with the same DAQ settings and with the same source position are compared. The first step of this selection process consists of finding anomalies in the energy spectrum, such as a shift of the *full-energy peak* of the 2.615 MeV γ rays or a non-expected spectral shape modulation. In a second step, the Gatti parameter is plotted against energy: in case of a problematic run, there is a shift in

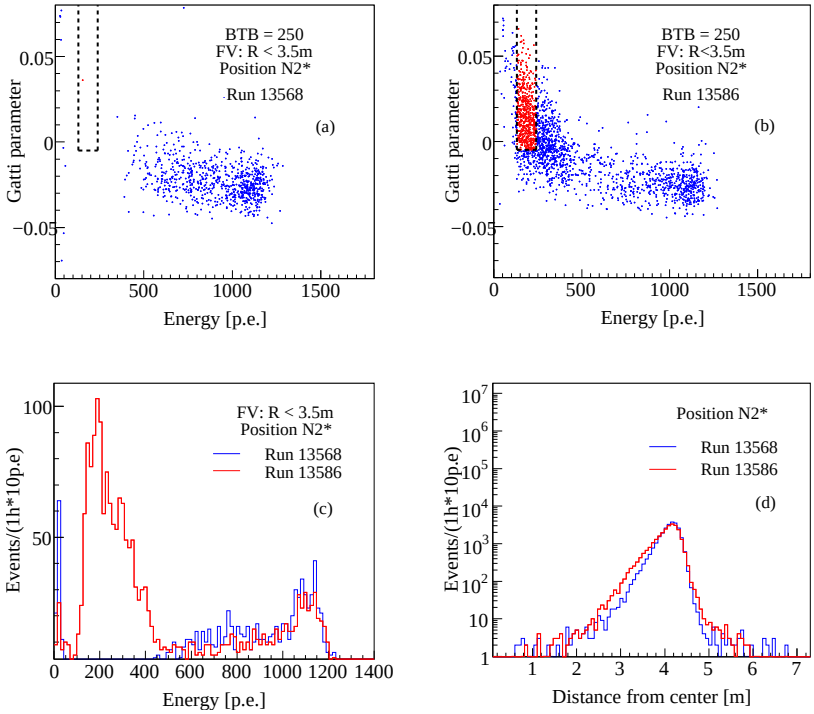

Figure 75: Same as in Figure 74 for runs taken with the ^{228}Th source in position N2*. The problematic run is ♯ 13586, while the non-problematic run is ♯ 13568.)

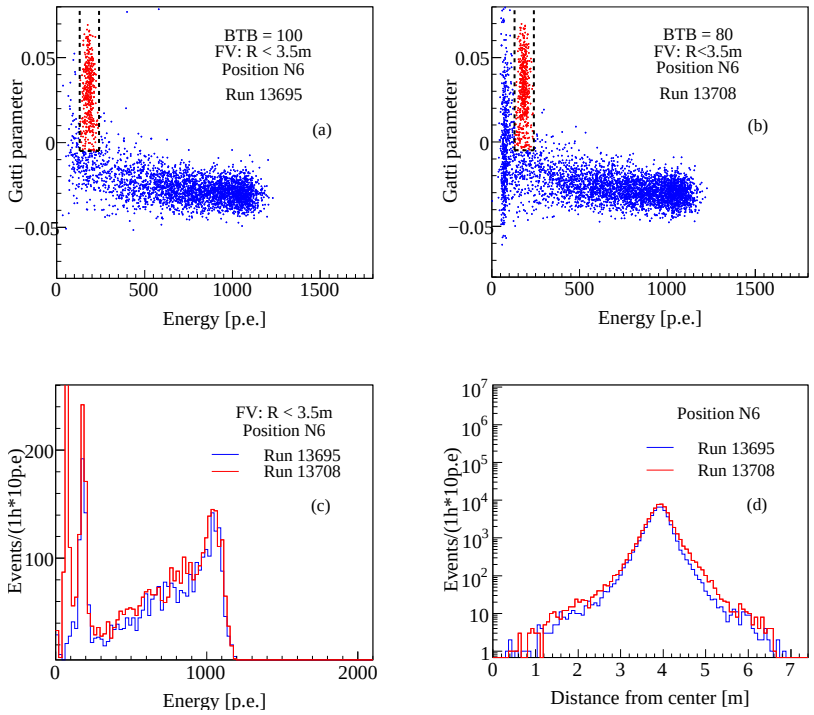

Figure 76: Comparison of two non-problematic runs taken with the ^{228}Th source in position N6. Run ♯ 13695 was taken with an energy threshold BTB=100, run ♯ 13708 with BTB=80. The additional events in the second run at lower energies $\lesssim$90 p.e. seems to be mis-reconstructed. Thus, an energy cut at <90 p.e. should be applied offline to all data.

source position	total lifetime [h]	non-problematic runs [h]	percentage [%]
N2*	17.96	7.72	43.0
N2	69.58	49.12	70.6
N6	108.97	108.97	100.0

Table 24: Lifetime of data collected during the first external calibration campaign in Borexino with the percentage of non-problematic runs taken in the three different positions.

energy to lower values of the external background events, but also a shift of the α particles from ^{210}Po. Finally, the radial distributions of problematic and non-problematic runs are compared.
Within the data collected in the three different source positions N2, N2* and N6, several runs with problematic energy spectra were found. The general problems are discussed in the following section:
Two representative runs taken with the ^{228}Th source in position N2 are shown in Figure 74. In the case of the problematic run, the *full-energy peak* of 2.615 MeV γ rays is shifted to lower energies by $\sim$23%. The Compton continuum sometimes shows a secondary maximum at $\sim$(700-900) p.e. The problematic run also contains a large quantity of α-like events shifted to $\sim$(100-150) p.e. Finally the reconstructed position of events is shifted inwards by $\sim$20 cm.
The characteristic properties of problematic runs taken with the ^{228}Th source in position N2* are shown in Figure 75. Even though the BTB threshold was set to 250, there are many α-like events in the approximate energy range (100,400) p.e. The reconstructed position of events is partially shifted inwards.
Concerning data collected in source position N6, all runs turn out to have a comparable energy spectrum down to 100 p.e. and thus the same quality. Runs taken with lower energy thresholds with BTB=80 show an increased number of mis-reconstructed events below 100 p.e. Comparing spectra from runs taken in source position N2 and N6, there is a shift of $\sim$9% to lower energies for N6. The assumption that all runs taken in source position N6 are problematic is wrong. This will be explained as a North-South asymmetry of the detector in Section 5.4.2.
The collected statistics of non-problematic data vary for the different source positions. They are summarized in Table 24. Note that the runs taken in source position N6 are all non-problematic. A detailed list of all runs is given in Table 36 in Appendix A.4. The effect causing "problematic runs" during the calibration with the external ^{228}Th source is related to the fact that a trigger rate of high-energetic (<2.615 MeV) events exceeding $\sim$20 Hz becomes problematic for the electronics chain[25]. Indeed, the DAQ worked in a more stable manner in source position N6 where the rate was reduced compared to position N2 due to the thicker buffer layer (see Tables 23 and 24).

Compatibility of data acquired with different energy thresholds During the first external calibration campaign, the BTB threshold was continuously lowered with the aim of extending the energy range to the lowest possible value without exceeding a problematic trigger-rate above $\sim$30 Hz. This is important for the study of the induced Compton continuum which becomes relevant the larger the *fiducial volume* is. Concerning source position N2, the BTB threshold was lowered in the following steps: 250, 200, 180, 100. In case of the source position N6 the BTB threshold was set mainly[26] to 100 and 80. The values BTB=100 and BTB=80 were found to be ideal for the main source positions N2 and N6, respectively. Table 23 reflects this approach.

[25] In normal runs the trigger rate is $\approx$12 Hz with a BTB=20, most of the events are low-energetic ^{14}C decays (<0.25 MeV)

[26] There are also two runs taken with BTB=200; due to the total lifetime of only 1.7 h these runs are not considered.

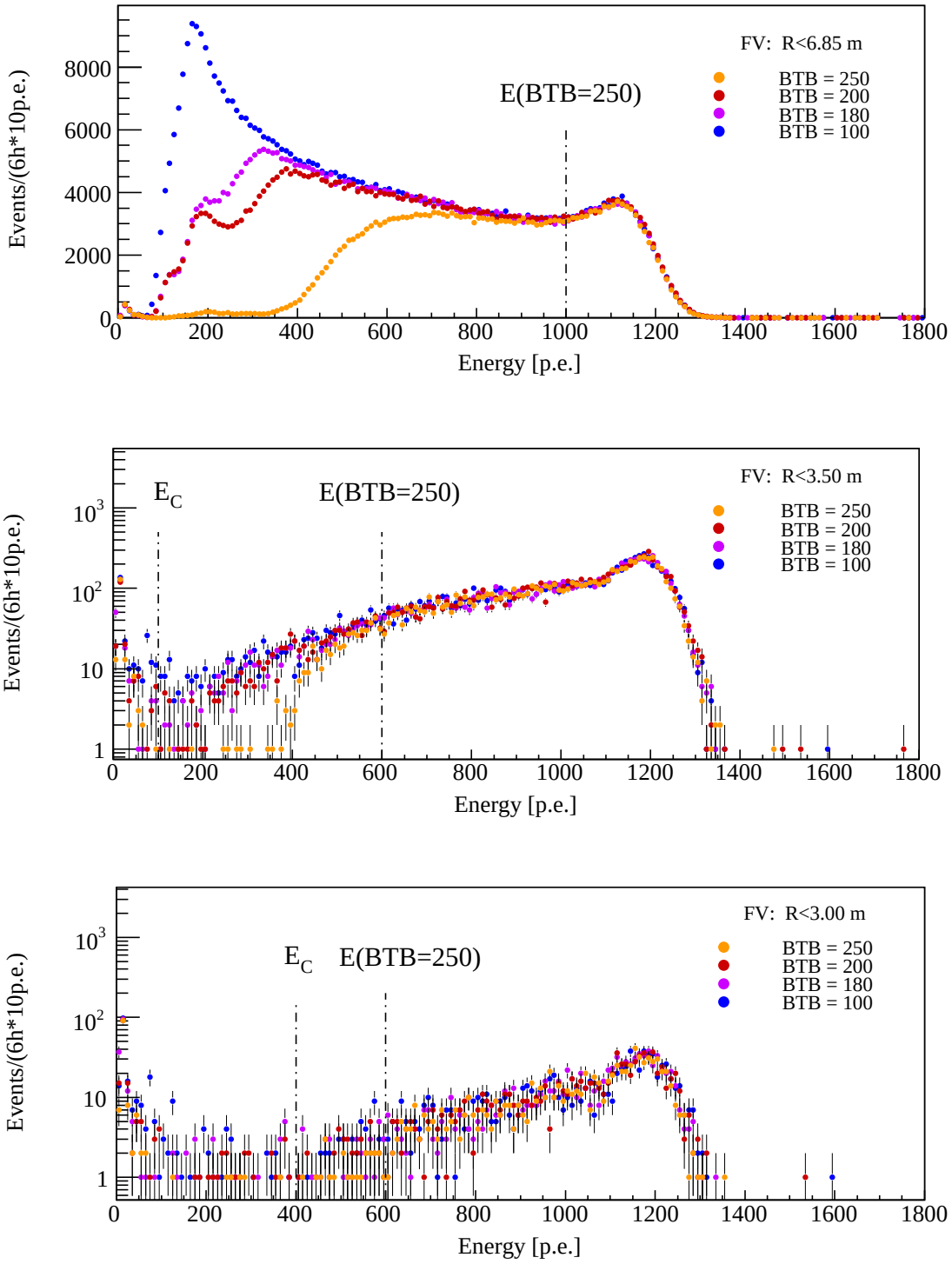

Figure 77: Energy spectra induced by the external ^{228}Th source for different *fiducial volumes* with radius R. The source position was N2 and the runs were taken with BTB thresholds 100, 180, 200 and 250. For *fiducial volumes* with radii lower than R<3.5 m, the Gatti cut in Equation (5.5) was applied. Further details are given in the text.

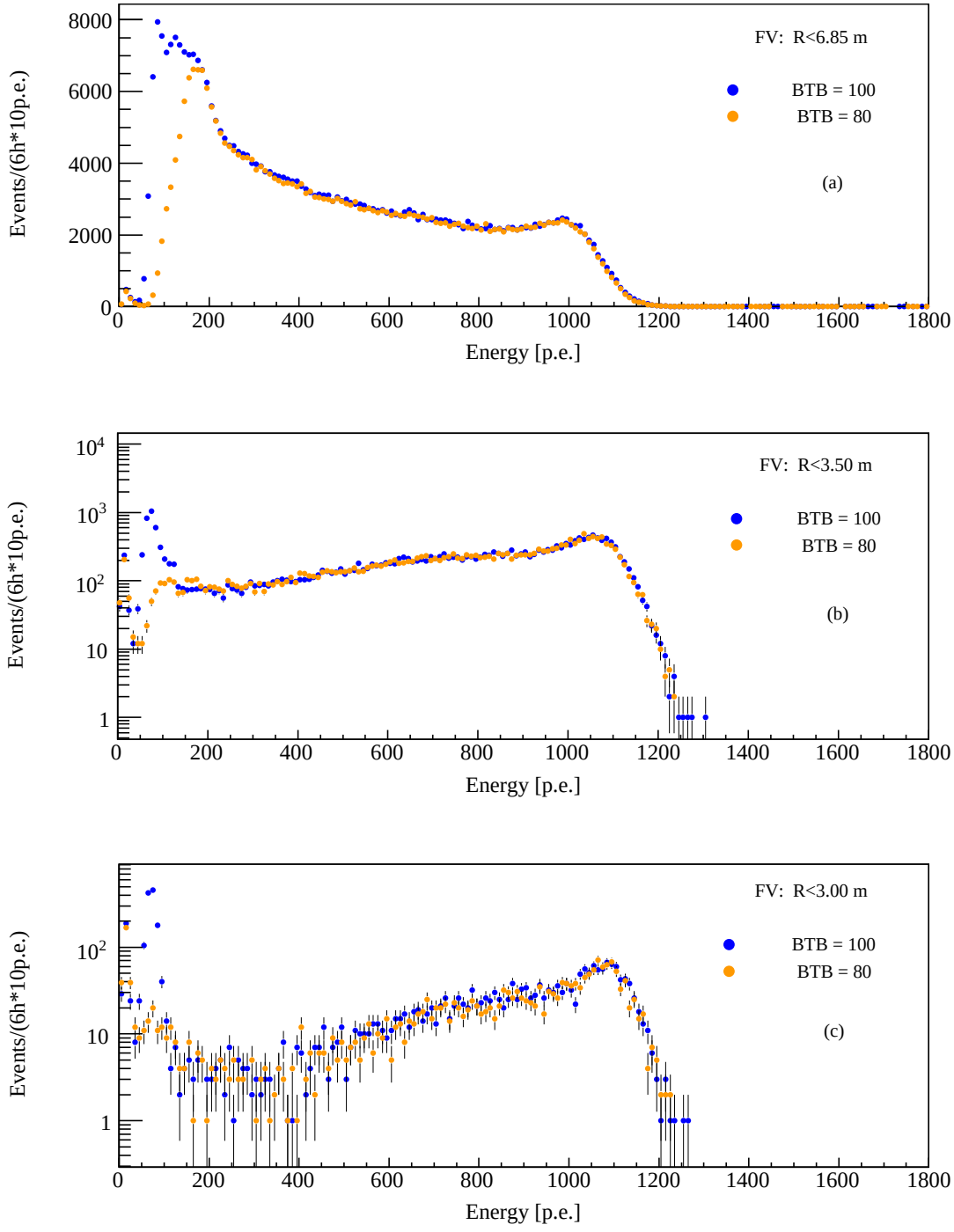

Figure 78: Energy spectra induced by the external ^{228}Th source for different *fiducial volumes* with radius R. The source position was N6 and the runs were taken with BTB thresholds 80 and 100. For *fiducial volumes* with radii lower than R<3.5 m, the Gatti cut in Equation (5.5) was applied. Further details are given in the text.

FV R [m]	E_C [pe]	E(BTB=100)	E(BTB=180)	E(BTB=200)	E(BTB=250)
6.85	0	100	500	650	1000
4.0	0	100	300	400	800
3.5	100	100	180	200	600
3.0	400	400	400	400	600
2.5	700	700	700	700	700

Table 25: Superposition of energy spectra taken with different BTB thresholds for the source position N2. The lower edge of the Compton continuum depends on the *fiducial volumes* radius R and is denoted with E_C. The energy value above which the reference energy spectrum taken with BTB=100 overlaps with the Compton continuum is denoted by E(BTB=100). The energy values above which the energy spectra taken with BTB>100 overlap with the reference spectrum are defined by E(BTB=N) where N>100. All energy values are in p.e. units and are approximative.

FV R [m]	E_C	E(BTB=80)	E(BTB=100)
6.85	0	80	100
4.0	0	80	100
3.5	0	80	100
3.0	400	400	400
2.5	700	700	700

Table 26: Analogue caption to Table 25 for source position N6. The reference energy spectrum has a BTB threshold equal 80. All energy values are in p.e. units and are approximative.

In order to obtain energy spectra and radial distributions of events with maximal statistics, one has to examine the possibility to superimpose data from runs taken with different BTB thresholds. This is demonstrated here for data collected with the source in position N2, where the lowest BTB threshold was set equal to 100.
First of all, the possibility to superimpose energy spectra obtained with different BTB energy thresholds depends on the *fiducial volume* radius. For each *fiducial volume* radius R we estimate the lowest energy E_C at which the Compton continuum ends. Above the energy value E(BTB=100), the reference energy spectrum taken with BTB=100 overlaps with the Compton continuum. Finally, above the value E(BTB=N) the energy spectrum with a BTB threshold N>100 superimposes with the reference spectrum. Then, the following relation can be defined: $E_C \leq$ E(BTB=100) $\leq$ E(BTB=N). If E(BTB=100)=E(BTB=N) is fulfilled, the spectra taken with a BTB threshold >100 can be superimposed with the reference spectrum.
Figure 77 shows the energy spectra obtained from data with different BTB thresholds for three different *fiducial volumes* of radius R. The top plot includes the energy spectra with events reconstructed within a in R<6.85 m, where the Compton continuum ends at E_C=0 keV. A line at 1000 pe marks the approximative threshold E(BTB=250) above which the energy spectrum at BTB=250 superimposes with that at BTB=100. The energy spectrum of events reconstructed within a *fiducial volumes* of radius R<3.5 m is shown in the middle plot of Figure 77. The Gatti cut in Equation (5.5) was applied. The Compton continuum ends around E_C ∼100 pe and E(BTB=250) drops to ∼600 pe. In the lower plot of Figure 77, the *fiducial volumes* radius was R<3.0 m. In this case, E_C becomes ∼400 pe and E(BTB=250)∼600 pe.
Figure 78 reflects the situation for energy spectra obtained from data which were acquired with the source in position N6.

All results are summarized in Table 25 for source position N2 and in Table 26 for source position N6.

Note that the reported values are approximative. The main conclusion from this analysis is that for a *fiducial volume* with radius R$\lesssim$3.5 m all runs acquired with BTB<180 can be superimposed. For R$\lesssim$3.0 m all runs with BTB<250 can be superimposed.
Further details about the shape of the energy spectra obtained in source positions N2 and N6 for different *fiducial volumes* are discussed in Section 5.4.2.

5.4.2 Analysis of the energy spectra

General considerations Figures 77 and 78 show the energy spectra obtained for the main positions N2 and N6. The Compton continuum decreases as a function of the radius R of the *fiducial volume*. It becomes slightly separated from the 2.615 MeV *full-energy peak* only for radii R below 3.0 m. Additionally, the Compton continuum is characterized by two quantities: (1) The end point at lower energies as a function of the radius R and (2) the ratio ρ between the number of events in the *full-energy peak* and the number of residue events distributed in the Compton tail. The first property was already defined in Section 5.4.1. The ratio ρ is defined as follows: The *full-energy peak* at 2.615 MeV is fitted with a Gaussian in the range that is not affected by the Compton continuum. Then the integral of the Gaussian is calculated and compared to the total number of residue events in the histogram.
The following analysis uses the maximum available statistics collected in the single source positions N2 and N6. The analysis focuses on spherical *fiducial volumes* with radii R smaller than 3.5 m, 3.0 m and 2.5 m which are relevant for neutrino analyses. Runs taken with different BTB thresholds are superimposed according to Tables 25 and 26. At lower energies, the Gatti cut in Equation (5.5) is applied and a lower threshold is set to 130 p.e. since mainly mis-reconstructed events are expected to contribute below this threshold.
In the following analysis the energy is expressed in units of the normalized charge variable Q_{rec} which has already been introduced in Equation (3.7). Since the formula modifies the energy value attributed to the events, the range of the Gatti cut in Equation (5.5) is adjusted to [130,400] npe.

Corrections of the charge variable and the energy scale The normalization of the charge variable according to Equation (3.7) leads to the spectra shown in the left plots of Figure 79. It is obvious that the *full-energy peak* for source position N6 is still shifted to lower energies if they are compared to those from position N2. Since position N6 lies in the southern hemisphere, where most of the disabled PMTs are located, this is attributed to a geometrical effect which still has to be corrected. An analytical expression has already been found during the internal calibration campaign, using the 2.2 MeV γ rays of an ^{241}Am^{9}Be source deployed in 29 positions [156]. The maximum distance of the ^{241}Am^{9}Be source from the center was 4.0 m including the region of interest of the present study. The linear correction function takes into account the North-South asymmetry in z direction, but also effects in the xy plane:

$$Q_{corr} = Q_{rec} \cdot \frac{1}{(1 + A \cdot Z \cdot |Z|^n + B \cdot |Z|^k)} \cdot \frac{1}{1 + C \cdot \left(\frac{d}{1+|Z|}\right)} \tag{5.6}$$

where d is the distance from the z axis, d=$\sqrt{(x^2 + y^2)}$, and A=8.65$\times 10^{-3}$, B=4.93$\times 10^{-5}$, C=2.1$\times 10^{-3}$, n=0.58, k=5.75.
Equation (5.6) was normalized to 1 for the central position. For this position, a second empirical expression which was already introduced in Section 5.4.1 can be used to define the energy scale in terms of MeV units. For this purpose we replace Q_{rec} in Equation (4.18) with Q_{corr} in Equation

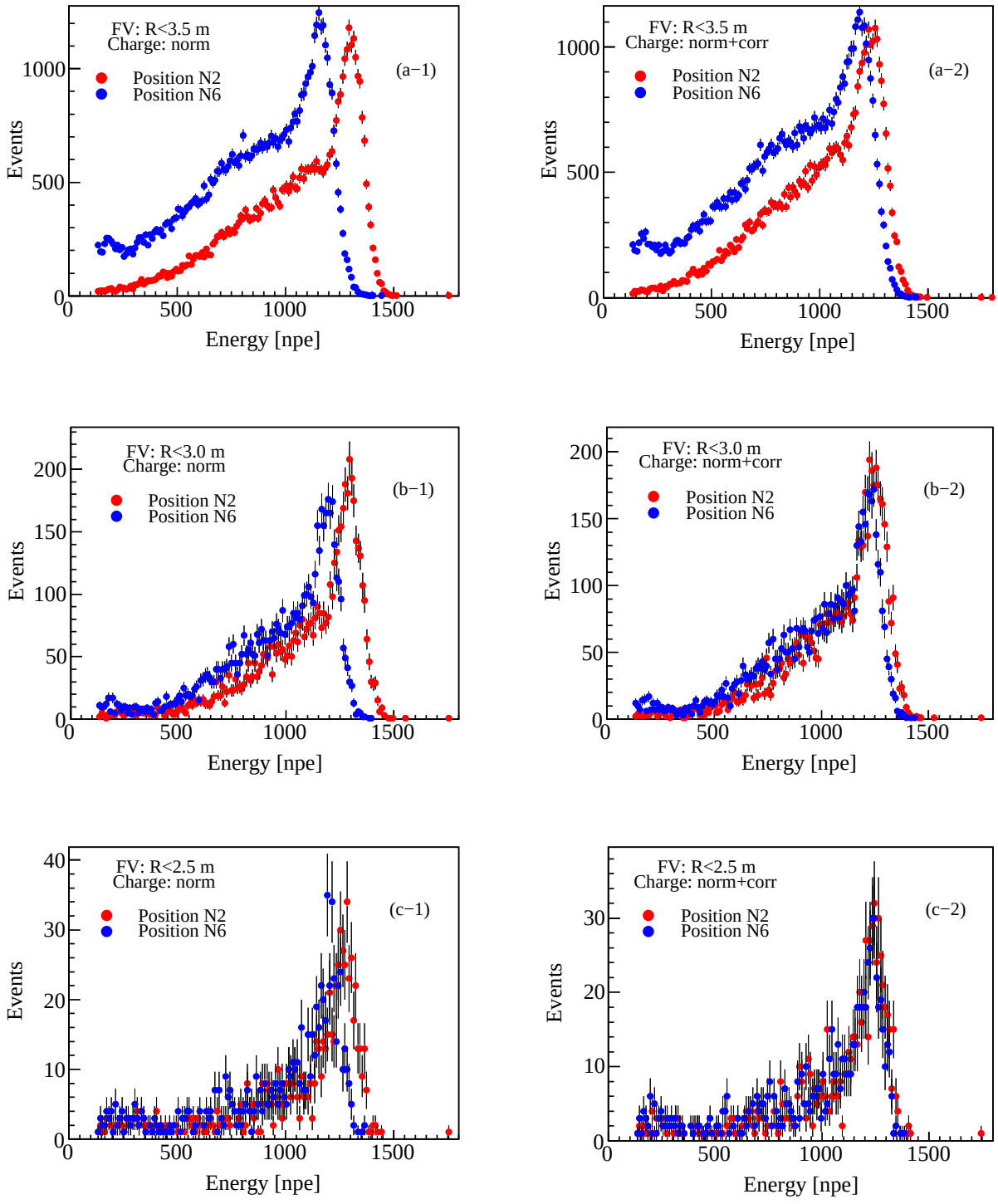

Figure 79: Energy spectra induced by the external ^{228}Th source placed in the northern (N2) and in the southern (N6) hemisphere of the Borexino detector. The North-South asymmetry is more distinctive for larger *fiducial volumes*. The charge correction leads to a notable improvement. However, only for a *fiducial volume* with radius R$\lesssim$3.0 m the corrected energy spectra taken with both source positions start to overlap.

Pos.	R [m]	E [npe]	E [MeV]	dE [%]	ρ	E_C [npe]	E_C [MeV]	dE_C [%]	ρ_C
N2	<3.5	1284.1±0.8	2.66	1.9	0.7	1229.2±0.9	2.55	-2.5	0.7
	<3.0	1277.4±1.8	2.65	1.4	0.9	1237.9±2.1	2.57	-1.8	1.1
	<2.5	1265.5±4.5	2.62	0.4	0.9	1238.7±4.9	2.57	-1.7	1.0
N6	<3.5	1161.7±2.3	2.41	-7.9	0.4	1188.5±0.9	2.46	-5.7	0.4
	<3.0	1190.9±2.9	2.47	-5.6	0.6	1218.2±1.9	2.53	-3.4	0.7
	<2.5	1205.2±6.0	2.50	-4.4	0.7	1225.4±4.5	2.54	-2.8	0.8

Table 27: Estimation of the mean value of the *full-energy peak* from 2.615 MeV γ rays emitted by the ^{228}Th source in positions N2 and N6. The uncorrected charge variable Q_{rec} (left) and the corrected one Q_{corr} (right) are reported for the study of the North-South asymmetry. The deviation dE and dE_C from the expected value at 2.615 MeV is given in percentage. The ratios ρ and ρ_C between the amount of the *full-energy peak* and the Compton events are also reported.

(5.6).
Table 27 summarizes the corrected and scaled mean values E_C of the *full-energy peak* at 2.615 MeV for the three different *fiducial volumes* with R smaller than 3.5 m, 3.0 m and 2.5 m and for both source positions N2 and N6. For *fiducial volumes* of radii smaller than R<3.0 m the values are only 1.7-3.4% lower than the nominal value at 2.615 MeV.
Table 27 also includes the scenario of applying Equation (4.18) directly to the uncorrected normalized charge variable Q_{rec}. In this case, the *full-energy peaks* that were obtained with the ^{228}Th source in position N2 and N6 would still differ by ∼7% and ∼10% for R<3.0 m and R<3.5, respectively.

Superposition of energy spectra from different source positions The most important question is related to the possibility of superimposing the energy spectra obtained from both source positions N2 and N6. If this is the case, the external background from the Stainless Steel, the PMTs and the light concentrators can be approximated in first order by the energy spectra obtained from the point-like γ source. In the negative case, one can use the energy spectra from the ^{228}Th source to tune a Monte Carlo code that is designed to simulate the entire spherical external background. From the right panels in Figure 79 it becomes clear that the correction according to Equation (4.18) leads to a notable improvement of the overlap of the energy spectra from source positions N2 and N6. However, for a *fiducial volume* with radius R<3.5 m, the *full-energy peaks* still have an energy shift of ∼4%. For *fiducial volumes* with radius R<3.0 m and R<2.5 m, the difference decreases to ∼2% and ∼1%. The observed energy shift can be explained by the fact that Equation (4.18) was tuned on 2.22 MeV γ rays, but might be energy dependent. The Compton continuum is higher for the source position N6 located in the southern hemisphere where the buffer layer is thicker (see Section 5.4.3). This is still visible for a *fiducial volume* with radius R<3.0 m: the *full-energy peak* obtained from source position N6 is decreased by ∼8% and the Compton continuum is increased. For R<2.5 m, the collected data is reduced, but the energy spectra seem to superimpose more accurately.
To quantify the difference between the energy spectra, the characteristic ratio ρ_C was introduced. Additionally, a Pearson χ^2 statistic tests of the histograms was performed as already used in Section 4.3.4. Using the original energy correction in Equation (4.18), the following results were obtained: For a *fiducial volume* with radius R<3.0 m, the histograms are non-identical (reduced χ^2/n.d.f. = 580/135), for R<2.5 m however, the probability of identity is >0.062 (χ^2/n.d.f. = 152/127).
From these observations one concludes that for a *fiducial volume* with radius R$\lesssim$3.0 m the measured energy spectra can be used as a first-order approximation in neutrino analyses. A complete

estimation of the global external background can be achieved by a specially developed Monte Carlo simulation that has previously been tuned on the ^{228}Th source measurements.
For a smaller *fiducial volume* with radius R<2.5 m, the measured energy spectra correspond to the overall shape of the external background and thus its spectral shape can be used as a fit component in neutrino analyses.

5.4.3 Analysis of the radial distribution

General considerations This paragraph is dedicated to the study of the radial distribution of the events induced by the external ^{228}Th source. In order to perform a correct analysis, the author of this thesis only used non-problematic runs (Section 5.4.1) in which the position reconstruction was successful (see Figures 74-76). However, the resulting spectrum is still affected by contaminants which have other radial distributions and hence distort the pure radial distribution of external γ rays from the ^{228}Th source. The contaminants are related to α particles from ^{210}Po in the bulk and impurities in the nylon of the *Inner Vessel*. In addition, there are noise signals below ∼120 npe (see Figure 73).
In this section, all three components are excluded by the following cuts:

- Rejection of the surface contamination of the *Inner Vessel*: The radius of the *fiducial volume* is set to R<3.5 m
- Rejection of ^{210}Po α particles: The Gatti cut in Equation (5.5) (with the energy-range corrected for [npe] according to Equation (5.6) is applied.
- Rejection of noise signals: All events with energy E<120 npe were rejected.

The radial distributions of the non-excluded events were subdivided into different energy ranges. The energy regions are [2.61,2.71] MeV, which includes a subsample of *full-energy peak* 2.615 MeV γ rays, and [0.80,2.72] MeV, which is relevant for the *pep* and CNO neutrino analysis.
Figure 80 depicts the radial distribution of events with energy [2.61,2.71] MeV which were measured while the source was positioned in position N2 and N6.
A first interesting parameter is the measurement of the absorption length λ in the aforementioned energy ranges. The results are summarized in Table 28. In the presented approach it is assumed that the γ rays emitted from the source are collimated. Hence, the radial distribution is fitted by a pure exponential function $e^{(-r/\lambda)}$. Energy events populating the Compton continuum tends to lead to a smaller[27] λ: Looking at the energy interval [0.80,2.72] MeV, one obtains λ=(25.4±0.2) cm and λ=(24.1±0.2) cm for both source positions N2 and N6, respectively. Considering only the energy events in the *full-energy peak* lying above the peak maximum at 2.615 MeV, the attenuation length is λ=(30.3±0.6) cm and λ=(26.7±0.4) cm for the source positions N2 and N6. The last two values are similar but not in agreement within their errors. The reason is that Compton-scattered γ rays contribute to the *full-energy peak* in a different way for the two source positions, introducing a systematical error which was not included in the total uncertainty budget. For comparison, the attenuation length for pseudocumene with a density of ρ=0.8761 g/cm^3 was calculated for 2.615 MeV γ rays using the NIST Photon Cross Sections Database XCOM [206]. The obtained value is λ_{calc}=27.1 cm.
Another interesting measurement is the estimation of the event-rates in different energy regions

[27] The 2.615 MeV γ rays alone would have a larger attenuation length denoted by λ_M. Since the Compton scattered photons have a lower attenuation length, the attenuation length λ of Compton and non-Compton scattered γ rays is $\lambda<\lambda_M$.

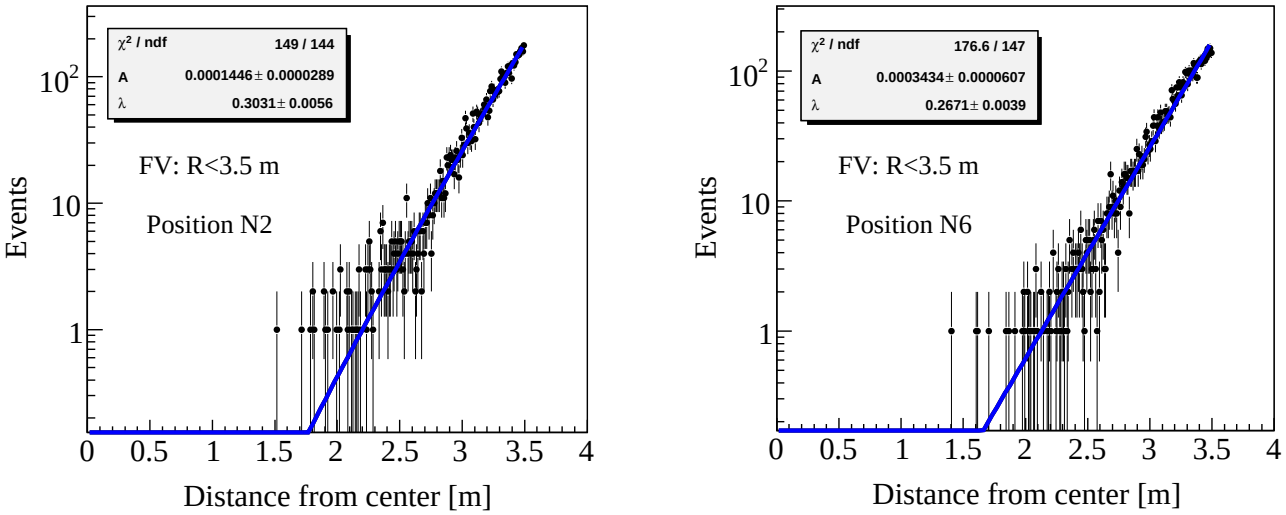

Figure 80: Radial distribution of a pure data-set of events induced by non-scattered 2.615 MeV γ rays emitted from the external ^{228}Th source.

Energy window	Position N2		Position N6	
[MeV]	λ [cm]	χ^2/ndf	λ [cm]	χ^2/ndf
(2.61,2.71)	30.3 ± 0.6	149/144	26.7 ± 0.4	177/147
(0.80,2.72)	25.4 ± 0.2	209/191	24.1 ± 0.2	182/195

Table 28: Measured attenuation length λ in pseudocumene for the 2.615 MeV *full energy peak* events in the energy windows [2.61,2.71] MeV and for events in [0.80,2.72] MeV. For the second energy interval including most of the Compton continuum, the attenuation length λ is smaller than for the events in the *full-energy peak*.

that were collected in a given *fiducial volume*. The rates are given for the energy ranges [0.25,0.8] MeV and [0.8,3.0] MeV in Table 29. The rates are not only important for neutrino analyses but also for testing MC simulations. Additionally, the rates are reference values for the required integration time in future calibration campaigns with the external ^{228}Th source.

Theoretical description of the radial distribution In order to describe the total radial behavior of the external γ rays from the ^{228}Th source, including the aforementioned contaminants in the bulk and possibly on the surface of the *Inner Vessel* nylon, one has to consider all radial distribution functions $\Phi(r)$ and the spatial resolution $p(r)$.

In general, we can assume that the resolution p(x,y,z,x_0,y_0,z_0) is a Gaussian function. It is used to establish the probability that the measured coordinates (x,y,z) of an event are located within an infinitesimal volume element dxdydz around the actual position (x_0,y_0,z_0) [207, 208]:

$$p(x,y,z,x_0,y_0,z_0)dxdydz = \frac{1}{\sigma_x\sigma_y\sigma_z\sqrt{(2\pi)^3}}\, e^{-\left(\frac{(x-x_0)^2}{2\sigma_x^2}+\frac{(y-y_0)^2}{2\sigma_y^2}+\frac{(z-z_0)^2}{2\sigma_z^2}\right)} dxdydz \qquad (5.7)$$

Herein, σ_x, σ_y and σ_z are the components of the detector resolution in x,y and z. In the following it is assumed that the detector resolution is constant in the entire detector volume and equal in

FV radius [m]	Position	Rate in [0.25,0.8] MeV [counts/h]	Rate in [0.8,2.7] MeV [counts/h]
<3.5 m	N2	30.3± 0.9	1138.1 ± 5.5
	N6	143.0± 2.1	1452.5 ± 6.4
<3.0 m	N2	3.0 ± 0.3	120.1 ± 1.8
	N6	5.9 ± 0.4	134.2 ± 1.9
<2.9 m	N2	2.4 ± 0.3	77.4 ± 1.4
	N6	4.0 ± 0.4	85.6 ± 1.6
<2.8 m	N2	1.9 ± 0.2	50.0 ± 1.2
	N6	3.2 ± 0.3	53.1 ± 1.2
<2.7 m	N2	1.6 ± 0.2	32.5 ± 0.9
	N6	2.6 ± 0.3	34.3 ± 1.0
<2.6 m	N2	1.3 ± 0.2	21.7 ± 0.8
	N6	2.2 ± 0.3	20.6 ± 0.8
<2.5 m	N2	1.1 ± 0.2	14.7 ± 0.6
	N6	1.8 ± 0.2	14.8 ± 0.6

Table 29: Measured event rates induced by the external Borexino ^{228}Th source. At the time of calibration the emission rate of the 2.615 MeV γ rays was (1.6695±0.1002)×10^6 counts/s. The dependence on the *fiducial volume* radius R is given for both positions N2 and N6.

all three Cartesian coordinates. So we introduced $\sigma = \sigma_x = \sigma_y = \sigma_z$. The spherical detector and the spherical probability density functions $\Phi(r)$ depending only on r motivates to express Equation (5.7) in spherical coordinates. The parametrization $x = r\cos\phi\sin\theta$, $y = r\cos\phi\cos\theta$ and $x = r\sin\phi$ together with the volume element $dxdydz = r^2\cos\phi\, drd\theta d\phi$ leads to

$$p(r,r_0) = \frac{r^2}{\sigma^3\sqrt{(2\pi)^3}} \int_0^{2\pi} \int_{-\pi/2}^{\pi/2} e^{-\left(\frac{(rcos\phi cos\theta - x_0)^2 + (rcos\phi sin\theta - y_0)^2 + (rsin\phi - z_0)^2}{2\sigma^2}\right)} cos\phi d\phi \qquad (5.8)$$

where $r_0 = (x_0,y_0,z_0)$ is the true radial event position.

The expected radial distribution of a certain subset of point-like events is given by $\phi(r_0)$. Then, the observed distribution $\Phi(r)$ is calculated by the convolution of $\phi(r_0)$ with the resolution $p(r,r_0)$ as follows:

$$\phi(r) = \int_0^{R_{IV}} \phi(r_0)p(r,r_0)dr_0 \qquad (5.9)$$

The boundary condition R_{IV} defines the radius of the *Inner Vessel*.

In the last step we have to define the probability density functions $\phi(r_0)$ which describe the distributions of the events. Several distribution types are considered: (i) events isotropically distributed in a spherical volume (V), (ii) events on a spherical surface (S) and (iii) events with a radial dependent distribution as in case of the external background (E).
In case of Borexino, a uniform distribution of events in the bulk (i.e. *Inner Vessel*) $\phi(r_0)_V$ has to be introduced for the α particles from ^{210}Po. Hence, $\phi(r_0)_V$ is equal to 1/V and becomes

$$\phi(r_0)_V = \frac{3}{R_{IV}^3} r_0^2 \qquad (5.10)$$

Contaminants in the nylon of the *Inner Vessel* might also contribute to the total radial distribution. This surface contamination $\phi(r_0)_S$ is defined as a Dirac-function in

$$\phi(r_0)_S = \frac{\delta(|r_0| - R_{IV})}{R_{IV}^2} \tag{5.11}$$

For the present analysis, the distribution of external events from the ^{228}Th source is crucial. We assume that the real position of the events follows an exponentially attenuated profile within the scintillation volume (ES), which decreases with smaller distance to the center. Additionally, we take into account an exponentially decreasing rate of events outside the *Inner Vessel* (EB), which are reconstructed in the buffer but partially deposit their energy in the scintillator. Then the probability density function $\phi(r_0)_E$ can be written as

$$\phi(r_0)_{ES} = \frac{\alpha(r_0) e^{-\frac{R_{IV}-r_0}{\lambda_{ES}}}}{\int_0^{R_{IV}} \alpha(r_0) e^{-\frac{R_{IV}-r_0}{\lambda_{ES}}}} \quad \text{for } r_0 < R_{IV} \tag{5.12}$$

$$\phi(r_0)_{EB} = \frac{\alpha(r_0) e^{-\frac{r_0-R_{IV}}{\lambda_{EB}}}}{\int_0^{R_{IV}} \alpha(r_0) e^{-\frac{r_0-R_{IV}}{\lambda_{EB}}}} \quad \text{for } r_0 > R_{IV} \tag{5.13}$$

where λ_{ES} and λ_{EB} are the absorption lengths in the scintillator and in the buffer, respectively. The factor $\alpha(r_0)$ in front of the exponential function was introduced in order to describe the radial dependence of the attenuation. In the extreme case of external γ rays coming from each direction (from SSS and PMTs or from the superposition of 4π distributed source positions) $\alpha(r_0)$ is equal to r_0^2. However, the present measurements were carried out in two source positions only. Since the γ rays from both source positions are partly collimated (Section 5.3) we fix the factor $\alpha(r_0)$ to 1.

The total radial distribution is calculated by the superposition $\phi(r)_{tot} = \sum_i^4 \phi(r)_i$, where $i \in \{V,S,EB,ES\}$. The analytical function $\phi(r)_{tot}$ contains eight free parameters: the already introduced variables R_{IV}, σ, λ_{ES}, λ_{EB} and the normalization factors N_V, N_S, N_{EB}, N_{ES}, one for each component $\phi(r)_i$. It was assumed that the uncertainty σ of the resolution is constant in the entire detector. The attenuation coefficients λ_{ES} and λ_{EB} and the normalization factors N_{EB}, N_{ES} are expected to be similar, but are still kept as independent fit parameters.

Figure 81 depicts the theoretical function $\phi(r)_{tot}$ where the realistic values R_{IV}=4.25 m, σ=12 cm and λ_{ES}=λ_{EB}=21 cm are used (see previous paragraph). The normalization factors are modulated to demonstrate their influence on $\phi(r)_{tot}$.

Figure 82 shows the fit of the measured radial distribution using the theoretical function $\phi(r)_{tot}$. One hour of lifetime from data collected in source position N2 was considered. Events with energies below 120 npe were rejected.
The fit was performed in the interval [0,5.8] m. Above the distance of 5.8 m, the measured distribution shows a secondary background of low energetic events which is not described by $\phi(r)_{tot}$. Below the distance of 5.8 m, the function $\phi(r)_{tot}$ accurately follows the measured curve in which only the statistical uncertainty is included (χ^2/n.d.f.= 287/184 = 1.56). The kink at ∼4.6 m is described by introducing $\phi(r_0)_{EB}$, because it could not be explained by the two components $\phi(r_0)_S$ and $\phi(r_0)_{ES}$ alone. The contribution of the events in the bulk is small compared to the number of the external γ rays. The surface distribution turns out to be negligible and was fixed to 1.

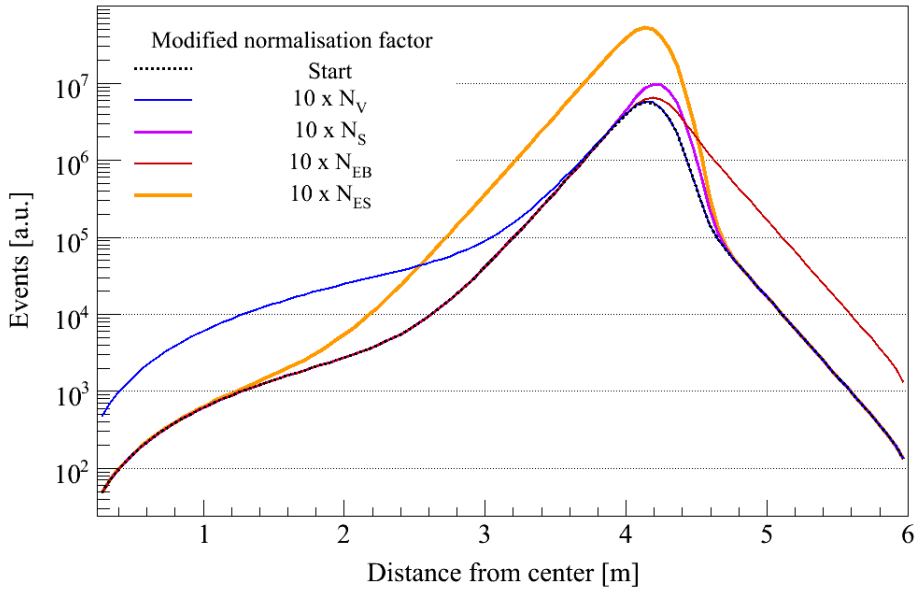

Figure 81: Representation of the radial distribution function $\phi(r)_{tot}$. The starting values for the eight free parameters of values of $\phi(r)_{tot}$ are: R_{IV}=4.25 m, σ=12 cm, $\lambda_{ES} = \lambda_{EB}$=21 cm, N_V=4.5×10^4, N_S=2×10^6, N_{EB}=2.5×10^6, N_{ES}=5×10^5. The first four parameters are kept constant, while the normalization factors are modulated.

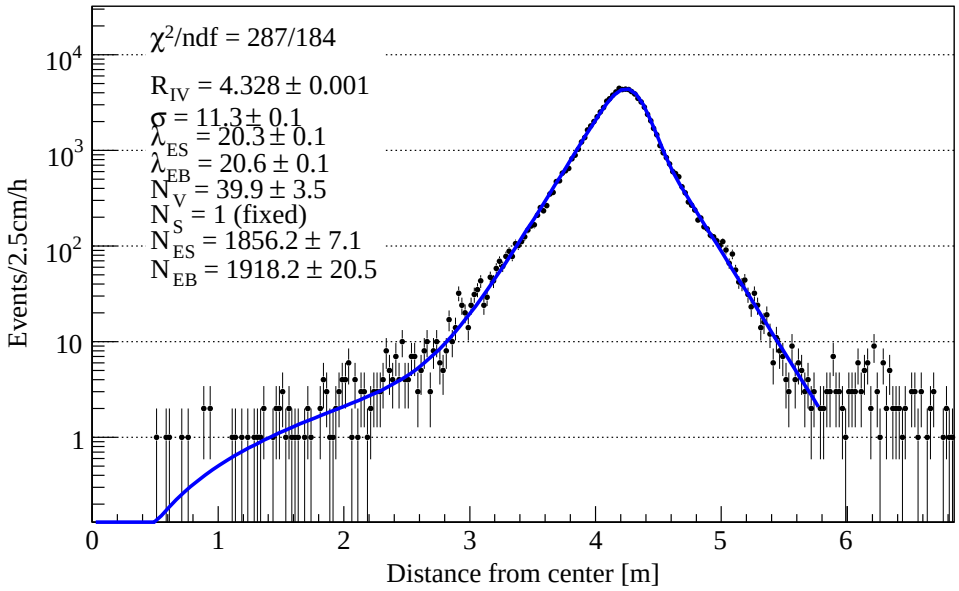

Figure 82: Fit of the radial distribution of events induced by the ^{228}Th source placed in position N2.

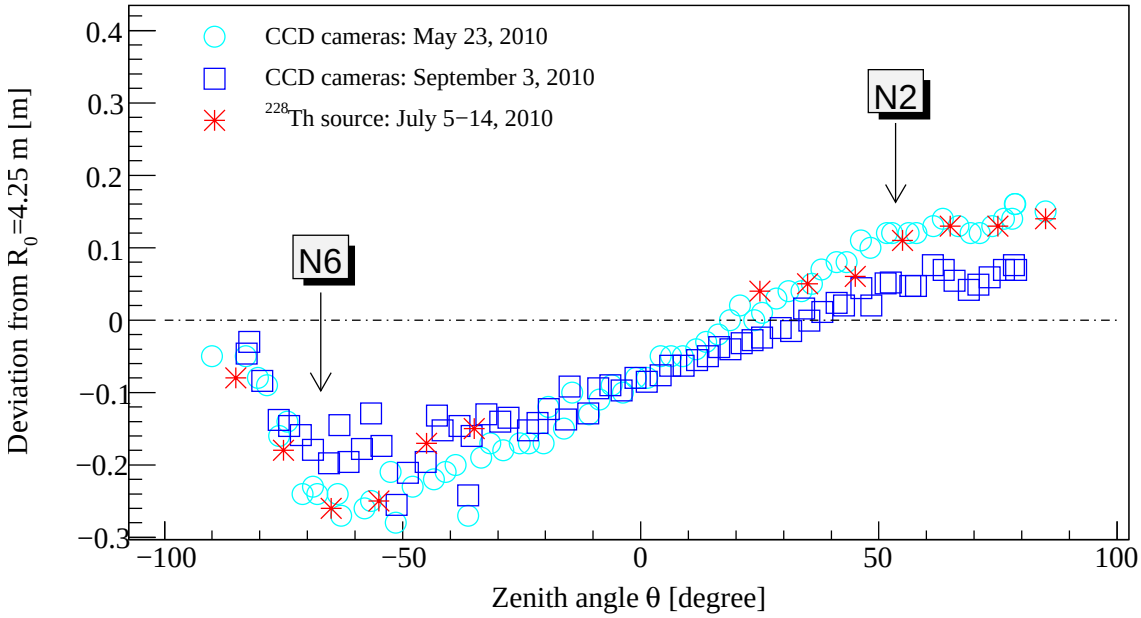

Figure 83: Tomography of the *Inner Vessel*: Measurement of the radius of the *Inner Vessel* as a function of the zenith angle θ (+90°: North pole; -90°: South pole). The curve obtained with the external γ source is compared to the measurements conducted with the CCD camera system before and after the external calibration campaign. Around source positions N2 and N6 there is very good agreement with the curves deduced from the CCD camera images. The estimation of the *Inner Vessel* radius in the region around [-30°,20°] was not possible, since this part of the detector was not irradiated by the ^{228}Th source.

The variance of the resolution is σ=(11.3 ± 0.1) cm. It is expected to scale proportional to $1/\sqrt{N}$, where N is the number of hit PMTs. For ^{14}C (140 keV, i.e. ∼60 hit PMTs) σ was equal to (41 ± 6) cm, for ^{214}Bi (∼2.0 MeV, i.e. ∼700 hit PMTs) σ=(13 ± 2) cm in x and y and σ=(14 ± 2) cm [65, 15]. Neglecting effects by multiple hit PMTs at higher energies, one expects σ ∼11 cm for 2.6 MeV γ rays (∼910 hit PMTs). Thus, the measured value is comparable with the expectation. The overall absorption lengths λ_{ES}=(20.3 ± 0.1) cm and λ_{EB}=(20.6 ± 0.1) cm and the normalization factors N_{EB} and N_{ES} are similar. Finally, the average radius of the *Inner Vessel* seen by the source in position N2 is R_{IV}=(4.328 ± 0.001) m. The importance of measuring R_{IV} is figured out in the next section.

Tomography of the Inner Vessel The previous paragraph has shown that the fit of the measured radial distribution of events induced by the external γ source allows to estimate the radius of the *Inner Vessel*. This leads to the question if the ^{228}Th source - by illuminating the detector from different positions - can be used to determine an angular dependent radius R_{IV}=$R_{IV}(\phi,\theta)$ and deduce the actual shape of the *Inner Vessel*.
At the beginning of data collection, the almost concentric and spherical vessel had a nominal radius of R_0 ≈4.25 m. Due to a leak and operations on the scintillator and buffer liquids (see Section 3.4.1), the *Inner Vessel* has continued to change its shape and its volume over the last two years. Currently, the monitoring of the vessel shape is performed by a system of six CCD cameras which are installed on the inner side of the Stainless Steel Sphere (see Section 3.1.1). For this purpose, the High Voltage of the PMTs has to be switched off to turn on the lights in the detector in order to take photos.

To test the novel approach with the Borexino ^{228}Th source, a data set containing 8 h and 16 h of data collected in source positions N2 and N6 was selected. The duration was restricted to 1 day to prove the feasibility of such a measurement.
To simplify the measurement, it was assumed that the radius $R_{IV}(\phi,\theta)$ is constant for a given zenith angle θ, so the radius becomes $R_{IV}=R_{IV}(\theta)$. Note that this assumption is reasonable since the buoyant force of the scintillator embedded in the buffer acts in vertical direction. Moreover, this tendency has also been confirmed by the evaluations based on the CCD camera system.
The angle θ of all reconstructed event positions was scanned in intervals of dθ=10°. The obtained radial distribution of all these subsets was fitted with the function $\phi(r)_{tot}$, where all fit parameters were first guessed by comparison with the radial profile, then fixed and released consecutively.
Figure 83 reports the result of the $R_{IV}(\theta)$-measurement. The measured distribution is compared to the curves obtained from CCD camera images taken on May 23, 2010 (♯ 3997) and September 3, 2010 (♯ 3999), i.e. before and after the external calibration campaign between July 5 and July 14, 2010. The curve obtained with the external ^{228}Th source is expected to lie in between. All three curves show values higher than R_0=4.25 m in the northern hemisphere and smaller values in the southern hemisphere of the detector. The curve measured with the ^{228}Th source is in good agreement with those obtained with the CCD cameras for angles closer to the source positions. The region in [-30°,20°] was not radiated, neither from the source in position N2 (θ=50.7°), nor in position N6 (θ=-66.9°). So the collected statistics are very limited and a fit of the radial distribution is not possible.
From the $R_{IV}(\theta)$-measurement I concluded that it is possible to estimate the *Inner Vessel* shape using an external ^{228}Th source of MBq activity placed at 6.85 m from the center of detector. With a count rate of $\sim 2\times10^6$ of 2.615 MeV γ rays per second, a well-founded result can be obtained after one day of data collection already, if the γ source is deployed in at least 3-4 positions.

5.5 Comparison of the calibration data with Monte Carlo simulations

5.5.1 Simulation of the point-like ^{228}Th source

The total external background from the Stainless Steel Sphere, the PMTs and light concentrators has been simulated by several collaborators in [188]. These studies often included approximative methods in order to generate and propagate billions of events to collect enough statistics in reasonable CPU time. The simulation tool `GENEB` (and a further developed code `GENROX`) was typically used [107].
In this work the author of this thesis performed Monte Carlo simulations of the external ^{228}Th source and compared it to data from the external calibration. The most complete and updated Borexino software packages `G4BX` and `BXELEC` within *Echidna cycle 12* (April 2010) were used (see Section 3.2.2).

Goal and MC settings The simulation of the external ^{228}Th source and of the total external background represent a challenge for all Monte Carlo codes used in Borexino. In a first simulation campaign it was investigated whether the most updated Borexino Monte Carlo code is able to reproduce with accuracy the data obtained from the ^{228}Th source. For this work, the author of this thesis did not introduced algorithms that would accelerate the processing of the photon progagation, but at the cost of introducing a bias. To speed up the collection of generated events whose centers of gravity are reconstructed within the *Inner Vessel*, only the following settings were imposed:

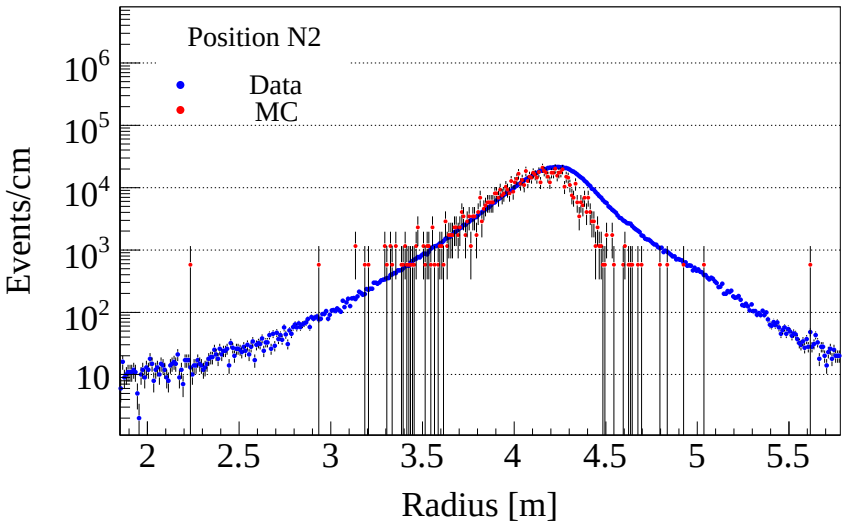

Figure 84: Monte Carlo simulation of the external ^{228}Th source in comparison with data: the radial distribution of the reconstructed events is different close to the edge of the *Inner Vessel* and in the near buffer region. The Monte Carlo simulation does not take into account the fact that the DMP concentration was lowered, causing more scintillation light as seen in data (see Section 3.4.1).

- Energy threshold: events which deposit an energy E<100 npe are rejected.
- Angular threshold: Particles which are not directed towards the center of the detector are not tracked if the angle $\beta >$ between the position (oriented toward the center) and the momentum of the particle exceeds $\beta >45°$. For a larger angle, the particles do not cross the scintillator vessel at all but only the buffer/Water Tank of Borexino.

In order to simulate the real experimental setup, the reentrant tubes in position N2 and N6 were implemented by I. Machulin. The source was placed within these tubes (*mother volumina*) at a distance of 685 cm from the center of the detector. In addition, the coordinates of the deformed *Inner Vessel* shape were implemented using the precise information from CCD camera images taken on May 23, 2010. Implementing the deformed vessel shape is essential as shown in Figure 79. If the two corrections are applied geometrical effects are expected to be small.

Results Several parameters of the Monte Carlo code like the Birks parameter (k_B), the light yield (LY) (see Section 3.1.2), but also the angular threshold were modulated in order to find the best agreement between MC and data. Typically 10^8 events were generated for a single parameter set. One cycle typically required 400 CPU hours [28]. For all simulations, a total of 4000 CPU hours was invested.
Figure 84 shows the radial distribution of the reconstructed positions of events from data and from MC. The MC simulated distribution differs from the data: the maximum of the distribution is shifted inwards by ∼5 cm and the number of events reconstructed in the buffer is smaller. This can be explained by the fact that the DMP concentration in the buffer assumed by the MC is still 5g/l, while at the time of the external calibration campaign it was only ∼2g/l (see Section 3.4.1), which caused more scintillation light events in the buffer.
Figure 85 shows the energy spectrum of all events reconstructed within the Inner Detector (R<6.85 m). The light yield (LY) in the Monte Carlo simulation that leads to a good agreement with the

[28] Performance of a single CPU: 30 events/s; in contrast, the ^{228}Th source generates 2×10^6 events/s.

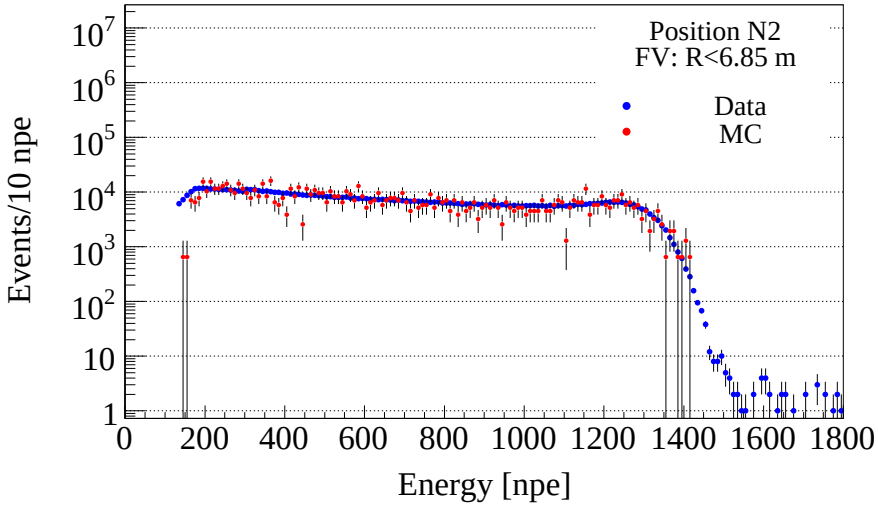

Figure 85: Monte Carlo simulation of the external ^{228}Th source in comparison with data: the energy spectra for a spherical *fiducial volume* with radius R<6.85 m. The spectra are in good agreement.

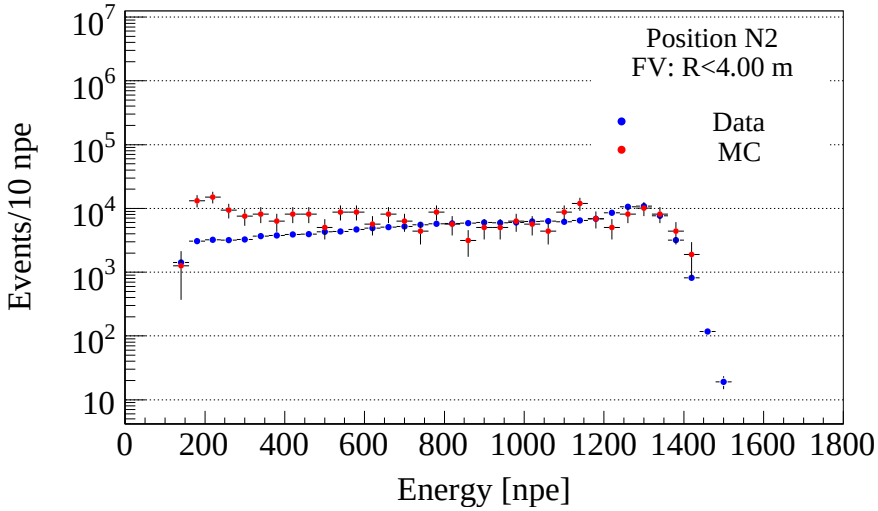

Figure 86: Monte Carlo simulation of the external ^{228}Th source in comparison with data: the energy spectrum for a spherical *fiducial volume* with radius R<4.00 m. At lower energies, the MC simulated spectrum shows more events.

data is LY=10300 photons/MeV. This value is ∼3% higher than that typically used for the energy region below 1 MeV. Moreover, within a *fiducial volume* of radius R<4.00 m (see Figure 86) the energy distributions show differences at lower energies: the Monte Carlo generated spectrum counts more events. A comparison of the energy distributions for smaller *fiducial volumes* with a radius smaller than R<3.50 m could not be performed due to the low statistics collected in the presented Monte Carlo simulation.

The discrepancies found between the external calibration data and the Monte Carlo simulations have not yet been completely solved. Further investigations are required in order to obtain a fully reliable simulation of the external background energy spectrum using the Borexino simulation tools `G4BX` and `BXELEC`. Once the discrepancy will be solved the Borexino simulation tools can be used to simulate precisely the external background including all relevant detector components (PMTs, light concentrators, Stainless Steel Sphere) as well as other γ lines from other radionuclides.

5.5.2 Spectral shape information from the calibration data

Besides the widespread number of already presented studies and applications, the main objective of the present work is the extraction of the spectral shape information from the external γ source. The spectral shape of the γ source is expected to be a first-order approximation of the real external background originating from the PMTs, the light concentrators and the stainless steel sphere. Their distance from the center of the detector is comparable to the distance of the source.
In order to obtain the spectral shape information, the *probability density function* (PDF) of events induced by the external γ source located at different positions has to be deduced. Then the PDFs can be used for the global fit of the total energy spectrum.
The PDFs for spherical, centered *fiducial volumes* with radii R<2.5 m and R<3.0 m are shown in Figure 87. The entries of the probability distributions are given in Table 34 and 35 in Appendix A.4. The maximal available statistics of non-problematic runs taken during the first external calibration campaign were included. Herein, the PDFs from data acquired for different source positions were combined after normalisation and correction of all energy values according to Equation (5.6). An energy cut at 300 npe was applied in order to reject the residue ^{210}Po events which were able to pass the Gatti cut in Equation (5.5). In the case of R<2.5 m, the measured PDFs of the single source positions were almost identical (see b-2 and c-2 of Figure 79). For this radius, the PDFs are independent of the grade of asphericity of the *Inner Vessel*. The non-identity increases for larger *fiducial volume* radii and originates from incompletely corrected geometrical effects and from the fact that the *Inner Vessel* was decentered and aspherical during the external calibration. Since the *Inner Vessel* continuously changed its shape during the data collection period, the PDFs changed also in time. This leads to the question if the measured PDFs for *fiducial volumes* with a radii smaller than R<3.0 m are representative of all data acquired in Borexino so far. In the entire period starting in May 2007 the *Inner Vessel* radius R_{IV} was always larger in the northern hemisphere (N) and smaller in the southern hemisphere (S), compared to the nominal value at R_{IV}=425 cm. This is also valid for the first external calibration campaign. The maximum and minimum *Inner Vessel* radii measured for different DAQ periods are given here [93]:

- Initial DAQ period (May 2007-spring 2008): +15 cm in the N-hemisphere, -15 cm in the S-hemisphere
- Increase and reduction of the leak (see Section 3.4) (April 2008-spring 2009): +35 cm in the N-hemisphere, -55 cm in the S-hemisphere (maximal asphericity)

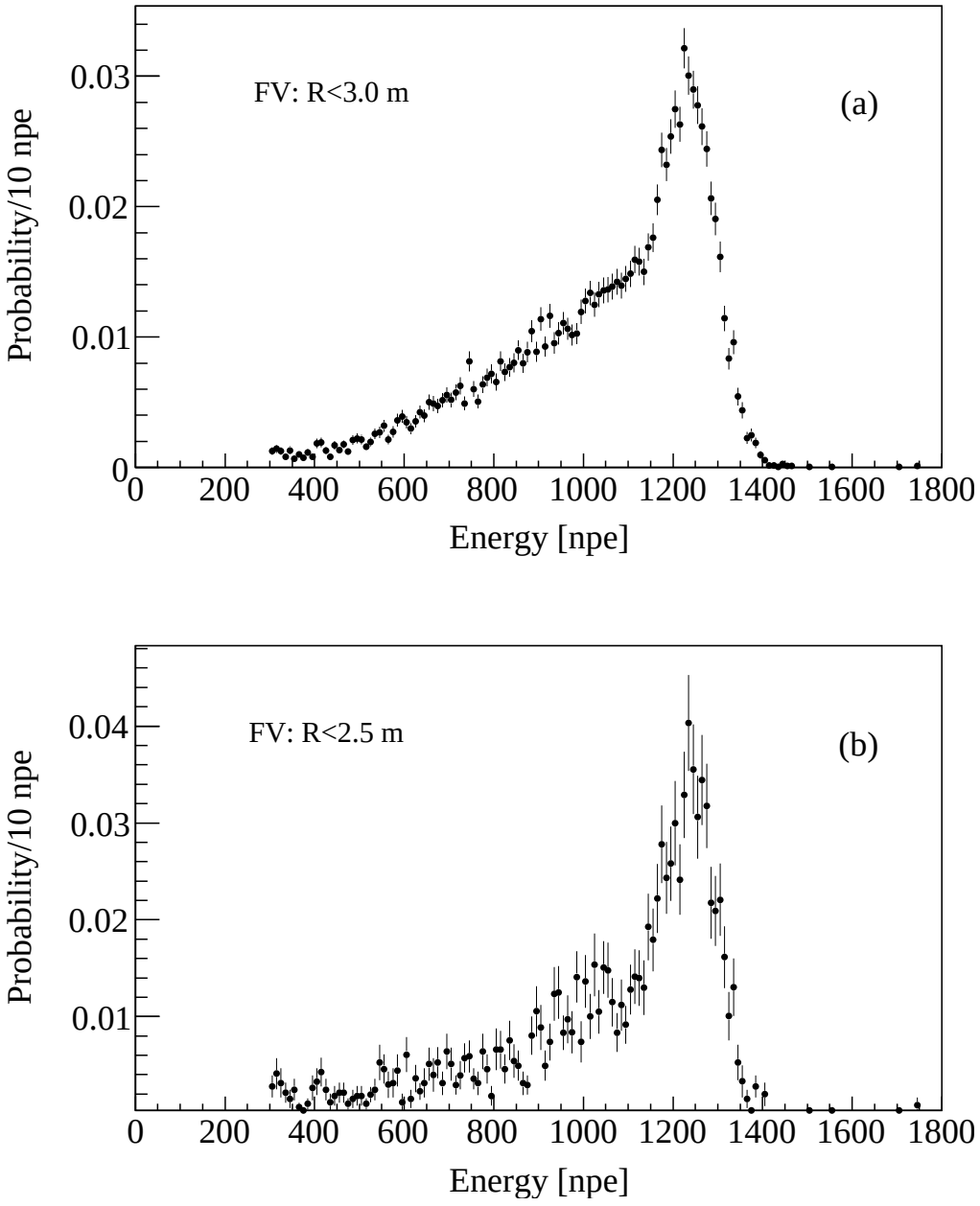

Figure 87: *Probability density functions* (PDF) of the external γ rays induced by the ^{228}Th source for spherical, centered *fiducial volumes* with radii (a) R<3.0 m and (b) R<2.5 m. Maximal available statistics were used. The energy variable charge was normalized and corrected according to Equation (5.6). The distributions are the average of the PDFs obtained from the measurements based on the two source positions N2 and N6. They include the information of the asphericity and decentricity of the *Inner Vessel* at the moment of measurement.

- Lowering asphericity (July 2009 to May 2010): from +25 cm to +15 cm in the N-hemisphere, from -35 cm to -25 cm in the S-hemisphere
- First external calibration campaign (July 2010): +15 cm in the N-hemisphere, -25 cm in the S-hemisphere
- After the first Water Extraction Campaign (see Section 3.4) (September 2010): +10 cm in the N-hemisphere, -20 cm in the S-hemisphere

The maximal asphericity was reached in 2008/2009 during the increase and the containment of the *Inner Vessel* leak. Apart this period of $\sim$1 year, the asphericity of the *Inner Vessel* during the external calibration campaign in July 2010 was similar or larger than in the other DAQ periods. Therefore, in terms of analyses based on *fiducial volumes* with radius R$\lesssim$3.0 m, the combination of the two single PDFs obtained in the first external calibration campaign can be considered as a good approximation of the energy spectrum of the external background for most of the DAQ periods.

6 Summary

The present work focused on the development and optimization of data analysis techniques and on the performance of an external calibration in the Borexino experiment. The main objective of these efforts is the identification and rejection of background components which still impede the first real-time detection of solar *pep* and CNO neutrinos in Borexino.

Muon-induced backgrounds play a major role in the abovementioned neutrino analysis. Cosmic-ray muons and muon showers crossing the Borexino detector induce a vast range of signals attributable to decays of radioisotopes and to neutron captures on protons and carbon atoms. The analysis presented in this thesis investigated several properties of the prompt muon signal and of the delayed signals detected in Borexino.

The study about muon events mainly aimed at determining the tracks of single muons. An analytical model of the propagation of light induced by muons crossing the detector was deduced. The model allows to reconstruct muon track points. A global fit procedure of the reconstructed muon track points was developed and validated using data. The obtained angular distributions of the incoming muons follow the geomorphological profile of the rock overburden and they are in good agreement with the results obtained in previous experiments.

The neutron background in Borexino has been examined and characterized. The rate of muon-induced neutrons in Borexino was analyzed and a road map for the estimation of the average neutron production per muon unit path length has been presented. A precise measurement of the capture time and propagation length of muon-induced neutrons and neutrons from an $^{241}Am^{9}Be$ calibration source was performed. The study of the propagation and of the initial energy of muon-induced neutrons allowed an insight into the production mechanisms responsible for the observed neutron emission. By combining the muon track information with the reconstructed position of neutrons, it was also possible to estimate the reliability of the position reconstruction algorithms for muon-induced neutrons. The obtained information is important for the identification of cosmogenic radioisotopes, which are correlated with the emitted neutrons in space and time.

The main analysis was the study of muon-induced radioisotopes, especially of ^{11}C. This radioisotope has a high production rate, which results to be $\sim$10 times higher than the predicted rate from the *pep* and CNO neutrino fluxes in the preferred energy window of observation at [0.8,1.3] MeV. In order to identify and reject ^{11}C, the efficiency and applicability of a *threefold coincidence* (TFC) method was investigated. This coincidence consists of the prompt muon signal, the delayed neutron capture on protons and the delayed ^{11}C decay. The validated TFC method was used for the determination of the ^{11}C spectral shape. Besides other possible applications, this information has allowed to determine the light yield and the quenching factor of the scintillator independent of other measurements.
A sophisticated strategy was developed which embeds the TFC method and other veto techniques in order to efficiently reject ^{11}C events with a loss of statistics of 61%. The ratio of the predicted neutrino rate to the residual ^{11}C rate was reduced to 1:1.7. Moreover, a statistical subtraction of the residual ^{11}C has provided an insight into other potential contaminants besides ^{11}C and demonstrated the possibility to detect solar *pep* and possibly also CNO neutrinos with Borexino.

In the present work it was recognized that the external background plays a major role in the *pep* and CNO neutrino analysis. In order to describe this background, an external calibration measurement with a gamma source has been carried out.

For this purpose, a custom-made 5.4 MBq ^{228}Th source was successfully produced, using a technique which foresees the embedment of the radioactive nuclides in gold. Compared to commercial sources based on ceramic subtrates, the indirect emission of neutrons via (α,n) within the source could be reduced. This facilitates the usage of a source of this type at the *Laboratori Nazionali del Gran Sasso*, where strict regulations are imposed on the usage of neutron sources. The ^{228}Th source was fully characterized in terms of gamma activity and neutron source strength.

The ^{228}Th source has been used for a first external calibration in Borexino, in which it was deployed in the detector in three different positions. The external calibration data can be used for a broad range of applications.

Concerning the position reconstruction of the collected events, the attenuation length in the Borexino scintillator was estimated for 2.6 MeV gamma rays. By comparing the event rate from the external ^{228}Th source with the rate from the external background, it was possible to estimate the ^{228}Th activity of all components in the outer parts of the detector contributing to the external background. By measuring the angular-dependent radial distribution of the events induced by the external source, it was demonstrated that a MBq ^{228}Th source can be used for an accurate scan of the boundary between scintillating and non-scintillating liquids in large-volume detectors. In the case of Borexino, one day of calibration with a 5 MBq ^{228}Th source is sufficient for a complete scan of the scintillator vessel. Thus, the ^{228}Th source might be used as a new monitor system complementary to the Borexino CCD camera system which is typically used for imaging the scintillator vessel.

As shown in this work, the study of the external calibration data also contributed to a deeper understanding of the detector response in terms of the energy reconstruction of events. The energy resolution at 2.6 MeV could be estimated and the 2.6 MeV gamma peak position revealed an additional calibration point for the determination of the energy scale. A North-South asymmetry in the energy reconstruction was also measured. This is due to a lower number of working PMTs in the lower hemisphere of the detector. This underlined the possibility to use the source for stability studies of the detector performance and of the energy response.
Finally, the spectral shape of the energy deposited from gamma rays originating from the external source was deduced. On the one hand, this information is useful for the tuning of the Borexino Monte Carlo code. This will allow a simulation of the entire external background and provide a more comprehensive picture of the spectral shape of this contaminant. On the other hand, the measured spectrum can be regarded as a first-order approximation of the external background and can therefore be used in global spectral fit analyses in Borexino.

A Appendix

A.1 Muontrack reconstruction

This section presents an algorithm for the reconstruction of the exit point of a relativistic muon which goes through a detector similar to the Inner Detector of Borexino (i.e. spherical shape, light collectors homogeneously mounted on the inner surface, filled with a liquid scintillator). The algorithm was developed by V.V. Kobychev and the author of this thesis.
The method is based on an analytical description of the propagating Cherenkov light and scintillation light wavefronts. For a given entry and exit point of the muon, the algorithm allows to determine the time when the primary wavefront reaches a given point on the inner surface of the detector (first part). On the other hand, by knowing the entry point of the muon and the *time-of-arrival* of the photons, one can deduce the position of the exit point (second part).

When a relativistic charged particle like a muon propagates faster than light through a dielectric medium, it produces Cherenkov light instantaneously. This light is emitted at a fixed vertex angle $\beta = \arcsin(\frac{1}{n})$, where n is the refraction index of the medium. The scintillation light is emitted isotropically with a delay of $\sim$1 ns after the muon has passed a given point in the detector. The superposition of the spherical scintillation light wavefront has two components: (i) a conical wavefront which has the same shape and almost the same phase-velocity[29] as the Cherenkov cone; (ii) a spherical wavefront which is adjacent to the conical one. The shape of the entire wavefront is depicted in Figure 88.

The first part of the algorithm describes the *time-of-arrival* t' of the first photon that reaches the point $\vec{h}$ on the inner side of the detector. A scheme used for the derivation of t' is shown in panel (a) of Figure 88. We assume that the entry point $\vec{r}_A$ and the exit point $\vec{r}_B$ of the muon track as well as the refraction index n are known. The vector which describes the muon position at a given time t is given by

$$\vec{r}_\mu(t) = \vec{r}_A + \vec{v}\,(t - t_A) \tag{A.1}$$

Herein, c is the speed of light, $\vec{v} = c \cdot (\vec{r}_B - \vec{r}_A)/\left|(\vec{r}_B - \vec{r}_A)\right|$ the normalized velocity vector of the muon and t_A the time when the muon entered the detector.
The position H on the inner surface of the detector, defined by the vector $\vec{h}$, is hit at the time t'. t' is given by:

$$t'(\vec{h},t) = t + \left|(\vec{r}_\mu(t) - \vec{h})\right| \frac{n}{c} \tag{A.2}$$

This formula is valid for any photon emitted along the muon track that reaches the point $\vec{h}$. Now we want to find the photon that reaches point $\vec{h}$ with the minimum arrival time t_M. This is calculated via the differentiation of Equation (A.2), which is set equal to 0. This is fulfilled for:

[29] The retardation effect of $\sim$1 ns in the scintillation light emission compared to the instantaneous Cherenkov light emission is small. In the case of Borexino, the PMT time jitter results to be few ns and the *time-of-arrival* of the generated photons in both processes can be several tens of ns.

$$c\,t_M \stackrel{!}{=} -\frac{\left|(\vec{r}_A - \vec{h}) \times \frac{\vec{v}}{c}\right|}{\sqrt{n^2-1}} - (\vec{r}_A - \vec{h}) \cdot \frac{\vec{v}}{c} \tag{A.3}$$

The emission point of the photon with the shortest *time-of-arrival* t_M is denoted with M. Then the *time-of-arrival* can be expressed as follows:

$$c\,t' = c\,t_M + \frac{n\,l}{\sin\alpha} \tag{A.4}$$

where $\alpha = \pi/2 - \beta = \arccos(1/n)$ and the length $l \equiv |HN|$ can be expressed via either $|(\vec{r}_A - \vec{h}) \times \vec{v}/c|$ or $c/n(t' - t_M)\ \sin(\alpha)$.
The length $q \equiv |NM|$ is introduced via $(ct_N - ct_M) = l\cot(\alpha)$. This relation allows to express ct_M on a different manner compared to Equation (A.3).
Furthermore, it can be shown that $n/\sin(\alpha) - \cot(\alpha) = \sqrt{n^2-1}$.
By substituting the introduced terms into Equation (A.4), one obtains:

$$c\,t' = c\,t_N + l\left(\frac{n}{\sin(\alpha)} - \cot(\alpha)\right) = c\,t_N + \left|\frac{\vec{v}}{c} \times (\vec{r}_A - \vec{h})\right| \sqrt{n^2-1} \tag{A.5}$$

Then, the length $s \equiv |AN|$ which is equal to $(ct_N - ct_A) = (\vec{r}_A - \vec{h}) \cdot \vec{v}/c$, is introduced. The substitution of s into Equation (A.4) finally leads to:

$$c\,t' = c\,t_A + \left|(\vec{r}_A - \vec{h}) \times \frac{\vec{v}}{c}\right| \sqrt{n^2-1} - (\vec{r}_A - \vec{h}) \cdot \frac{\vec{v}}{c} \tag{A.6}$$

Equation (A.6) is valid for the case that $t_B > t_M > t_A$.
In the case of $t_A > t_M$, the wavefront is spherical and the solution is simplified to: $c\,t' = c\,t_A + \left|(\vec{r}_A - \vec{h})\right|\ n$.
In the case of $t_A < t_M$, where scintillation light is isotropically emitted from the point B, the solution is $c\,t' = c\,t_B + \left|(\vec{r}_B - \vec{h})\right|\ n$.

In Equation (A.6), the *time-of-arrival* t' is a function of $t' = t'(\vec{r}_A,\vec{r}_B,\vec{h},t_A,c,n)$, where the entry and the exit point are fixed and t' is deduced. In the real situation however, the vector $\vec{r}_B$ might be unknown. The second part of the algorithm aims to invert Equation (A.6) in order to express the exit point vector $\vec{r}_B$ as function of $\vec{r}_B = f(\vec{r}_B)(\vec{r}_A,\vec{h},t',t_A,c,n)$. Since Equation (A.6) is scalar, it is not possible to deduce the three components of the vector $\vec{r}_B$. However, it is possible to estimate the angle ϕ between $(\vec{r}_A - \vec{h})$ and $\vec{v}/c$. If ϕ is calculated for a large number N of points H on an arbitrarily chosen circle along the Inner Detector surface (in panel (b) of Figure 88 only four exemplary points are drawn), it is possible to deduce a point C crossed by the muon. The point C is located in the plane in which the circle was placed. Moreover, C is normally not equal to the exit point B but lies on the same trajectory as $(\vec{r}_A - \vec{r}_B)$. A series of circles can be defined to get an optional number of points along the muon track intersection with the detector.
In the following section, the angle ϕ is exemplarily calculated for one individual vector $\vec{h}$.
First, the absolute value of the vector product $\left|(\vec{r}_A - \vec{h}) \times \vec{v}/c\right| = \left|(\vec{r}_A - \vec{h})\right|\ |\vec{v}/c|\ \sin(\phi)$ and of the scalar product $(\vec{r}_A - \vec{h}) \cdot \vec{v}/c = \left|(\vec{r}_A - \vec{h})\right|\ |\vec{v}/c|\ \cos(\phi)$ is applied to Equation (A.6). This introduces the angle ϕ. By dividing both sides in Equation (A.6) by $\left|(\vec{r}_A - \vec{h})\right|$, it follows:

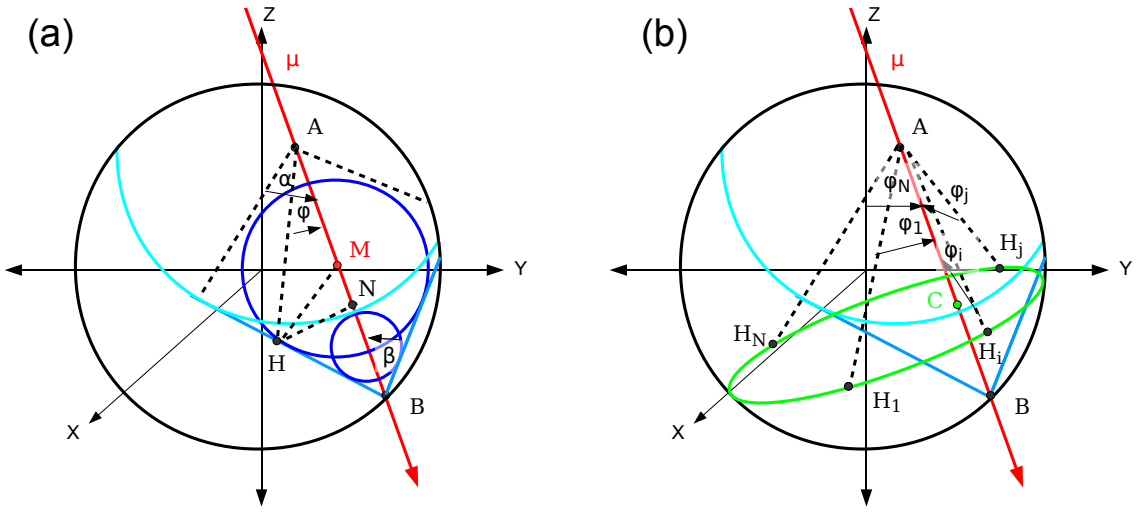

Figure 88: Reconstruction of the exit point of a single muon crossing the Inner Detector of Borexino. Panel (a) defines the *time-of-arrival* of the first photon reaching point H for the case that the entry point A and the exit point B of the track are known. Panel (b) defines the muon track point C for the case that the entry point A and the *time-of-arrival* of the photons at N different positions on the detector inner surface are known.

$$\frac{c\ (t' - t_A)}{\left|(\vec{r}_A - \vec{h})\right|} = \sqrt{n^2 - 1}\ \sin(\phi) - \cos(\phi) \tag{A.7}$$

In order to have ϕ as argument of one single function, the prefactors of the sine and cosine function on the right side of Equation (A.7) are transformed according to:

$$\sqrt{n^2 - 1} = a\cos(\delta) \tag{A.8}$$

$$-1 = a\sin(\delta) \tag{A.9}$$

Herein, a is a not yet defined constant and δ an unknown constant phase.
The transformation of the constants allows to apply the addition theorem as follows:

$$a\cos(\delta)\sin(\phi) + a\sin(\delta)\cos(\phi) = a\sin(\phi + \delta) \tag{A.10}$$

As a consequence, the variable phase ϕ no longer appears in two trigonometric functions but only in one.
For the estimation of the constant a, both sides of Equations (A.8) and (A.9) are squared and then summed. This leads to $(\sqrt{n^2 - 1})^2 + 1^2 = a^2$. The resulting relation $a = \pm n$ is substituted into the original Equations (A.8) and (A.9) in order to deduce the value for the constant phase δ. There are four possible solutions:

$$\delta = \begin{cases} \arccos\left(\pm\sqrt{1-\frac{1}{n^2}}\right), \\ \arcsin\left(\mp\frac{1}{n}\right) \end{cases} \tag{A.11}$$

In all four cases, the absolute value of δ is equal for a given index of refraction n, only the sign changes. Hence, only two solutions are left. The combination of Equation (A.10) with Equation (A.7) leads to the following two solutions for the angle ϕ:

$$\phi_{1,2} = \arcsin\left(\frac{c}{n}\frac{(t'-t_A)}{\left|(\vec{r}_A-\vec{h})\right|}\right) + \arcsin\left(\pm\frac{1}{n}\right) \tag{A.12}$$

One of the two solutions can be excluded by comparing the ϕ values calculated for different positions H. The values that converge on a common trajectory of the muon are finally selected.

A.2 Borexino: background and results

Solar neutrinos

	Ref.	Measured rate R [events/d/100ton]	Expected rate R_{th} [events/d/100ton]
^{7}Be ν:	[64, 65]	$49 \pm 3_{stat} \pm 4_{syst}$	wo. ν-osc.: 74 ± 4 (GS98) w. ν-osc. 48 ± 4 (incl. MSW+LMA+GS98)
^{8}B ν:	[15]	>3 MeV: $0.217 \pm 0.038_{stat} \pm 0.008_{syst}$ >5 MeV: $0.134 \pm 0.022_{stat}\ ^{+0.008}_{-0.007\ syst}$	
	Ref.	Ratio: meas./pred. flux (wo. luminosity constrain)	Ratio: meas./pred. flux (w. luminosity constrain)
pp ν:	[65]	$f_{pp} = 1.04^{+0.13}_{-0.19}$	$f_{pp} = 1.005^{+0.008}_{-0.020}$
CNO ν:	[65]	$f_{CNO} < 6.27$ (90% C.L.)	$f_{CNO} < 3.80$ (90% C.L.)

Anti-neutrinos

	Ref.	Measured rate R [events/y/100ton]	Expected rate R_{th} [events/y/100ton]
Geo-$\overline{\nu}$:	[68]	$3.9^{+1.6}_{-1.3}$	BSE_1: $2.5^{+0.3}_{-0.5}$ [66] BSE_2: 2.5 ± 0.2 [70] BSE_3: 3.6 [71] Max.: 3.9; Min.: 1.6
Reactor-$\overline{\nu}$:	[68]	$4.3^{+1.7}_{-1.4}$	Without ν-osc.: 6.5 ± 0.4 With ν-osc.: 3.7 ± 0.2
Solar-$\overline{\nu}$:	[72]	*Hypothetic particle; Transition prob.:* $\nu \rightarrow \overline{\nu}$: $<1.3\times10^{-4}$ (90% C.L)	

Nuclear / elementary particle physics

	Ref.	Phenomenon	Upper limit (90% C.L.)
	[65]	*Neutrino magnetic moment*	$< 5.4 \times 10^{-11}\,\mu_B$
	[69]	*Relative strength on Pauli-forbidden to normal transitions*	$\delta^2_\gamma \leq 2.2\times10^{-57}$ $\delta^2_N \leq 4.1\times10^{-60}$ $\delta^2_\beta \leq 2.1\times10^{-35}$

Table 30: Borexino: main physics results obtained in the period 2007-2010. Details and abbreviations can be found in Section 2.3.

Contaminant	Source	Normal/Expected conc./flux/rate	Required	Reduction method	Achieved in Borexino
μ	cosmic	200/s/m^2 (at sea level)	$\sim10^{-10}$	underground,OD veto Pulse-shape	$<10^{-10}$
^{11}C	in-situ μ-ind.	$\sim$15 c/d/100		TFC-method	$\sim$27 c/d/100
Ext. γ/n	rock			WT shielding, FV cut	
Ext. γ	PMTs, SSS, vessels			material selection buffer, FV cut	
^{14}C	Intrinsic in PC/PPO	$\sim10^{-12}$	10^{-18}	Old oil, tests in CTF	$\sim2\times10^{-18}$ g/g
^{238}U	Dust	$\sim10^{-16}$-10^{-15} g/g	$<10^{-16}$ g/g	see Section 3.1.1	$(1.6\pm0.1)\times10^{-17}$ g/g
^{232}Th	Dust	$\sim10^{-16}$-10^{-15} g/g	$<10^{-16}$ g/g	see Section 3.1.1	$(6.8\pm1.5)\times10^{-18}$ g/g
$^{40}K_{nat}$	Dust	$\sim10^{-14}$ g/g			Spectral fit: $\leq3\times10^{-16}$ g/g
^{7}Be	Cosmogenic (at sea level)	$\sim3\times10^{-2}$ Bq/t	$<10^{-6}$ Bq/t	Fast procurement, distillation	not measurable
^{222}Rn	Emanation	100 atoms/cm^3 (air)	$<10^{-16}$ g/g		$\sim10^{-17}$ g/g
^{210}Po	Surface cont. (from ^{222}Rn)		1 c/d/t	Cleanliness, dist. α/β stat. subtr.	$\sim$70 c/d/t (May 2007) $\sim$0.01 c/d/t
^{210}Pb	Surface cont. (from ^{222}Rn)			Cleanliness, dist.	not measurable not in equil. with ^{210}Po
^{222}Rn	air, emanation from materials	$\sim$10 Bq/L (air) $\sim$100 Bq/L (water)	$<$1 c/d/100t	N_2 stripping	$\sim$0.02 c/d/ton
^{39}Ar	air/nitrogen	$\sim$17 mBq/m^3 (air)	$<$1 c/d/100t	Select vendor, leak tightness	not measurable
^{85}Kr	air/nitrogen	$\sim$1 Bq/m^3 (air)	$<$1 c/d/100t	same as for ^{39}Ar	Spectral fit: (25$\pm$5) c/d/100t Fast coinc.: (30$\pm$5) c/d/100t

Table 31: Borexino main background sources, the normal/required/achieved background levels including the rejection methods. The intrinsic contamintants are given for the initial phase of the experiment in May 2007 in case they changed in the meantime. For the concentrations of ^{238}U and ^{232}Th secular equilibrium is assumed.

A.3 Radioactive decay chains

Figure 89: ^{238}U decay chain: Data were taken from the Lund/LBNL Nuclear Database [106].

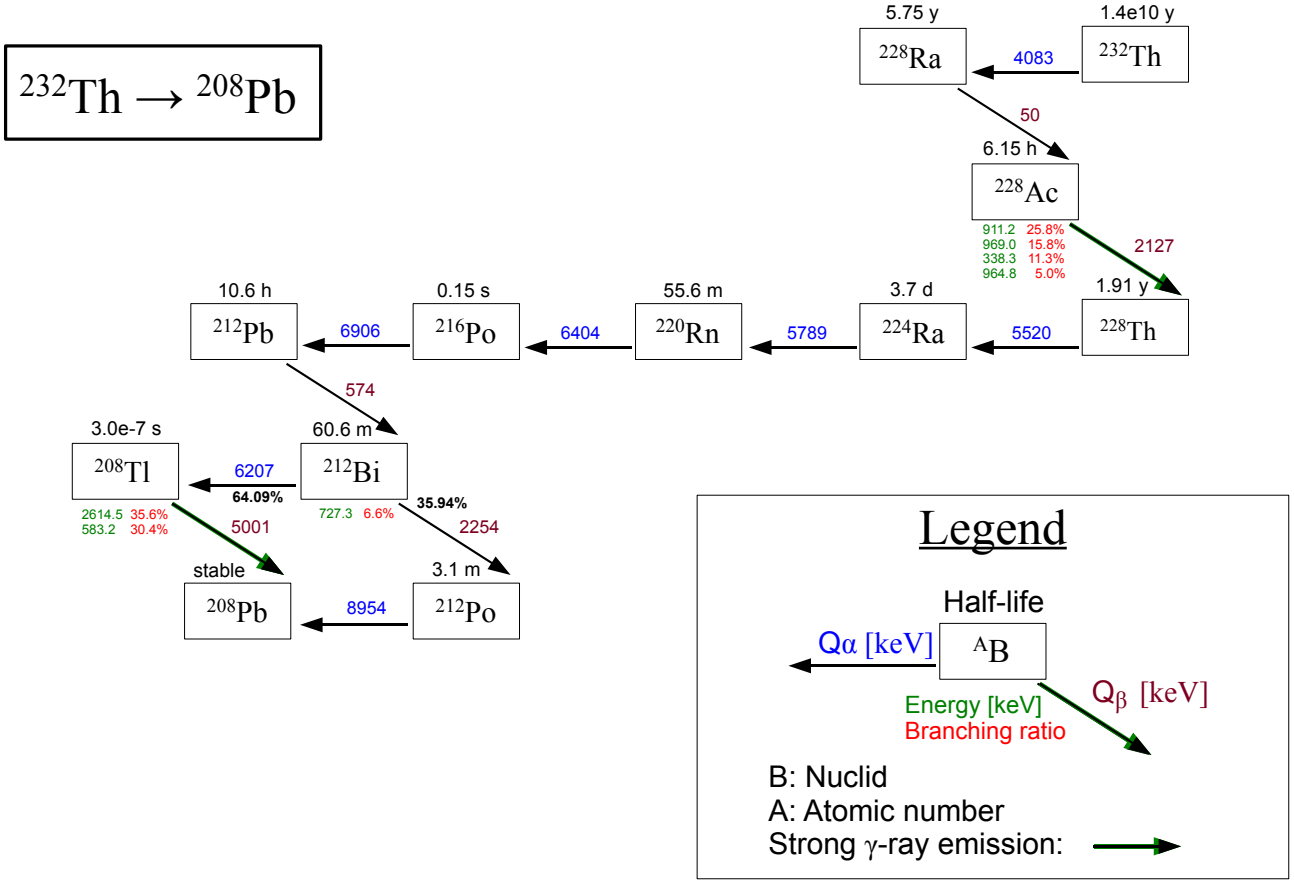

Figure 90: ^{232}Th decay chain: Data were taken from the Lund/LBNL Nuclear Database [106].

A.4 Reference tables

M_n	Run	ID_n	IP	M_n	Run s	ID_n	IP	M_n	Run s	ID_n	IP
244	9977	157013	2.06	140	12739	643062	1.89	109	12498	349263	2.07
226	7930	217815	2.26	139	8436	323632	3.86	109	12958	43713	4.17
214	10773	111643	4.7	139	12668	197184	3.88	109	13924	70130	1.83
213	12995	126140	4.15	138	8034	283014	5.62	107	12649	95123	2.99
210	6922	18321	4.73	137	7813	616757	3.35	105	11251	305952	2.11
191	11685	118122	2.58	137	8375	252533	4.5	105	11257	302707	1.09
187	10065	189742	3.59	135	9979	56541	2.22	105	11311	127368	1.28
184	9716	4134	3.06	135	11682	63420	4.52	105	12051	300062	3.79
182	10907	46960	1.85	133	7654	520006	0	105	12637	625040	3.01
181	8774	120221	4.34	133	9804	253865	4.08	105	12839	531912	3.28
180	7556	386594	0	133	9964	213651	2.19	104	7680	216596	0
179	12036	412068	3.1	133	10113	17578	4.72	104	8527	112870	6.36
178	11399	160161	1.43	131	7869	71946	2.16	103	7195	232077	3.76
177	13238	171685	3.74	131	9104	263318	3.24	103	9337	25782	3.06
175	10800	108255	1.09	131	9788	347560	5.74	103	10863	163281	3.01
175	11653	47032	0	131	11468	187162	0	103	11271	590590	3.8
173	6988	139521	0	126	8405	532266	2.77	102	8135	389327	3.02
173	8051	301239	1.19	126	9359	397169	1.41	102	12325	311186	2.61
172	8625	596423	3.93	125	7180	333296	0.77	101	7486	116492	3.73
170	10172	93951	2.92	125	11600	594837	3.32	101	8929	204780	2.51
169	7027	228038	4.65	124	11608	41724	3.96	101	9781	123024	2.11
169	12635	81948	2.58	124	12536	529390	2.26	101	11093	85258	1.05
166	7189	44582	1.5	123	8236	246378	3.72	101	12418	77536	2.52
166	7334	173998	1.96	123	9150	211474	4.73	100	7529	364744	0
165	9625	125796	2.01	122	8424	400856	2.71	100	8455	378758	0.79
163	8247	464614	2.69	121	12678	180768	3.47	100	9793	602749	6.43
162	7882	541005	6	119	12486	393890	1.57	100	11438	311221	4.42
161	7678	260751	0.33	118	11549	340930	4.1	100	12804	614232	1.5
160	8593	615503	0.95	118	12291	43242	4.62	99	10500	323899	2.07
158	10955	156479	2.76	116	10842	221366	3.87	99	11145	158440	2.27
157	10099	464002	2.75	116	12541	251995	2.76	99	12529	163405	1.72
155	13416	84270	2.72	116	13386	355016	1.46	99	12853	77298	4.06
154	12032	540062	3.07	115	7728	524172	2.88	98	7504	425151	3.72
153	7844	478931	3.08	114	8109	647794	1.44	98	10627	34045	3.77
152	9308	639568	0	113	9902	548873	0	98	12647	464046	2.17
151	7922	242354	2.31	113	9974	597560	3.16	97	9413	455802	1.46
150	9262	43891	1.83	112	8485	11856	2.65	97	11562	500637	2.72
150	12407	81883	1.66	112	8553	367973	0	96	10620	316706	5.45
150	13460	454208	2.98	112	12726	115298	1.6	96	13462	64641	3.18
149	9050	120976	1.88	112	13788	221303	1.81	95	8218	362214	2.17
149	13461	502302	3.62	111	7939	535653	2.49	95	9273	187016	4.61
148	10089	23101	3.96	111	8255	289301	5.39	95	9347	6790	1.2
145	9736	262302	0.51	111	11375	77017	3.61	94	6911	96331	0.76
143	8435	537917	1.17	111	12181	387259	2.18	93	10117	2409	3.02
143	9935	604413	1.56	110	7232	409825	1.76	93	12491	8134	2.72
141	8635	273370	1.81	110	7410	115697	0.63	93	13091	4150	3.71
141	9072	88558	2.64	110	8633	368964	0	93	13534	126366	3.24
141	9340	504995	0	110	10265	444967	3.97	93	13798	248061	0.72
141	11288	437781	5.85	110	11289	182726	2.81	92	6978	315292	2.67
140	11465	578620	0	110	13399	406291	2.21	92	8452	285787	4.69

Table 32: The 150 neutron events with the highest multiplicity M_n in the time period from January 13, 2008 to August 7, 2010 (843.8 d, 662.1 d of lifetime). The events are defined by their run and identification (ID) number. The track of the parent muons has often been reconstructed successfully, if not, it is denoted by zero. The distance of the muon tracks from the detector center is given by the impact parameter (IP) in units of meters.

FV_1		FV_2		FV_1		FV_2	
npe	entries	npe	entries	nhits	entries	nhits	entries
350	1	400	3	290	1	340	1
390	1	410	1	320	1	350	1
400	2	420	2	340	1	360	1
410	2	430	9	350	1	370	8
420	2	440	10	370	11	380	13
430	7	450	17	380	14	390	24
440	9	460	27	390	26	400	35
450	16	470	36	400	37	410	50
460	30	480	36	410	46	420	50
470	37	490	37	420	53	430	65
480	34	500	43	430	68	440	64
490	34	510	50	440	68	450	80
500	46	520	42	450	90	460	75
510	50	530	61	460	83	470	85
520	41	540	68	470	78	480	63
530	59	550	55	480	65	490	89
540	72	560	60	490	101	500	83
550	58	570	56	500	83	510	94
560	58	580	54	510	95	520	88
570	54	590	57	520	91	530	81
580	57	600	73	530	75	540	94
590	57	610	59	540	101	550	79
600	84	620	55	550	87	560	78
610	59	630	52	560	80	570	79
620	56	640	58	570	79	580	60
630	55	650	65	580	57	590	66
640	55	660	59	590	64	600	51
650	63	670	47	600	53	610	51
660	54	680	60	610	45	620	41
670	53	690	57	620	36	630	29
680	67	700	60	630	28	640	39
690	56	710	48	640	40	650	26
700	58	720	38	650	21	660	21
710	47	730	35	660	20	670	13
720	44	740	34	670	12	680	9
730	39	750	36	680	9	690	5
740	33	760	34	690	5	700	7
750	36	770	35	700	7	710	2
760	33	780	32	710	2	750	1
770	39	790	33	750	1	760	2
780	33	800	19	760	2		
790	32	810	15				
800	20	820	13				
810	15	830	14				
820	14	840	12				
830	14	850	10				
840	11	860	5				
850	9	870	4				
860	5	880	9				
870	4	890	4				
880	10	900	1				
890	5	920	1				
900	1	930	1				
910	1	950	1				

Table 33: ^{11}C energy spectrum expressed via the normalized charge variable (Unit: [npe]) and the normalized number of hits (Unit: [nhits]). The content of ^{11}C in the used data set is ∼97%. The total lifetime corresponds to 562 days. The radial and z-cut for the *fiducial volumes* FV_1 and FV_2 are: R<3.067 m and $|z|$ <1.67 m, and R<2.8 and -2.4 m<z<2.2 m, respectively.

Bin	Probability	Bin	Probability	Bin	Probability
31	2.78 ± 1.15	70	6.40 ± 1.83	109	11.20 ± 2.64
32	4.12 ± 1.61	71	5.10 ± 1.71	110	9.16 ± 1.95
33	3.14 ± 1.51	72	2.93 ± 0.98	111	12.80 ± 2.58
34	2.13 ± 1.05	73	3.94 ± 1.46	112	14.13 ± 2.82
35	1.48 ± 0.95	74	5.72 ± 1.51	113	13.98 ± 2.88
36	2.46 ± 1.10	75	5.90 ± 1.66	114	13.00 ± 2.83
37	0.65 ± 0.46	76	3.59 ± 1.08	115	19.25 ± 3.42
38	0.33 ± 0.33	77	3.11 ± 1.20	116	17.92 ± 3.23
39	0.98 ± 0.56	78	6.40 ± 1.83	117	22.19 ± 3.56
40	2.64 ± 1.30	79	4.59 ± 1.53	118	27.79 ± 4.02
41	3.29 ± 1.38	80	1.81 ± 1.00	119	24.32 ± 3.71
42	4.27 ± 1.49	81	6.60 ± 2.16	120	25.80 ± 3.83
43	2.46 ± 1.10	82	6.58 ± 1.95	121	29.98 ± 4.35
44	1.16 ± 0.89	83	4.59 ± 1.53	122	24.14 ± 3.65
45	1.81 ± 1.00	84	7.55 ± 2.03	123	32.91 ± 4.46
46	2.13 ± 1.05	85	5.42 ± 1.74	124	40.32 ± 4.94
47	2.13 ± 1.05	86	4.92 ± 1.56	125	35.55 ± 4.65
48	0.98 ± 0.56	87	3.11 ± 1.20	126	30.60 ± 4.28
49	1.48 ± 0.95	88	2.93 ± 0.98	127	34.42 ± 4.65
50	1.81 ± 1.00	89	8.03 ± 1.97	128	31.75 ± 4.37
51	1.81 ± 1.00	90	10.54 ± 2.60	129	21.74 ± 3.71
52	0.98 ± 0.56	91	8.89 ± 2.32	130	20.91 ± 3.62
53	1.96 ± 0.80	92	4.92 ± 1.56	131	22.07 ± 3.72
54	2.46 ± 1.10	93	7.38 ± 1.91	132	16.14 ± 3.20
55	5.27 ± 1.84	94	12.35 ± 2.79	133	10.04 ± 2.49
56	4.59 ± 1.53	95	12.50 ± 2.72	134	13.03 ± 2.97
57	2.96 ± 1.34	96	8.33 ± 1.77	135	5.27 ± 1.84
58	3.14 ± 1.51	97	9.72 ± 2.47	136	3.32 ± 1.66
59	4.44 ± 1.64	98	8.38 ± 2.20	137	1.48 ± 0.95
60	1.16 ± 0.89	99	14.10 ± 2.66	138	0.33 ± 0.33
61	6.07 ± 1.80	100	7.41 ± 2.12	139	2.78 ± 1.15
62	1.48 ± 0.95	101	13.63 ± 2.71	141	1.98 ± 1.22
63	3.61 ± 1.42	102	10.01 ± 2.31	151	0.33 ± 0.33
64	2.28 ± 0.86	103	15.34 ± 3.23	156	0.33 ± 0.33
65	3.14 ± 1.51	104	10.49 ± 2.26	171	0.33 ± 0.33
66	5.1 ± 1.71	105	15.08 ± 2.72	175	0.83 ± 0.83
67	3.97 ± 1.72	106	14.78 ± 2.86	181	2.31 ± 1.26
68	5.24 ± 1.59	107	11.49 ± 2.50		
69	3.11 ± 1.20	108	8.35 ± 1.99		

Table 34: Probability density function of events from the external ^{228}Th source reconstructed within a *fiducial volume* with radius R<2.5 m. Energy scale: 10 npe/bin.

Bin	Probability	Bin	Probability	Bin	Probability
31	1.26 ± 0.29	72	5.75 ± 0.62	113	15.78 ± 1.06
32	1.43 ± 0.32	73	6.26 ± 0.65	114	14.99 ± 1.02
33	1.26 ± 0.29	74	4.90 ± 0.54	115	16.90 ± 1.04
34	0.82 ± 0.23	75	8.12 ± 0.77	116	17.62 ± 1.10
35	1.31 ± 0.31	76	6.00 ± 0.61	117	20.53 ± 1.18
36	0.65 ± 0.18	77	5.05 ± 0.53	118	24.36 ± 1.32
37	1.00 ± 0.21	78	6.35 ± 0.63	119	23.23 ± 1.28
38	0.73 ± 0.19	79	6.89 ± 0.68	120	25.37 ± 1.32
39	1.15 ± 0.27	80	7.17 ± 0.74	121	27.48 ± 1.43
40	0.80 ± 0.24	81	6.56 ± 0.66	122	26.32 ± 1.35
41	1.84 ± 0.35	82	8.14 ± 0.76	123	32.16 ± 1.54
42	1.92 ± 0.36	83	7.31 ± 0.68	124	30.04 ± 1.47
43	1.30 ± 0.29	84	7.67 ± 0.70	125	28.97 ± 1.44
44	0.82 ± 0.23	85	8.02 ± 0.75	126	27.78 ± 1.45
45	1.70 ± 0.34	86	9.00 ± 0.76	127	26.15 ± 1.41
46	1.32 ± 0.27	87	8.00 ± 0.73	128	24.42 ± 1.37
47	1.75 ± 0.33	88	8.85 ± 0.79	129	20.63 ± 1.29
48	1.23 ± 0.27	89	10.46 ± 0.85	130	19.05 ± 1.26
49	2.10 ± 0.38	90	8.86 ± 0.78	131	16.15 ± 1.18
50	2.22 ± 0.38	91	11.37 ± 0.90	132	11.43 ± 0.97
51	2.15 ± 0.37	92	9.28 ± 0.78	133	8.35 ± 0.83
52	1.60 ± 0.29	93	11.62 ± 0.92	134	9.60 ± 0.93
53	1.96 ± 0.33	94	9.55 ± 0.84	135	5.43 ± 0.69
54	2.58 ± 0.42	95	10.29 ± 0.85	136	4.37 ± 0.63
55	2.69 ± 0.45	96	11.07 ± 0.87	137	2.26 ± 0.45
56	3.19 ± 0.45	97	10.64 ± 0.85	138	2.48 ± 0.49
57	2.13 ± 0.36	98	10.15 ± 0.81	139	1.88 ± 0.41
58	2.72 ± 0.45	99	10.28 ± 0.81	140	0.94 ± 0.30
59	3.62 ± 0.49	100	11.93 ± 0.93	141	0.56 ± 0.23
60	3.91 ± 0.51	101	12.77 ± 0.95	142	0.14 ± 0.11
61	3.46 ± 0.46	102	13.37 ± 0.95	143	0.14 ± 0.11
62	2.97 ± 0.43	103	12.49 ± 0.95	144	0.04 ± 0.04
63	3.53 ± 0.47	104	13.27 ± 0.96	145	0.25 ± 0.15
64	4.24 ± 0.50	105	13.58 ± 0.98	146	0.10 ± 0.10
65	3.97 ± 0.50	106	13.64 ± 0.98	147	0.10 ± 0.10
66	5.01 ± 0.60	107	13.88 ± 0.99	151	0.04 ± 0.04
67	4.90 ± 0.59	108	14.24 ± 1.00	156	0.04 ± 0.04
68	4.72 ± 0.56	109	13.94 ± 0.99	171	0.04 ± 0.04
69	5.16 ± 0.55	110	14.46 ± 1.00	175	0.10 ± 0.10
70	5.56 ± 0.60	111	14.85 ± 1.01	181	0.73 ± 0.23
71	5.17 ± 0.57	112	15.94 ± 1.05		

Table 35: Probability density function of events from the external ^{228}Th source reconstructed within a *fiducial volume* with radius R<3.0 m. Energy scale: 10 npe/bin.

Source position	BTB	Non-problematic runs	Problematic runs
N2*	250	13561,13568,13571,13573, 13575,13579,13581,13590, 13595-13597,13602,13604, 13608	13564(G),13565(G),13567(G), 13569(G),13570(G),13574(E), 13576(G),13577(G),13578(E), 13580(G),13583(G)-13589(G), 13591(G)-13594(G),13609(G), 13598(G)-13601(G),13606(G)
N2	250	13621-13636	13610(E)-13612(E), 13614(E)-13620(E)
	200	13640,13642-13654	13637(E)-13639(E)
	180	13655,13659-13662	–
	100	13663,13672,13674-13686	13664(E)-13671(E)
N6	200	13687,13688	–
	100	13689,13690,13692-13699	–
	80	13701-13711,13713, 13715-13726,13730-13739, 13743-13756	–

Table 36: First external calibration campaign in Borexino (from July 5 to July 14, 2010). List of all accepted and rejected runs for all source positions in dependence of the BTB energy threshold. Abbreviations: (G) = Most events tend to have a negative, α-like Gatti parameter; (E) energy spectrum shifted to lower energies and positions of events are partially reconstructed more towards the detector center.

A.5 Reference plots

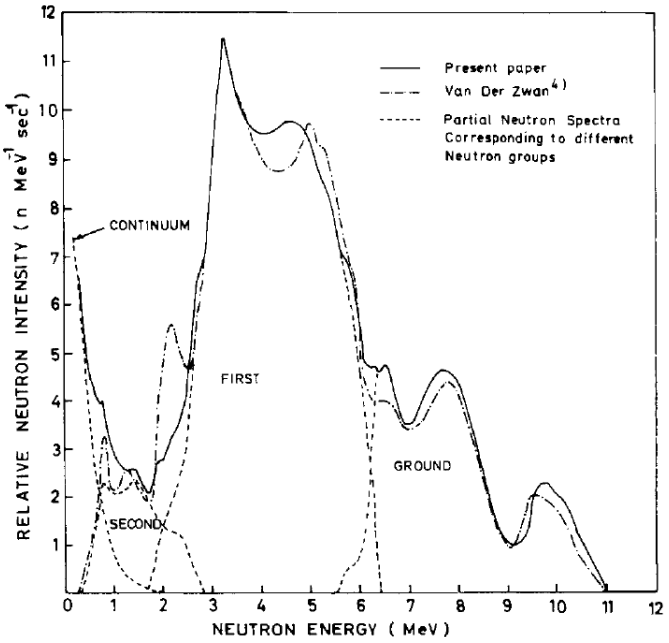

Figure 91: Neutron spectrum of an ^{241}Am^{9}Be source calculated by [150]. Secondary reactions are not included.

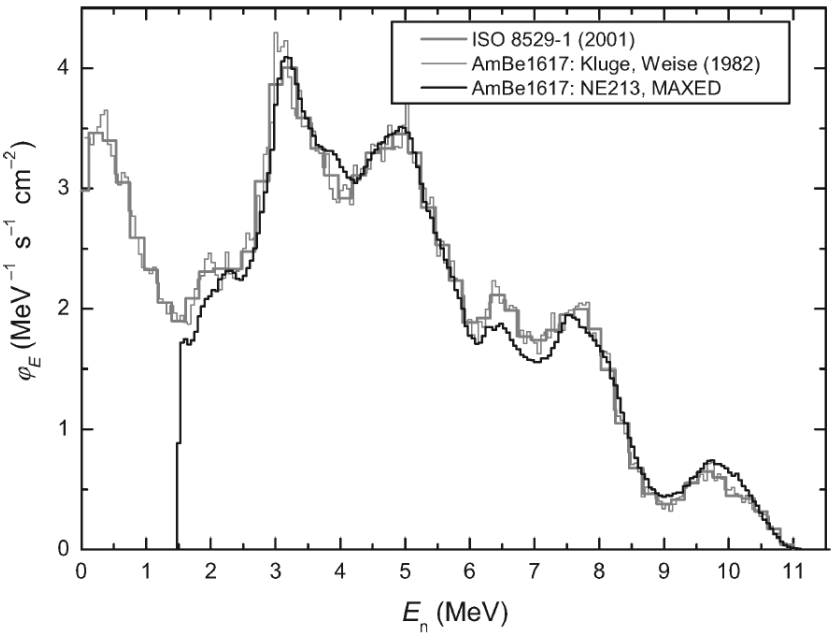

Figure 92: Measurement of neutron spectrum of an ^{241}Am^{9}Be source with two different methods: (i) liquid scintillation detector (NE213) by A. Zimbal and (ii) high-resolution ^{3}He semiconductor sandwich spectrometer by Kluge et al. [151]. The latter one was the foundation for the ISO recommended spectrum in ISO 8529-1 (2001).

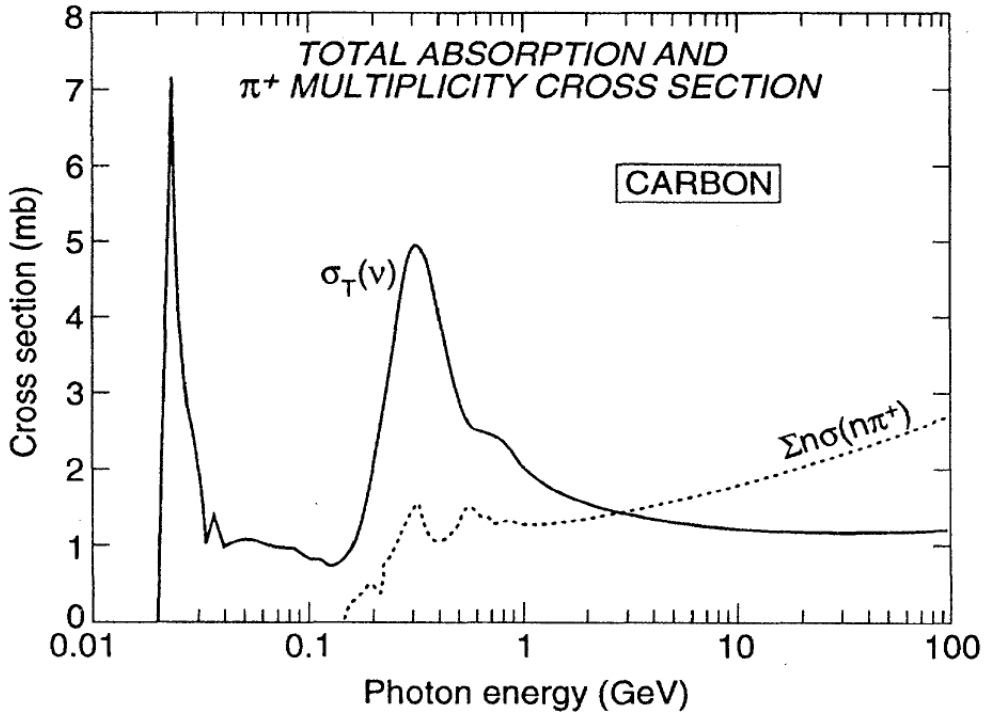

Figure 93: Total absorption cross section for the photo-nuclear reaction ^{12}C(γ,n)^{11}C and the weighted π^+ photoproduction cross section $\sigma n\sigma(n\pi^+)$ (dashed line). The photonuclear interaction dominates at lower incident γ energies with the GDR around 30 MeV. (taken from [166])

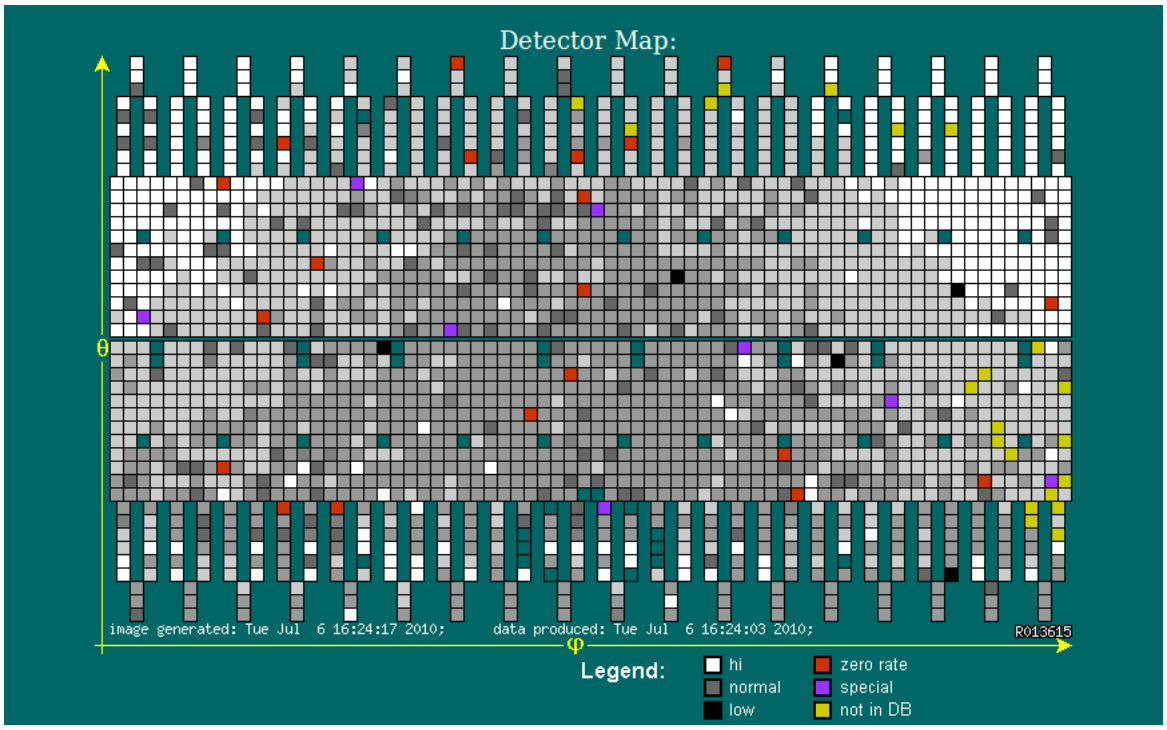

Figure 94: Screen shot: Borexino online monitor during calibration with the external ^{228}Th source deployed in position N2 (northern hemisphere).

[ID] FE & Sum OD HVD values map | FE values map | Scalers values map | Scalers color map

FE board:	1	2	3	4	5	6	7	8	9	10	11	12	13	14	status
RACK 1	6.1	6.7	8.1	7.7	12.8	7.0	13.7	6.8	12.0	4.8	1.8	2.6	4.8	6.5	
RACK 2	4.3	7.4	1.8	7.3	3.3	7.2	8.9	6.1	6.8	4.5	8.0	5.7	3.7	7.5	
RACK 3	5.5	3.6	4.7	6.0	3.9	13.6	15.3	5.2	5.0	6.2	6.1	4.1	3.4	2.5	
RACK 4	22.8	5.7	10.6	5.2	3.3	4.4	2.5	1.6	4.1	6.1	5.0	2.3	1.7	3.3	
RACK 5	14.3	8.2	5.9	6.0	10.8	17.1	14.4	5.1	6.2	4.3	8.9	4.1	6.1	6.1	
RACK 6	9.3	10.6	5.0	7.7	3.4	7.3	5.4	5.2	3.9	6.1	6.2	10.2	2.7	5.3	
RACK 7	10.2	3.8	5.3	3.9	4.9	4.0	4.3	4.5	6.9	6.3	5.3	5.8	2.6	3.0	
RACK 8	2.8	29.5	1.0	3.7	5.6	8.4	2.0	5.0	11.4	20.8	19.7	4.8	15.4	6.1	
RACK 9	6.2	5.5	3.6	2.7	10.6	9.1	15.4	13.1	48.3	34.6	87.5	19.6	39.0	14.2	
RACK 10	9.0	1.7	11.2	5.2	29.0	4.6	27.6	6.3	13.5	21.7	13.4	7.6	8.3	3.3	
RACK 11	2.8	5.7	4.9	5.3	11.7	6.7	11.1	9.9	7.7	6.4	5.3	5.6	5.2	31.7	
RACK 12	9.3	8.8	5.7	7.2	7.6	7.4	15.0	7.1	13.6	16.6	10.6	5.0	16.5	4.3	
RACK 13	5.7	7.6	4.0	5.8	6.9	10.7	7.4	10.6	5.5	4.1	5.0	6.1	3.8	5.3	
FE board:	1	2	3	4	5	6	7	8	9	10	11	12	13	14	status
												Racks Avrg. Temperature (°C)			45.2
OD HV Sums	97.5	44.1	19.8	13.8	21.1	17.7	17.0	61.2	9.5	-	-	-	-	-	OD HV Sums

Figure 95: Screen shot: Borexino scalers during calibration with the external ^{228}Th source deployed in position N2. The rates are given in kHz.

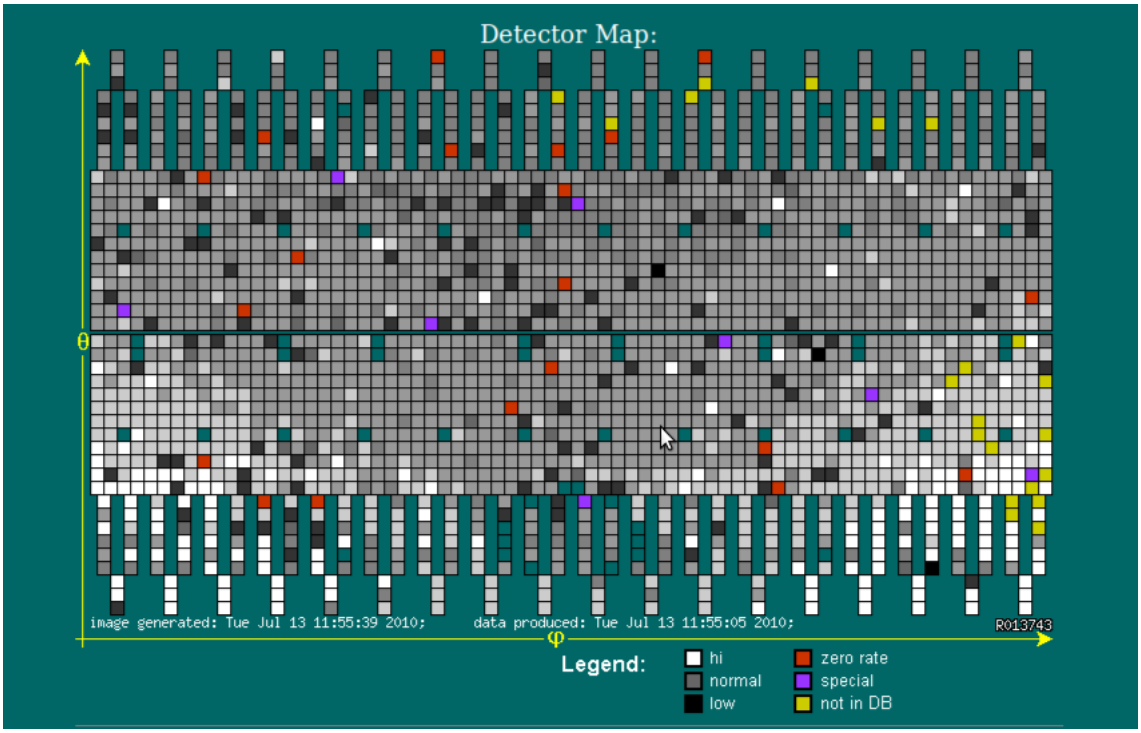

Figure 96: Same as in Figure 94 for the ^{228}Th source deployed in position N6 (southern hemisphere).

[ID] FE & Sum OD HVD values map FE values map Scalers values map Scalers color map

FE board:	1	2	3	4	5	6	7	8	9	10	11	12	13	14	status
RACK 1	2.8	4.0	2.4	3.9	12.3	4.8	8.3	8.0	4.6	3.6	1.6	1.9	3.5	1.7	
RACK 2	4.4	7.5	1.9	6.0	2.6	5.8	8.3	5.1	5.7	4.0	7.9	4.4	2.5	6.3	
RACK 3	5.3	3.3	4.2	4.8	3.0	14.4	13.3	5.5	4.9	5.8	6.0	3.0	2.4	1.6	
RACK 4	23.5	6.2	9.7	5.8	3.2	4.6	2.0	1.2	3.3	5.3	5.4	1.5	1.4	2.4	
RACK 5	12.1	7.1	5.0	6.2	6.5	14.7	14.6	6.1	6.4	5.7	9.4	4.3	7.7	5.1	
RACK 6	8.3	9.1	5.6	6.3	3.5	7.1	5.5	5.4	3.8	5.8	6.9	11.1	3.1	4.8	
RACK 7	10.3	4.7	6.5	4.9	5.3	5.0	4.1	6.5	4.6	7.7	6.1	6.2	4.7	5.0	
RACK 8	1.5	18.8	0.6	2.4	2.5	6.5	1.3	2.0	3.8	5.1	5.0	1.8	4.2	3.1	
RACK 9	5.8	5.3	2.5	2.6	7.3	5.1	4.4	4.9	6.9	7.5	4.7	7.6	2.5	3.9	
RACK 10	3.1	0.9	5.9	34.5	27.7	34.9	82.6	11.9	20.8	33.6	22.8	13.7	16.1	9.3	
RACK 11	3.4	8.3	7.4	10.9	13.9	8.5	10.2	8.2	7.7	6.6	4.7	5.8	4.5	14.4	
RACK 12	6.0	5.4	5.1	8.9	9.3	4.1	12.9	3.7	6.6	4.6	6.5	4.7	15.4	4.4	
RACK 13	12.9	3.7	7.0	12.3	22.1	9.9	6.8	8.1	5.9	4.6	5.1	6.3	3.2	4.0	
FE board:	1	2	3	4	5	6	7	8	9	10	11	12	13	14	status
												Racks Avrg. Temperature (°C)			44.9
OD HV Sums	106.8	47.0	22.3	18.3	25.6	26.4	19.4	61.8	13.6	-	-	-	-	-	OD HV Sums

Figure 97: Same as in Figure 95 for the ^{228}Th source deployed in position N6.

References

[1] J.N. Bahcall, "Neutrino Astrophysics", Cambridge University Press, Cambridge, England (1989)

[2] W.C. Haxton, "The solar neutrino problem", *Annu. Rev. Astron. Astrophys.* **33** (1995), pp. 459-503

[3] V. Castellani et al., "Solar neutrinos: Beyond standard solar models", *Phys. Rep.* **281** (1997), pp. 309-398

[4] A. Kirsten, "Solar neutrino experiments: results and implications", *Rev. Mod. Phys.* **71** (1999), pp. 1213-1232

[5] B. Pontecorvo, *Jour. Exp. Theoret. Phys.* **34** 247 (1958)

[6] Z. Maki, M. Nakagava, and S. Sakata, *Prog. Theor. Phys.* **28** 870 (1962)

[7] B. Pontecorvo, *Jour. Exp. Theoret. Phys.* **53** 1717 (1967)

[8] S. Eidelmann et al., from: "Particle Data Group - The Review of Particle Physics", "Ch. 15: Neutrino mass, mixing, and flavor change", *Phys. Lett. B* **592** (2004); `http://pdg.lbl.gov`

[9] M.C. Gonzalez-Garcia, and M. Maltoni, "Phenomenology with Massive Neutrinos", *Phys. Rept.* **460**, (2008) pp. 1-129

[10] T. Schwetz, M. Tortola, and J.W.F. Valle, "Three-favour neutrino oscillation update", *New J. Phys.* **10**, (2008), p. 113011 ; `arXiv:hep-ph/0808.2016`

[11] M.C. Gonzalez-Garcia, M. Maltoni, and J. Salvado, "Updated global fit to three neutrino mixing: status of the hints of theta13 $>$ 0", *J. High-Energy Phys.* **04** 056 (2010); `arXiv:hep-ph/1001.4524v3`

[12] A.Yu Smirnov, "The MSW effect and Solar Neutrinos", *11^{th} workshop on Neutrino Telescopes, Venice, March 11-14 2003, (2003)*; `arXiv:hep-ph/0305106`

[13] G. Gelmini, and E. Roulet, "Neutrino Masses", *Rept. Prog. Phys.* **58** 1207 (1995)

[14] D. Franco, Ph.D. thesis, Universitá degli Studi di Milano (2004)

[15] G. Bellini et al. (Borexino collaboration), "Measurement of the solar 8B neutrino rate with a liquid scintillator target and 3 MeV energy threshold in the Borexino detector", *Phys. Rev.* **D82** 033006 (2010); `arXiv:astro-ph/0808.2868v3`

[16] M. Apollonio et al., "Search for neutrino oscillations on a long base-line at the CHOOZ nuclear power station", *Eur. Phys. J. C* **27** (2003), pp. 331-374

[17] M. Maltoni et al., "Status of global fits to neutrino oscillations", *New J. Phys.* **6** 122 (2004)

[18] M. Fukugita, and T. Yanagida, "Baryogenesis Without Grand Unification", *Phys. Lett. B* **174** 45 (1986)

[19] M. Mezzetto, and T. Schwetz, "ϑ_{13}: phenomenology, present status and prospect" (2010); `arXiv:hep-ph/1003.5800`

[20] H.V. Klapdor-Kleingrothaus et al., "Evidence for Neutrinoless Double Beta Decay", *Mod. Phys. Lett. A* **16** (2001), pp. 2409-2420; `arXiv:hep-ph/0201231`

[21] H.V. Klapdor-Kleingrothaus et al., "Latest Results from the Heidelberg-Moscow Double-Beta-Decay Experiment", *Eur. Phys. J. A* **12** 147 (2001); `arXiv:hep-ph/0103062`

[22] M. Lindner, A. Merle, and W. Rodejohann, "Improved Limit on ϑ_{13} and Implications for Neutrino Masses in Neutrino-less Double Beta Decay and Cosmology", *Phys. Rev. D* **73** 053005 (2006); `arXiv:hep-ph/0512143`

[23] W. Maneschg, A. Merle, and W. Rodejohann, "Statistical Analysis of future Neutrino Mass Experiments including Neutrino-less Double Beta Decay, *Europhys. Lett.* **85** 51002 (2009); `arXiv:hep-ph/0812.0479`

[24] H.M. Antia et al., "Lectures on Solar Physics", *edited by H.M Antia, A. Bhatnagar, and P. Ulmschneider*, Springer Verlag Berlin Heidelberg (2003)

[25] J. Christensen-Dalsgaard, "Helioseismology", *Rev. Mod. Phys.* **74** 1073 (2002); `arXiv:astro-ph/0207403v1`

[26] A. Unsöld, and B. Baschek, "Der neue Kosmos", *6th edition*, Springer-Verlag (1999)

[27] S. Hannestad, "Primordial Neutrinos", *Ann. Rev. Nucl. Part. Sci.* **56** (2006), pp. 137-161; `arXiv:hep-ph/0602058`

[28] A. Osipowicz et al. (KATRIN collaboration), "KATRIN: A next generation tritium beta decay experiment with sub-eV sensitivity for the electron neutrino mass" (2001), `arXiv:hep-ex/0109033`

[29] P. Minkowski, *Phys. Lett. B* **67** 421 (1977)

[30] S.P. Mikheev, and A. Yu. Smirnov, *Sov. J. Nucl. Phys.* **42** 913 (1985)

[31] L. Wolfenstein, *Phys. Rev. D* **17** 2369 (1978)

[32] J.N. Bahcall, M. H. Pinsonneault, and G. J. Wasserburg, "Solar models with helium and heavy-element diffusion", *Rev. Mod. Phys.* **67** (1995), pp. 781-808

[33] N. Grevesse, and A. J. Sauval, "Standard Solar Composition", *Space Sci. Rev.* **85** 161 (1998)

[34] M. Asplund, N. Grevesse, and A. J. Sauval, "The solar chemical composition", *review presented at "Cosmic abundances as records of stellar evolution and nucleosynthesis", F.N. Bash and T.G. Barnes eds., ASP conf. series, Nucl. Phys. A* **777** (2006), pp. 1-4; `arXiv:astro-ph/0410214v2`

[35] N. Grevesse et al., "The chemical composition of the Sun", *Astrophys. Space Sci.* **328** (2010), pp. 179-183

[36] K. Lodders, "Solar System Abundances of the Elements", *Astrophysics and Space Science Proceedings, A. Goswami and B.E. Reddy eds.*, Springer-Verlag Berlin Heidelberg (2010), pp. 379-417

[37] J.N. Bahcall, M.C. Gonzalez-Garcia, and C. Peña-Garay,"Does the Sun Shine by *pp* or CNO Fusion Reactions?", *Phys. Rev. Lett.* **90** 131301 (2003), pp. 1-4

[38] A. Serenelli, "New results on standard solar models", *Astrophys. Space Sci.* **328** (2010), pp. 13-21; `arXiv:astro-ph/0910.3690v1`

[39] J.N. Bahcall, A.M. Serenelli, and S. Basu, "New solar opacities, abundances, helioseismology, and neutrinos", *Astrophys. J.* **621** (2005), pp. L85-L88

[40] N.R. Badnell et al., "Updated opacities from the Opacity Project", *Mon. Not. R. Astron. Soc.*, **360** (2005), pp. 458-464; `arXiv:/astro-ph/0410744`

[41] J.N. Bahcall, and A.M. Serenelli, "How do uncertainties in the surface chemical composition of the Sun affect the predicted solar neutrino fluxes?", *Astrophys. J.* **626** 530 (2005)

[42] C. Peña-Garay, A.M. Serenelli, "Solar neutrinos and the solar composition problem" (2008); `arXiv:astro-ph/0811.2424`

[43] J.N. Bahcall, "Solar neutrinos: Where We Are, What We Need", *Nucl. Phys. A* **631** (1998), pp. 29c-41c; `arXiv:nucl-th/9802050v1`

[44] C. Arpesella et al. (Borexino collaboration), "New results on solar neutrino fluxes from 192 days of Borexino data", *Phys. Rev. Lett.* **101** 091302 (2008)

[45] N. Grevesse, *invited talk at workshop "The physics of the Sun and the solar neutrinos: 2nd ", October 4-5 2010, Lab. Naz. del Gran Sasso, L' Aquila*, `http://physun2010.mi.infn.it/`

[46] S. Basu, and H.M. Antia, "Constraining Solar Abundances Using Helioseismology" *Astrophys. J.* **606** 85 (2004); `arXiv:astro-ph/0403485v1`

[47] J. Montalban et al., *Proc. at SOHO14/GONG2004 Workshop "Helio- and Asteroseismology: Towards a Golden Future", D. Danesy ed., ESA SP-559* **574** (2004)

[48] J. Montalban et al., "The new solar abundances - Part II: the crisis and possible solutions", *Comm. Astroseism.* **147** 80 (2006)

[49] J.A. Guzik, L.S. Watson, and A.N. Cox, "Can Enhanced Diffusion Improve Helioseismic Agreement for Solar Models with Revised Abundances?" *Astrophys. J.* **627** 1049 (2005)

[50] M. Castro, S. Vauclair, and O. Richard, "Low abundances of heavy elements in the solar outer layers: comparisons of solar models with helioseismic inversions" (2006); `arXiv:astro-ph/0611619`

[51] B.T. Cleveland et al., "Measurement of the Solar Electron Neutrino Flux with the Homestake Chlorine Detector", *Astrophys. J.* **496** 505 (1998);

[52] K. Lande, and P. Wildenhain, "The Homestake chlorine solar neutrino experiment - past, present and future", *Nucl. Phys. B Proc. Suppl.* **118** 49 (2003)

[53] R. Davis, *Nobel Prize Lecture* (2002)

[54] J.N. Abdurashitov et al. (SAGE collaboration), "Measurement of the Solar Neutrino Capture Rate by SAGE and Implications for Neutrino Oscillations in Vacuum", *Phys. Rev. Lett.* **83** (1999), pp. 4686-4689

[55] W. Hampel et al. (GALLEX collaboration), "GALLEX solar neutrino observations: Results for GALLEX IV", *Phys. Lett. B* **447** 127 (1999)

[56] M. Altmann et al. (GNO collaboration), "Complete results for five years of GNO solar neutrino observations", *Phys. Lett. B* **616** 174 (2005); `arXiv:hep-ex/0504037v1`

[57] F. Käther et al., "Reanalysis of the GALLEX solar neutrino flux and source experiments", Phys. Lett. B **685** 1 (2010); `arXiv:hep-ex/1001.2731v1`

[58] K.S. Hirata et al. (KamiokaNDE Collaboration), "Observation of 8B solar neutrinos in the Kamiokande-II detector", *Phys. Rev. Lett.* **63** (1989), pp. 16-19

[59] J.P. Cravens et al. (SuperKamiokaNDE Collaboration), "Solar neutrino measurements in Super-Kamiokande-II", *Phys. Rev. D* **78** 032002 (2008)

[60] J. Hosaka et al. (SuperKamiokaNDE Collaboration), "Solar neutrino measurements in Super-Kamiokande-I", *Phys. Rev. D* 73, 112001 (2006)

[61] B. Aharmim et al. (SNO Collaboration), "Determination of the ν_e and total 8B solar neutrino fluxes using the Sudbury Neutrino Observatory Phase I data set", *Phys. Rev. C* **75** 045502 (2007)

[62] B. Aharmim et al. (SNO Collaboration), "Low Energy Threshold Analysis of the Phase I and Phase II Data Sets of the Sudbury Neutrino Observatory", *Phys. Rev. C* **81** 055504 (2010); `arXiv:nucl-ex/0910.2984v2`

[63] C. Arpesella et al. (Borexino collaboration), "Borexino at Gran Sasso - Proposal for a real time detector for low energy solar neutrinos", *ed. By I.N.F.N.* (August 1991); "A real time detector for low energy solar neutrinos", *ed. By Princeton University* (December 1992)

[64] C. Arpesella et al. (Borexino collaboration), "First real time detection of 7Be solar neutrinos by Borexino", *Phys. Lett. B* **658** (2008), pp. 101-108; `arXiv:astro-ph/0708.2251v2`

[65] C. Arpesella et al. (Borexino collaboration), "Direct Measurement of the 7Be Solar Neutrino Flux with 192 Days of Borexino Data", *Phys. Rev. Lett.* **101** 091302 (2008); `arXiv:astro-ph/0805.3843v2`

[66] F. Mantovani et al., "Antineutrinos from Earth: A reference model and its uncertainties", *Phys. Rev. D* **69** 013001 (2004); `arXiv:hep-ph/0309013v2`

[67] T. Araki et al. (KamLAND collaboration), *Nature* **436** 499 (2005); S. Abe et al. (KamLAND collaboration), *Phys. Rev. Lett.* **100** 221803 (2008)

[68] G. Bellini et al. (Borexino collaboration), "Observation of Geo-Neutrinos", *Phys. Lett. B* **687** (2010), pp. 299-304; `arXiv:hep-ex/1003.0284v2`

[69] G. Bellini et al. (Borexino collaboration), "New experimental limits on the Pauli-forbidden transitions in 12C nuclei obtained with 485 days Borexino data", *Phys. Rev. C* **81** 034317 (2010); `arXiv:hep-ex/0911.0548v1`

[70] G.L. Fogli et al.,"Geo-neutrinos: A systematic approach to uncertainties and correlations", *Phys. Scr.* **89** (2006); `arXiv:physics/0608025`

[71] C.G. Rothschild, M.C. Chen, and F.P. Calaprice, "Antineutrino Geophysics with Liquid Scintillator Detectors", *Geophy. Res. Lett.* **25** 1083 (1998); `arXiv:nucl-ex/9710001v2`

[72] G. Bellini et al. (Borexino collaboration), "Study of solar and other unknown anti-neutrino fluxes with Borexino at LNGS" (2010), `arXiv:hep-ex/1010.0029v1`

[73] F. Calaprice et al., "The Borexino Supernovae Alarm System", Borexino internal note, February 2009

[74] S.A. Colgate, and R.H. White, "The hydrodynamic behavior of supernovae explosions", *Astrophys. J.* **143** (1966), pp. 626-681

[75] J.R. Wilson, "Numerical Astrophysics", *eds. J. Centrella et al.*, Jones & Bartlett, Boston (1986)

[76] J. N. Bahcall, A. Dar, and T. Piran, "Neutrinos From the Supernova in the LMC", *Nature* **326** 6109 (1987 March 12), pp. 135-136

[77] P. Antonioli et al., "SNEWS: The SuperNova Early Warning System", *New Jour. Phys.* **6** 114 (2004)

[78] G. Imbriani et al., "The bottleneck of CNO burning and the age of Globular Clusters", *Astron. Astrophys.* **420** 625 (2004), pp. 625-629

[79] M. Deutsch et al., "Proposal for a Cosmic Ray Detection System for the Borexino Solar Neutrino Experiment", `http://borex.princeton.edu/public-docs/papers/muon-paper.pdf` (1996)

[80] C. Galbiati et al., "Cosmogenic ^{11}C production and sensitivity of organic scintillator detectors to *pep* and CNO neutrinos", *Phys. Rev. C* **71** 055805 (2005); `arXiv:hep-ph/0411002v2`

[81] H. Back et al. (Borexino collaboration), "CNO and *pep* neutrino spectroscopy in Borexino: Measurement of the deep-underground production of cosmogenic ^{11}C in an organic liquid scintillator", *Phys. Rev. C* **74** 045805 (2006); `arXiv:hep-ex/0601035v4`

[82] C. Arpesella et al. (Borexino collaboration), "Borexino at Gran Sasso - Proposal for a real time detector for low energy solar neutrinos", *ed. By I.N.F.N.* (August 1991); "A real time detector for low energy solar neutrinos", *ed. By Princeton University* (December 1992)

[83] G. Alimonti et al. (Borexino collaboration), "Light propagation in a large volume liquid scintillator", *Nucl. Inst. Meth. A* **440** (1998), pp. 360-371

[84] H.O. Back et al. (Borexino collaboration), "Pulse-shape discrimination with the Counting Test Facility", *Nucl. Inst. Meth. A* **584** (2007), pp. 98-113; `arXiv:physics/0705.0239v1`

[85] H.O. Back et al. (Borexino collaboration), "New limits on nucleon decays into invisible channels with the Borexino Counting Test Facility", *Phys. Lett. B* **563** (2003), pp. 23-34; `arXiv:hep-ex/0302002v2`

[86] H.O. Back et al. (Borexino collaboration), "Study of the neutrino electromagnetic properties with the prototype of the Borexino detector", *Phys. Lett. B* **563** (2003), pp. 35-47

[87] H.O. Back et al. (Borexino collaboration), "New experimental limits on violations of the Pauli exclusion principle obtained with the Borexino counting test facility", *Eur. Phys. J. C* **37** (2004), pp. 421-431; `arXiv:hep-ph/0406252v1`

[88] G. Alimonti et al. (Borexino collaboration), " The Borexino detector at the Laboratori Nazionali del Gran Sasso", *Nucl. Inst. Meth. A* **600**, pp. 568-593; `arXiv:physics/0806.2400v1`

[89] G. Bellini et al. (Borexino collaboration), "Muon and Cosmogenic Neutron Detection in Borexino", *accepted for publication in JINST* (February 2011); `arXiv:physics.ins-det/1101.3101v2`

[90] D. D'Angelo, Ph.D. thesis, Technische Universität München (2006)

[91] M. Wurm, Ph.D. thesis, Technische Universität München (2009)

[92] L. Oberauer, "Light Concentrators for Borexino and CTF", *Nucl. Inst. Meth. A* **530** (2004), pp. 453-462; `arXiv:physics/0310076v2`

[93] S.E. Hardy, Ph.D. thesis, Virginia Polytechnic Institute and State University (2010)

[94] R.B. Vogelaar et al., "Removal of cosmogenic ^{7}Be from scintillators", *Nucl. Inst. Meth. A* **372** (1996), pp. 59-66

[95] H. Simgen, and G. Zuzel, "Ultrapure Gases-From the Production Plant to the Laboratory", *Topical Workshop on Low Radioactivity Techniques: LRT 2006, Aussois (France), 45, ed. P. Loaiza*, *AIP Conf. Proc.* **897**, Springer, (2007)

[96] J. Benzinger et al., "The fluid-filling system for the Borexino solar neutrino detector", *Nucl. Inst. Meth. A* **608**, pp. 464-474

[97] G. Alimonti et al. (Borexino collaboration), "The liquid handling systems for the Borexino solar neutrino detector", *Nucl. Inst. Meth. A* **609** (2009), pp. 58-78

[98] G. t'Hooft, "Prediction for neutrino-electron cross-sections in Weinberg's model of weak interactions", *Phys. Lett. B* **37**, (1971), pp. 195-196

[99] J.B. Birks, "Scintillations from organic crystals: Specific fluorescence and relative response to different radiations", *Proc. Phys. Soc. A* **64** (1951), pp. 874-877

[100] J.B. Birks, "The Theory and Practice of Scintillation Counting", Pergamon Press (1964)

[101] G. Alimonti et al. (Borexino collaboration), "Light propagation in a large volume liquid scintillator", *Nucl. Inst. Meth A* **440** (2000), pp. 360-371

[102] G. Ranucci, et al., "A sampling board optimized for pulse shape discrimination in liquid scintillator applications", *IEEE Trans. Nucl. Sci.* **51** 4 (2004); pp. 1784-1790

[103] E. Gatti, and F. De Martini, "A new linear method of discrimination between elementary particles in scintillation counters", *Nucl. Electr.* **2** (1962), IAEA Wilen, pp. 265-276

[104] H.O. Back et al. (Borexino collaboration), "Pulse-Shape discrimination with the Counting Test Facility", *Nucl. Inst. Meth. A* **584** (2008), pp. 98-113; `arXiv:physics/0705.0239`

[105] Homepage of the data analysis framwork `ROOT`; `http://root.cern.ch/drupal/`

[106] The Lund/LBNL Nuclear Database, Version 2.0, February 1999, `http://nucleardata.nuclear.lu.se/nucleardata/toi/index.asp`

[107] B. Caccianiga et al., "GENEB: GEneration of NEutrino and Background", Borexino Internal Report, October 1997

[108] W.R. Nelson, H. Hirayama, and D.W.O. Rogers, "The EGS4 code system", *SLAC-265 UC-32* (1985), pp. 1-398

[109] S. Agostinelli et al. (GEANT collaboration), "GEANT4: A Simulation toolkit", *Nucl. Inst. Meth. A* **506** (2003); pp. 250-303

[110] J. Allison et al. (GEANT collaboration), "Geant4 developments and applications", *IEEE Transact. Nucl. Scie.* **53** 6 (2006); pp. 3842-3849

[111] J. Bieringer et al., "Trace analysis of aerosol bound particulates and noble gases at the Bfs in Germany", *Proc. to 5th ICRM-LLRMT '08*, *Appl. Rad. Isot.* **67** 5 (2009), pp. 672-677

[112] M. Pallavicini et al. (Borexino Steering Committee), "Update on Borexino Purification Campaign", Borexino internal note, 2010

[113] M. Shapiro, "Cosmic Radiation in Contemporary Astrophysics", Reidel Publishing House (1986)

[114] Dunai Tibor J., "Cosmogenic Nuclides: Principles, Concepts and Applications in the Earth Surface Sciences", Cambridge University Press (2010) ISBN: 0521873800, pp. 1-198

[115] K. Nakamura et al. (Particle Data Group), *J. Phys. G* **37** 075021 (2010)

[116] A. Tang et al., "Muon simulations for Super-Kamiokande, KamLAND, and CHOOZ", *Phys. Rev. D* **74** 053007 (2006)

[117] M. Ambrosio et al. (MACRO collaboration), "Vertical muon intensity measured with MACRO at the Gran Sasso Laboratory", *Phys. Rev. D* **52** (1995)

[118] M. Selvi (LVD collaboration), "Analysis of the seasonal modulation of the cosmic muon flux in the LVD detector during 2001-2008", *Proceedings of the 31st ICRC, Lodz, Poland, July 2009* (2009)

[119] L. Oberauer, and S. Schönert, "Status Report on the Borexino Muon Identification System", Borexino internal report (1998)

[120] T. Lewke, "Calibration and Efficiency Determination of the Borexino Muon Veto Based on the First Realtime Measurements of ^{7}Be Solar Neutrinos", diploma thesis, Technische Universität München (2007)

[121] M. Ambrosio et al. (MACRO collaboration), "Seasonal variations in the underground muon intensity as seen by MACRO", Astrop. Phys. **7** (1997), pp. 109-124

[122] A. Bouchta et al. (AMANDA collaboration), "Seasonal variation of the muon flux seen by AMANDA", *Proc. of the 26th International Cosmic Ray Conference, August 17-25, 1999, Salt Lake City, USA HE.3.2.11* (1999)

[123] E.W. Grashorn et al. (MINOS collaboration), "Observation of seasonal variations with the MINOS far detector" *Proc. of the 30th International Cosmic Ray Conference, July 3-11, 2007, Mérida, Mexico* (2007); `arXiv:hep-ex/0710.1616v1`

[124] S. Tilav et al. (IceCube collaboration), "Atmospheric Variations as observed by IceCube", *Proc. of the 31st ICRC, Lodz, Poland, July 2009* (2009); `arXiv:astro-ph/1001.0776v2`

[125] `http://chemicalland21.com/industrialchem/organic/PSEUDOCUMENE.htm`

[126] M. Ambrosio et al. (MACRO collaboration), "High energy cosmic ray physics with underground muons in MACRO. II. Primary spectra and composition", *Phys. Rev. D* **56** (1997); pp. 1418-1436

[127] P.G. Catalano et al., "Caratteristiche geolitologiche e strutturali dell' ammasso roccioso sovrastante il laboratorio INFN", *ANAS report* (1986) (unpublished); *Mem. Soc. Geol. Ital.* **35** 647 (1986)

[128] M. Ambrosio et al. (MACRO collaboration), "High energy cosmic-ray physics with underground muons in MACRO. I. Analysis methods and experimental results", *Phys. Rev. D* **56** (1997), pp. 1407-1417

[129] `http://proj-cngs.web.cern.ch/proj-cngs/`

[130] M. Pallavicini et al., "A short note about spallation neutron detection", Borexino internal note, July 2007

[131] A. Razeto et al., "Preliminary results from the test aimed at improving the μ-induced neutron detection with Laben electronics", Borexino internal note, October 2007

[132] S. Davini, "Determination of laben neutron clustering efficiency and studies on neutron energy reconstruction and corrections for cosmogenic neutron capture events", Borexino internal note, December 2009

[133] E. Litvinovich et al., "FADC data. User's guide", version 1.0 October 1 2010, Borexino internal note, October 2010

[134] R. Saldanha, Talk at Borexino General Meeting, January 2008

[135] Q. Meindl, Technische Universität München, private communication (2010)

[136] N. Agafonova et al. (LVD collaboration), "The Measurement of the Total Specific Muon-Generated Neutron Yield Using LVD", *29th International Cosmic Ray Conference Pune* **9** (2005), pp. 239-242

[137] H.M. Araujo et al., "Muon-induced neutron production and detection with GEANT4 and FLUKA", *Nucl. Inst. Meth. A* **545** (2005), pp. 399-411

[138] M. Aglietta et al. (LVD collaboration), "Measurement of the Neutron Flux Produced by Cosmic-Ray Muons with LVD at Gran Sasso", *Proceedings of the 26th International Cosmic Ray Conference, Salt Lake City, USA*, Vol. **2** (1999), p. 44; `arXiv:hep-ex/hep-ex/9905047`

[139] A. Fassò et al., *Proceedings of the 3rd Workshop on Simulating Accelerator Radiation Environments (SARE 3)*, *edited by H. Hirayama*, *KEK Proceedings* No. **97-5**, KEK, Tsukuba, Japan (1997), pp. 32

[140] Y.-F. Wang et al., "Predicting neutron production from cosmic-ray muons", *Phys. Rev. D* **64** 013012 (2001)

[141] V.A. Kudryavtsev, N.J.C. Spooner, and J.E. McMillan, "Simulation of muon-induced neutron flux at large depths underground", *Nucl. Inst. Meth. A* **505** (2003), pp. 688-698

[142] H. Küsters, "Fast Neutron Scattering Models, Slowing Down and Formation of Reactor Spectra", *KFK 1295* (1970)

[143] J.P. Ligou, "Elements Of Nuclear Engineering", Harwood Academic Publishers GmbH (1986); *English translation of "Installations nucléaires" by J. P. Ligou, Presses polytechniques Romandes* (1982)

[144] W.J. Nellis, "Slowing-down distances and times of 0.1 to 14-MeV neutrons in hydrogenous materials", *A. J. Phys.* **45** 445 (1977)

[145] R.A. Forrest, and M.G. Sowerby, Kaye and Laby Online, 16th Edition of Kaye and Laby's Tables of Physical and Chemical Constants (1995); `http://www.kayelaby.npl.co.uk/toc/`

[146] J.M. Blatt, and V.F. Weisskopf, "Theoretical nuclear physics", John Wiley and Sons Inc., New York (1952)

[147] H.W. Geiger, and L. Van Der Zwan, "Radioactive Neutron Source Spectra from ^{9}Be(α,n) cross section data", *Nucl. Inst. Meth. A* **131** (1975), pp. 315-321

[148] A. Zimbal, "Measurement of the spectral fluence rate of reference neutron sources with a liquid scintillator detector", *Rad. Prot. Dos.* **126** (1-4) (2007), pp. 413-417

[149] H.W. Geiger, and C.K. Hargrove, "Neutron spectrum of an ^{241}Am-Be(α,n) source", *Nucl. Phys.* **53** (1964), pp. 204-208

[150] A.D. Vijaya, and A. Kumar, "The neutron spectrum of Am-Be neutron sources", *Nucl. Inst. Meth. A* **111** (1973), pp. 435-440

[151] H. Kluge, and K. Weise, "The neutron energy spectrum of a ^{241}Am-Be(α,n) source and resulting mean fluence to dose equivalent conversion factors", *Rad. Prot. Dos.* **2** (2) (1982), p.85-93

[152] A.J. Peurrung et al., "Direct Fast-Neutron Detection: a Progress Report", Pacific Northwest National Laboratory, Richland, Washington, *PNNL-1* 1994 (1998)

[153] International Standard ISO 8529 Reference neutron radiations - Part 1: Characteristics and methods of production (2001)

[154] J. Chen et al., "The experimental determination of the fraction of neutrons below 1.5 MeV for the Chinese-made Am-Be neutron source", *Nucl. Inst. Meth. A* **583** (2007), pp. 407-411

[155] A. Derbin, and V. Muratova, "Energy calibration with ^{241}Am^{9}Be neutron source", Borexino internal note (2009)

[156] A. Derbin et al., "The study of the registered Charge and the Gatti parameter vs. the AmBe neutron source position", Borexino internal note (2009)

[157] `http://environmentalchemistry.com/yogi/periodic/crosssection.html`

[158] D. Reilly et al., "Passive Nondestructive Assay of Nuclear Materials", Los Alamos National Laboratory, Los Alamos, New Mexico, *LA-UR-90-732* (1991)

[159] S. Abe et al. (KamLAND collaboration), "Study of the Production of Radioactive Isotopes through Cosmic Muon Spallation in KamLAND", *Phys. Rev. C* **81** 025807 (2010); `arXiv:hep-ex/0907.0066v2`

[160] V.A. Kudryavtsev et al., "Neutron background at Boulby mine", IDM 2002, York (UK), September 2-6 2002

[161] B.L. Berman, and S.C. Fultz, "Measurement of the giant dipole resonance with monoenergetic photons", *Rev. Mod. Phys.* **47** 713 (1975)

[162] F.E. Bertrand, "Excitation of the giant isoscalar monopole resonance in ^{144}Sm and ^{154}Sm via inelastic proton scattering", *Ann. Rev. Nucl. Part. Sci.* **26** 457 (1976)

[163] J. Speth, and A. Van der Woude, "Giant resonances in nuclei", *Rep. Progr. Phys.* **44** 719 (1981)

[164] A. Van der Woude, "Giant Resonances", *Prog. in Part. Nucl. Phys.* **18** 217 (1987)

[165] P. Chomaz, "Collective excitations in nuclei", *Report No. GANIL-P-98-01, in: 16e'me' ecole Internationale Joliot-Curie de Physique Nucle'aire, Maubuisson, France, 8-13 Sep 1997* (1997), pp. 107-181

[166] J. Delorme et al., "Pion and neutron production by cosmic-ray muons underground", *Phys. Rev. C* **52** (1995)

[167] V.F. Weisskopf, "Statistics and Nuclear Reactions", *Phys. Rev.* **52** (1937), pp. 295-303

[168] V.F. Weisskopf, and D.H. Ewing, "On the Yield of Nuclear Reactions with Heavy Elements", *Phys. Rev.* **57** (1940), p. 472-485

[169] E.D. Courant, "Direct Photodisintegration Processes in Nuclei", *Phys. Rev.* **82** (1951), pp. 703-709

[170] K.G. Dedrick, "Deuteron-Model Calculation of the High-Energy Nuclear Photoeffect", *Phys. Rev.* **100** (1955), pp. 58-66

[171] J.A. Rawlins, "Investigation of high-energy photoneutrons from carbon", *Nucl. Phys. A* **122**, 1 (1968), pp. 128-144

[172] F.F. Khalchukov et al., "Hadrons and other secondaries generated by cosmic-ray muons underground", *Il Nuovo Cimento C* **18** 5 (1995), pp. 517-529

[173] T. Hagner et al., "Muon-induced production of radioactive isotopes in scintillation detectors", *Astropart. Phys.* **14** (2000), pp. 33-47

[174] V.A. Kudryavtsev et al., "Muon simulations for Super-Kamiokande, KamLAND, and CHOOZ", *Phys. Rev. D* **74** (2006) 053007; `arXiv:hep-ph/0604078v2`

[175] `http://nucleardata.nuclear.lu.se/nucleardata/toi/nucSearch.asp`

[176] M. Deutsch, "Evidence for the Formation of Positronium in Gases", *Phys. Rev.* **82** (1951), pp. 455-456

[177] A. Badertscher et al., "An Improved Limit on Invisible Decays of Positronium", *Phys. Rev. D* **75** (2007) 032004; `arXiv:hep-ex/0609059`

[178] A. Czarnecki, and S.G. Karshenboim, "Decays of Positronium", *Proc. of the 14th International Workshop on High Energy Physics and Quantum Field Theory (QFTHEP99, Moscow 1999)*, *B.B. Levchenko and V.I. Savrin (eds.)*, MSU-Press 2000, pp. 538-544. `arXiv:hep-ph/9911410v1`

[179] S.G. Karshenboim, "Precision Study of Positronium: Testing Bound State QED Theory", *Int. J. Mod. Phys. A* **19** (2004), pp. 3879-3896

[180] D. Franco, G. Consolati, and D. Trezzi, "Positronium signature in organic liquid scintillators for neutrino experiments", *Phys. Rev. C* **83** (2011) 015504; `arXiv:physics.ins-det/1011.5736v2`

[181] B.A Brown, and A. Garcia, "Shape of the β spectra in the A=14 system", *Phys. Rev. C* **52** 6 (1995), pp. 3416-3427

[182] N.D. Gagunashvili, "Comparison of weighted and unweighted histograms" (2006); `arXiv:physics/0605123v1`

[183] P. Belli et al., *Il Nuovo Cimento* **101** A, N.6 (1989), pp. 959-966

[184] C. Arpesella et al. (Borexino collaboration), "Measurement of extremely low radioactivity levels in Borexino", *Astropart. Phys.* **18** (2002), pp. 1-25

[185] L. Cadonati, Ph.D. thesis, Princeton University (2001)

[186] G. Zuzel et al., "Ultra-traces of ^{226}Ra in nylon used in the BOREXINO solar neutrino experiment", *Nucl. Instrum. Meth. A* **498** 1-3 (2003), pp. 240-255

[187] W. Maneschg, Proposal to the Borexino Steering Committee, August 2009

[188] J.C. Maneira, Ph.D. thesis, University of Lisboa (2001)

[189] H.O. Back, Ph.D. thesis, Virginia Polytechnic Institute and State University (2004)

[190] E.D. Arthur et al., "SOURCES 4A: A code for Calculating (αn), Spontaneous Fission, and Delayed Neutron Sources and Spectra", *LA-13639-MS*, September 1999

[191] M. Tarka, University of Zürich, private communication

[192] A.A. Bauer, and F.A. Rough, "Constitution of uranium and thorium alloys", *BMI-1300* (1958)

[193] C. Laubschat, W.-D. Schneider, "Actinide-nobel-metal system: An x-ray photoelectron-spectroscopy study of thorium-platinum, uranium-platinum, and uranium-gold intermetallics", *Phys. Rev B* **23** 3 (1981)

[194] Accelerator Division, Institut de Physique Nucléaire, Orsay, "Rapport d` attivité 2004-05", `http://ipnweb.in2p3.fr/~divac/Accelerator Division.pdf`

[195] E.K. Hyde, "The radiochemistry of Thorium", University of California, Berkeley, California, *NAS-NS 3004* (1960)

[196] R. Eichler, PSI, private communication

[197] M. Laubenstein, LNGS, private communication

[198] W. Maneschg, Diploma thesis, Universität Heidelberg (2007)

[199] S. Neumaier, R. Zwiener, and J. Böhm (eds.), "Experimente im Untergrundlaboratorium UDO der PTB im Bergwerk Asse II - Rückblick und Perspektiven", *PTB-Bericht PTB-DOS-43*, Physikalisch-Technische Bundesanstalt Braunschweig und Berlin, ISBN 3.89701-959-0 (2003), pp. 32-34

[200] B. Wiegel et al., "Spectrometry with the PTB Neutron Multisphere Spectrometer (NEMUS) at Flight Altitudes and at Ground Level", *Nucl. Instrum. Meth. A* **476** (2002), p. 52-57

[201] International Standard ISO 8529-1 (2001)

[202] J.W. Marsh, D.J. Thomas, and M. Burke, "High resolution measurements of neutron energy spectra from Am-Be and Am-B neutron sources", *Nucl. Instrum. Meth. A* **366** (1995), pp. 340-348

[203] International Organization for Standarization (ISO): Guide to the Expression of Uncertainty in Measurements (1995)

[204] D. Budjas et al., "Production and characterisation of a custom-made ^{228}Th source with reduced neutron source strength for the Borexino experiment", paper in preparation

[205] H.-G. Vogt, and H. Schulz, "Grundzüge des praktischen Strahlenschutzes", ISBN 3-446-22850-0 (2004)

[206] M.J. Berger et al., "XCOM: Photon Cross Sections Database", NIST (2009); `http://www.nist.gov/pml/data/xcom/index.cfm`

[207] P. Lombardi, and G. Ranucci, "Time and position distributions in large volume spherical scintillation detectors", (2006) `arXiv:physics/0610080`

[208] K.B. McCarty, Ph.D. thesis, Princeton University (2006)

Acknowledgements

At the end of this work I want to express my gratitude to everybody who supported and encouraged me during this exciting period of my scientific career. This work would have never been accomplished without your great help.

First of all I would like to thank my mentors, Prof. W. Hampel and Prof. S. Schönert, and Prof. M. Lindner for giving me the opportunity to work at MPIK and to participate in the Borexino experiment, where I was able to work in an international collaboration, thus gaining invaluable experience and knowledge. I really appreciate their confidence in all my activities over many years. I also want to express my gratitude to Prof. W. Krätschmer for his interest in this thesis and for his contribution.

I am grateful to the *Graduiertenakademie der Universität Heidelberg* for its financial support by awarding me an LGFG grant during the course of my Ph.D. program.

A special thanks goes to all my colleagues and friends in the Borexino collaboration.
I thank Prof. G. Bellini and Prof. M. Pallavicini for involving me in several working groups and for paying attention to my requests and needs in important situations.
I am very much indebted to D. Franco, A. Razeto and D. D'Angelo for showing me all facets of Borexino including how the detector works, the magic of Echidna and data analysis in general.
A sincere thanks to Aldo Ianni for being a great partner in research and for his endless support. A special thanks to S. Hardy for providing me with useful information about the external calibration system and about the *American way of life*. Thanks a lot to I. Machulin for his invaluable help and interesting discussions about the world around Monte Carlo simulations.
Thanks to Prof. F. von Feilitzsch and Prof. L. Oberauer for giving me the opportunity to spent time at TUM. A special thanks to all "Münchner Jungs", Michi, Quirin, Timo and Jürgen, for our great team work on cosmogenics and for a lot of fun in Bavaria and abroad. Thanks to L. Papp and G. Korga for their explanations about the electronics of Borexino, for unconditional support and humorous discussions. Nagyszerüek vagytok, meg lehet bizni bennetek! Thanks to S. Gazzana, A. Goretti, Andrea Ianni, P. Lombardi and A. Brigatti for their support and for providing me with information about operations on the detector. I would also like to thank Prof. B. Vogelaar and Prof. F. Calaprice for interesting discussions and for their support.
"Un grazie di cuore" to Chiara, Alessandra, Elena, Margherita, Gemma, Livia, Sandra, Francesco, Nicola, Yusuke, Yura, Evgeny, Kirill, Vladislav, Alvaro, Richard, John, Szymon, Daniel, Paolo R., Stefano D., Stefano P., Carlo, Paolo S. and all the other collaborators for a great time spent together at meetings, on shifts and in *ristoranti*.

Concerning the custom-made thorium source for Borexino, I am very grateful to M. Tarka and R. Santorelli, University of Zürich. A great thanks to the "Schweren Jungs" K. Eberhardt, R. Eichler and R. Dressler from PSI, Villigen, and from Institut für Kernchemie in Mainz for their great work on the construction of the source. I would like to thank B. Wiegel and A. Zimbal at PTB, Braunschweig, for their large effort in measuring the neutron source strength and for showing me their facilities. Thanks to O. Scheibe from Eckert und Ziegler Nuclitec GmbH, Braunschweig, for continuous cooperation and for patiently listening to all my requests. Thanks to all those responsible for the radioprotection departments at the different institutes: J. Schreiner, R. Lackner, B. Praast, H. Keller, L. Lembo, A. Giampaoli and M. Laubenstein. It was a real pleasure working with all of you. The realization and characterization of the source is a masterpiece of interdisciplinary cooperation! Finally, I want to thank H.O. Back who worked on the external calibration system years ago and who shared useful information with me.

I am deeply indebted to H. Simgen, my office colleague at MPIK for four years, for his friendship, for precious conversations and for continuously encouraging and trusting me.
I would also like to thank G. Zuzel for his inspiring and helpful comments on my analysis and for an unforgettable trip to Gran Sasso with a broken car.

To everybody working at MPIK: "Thank you very much!". My gratitude especially goes to Alex, Marik, Dusan, James, Alexey, Mark W., Sebastian, Gerd, Herbert, Florian, Mark H., Bernhard, Konstantin, Oleg, Albert, Julia, Bernd, Christian, Christoph, Stefan, Conradin, Ute, Josefa, Erich, Reinhard and Erhard. Thanks also to K. Jänner, M. Reissfelder and D. Schneider for highly efficient work in the mechanical and electronics workshop. A special thanks to F. Köck for the installation of Echidna-related software tools on the MPIK cluster. Many thanks to A. Berneiser for her professional support in bureaucratic issues and for keeping everybody in a good mood.

Thanks to all people from *Laboratori Nazionali del Gran Sasso* and from L' Aquila who strongly support the scientists.

I like to thank the *triumviratus* consisting of Daniel, Bernhard S. and Oliver for their enduring friendship and loyalty over many years. Thanks to Thomas and Norbert for sharing culinary and cultural experiencies, and thanks to Anita, the person I admired the most. I would like to thank M. Thiel, one of the greatest but unrecognized minds of our century, for discussions about philosophy and for his deep friendship. Many thanks to Frank and to my neighbors Betty and Martin for all kinds of help, from watering flowers to proofreading.

Enfin oressi rengrazié döta mia familia, mi genitûrs, fredesc y sorûs, gragn y pici, y a chi co a cherdü en me y tles steres. Al ne é nia sté saurí, mo vigne gota de soiûs a paié la mëia.
Ein großes Dankeschön an Hannelore und Werner!

En iolan sonza confin a Yvonne por söa pazionza y so aiüt gaiêrt. Iolan por en monn da corú.